Towards Coupling Superconducting Flux Qubits to Single Bismuth Donors in Silicon

Tikai Chang

Department of Physics

Ph.D. Thesis

Submitted to the Senate of Bar-Ilan University

Ramat-Gan, Israel November 20, 2022

The results described in this document are confidential and not for public dissemination.

This work was carried out under the supervision of Dr. Michael Stern (Department of Physics, Bar Ilan University)

Abstract

Quantum computers have triggered intense interest since the discovery of the first quantum algorithms two decades ago. Indeed, it was shown theoretically that these computers can solve easily certain computationally demanding problems like factoring large numbers into prime numbers or searching efficiently in databases. These unique features have lead scientists to imagine building quantum processors based on various physical realizations.

The construction of a quantum computer represents a tremendous scientific and technological challenge due to the extreme fragility of quantum information. The physical support of quantum information, namely a quantum bit (qubit), must at the same time be strongly coupled by gates to compute information, and well decoupled from its environment to keep its quantum behavior. An interesting physical system for realizing such qubits are magnetic impurities in semiconductors, such as bismuth spins in silicon. Indeed, spins in semiconductors can reach extremely long coherence times - of the order of seconds. Yet it is extremely difficult to establish and control an efficient spin-spin coupling. The objective of this work is to solve this problem and to develop an efficient way to couple reliably distant spins. To achieve this goal, we use a superconducting circuit called flux qubit, which behaves as a mediator - or quantum bus - between different spins.

In this thesis, we develop the necessary tools to solve several major experimental issues for the realization of this scheme. First, in order to use the flux qubit as a quantum bus, we need to reach the so-called strong coupling regime, where the coupling between the mediator and the spin is greater than its decoherence rate. In a first work, we demonstrate flux qubits with unprecedented and reproducible coherence properties ($T_1 \sim 15-20\,\mu s$, $T_{2E}^{\varphi} \sim 15-30\,\mu s$), which makes this regime attainable. Secondly, the flux qubit transition frequency should be controllable in order to switch on and off its coupling to the spin. In a second work, we demonstrate tunable flux qubits with long coherence times, one to two orders of magnitude longer than the state of the art. Finally, bismuth donors should be localized in the close vicinity of the qubit loop, in order to maximize the coupling. Yet, the presence of a metallic circuit close to the donors may ionize them. This effect should be controlled by the application of a gate voltage. To achieve this, we developed flux qubits with thin constrictions ($20-30\,nm$) and readout resonators with Bragg Filters that allow the application of a voltage bias on the substrate, while keeping the flux qubits protected from relaxation and decoherence.

Contents

1 Scientific background

1.1 DiVincenzo's criteria for quantum computation

In 1982, Richard Feynman suggested harnessing the strange properties of entanglement and superposition in Quantum Mechanics to build a computer. Summarized in a famous quote "Nature isn't classical, dammit, and if you want to make a simulation of nature, you'd better make it quantum mechanical", the initial motivation was to build a device capable of quantum simulation, capable of aiding our understanding in various fields such as condensed matter physics and bio-chemistry. Years later, the first quantum algorithms were invented. Shor's Prime Factorisation algorithm [1] and Grover's Search algorithm [2] have shown that a *Universal Quantum Computer* may solve certain algorithmic problems that have exponential complexity on a classical computer.

The physical implementation of quantum processors requires stringent conditions on both the qubit register and the set of quantum gates able to manipulate it. These properties are summarized in the so-called DiVincenzo's criteria [3]:

1. The physical system must be scalable
2. The qubit register can be properly initialized
3. The set of quantum gates must be sufficient to manipulate the qubit register
4. The gate operations have high fidelity
5. The state of the qubit register can be efficiently readout after the calculation is performed

In the last two decades, different physical implementations have been thoroughly explored. Among them, cold ions in laser traps [4, 5], quantum dots in semiconductors [6, 7], nuclear/electronic spins in semiconductors [8] and superconducting qubits [9, 10]. Each of these different implementations has its own advantages and drawbacks. For instance, spins in semiconductors can store safely quantum information with low error rates [11, 12], but are hard to manipulate and readout. Superconducting qubits [9, 10] are scalable, easy to measure but have relatively low fidelities. Over the years, the fidelity of various superconducting qubits has been constantly improved and their coherence time has considerably increased from a few nanoseconds [13, 14, 15] to the millisecond range [16, 17, 18], allowing for the recent race of Tech Giants such as IBM and Google to demonstrate Quantum Supremacy [19].

A promising research direction is to combine spins and superconducting circuits and build a hybrid quantum system that would hopefully inherit the advantages of each one of the different components [20, 21]. Indeed, spins in semiconductors with their low error rates are perfect system to store reliably the quantum information while superconducting qubits are perfect systems to process easily fast quantum gates, thanks to their strong coupling with external fields. This situation resembles that in classical computers where electronic circuits and magnetic drives achieve respectively fast processing and robust long-time information storage.

The key requirement for this hybrid architecture is to ensure that the different components can efficiently communicate with each other. In quantum optics, this condition is called the *strong coupling regime*. This regime can be achieved by using a quantum bus, which acts as a bridge between spins and superconducting circuits. The ultimate goal of this PhD project is to fabricate such a quantum bus and reach the strong coupling regime between the electronic spin of a donor in silicon and a superconducting circuit. This achievement would pave the way for the realization of a spin-based quantum processor.

1.2 Towards building a spin-based quantum processor

Spin-based quantum processors are often considered as one of the major candidate for the physical realization of quantum processors. In the following, we will analyze briefly the advantages and drawbacks of such a technology using the DiVicenzo criteria as a guideline.

Scalability - Spin-based platforms for quantum technology is appealing thanks to the maturity of the semiconductor manufacturing industry. In particular, ion implantation is a key process to doping semiconductors. This process has been refined in recent years to the point of resolving temporally spin implantation events [22, 23] as well as the control of the spatial location of implantation using nanostencil fabricated in an AFM cantilever [24]. The integration of spins with metal-oxide-semiconductor (MOS) nanostructures is also a standard process in the foundaries. It is thus clear that spin-based platforms perform well in terms of DiVincenzo's criterion for scalability.

Manipulation with low error rates - Single qubit operations can be implemented by placing a MW antenna close to the spin, allowing for the application of MW pulses with a given amplitude and duration [25, 26]. Such quantum operations may have extremely low error rates. Indeed, by choosing a proper spinless surrounding lattice, an electron spin such as the one bound to a phosphorus donor in isotopically purified silicon can achieve very long coherence times of hundreds of microseconds [11, 12], and its nuclear spin can reach more than 3 orders of magnitude longer. Other donors in the group V such as bismuth also possess similar long coherence times [27].

Spin readout - Regarding the measurement capability of such platforms, a single shot method has been developed [26] for phosphorous impurities in silicon as presented in Fig.1.1. Voltages applied on top gates TG, LB, RB form a quantum dot for a 2D electron gas situated in the Si substrate [28]. This quantum dot acts as a single electron transistor and is used to measure Coulomb conductance peaks. Tuning the electro-chemical potential of the quantum dot (using the PL gate in the figure), the electron of the donor may leak into the quantum dot depending on the paramagnetic alignment of its nuclear/electronic spin. The electron thus serves as an ancilla qubit for quantum non-demolition measurement of the single ^{31}P nuclear spin. The controlled leak and recapture of the electron also serves as a good way to initialize the spin qubit.

Several other different methods for spin readout have been implemented in the last two decades. For instance, one can detect the spin-dependent fluorescence of a single NV center in diamond [29]. The advantage of this technique is that it can be implemented at room temperature and that many

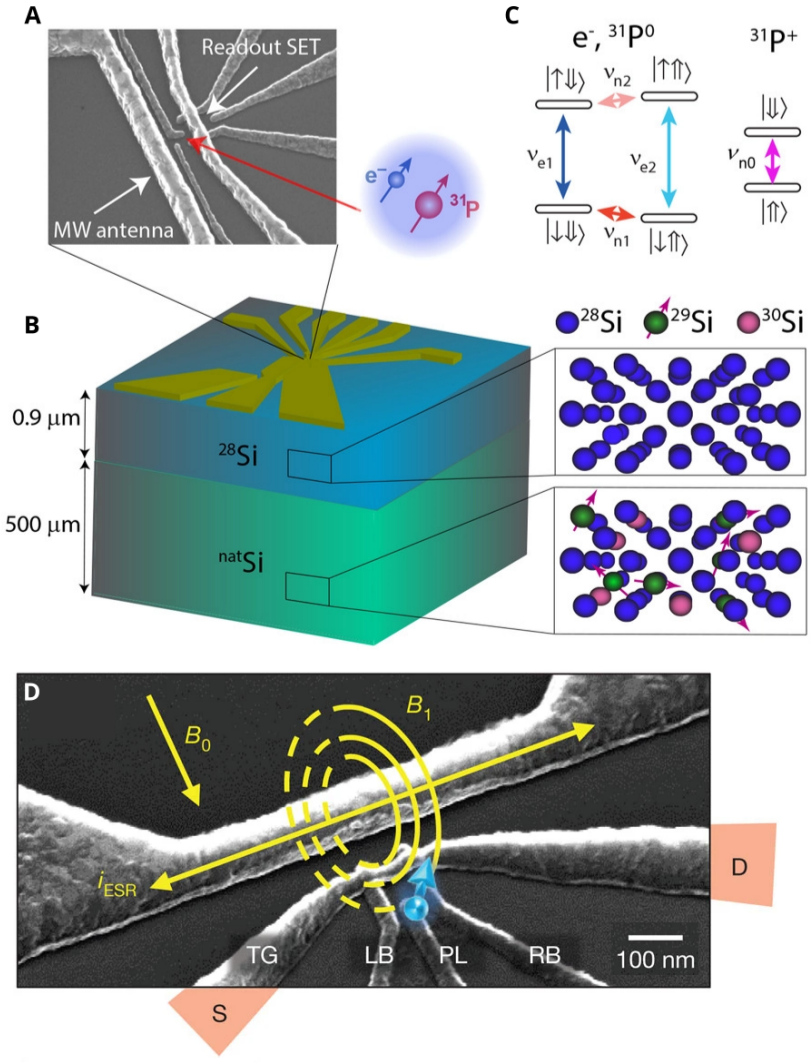

Figure 1.1: **A.** Scanning electron micrograph of the readout and control device of a single-donor Si:P implanted at a depth of 15 nm below the sample surface. **B.** Isotopically enriched ^{28}Si epilayer can be employed to enhance spin coherence times. **C.** Energy levels and transitions of states involving different electron (simple arrow in ket notation) and nuclear (double arrow) spins. **D.** Close up showing the single donor spin (blue arrow). A static magnetic field B_0 is applied in the plane parallel to the substrate surface whereas the AC field generated by the antenna is perpendicular to the substrate plane. Adapted from Ref.[8, 26]

individual spins can be selectively readout using the same confocal microscope and optical single-photon detector. Along these lines, a more general method has been developped recently. This method can also detect many individual spins with the same device. Moreover, it can be adapted to the measurement of almost any kind of spin species at cryogenic temperatures. It consists of enhancing the Purcell emission of a photon by a spin embedded into a resonant cavity, and its subsequent detection by a single microwave photon detector (SMPD) [30].

The major challenge that remains for a quantum processor architecture based on electron/nuclear spin is the realization of gates between distant individual spins [31] required for full control of the qubit register.

1.3 Coupling distant individual spins

There are two strategies when it comes to coupling distant spins. We can either employ a direct coupling between neighboring spins, or we can use an indirect coupling method where a common intermediate element may couple two distant spins.

1.3.1 Direct coupling

The Kane Computer [32] is a well known proposal involving inter-coupled spins controlled electrically using an array of top gates. The coupling between adjacent spins is achieved by controlling the exchange interaction. The idea is to tune the overlap of the electron wave function of neighboring spins using voltage gates. The Pauli exclusion principle gives rise to a spin-dependent interaction, from which two-qubit gates can be implemented. Despite potentially reaching coupling strengths of the order of GHz [33, 34, 35], the exchange interaction requires the donors to be placed within 15 nm or less from each other, posing a significant challenge to the fabrication tolerances and the space for the auxiliary structures needed for control, readout and interconnections.

A recent strategy consists in implementing the so-called Flip-Flop interaction for phosphorous donors [36, 37] which has less stringent requirements on the inter-spin distance ($\sim$150 nm). The working principle of this technique is shown in Fig.1.2. A strong magnetic field B_0 is applied ($(\gamma_e + \gamma_n) B_0 \gg A$, where $\gamma_{e/n}$ are the electronic and nuclear gyromagnetic ratios and A is the hyperfine coupling strength) such that the spin eigenstates are separable $\{|\downarrow\Downarrow\rangle, |\downarrow\Uparrow\rangle, |\uparrow\Downarrow\rangle, |\uparrow\Uparrow\rangle\}$. An electric field E_z applied by a gate induces a spatial separation in the electron wave function and the nucleus, and thus the hyperfine interaction strength $A(E_z)$ can be reduced from around 100 MHz down to zero. Since the hyperfine interaction $A\ S \cdot I$ is transverse in the Flip-Flop (FF) basis $|\uparrow\Downarrow\rangle, |\downarrow\Uparrow\rangle$, the two states mix and lead to a tunable splitting $\epsilon_{ff} = \sqrt{(\gamma_e + \gamma_n)^2 B_0^2 + A^2}$ arising from the diagonalization of the Hamiltonian

$$\begin{aligned} H/\hbar &= B_0 (\gamma_e S_z - \gamma_n I_z) + A\ S \cdot I \\ &= (\gamma_e + \gamma_n) B_0 \frac{\sigma_z^{FF}}{2} + A \frac{\sigma_x^{FF}}{2} \end{aligned}$$

the hyperfine strength can be directly modulated by an AC electric field, enabling single qubit Rabi

oscillations. In [37], the maximal Rabi frequency observed was $\Omega/2\pi = 120\,\text{kHz}$. The coherence times of the flip-flop qubit are $T_1 = 173\,\text{s}$ and a pure dephasing rate $T_2 = 4.1\,\mu\text{s}$ and $T_{2E} = 184\,\mu\text{s}$. Experiments have yet to be performed in the large-dipole regime as shown in Fig.1.2. In this regime, the donor is half-ionized and the wavefunction is equally shared between the donor center and the interface quantum dot. According to theory [36], it may allow for one-qubit and two-qubit gate times to reach the order of $50 \sim 100\,\text{ns}$ thanks to the large generated dipole.

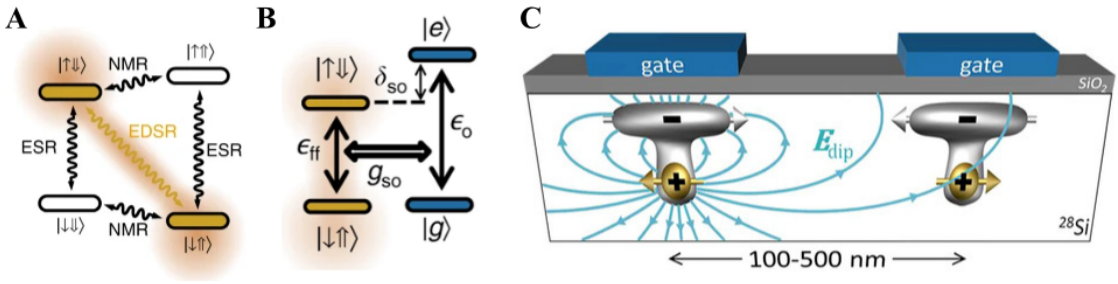

Figure 1.2: **The large-dipole regime**. **A.** Si:P electron-nuclear spin levels, showing standard electron spin resonance (ESR) and nuclear magnetic resonance (NMR) transitions, together with hyperfine-enabled electric dipole spin resonance. **B.** Hybridization of the flip-flop TLS and the charge qubit TLS. **C.** Long-range coupling between the hybridized spin-qubits. Adapted from Ref.[36].

1.3.2 Indirect coupling

In the previous section we mentioned two ways of directly coupling spins up to a few hundreds nm apart. In contrast, indirect coupling strategy involves using a common intermediate element such as a superconducting resonator to couple to two distant spins at much longer distances. To check the feasibility of such an idea, let us estimate the order of magnitude of magnetic coupling strength to a superconducting circuit [38]. The amplitude of the AC magnetic field generated by the circuit can be straightforwardly determined by using Biot and Savart law. Assuming an infinitely thin wire, the field amplitude is given by $B = \frac{\mu_0 I}{2\pi r}$ where I is the current flowing in the wire, and r the distance from the wire to the spin. The quantum treatment of the circuit replaces I by its operator $\hat{I}$ which can be written as a function of annihilation and creation operators a and $a^\dagger$ as

$$\hat{I} = \delta I \left(a + a^\dagger\right)$$

where

$$\delta I = \omega_r \sqrt{\frac{\hbar}{2Z_0}} \tag{1.1}$$

are the quantum fluctuations of the current, Z_0 being the characteristic impedance of the resonator and ω_r its resonance frequency. Assuming that the AC magnetic field $\vec{B} = B\,\vec{e_x}$ is oriented in a direction

perpendicular to the spin axis ($\vec{e_z}$), the magnetic coupling $H_c = \gamma_e \vec{S} \cdot \vec{B}$ is given by

$$\begin{aligned} H_c/\hbar &= \gamma_e \left(S_x \vec{e_x} + S_y \vec{e_y} + S_z \vec{e_z}\right) \cdot \vec{B} \\ &= \gamma_e \cdot \frac{\mu_0 \delta I}{2\pi r} S_x \left(a + a^\dagger\right) \end{aligned}$$

where $\gamma_e = 2\pi \cdot 27.997\,\mathrm{GHz\,T^{-1}}$ is the electron gyromagnetic ratio. We thus get the coupling constant

$$\frac{g}{2\pi} = \frac{\gamma_e}{2\pi} \cdot \frac{\mu_0 \delta I}{2\pi r} \left|\langle \uparrow | S_x | \downarrow \rangle\right| = 2.8 \frac{\delta I\,[\mathrm{nA}]}{r\,[\mu\mathrm{m}]}\,[\mathrm{Hz}] \tag{1.2}$$

where the current fluctuations δI of an LC resonator having a frequency in the GHz range is comprised between $20 \sim 50\,\mathrm{nA}$. Thus, we obtain a coupling constant $g \sim 1\,\mathrm{kHz}$ for a spin situated at a distance of 100 nm from the circuit.

One solution to overcome this weak coupling is to couple to a large ensemble of N_{ens} spins. This approach will increase the effective coupling strength by a factor $g_{ens}/g = \sqrt{N_{ens}}$ [39, 40] and allow to reach the strong coupling regime. In recent years, various realizations of such strong coupling to spin ensemble have been demonstrated in different substrates such as diamond [41, 42] and Y2SiO5 crystal [43, 44]. Typically, the low-power transmission was measured for a resonator and the width of the vacuum Rabi splitting gave a measurement of the coupling [41]. Built upon the foundation of this work, several attempts to use the dark modes of the collective spin ensemble were made in [40, 45, 46]. The elegant idea is to use time-reversal π pulse as a way to *rewind the cassette* and playback the stored quantum states in the dark states of the spin, therefore harnessing the spin ensemble as a multi-mode quantum memory. This memory can be reinitialized to its ground state by engineering the Purcell decay of the ensemble into the resonator [47]. Yet, due to the leakage from the bright mode to the dark modes, the storage efficiency of such memories remains rather low.

The strong coupling regime can also be observed by translating the spin degree of freedom into an electrical dipole. This is interesting because the coupling strength of an electrical dipole to a microwave resonator may be orders of magnitude larger than for a magnetic dipole. Assuming that the AC electric field generated by the resonator $\vec{E} = E\,\vec{e_z}$ is parallel to the dipole axis ($\vec{e_z}$), the electric coupling $H_c = -\vec{E} \cdot \vec{D}$ can be written as

$$H_c = \boldsymbol{i} e \delta V \left(d/r\right) \sigma_x \left(a - a^\dagger\right)$$

We thus get the coupling constant

$$\frac{g}{2\pi} = \frac{e\delta V}{h} \frac{d}{r} = 240 \left(\frac{d}{r}\right) \left(\delta V\,[\mu\mathrm{V}]\right)\,[\mathrm{MHz}]$$

where r is the inter-gate distance, d the dipole size, and $\delta V = \omega_r \sqrt{\frac{\hbar Z_0}{2}}$ are the voltage quantum fluctuations of the resonator. For $\delta V \approx 1\,\mu\mathrm{V}$, $d \approx 2\,\mathrm{nm}$ and $r \approx 1\,\mu\mathrm{m}$, we get $g/2\pi \approx 500\,\mathrm{kHz}$. In 2015, Viennot et al. [48] have used such a method and translated an electron spin in a carbon

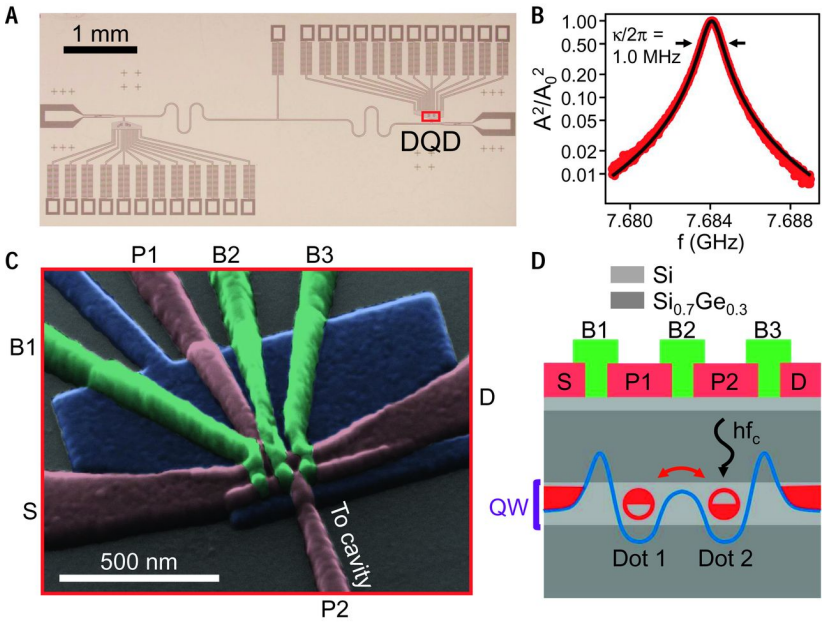

Figure 1.3: **Electrical coupling of a quantum dot**. **A.** Optical image of a superconducting cavity containing a Si double quantum dot (DQD). **B.** Cavity transmission as a function of frequency f and its fit to a Lorentzian (black line). **C.** Tilted-angle false-color scanning electron microscope image of the DQD, with plunger (P1, P2) and barrier gates (B1-B3). **D.** Schematic cross-section through the DQD gates and Si/SiGe heterostructure. An excess electron is confined in the quantum well (QW) within the double-well potential (blue line) created by the gate electrodes. A cavity photon interacts with the electron. Adapted from Ref.[49]

nanotube into an electrical dipole by the application of a local magnetic gradient in order to reach the strong coupling regime. Along these lines, Petta and coworkers have demonstrated the strong coupling between a silicon double quantum dot and a microwave coplanar waveguide resonator [49]. They then added a cobalt micro-magnet to transfer the spin degree of freedom to the position of the electron in the double quantum dot [50]. A spin–photon coupling rates of up to 11 MHz was reported and the strong coupling was achieved. However, due to the presence of charge noise, the spin decoherence rate was severely degraded to a few megahertz.

1.4 Situating our work

Clearly, using an electrical degree of freedom is a good solution for reaching the strong coupling regime between a nano-object and a microwave resonator. However, the same electrical degree of freedom makes this nano-object sensitive to electrical noise which implies a severe degradation of its coherence properties. A spin is intrinsically immune to charge noise, but its magnetic coupling to a circuit requires large current quantum fluctuations. The ultimate goal of this work is to develop a circuit with such large fluctuations in order to make it possible to reach the strong coupling regime with a single spin, without compromising the coherence properties of the spin.

2 Methodology

As mentioned earlier in Eq.1.1, the current quantum fluctuations of a linear resonator are completely determined by the resonance frequency and the characteristic impedance of the resonator. In practice, it is difficult to decrease the characteristic impedance below $10\,\Omega$ [51], which limits the current quantum fluctuations in the range of $20 - 50\,\mathrm{nA}$ for a linear system. In our project, we make use of a highly non-linear superconducting circuit which can reach much higher current quantum fluctuations up to $500\,\mathrm{nA}$. This circuit is called a flux qubit. In this thesis, we show that the coherence time of this circuit can reach $30\,\mu\mathrm{s}$ (see section §6.1).

The second parameter to enhance the coupling is the distance between the spin and the circuit. Bismuth donors in silicon (Si:Bi) are a good choice since they possess long coherence times ($\sim 200\,\mu\mathrm{s}$) and can be implanted with good yield and low straggling ($4.5\,\mathrm{nm}$ at 40keV). Furthermore, their transition frequencies at low magnetic fields ($B < 100\,\mathrm{G}$) are convenient for resonantly coupling with flux qubits at $f \sim 7.4\,\mathrm{GHz}$. In this range of frequencies, flux qubits are relatively well protected from flux noise, which is often considered as the main source of dephasing of these qubits (see section §3.5).

By implanting precisely spins at a depth of $\sim 25\,\mathrm{nm}$ in the close vicinity of a thin nanowire where the current fluctuations are concentrated, we could reach a coupling strength of $g/2\pi = 25 - 50\,\mathrm{kHz}$. We thus expect to have $gT_2 \sim 10$, reaching the strong coupling regime.

2.1 Bismuth Donors in Silicon

Bismuth donors appear naturally in bulk silicon. These are impurity centers where a substitution of a silicon atom by a bismuth atom has occurred. Silicon being part of the IV group, one silicon atom can form four covalent bonds in the lattice structure. Bismuth is however in the V group, having one more valence electron. As a result, one excess non-bonding electron may easily be ionized to form a fully occupied outer valence shell. In semiconductor terminology, bismuth is a shallow[1] donor, with a binding energy of $E_{B,\mathrm{Si:Bi}} = 71$ meV.

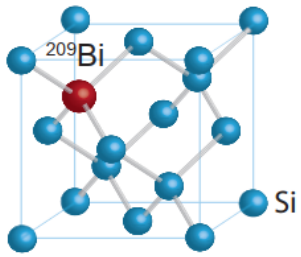

Bi is the heaviest stable group V donor, with an atomic mass of 209 u. The choice of using bismuth thus results in reduced straggling when implanted to a certain depth in silicon compared to other group V donors [52]. It also has the largest hyperfine coupling of all group V donors, which increases

[1] its level is only slightly lower than the conduction band such that thermal excitations may easily populate/depopulate it, leading to charge conduction.

its zero-field transition energy to a frequency ∼7.4 GHz, and is thus well adapted to superconducting circuits.

2.1.1 Energy Spectrum of a bismuth donor

Hamiltonian The bismuth donor has a nuclear spin $I = \frac{9}{2}$ and an electron spin $S = \frac{1}{2}$. The Hamiltonian of a single bismuth donor in Silicon can be written as follows[2]

$$H_{\text{Si:Bi}}/\hbar = +\gamma_e \vec{S}\cdot\vec{B} - \gamma_n \vec{I}\cdot\vec{B} + A\,\vec{S}\cdot\vec{I}$$

The first two terms in the Hamiltonian are respectively the Zeeman electronic and nuclear terms, where $\gamma_e/2\pi = 27.997\,\text{GHz}\,\text{T}^{-1}$ and $\gamma_n/2\pi = 6.962\,\text{MHz}\,\text{T}^{-1}$ are the electron (resp. nuclear) gyromagnetic ratios. The last term is the hyperfine coupling term ($A/2\pi = 1.48\,\text{GHz}$) and is isotropic due to the symmetry of the donor.

Ground and excited manifolds of eigenstates After diagonalization of the Hamiltonian, we get twenty eigenstates. At zero magnetic field, the ground and excited states of the system are multi-degenerate, and form two manifolds separated by $f = 7.377\,\text{GHz}$. Nine states of different total angular momenta form the ground state $|G\rangle$ and eleven states form the excited state denoted in the following as $|E\rangle$. When a non-zero magnetic field is applied, the degeneracy is lifted. In Fig.2.1, we label the eigenstates according to their total angular momentum $m_{tot} = m_S + m_I$, i.e. $|G, -4\ldots+4\rangle$ and $|E, -5\ldots+5\rangle$.

In order to estimate the transition matrices it is convenient to write these states in the tensor product basis $|-\frac{9}{2}\ldots+\frac{9}{2}, \downarrow/\uparrow\rangle$. For instance,

$$|G,+4\rangle = 0.95\,|\frac{+9}{2},\downarrow\rangle - 0.32\,|\frac{+7}{2},\uparrow\rangle$$
$$|G,-4\rangle = 0.32\,|\frac{-7}{2},\downarrow\rangle - 0.95\,|\frac{-9}{2},\uparrow\rangle$$

while the two lowest and two highest excited states are

$$|E,-5\rangle = |\frac{-9}{2},\downarrow\rangle$$
$$|E,-4\rangle = 0.95\,|\frac{+9}{2},\downarrow\rangle + 0.32\,|\frac{+7}{2},\uparrow\rangle$$
$$|E,+4\rangle = 0.32\,|\frac{+9}{2},\downarrow\rangle + 0.95\,|\frac{+7}{2},\uparrow\rangle$$
$$|E,+5\rangle = |\frac{+9}{2},\uparrow\rangle$$

[2]The dot product expressions can be expanded into a sum of components along the three axes (e.g. $\vec{S}\cdot\vec{I} \equiv S_x I_x + S_y I_y + S_z I_z$).

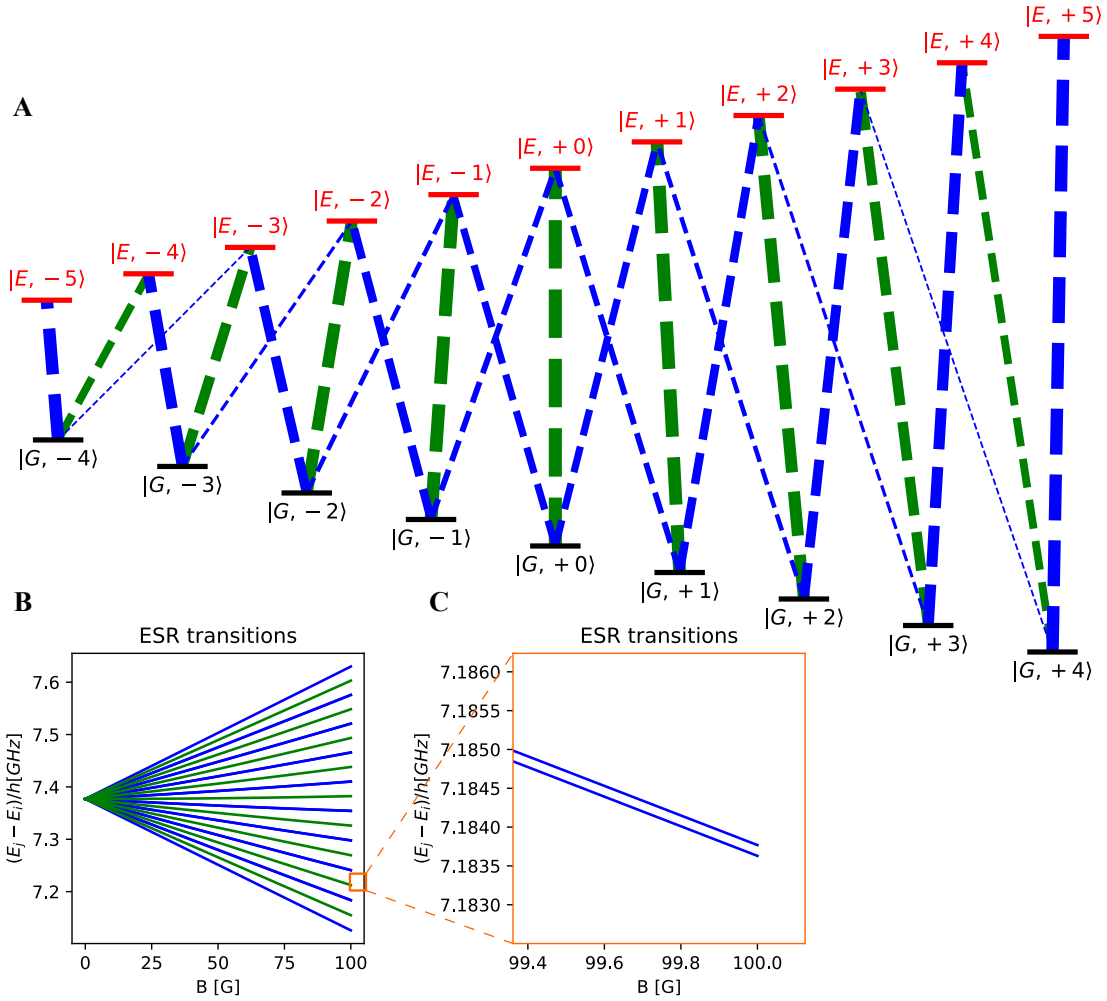

D

$\lvert S_x\rvert/\lvert S_z\rvert$	$\lvert G,-4\rangle$	$\lvert G,-3\rangle$	$\lvert G,-2\rangle$	$\lvert G,-1\rangle$	$\lvert G,0\rangle$	$\lvert G,1\rangle$	$\lvert G,2\rangle$	$\lvert G,3\rangle$	$\lvert G,4\rangle$
$\lvert E,-5\rangle$	0.47								
$\lvert E,-4\rangle$	0.30	0.42							
$\lvert E,-3\rangle$	0.07	0.40	0.37						
$\lvert E,-2\rangle$		0.12	0.46	0.32					
$\lvert E,-1\rangle$			0.17	0.49	0.27				
$\lvert E,0\rangle$				0.22	0.50	0.22			
$\lvert E,-1\rangle$					0.27	0.49	0.17		
$\lvert E,-2\rangle$						0.32	0.46	0.12	
$\lvert E,-3\rangle$							0.37	0.40	0.07
$\lvert E,-4\rangle$								0.42	0.30
$\lvert E,-5\rangle$									0.47

Figure 2.1: **A.** S_z (green) and S_x (blue) ESR transition rules at $B = 1$ G. The linewidth is proportional to the transition strength $\left|\langle i|\, S_{x/z}\, |j\rangle\right|/\hbar$. On the top right, we show the transition frequencies as a function of the magnetic field. A zoom showing the degenerate Sx transitions is shown in the bottom right. **B.** The dependence of the $S_{x/z}$ transition frequencies on the magnetic field **C.** Close-up view of the S_x doublet ($|G,i\rangle \to |E,i+1\rangle$ and $|G,i+1\rangle \to |E,i\rangle$) at $B = 100$ G. **D.** Table showing the transition strengths at the low magnetic-field limit.

Transition rules As shown in Fig.2.1A, there is a total of 27 ESR transitions that link the excited state manifold to the ground state manifold.

The operator S_x allows for ESR transitions from $|G, m_{tot}\rangle$ to $|E, m_{tot} \pm 1\rangle$. These transitions are represented in blue in the figure. It is noteworthy that the energy corresponding to the transition $|G, m_{tot}\rangle \leftrightarrow |E, m_{tot} + 1\rangle$ and to the transition $|G, m_{tot} + 1\rangle \leftrightarrow |E, m_{tot}\rangle$ are almost degenerate (see Fig.2.1C).

The operator S_z which conserves angular momentum, links the states $|G, m_{tot}\rangle$ to the states $|E, m_{tot}\rangle$. These transitions are represented in green color in the figure.

In Fig.2.1D, we calculated the relative strength of the different possible transitions that connect the ground manifold to the excited one. The transition frequencies at low fields are well described by

$$\Delta\omega\left(\langle G, m_{tot}| S_x |E, m_{tot} + 1\rangle\right) \approx 5A + \frac{2m_{tot} + 1}{10}\gamma_e B_0 \tag{2.1}$$
$$\Delta\omega\left(\langle G, m_{tot}| S_z |E, m_{tot}\rangle\right) \approx 5A + \frac{2m_{tot}}{10}\gamma_e B_0$$

Population within the ground state manifold When the external magnetic field is 1 G, the splitting between the internal levels of the ground state manifold is 300 kHz only. Even at 100 G, the splitting is 30 MHz. The temperature at which our experiments are carried out ($T = 15$ mK) corresponds to $k_B T/h = 300$ MHz, which is hot with respect to the energy difference between the hyperfine states. At thermal equilibrium, we expect therefore a random uniform occupation of the ground state manifold. Each spin will have a different hyperfine state. This makes them individually addressable, given that the expected linewidth (~ 1 kHz) of individual spins is much smaller than the level spacing.

2.1.2 Long coherence times T_1 and T_2

Extremely long relaxation times at dilution temperatures At low temperature, the relaxation time T_1 of donors in silicon can be extremely long. In Ref.[26], the relaxation time of a single phosphorous donor was measured to be $T_1 \sim 0.7$ s. In Ref.[47] non-radiative energy relaxation of an ensemble of bismuth donors was measured to be 1500 s at dilution temperatures $T \approx 20$ mK. The coherence of bismuth donors is thus limited mainly by pure dephasing.

Decoherence mechanisms of bismuth donors The coherence time of donors in silicon is expected to be long due to their spinless environment (^{28}Si). However, the presence of a spin-1/2 isotope ^{29}Si naturally present in silicon with an abundance of 4.7% limits it substantially. For instance in Ref.[26], the coherence time of a single phosphorous donor was limited by these isotopes to $T_2^* \approx 55$ ns. This time can be extended by dynamical decoupling using an Hahn-Echo sequence ($\pi/2 - \tau - \pi - \tau -$Echo) up to $T_2 \approx 0.2$ ms. By using an isotopically purified sample, Ref.[12] extended coherence times to $T_2^* = 270$ µs and $T_2 = 1$ ms. In these samples [26, 12], the spins are located close to the surface which limits their dephasing due to defects such as dangling bonds.

Si:P	Impurity concentration (cm^{-3})	^{29}Si density (ppm)	Coherence time (ms)	Ref.
Single donor	10^{12}	47000 (^{nat}Si)	$T_2 = 0.206$ / $T_2^* = 55 \cdot 10^{-6}$	[26]
	10^{12}	800	$T_2 = 1$ / $T_2^* = 0.27$	[12]
Ensemble	[2-5]$\times 10^{14}$	800	$T_2 = 6.5$	[53]
	8.7×10^{14}	50	$T_2 = 2.8$	[54]
	1×10^{15}	800	$T_2 = 4$	[53]
	1.6×10^{16}	50	$T_2 = 0.27$	[54]

Si:Bi	Impurity concentration (cm^{-3})	^{29}Si density (ppm)	Coherence time (ms)	Ref.
Ensemble	3.6×10^{14}	100	$T_2 \approx 50$ / $T_2^{CT} = 2700$	[27]
	1×10^{15}	47000 (^{nat}Si)	$T_2 \approx 0.8$ / $T_2^{CT} = 93$	
	2×10^{15}	100	$T_2 \approx 15$ / $T_2^{CT} = 500$	
	4.4×10^{15}	100	$T_2 = 6$ / $T_2^{CT} = 170$	
	8×10^{16}	500	$T_2 \sim 3.3$ / $T_2^{CT} \sim 300$	[55]

Table 2.1: Coherence properties of donors in silicon versus impurity and ^{29}Si concentration.

In ensemble experiments, the principal mechanism of decoherence arises from the magnetic dipole dipole interactions with surrounding impurities. These are depicted in Fig.2.2 and include flip-flops, spectral and instantaneous diffusion to neighboring spins. As a result of these interactions, T_2 decreases with increasing impurity concentration as shown in Tab.2.1. Spectral diffusion consists of the dephasing of the central spin through interaction with other non-resonant spins (see Fig.2.2). Instantaneous diffusion and direct flip-flops concern only dipole interaction with resonant spins. Some of these mechanisms can be canceled by Hahn-echo ($\pi/2 - \tau - \pi - \tau-$Echo) and some cannot. Indeed, if the neighboring spins also fall within the bandwidth of the π pulse, they are also flipped and the sign of the interaction term is not reversed. As a consequence, instantaneous diffusion (ID) and direct flip-flops (dFF) cannot be canceled by spin echo.

One particularity of Si:Bi compared to Si:P is the presence of clock transitions [27], which are magnetic sweet spots where the slope $\partial f/\partial B$ of transition frequency locally becomes zero. Spins operating under a clock transition have better coherence properties due to their insensitivity to variations of the surrounding magnetic field. Therefore, spectral and instantaneous diffusion mechanisms are canceled, leaving only direct and indirect flip-flops (iFF). At clock transition, it was possible to measure a coherence time up to 2.7 s in an isotopically purified sample [27].

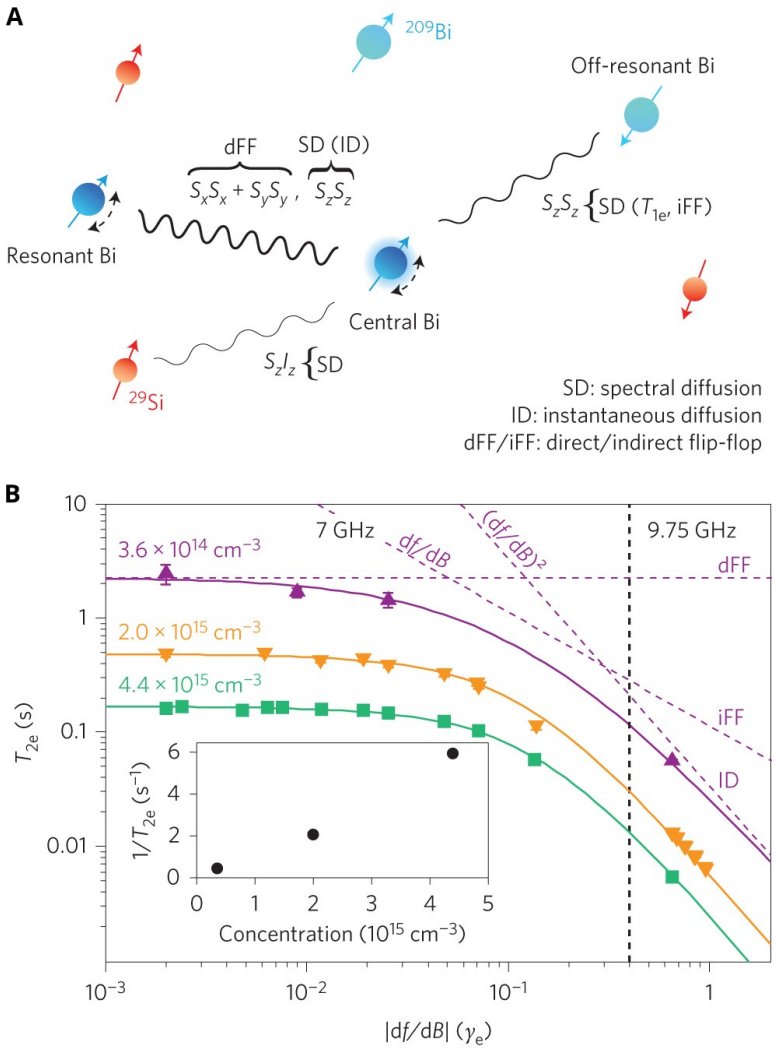

Figure 2.2: **A.** Decoherence mechanisms arising from dipole-dipole interaction **B.** Dependency on df/dB of the various mechanisms in Si:Bi. Image adapted from [27].

Interpolating to our single spin experiment in ^{28}Si:Bi The exact clock transitions requires however a strong magnetic field ($25 \sim 200\,\mathrm{mT}$ for ESR clock transitions) which are difficult[3] to reach in this project.

The average dipole coupling rate between two nearest neighbor Bi donor electron spins is about $1\,\mathrm{kHz}$ for a donor concentration of $10^{17}\mathrm{cm}^{-3}$. This coupling is 3 orders of magnitude smaller than the strain-induced inhomogeneous broadening separating different spins $\sim 2\,\mathrm{MHz}$ (see Fig.2.4). As a result, resonant mechanisms such as direct flip-flops and instantaneous diffusion is largely absent for the spins we consider.

Using an isotopically purified sample, the only remaining mechanism affecting T_2 are the indirect

[3]The out-of-plane field are in the order of a few G (see section §2.2), in-plane field applied by a vector magnet can reach 100 G (see section 2.3.1)

flip-flops from non-resonant bismuth donors. From the asymptotic line in Fig.2.2, we can estimate this to be in the order of 200 µs for an impurity concentration of $2 \times 10^{17}\mathrm{cm}^{-3}$ (see Fig.2.2B, iFF at $|\partial f/\partial B|\,/\gamma_e = 1$). This estimation is comparable to $T_2^* = 0.27\,\mathrm{ms}$ measured in [12] for single donor spins in the vicinity of the surface, where coherence is likely limited by surface defects. We therefore have good reason to believe these numbers will be similar in magnitude in our devices, given that the donor target (Si:Bi instead of Si:P) sees an environment almost identical (same ^{29}Si density, same thermally grown oxide) to that of [12], except the contribution of indirect flipflops with the surrounding donor spins.

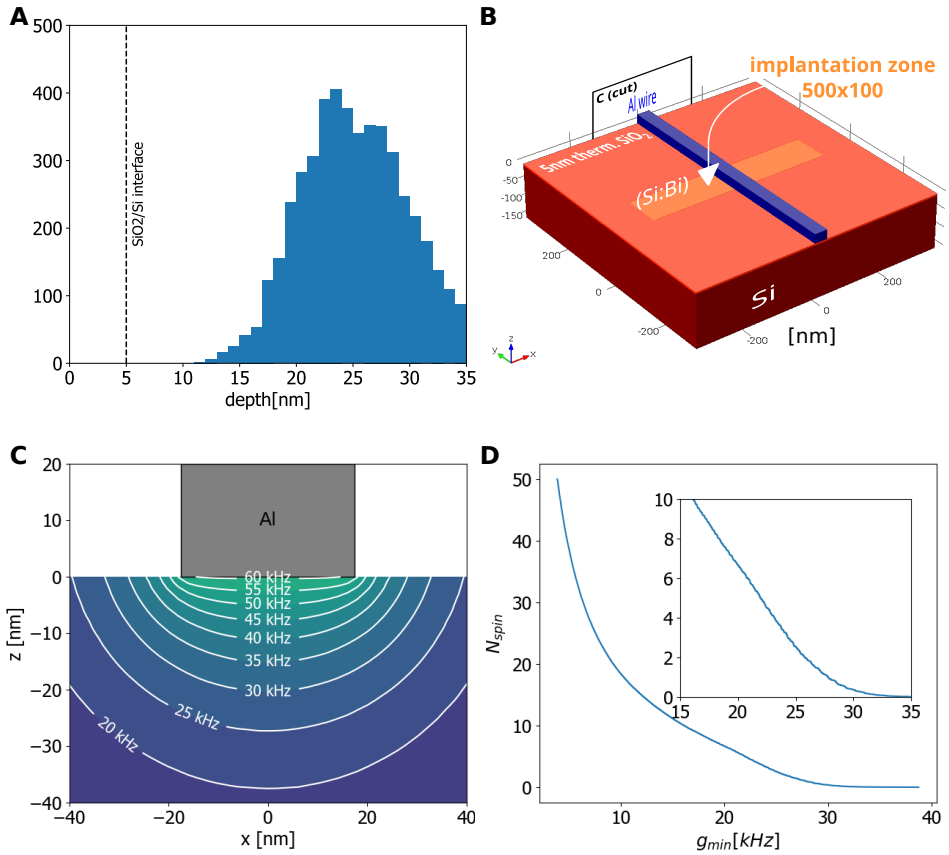

Figure 2.3: **A.** The implantation profile calculated using SRIM for an ion energy of 40 keV into a silicon substrate covered with 5 nm of thermally grown SiO_2. **B.** Top view of the implantation region crossed by a thin aluminum wire. **C.** Cut of a 35-nm wire and map of the coupling strength to the circuit in kHz assuming current fluctuations $\delta I = 350\,\mathrm{nA}$ calculated using Comsol. **D.** Monte Carlo simulation showing the expected number of implanted spins with a coupling constant higher than g_{min}, assuming 50 activated spins in the implantation region.

2.1.3 Shallow Implantation and use of a local constriction

In this work, the Bi donors are positioned at a depth of $\approx 25\,\mathrm{nm}$ below the surface by ion implantation with an energy of 40 keV (see Fig.2.3A for implantation profile). The region of implantation is defined by e-beam lithography using a PMMA mask (200 nm) with an opening of size $500 \times 100\,\mathrm{nm}$, which

blocks the ion beam efficiently. The implantation area density is $1-2\cdot10^{11}\mathrm{cm}^{-2}$, which translates into a peak density of bismuth impurities of $1-2\cdot10^{17}\mathrm{cm}^{-3}$. Taking into account an activation ratio of 60%, this density corresponds to a total of 30-60 electron spins. A thin wire of aluminum ($35\times500\,\mathrm{nm}$) crosses the implantation region and couples to the spins as represented in Fig.2.3B.

In Fig.2.3C, we represent a cross-section of this wire and the spatial distribution of the coupling assuming current fluctuations of $\delta I = 350\,\mathrm{nA}$. The coupling is taken to be maximal and thus calculated for an AC magnetic field where the total total angular momentum of the system is zero ($\langle E,0|\,S_z\,|G,0\rangle = 0.5$ according to Fig.2.1D).

In Fig.2.3D, we represent a graph showing a Monte Carlo simulation of the expected number of spins with a coupling higher than a given threshold. As can be seen, one can expect to have 2 spins with a coupling higher than 26 kHz.

Inhomogeneous lattice strain Due to the close proximity to the aluminum wire, mechanical stress resulting from the mismatch of the coefficient of thermal expansion induces a shift in the hyperfine coupling strength. This shift has been shown experimentally to be dependent on the hydrostatic components of the strain [56]. To first approximation, one may introduce modifications to the constant A dependent on diagonal terms of the strain tensor ε.

$$\frac{\Delta A}{A} = \frac{K}{3}\left(\varepsilon_{xx}+\varepsilon_{yy}+\varepsilon_{zz}\right)$$

where numerical value for the unitless constant $K = 19.1$ has been extracted experimentally [57].

For coupling to a single spin, this strain is rather advantageous. Indeed, the constriction induces a point of hydrostatic singularity, and in the range of a few 10 nm, all single spins have different transition frequencies (see Fig.2.4). In Fig.2.4B, we show a Monte Carlo simulation of the number of implanted spins with a given strain shift, assuming 50 spins in the implantation region.

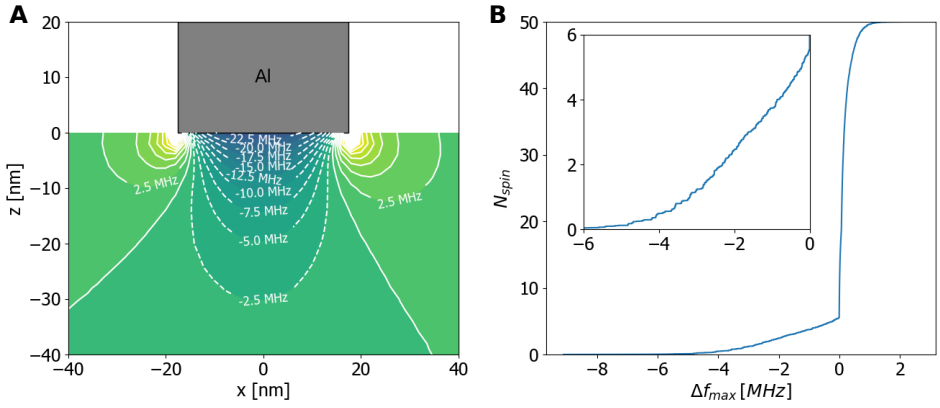

Figure 2.4: **A.** Strain-induced shift of the ESR absorption due to the presence of a 35 nm-wide wire calculated using Comsol. **B.** Monte Carlo simulation showing the expected number of implanted spins with a strain-induced shift smaller than $\Delta f_{\max}$, assuming 50 activated spins in the implantation region.

Schottky barrier The aluminum deposited directly on top of a native silicon substrate gives rise to a Schottky barrier in which the bismuth donors may be ionized [39]. Indeed, the aluminum has a higher work function[4] $\Phi = 4.25\,\mathrm{V}$ than the electron affinity[5] in silicon $\chi = 4.05\,\mathrm{V}$. Bismuth is a shallow donor situated at $E_{Bi} = E_C - E_{B,\mathrm{Si:Bi}}$, where $E_{B,\mathrm{Si:Bi}} = 71\,\mathrm{mV}$ is the binding energy of the donor. Thus, an electron occupying the donor site is situated at a higher electrochemical potential than the Fermi level of the aluminum, leading to spontaneous ionization of the donors in the so-called *depletion zone* (see Fig.2.5B). The presence of these ionized donors and the aluminum surface charges creates an electric field which bends the bands. The band-bending at the interface re-establishes the chemical potential equilibrium (see Fig.2.5B) and adapts the size of the depletion zone. In order to determine the depth of this depletion zone, one can write Poisson equation in the silicon:

$$\frac{d^2}{dx^2} E_0 = q\rho/\varepsilon_0\varepsilon_r$$

where $q = +e$ is the charge of the ionized impurities and ρ is their density. The resulting parabolic shift of the potential E_0 in the depletion zone bridges the difference ΔE_F between the Fermi level in the aluminum and in silicon. At temperatures close to absolute zero, the value of the Fermi level in the silicon will be roughly equal to energy of the dominant dopant (Si:P). We thus obtain

$$z_d = \sqrt{\frac{2\varepsilon_r\varepsilon_0\Delta E_F}{e\rho}} \sim \sqrt{\frac{2\varepsilon_r\varepsilon_0\left(\Phi - \chi - E_{\mathrm{bind}}\right)}{e\rho}} \tag{2.2}$$

The background residual density of phosphorous impurities in our intrinsic sample is $\sim 3 \cdot 10^{16}\mathrm{cm}^{-3}$, and thus the depletion region extends up to $\sim$80 nm in the sample. This depth is larger than the implantation profile of bismuth donors and thus most of the implanted spins will be ionized. It is important to note that dipoles or charges originating from dangling bonds at the chemical interface can introduce local inhomogeneities in the electric field of the boundary and thus make the problem difficult to solve in practice [55].

A well-known solution to this problem consists of introducing a thin insulating layer of SiO_2 in order to prevent the exchange of electrons between the substrate and the aluminum. This solution is in fact widely used since many years in the industry of semiconductors. By applying a positive voltage on the top electrode (see Fig.2.5D), it is possible to create a thin layer of 2D electron gas (2DEG) and to be assured that the donors cannot be ionized. Consequently, our work employs these thermally-grown oxide (see section §4.2).

In the following, we will introduce (see section 3.3.3) a new resonator design in which the aluminum wire can be connected to a DC voltage. This is achieved by replacing one of the coupling capacitors with a Bragg Filter, which naturally allows for DC biasing of the central strip of a coplanar resonator. The voltage bias is applied directly between the ground plane and this central strip. Since the oxide layer is present both in the ground plane and the central strip, but with *very* different surface areas,

[4] energy to ionize an electron occupying the Fermi level into a free electron
[5] energy to ionize an electron at the bottom of the conduction band

we may assume that the chemical potential difference falls mostly on the oxide layer of the central strip.

Experimentally, we should connect the anode of the DC source to the ground plane and the cathode to the central stripline. The voltage of at least $V \geq E_{\mathrm{Si:Bi}} - E_{F,Al} = 0.129\,\mathrm{V}$ should be maintained while the cooldown occurs, such that the donors retains its electron and converges into the unionized state.

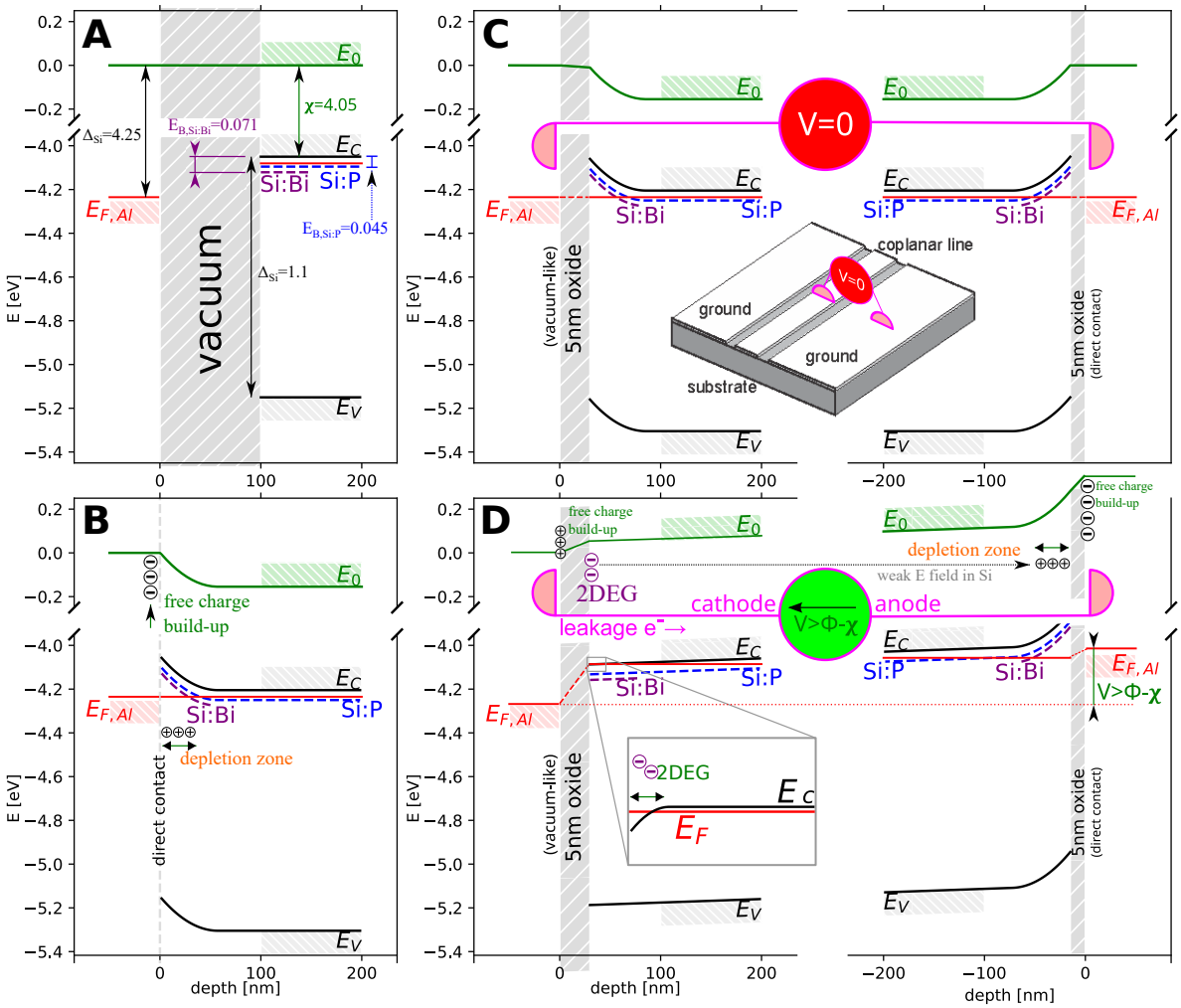

Figure 2.5: **Solving the Poisson equations A.** Isolated aluminum and Si bulk with Si:P background concentration, and a surface implantation of Si:Bi. **B.** Direct contact. Electrons flow from nearby donors, into the metal surface region, forming a depletion zone and rectifying the Fermi level. **C.** Due to difference ($\sim$ 1000 times) in surface area, we model a vacuum-like contact under the coplanar line, and a direct contact under the ground plane. Under zero bias, electrons from the depletion region leak through the ground plane contact forming and distributing on both terminal surface. **D.** Application of a bias that is greater than $\Phi - \chi$ may lead to creation of a 2D electron gas.

2.2 Flux Qubit

The so-called superconducting flux qubit fulfills many requirements necessary to couple strongly to bismuth donors - It may be designed to have a splitting around 7.4 GHz and also have $\delta I \sim 350$ nA. For flux qubits in this range, long relaxation times of up to 20 µs and echo coherence times of up to 30 µs were measured in this thesis.

Strategies [58, 59, 60] using the flux qubit as a bus has already been considered for coupling with single spins, in particular for NV centers: [61] proposed using the same flux qubit to couple to two different spins, whereby an entangling gate can be achieved through adiabatic elimination of the flux qubit state; [59] proposed using the flux qubit to directly introduce a spin-state-dependent splitting in the resonator line; Finally, [60] proposed using Rabi drives to bridge the gap between a spin and a flux qubit.

In the following, we will give a brief introduction to the flux qubit. Then, we will discuss the main challenges of working with flux qubits, namely, the control and reproducibility of the gap and coherence properties. Finally, we will present different strategies for bringing the bismuth donor and flux qubit transition energy into resonance, such as the proposal in Ref.[60].

2.2.1 Flux qubit short description

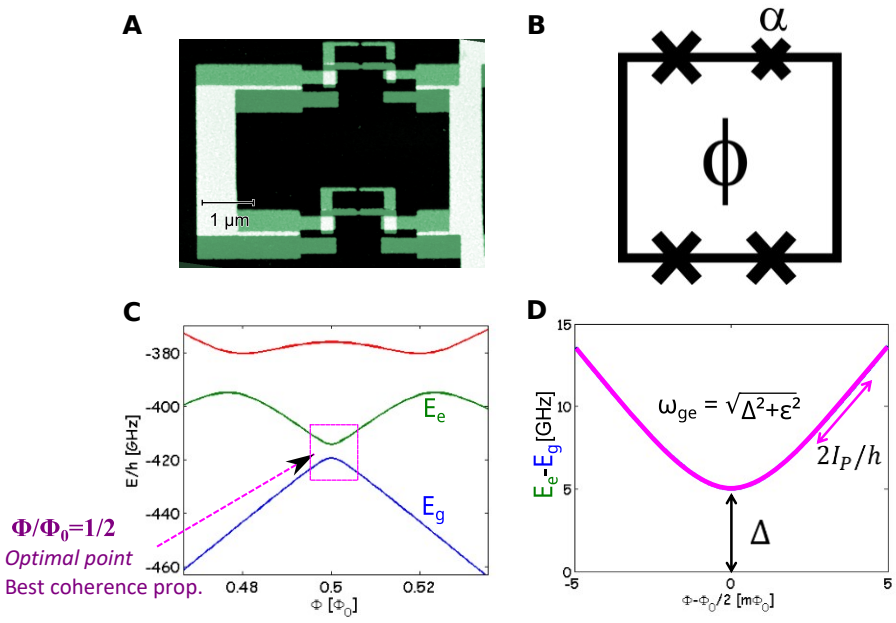

Figure 2.6: **Brief introduction to a flux qubit. A.** Afm micrograph of a flux qubit. **B.** Equivalent circuit of a flux qubit. **C.** Energy levels of a flux qubit. A good two-level system appears near the optimal point. **D.** Hyperbolic transition energy around the optimal point.

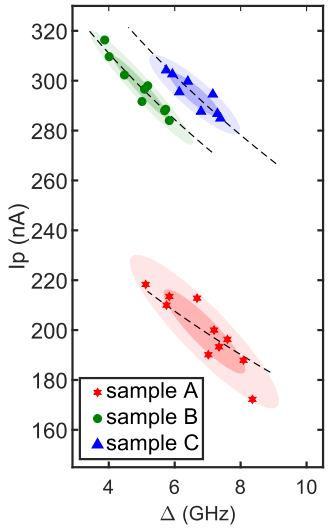

Figure 2.7: **Reproducibility and control of the gap.** Persistent current I_P versus gap Δ of the qubits of sample A (native oxide, red stars), sample B (5 nm grown silicon oxide layer, green dots) and sample C (5 nm grown silicon oxide layer, blue triangles). The colored regions are obtained by assuming a normal distribution along axes defined by principal component analysis (PCA). The probability to find a qubit within the dark (resp. light) colored area is 50% (resp. 90%). The dashed black lines are obtained by numerical simulations of the flux qubits (see section §2.2 at their average value $\left(\langle E_J\rangle_{A/B/C}, \langle E_c\rangle_{A/B/C}, \langle\alpha\rangle_{A/B/C}\right)$ while varying the parameter α by $\pm 5\%$.

The superconducting flux qubit is a micron-size superconducting aluminum loop intersected by several Josephson junctions, among which one is smaller than others by a factor α [62, 63, 64, 65, 66], as shown in Fig.2.6A-B. When the flux threading the loop is close to half a flux quantum $\Phi_0/2$ $(= h/(4e))$, the splitting between two lowest levels $|g\rangle$ and $|e\rangle$ are far detuned from other energy splittings (e.g. difference between red level and green level in Fig.2.6C), making the flux qubit a *true* two-level system (TLS) with high anharmonicity.

The so-called gap Δ and persistent current I_P can be extracted as phenomenological parameters by fitting the energy splitting between $|g\rangle$ and $|e\rangle$ as a hyperbolic function of the magnetic bias near to the optimal point, as shown in Fig.2.6D. The hyperbolic dependence of the splitting makes the qubit immune to magnetic noise in first order at $\Phi_0/2$, making it the preferred working point for obtaining the best coherence properties [67, 68]. In section §3.1, a rigorous quantum-mechanical treatment of the flux qubit will be presented.

2.2.2 Controlling the gap and persistent current

One major challenge with the flux qubit is the difficulty of controlling the gap solely through design, as well as the device-to-device reproducibility. In this thesis, a better understanding of the geometrical capacitance (see section 3.1.3) and meticulous calibration of the junction design parameters using on-chip test junctions has led to a much better gap predictability starting from design parameters.

In terms of reproducibility[6], major improvements were achieved using different techniques. Firstly, performing evaporation at cold temperatures ($\sim -40\,^{\circ}\mathrm{C}$) greatly reduces the grain size and improves the junction surface smoothness. Secondly, regarding the electron beam patterning of the evaporation mask, systematic re-focusing and re-calibration by laser interferometer of the surface level was carried out during lithography writing. Lastly, data measured in this work seems to indicate that thermally grown oxide may have a positive effect on the spread of the gap. Overall, we were able to measure a mere spread of 6.9 ± 1GHz, 5.1 ± 0.7 GHz and 6.6 ± 0.6 GHz for three different samples, each having different junction design parameters. This is a substantial improvement of the flux qubit[7] gap control, compared to previous reports [70]. These results are presented with more detail in section §6.1.

2.2.3 Relaxation and dephasing

A limited coherence time is one of the challenges of working with flux qubits [64, 65, 71, 67]. Long coherence times reported in previous works relate only to a few singular flux qubits [67]. In the last years, flux qubits embedded in 3D cavities [70] or in coplanar resonators [66] have exhibited more reproducible and generally improved relaxation times. More recently, a new design - the so-called *capacitively shunted flux qubit* - has shown even better coherence properties [69]. However, the shunting capacitance used to better control the qubit strongly decreases its anharmonicity. More importantly, it reduces the persistent current, which is required for magnetic coupling to electron spins.

In this thesis, we demonstrate *consistent* measurements of long relaxation times $T_1 \sim 15 - 20\,\mu\mathrm{s}$ and long pure dephasing times $T_{2E}^{\phi} \sim 15 - 30\,\mu\mathrm{s}$ for flux qubits that are galvanically coupled to a 2D coplanar waveguide resonator (see section §6.1). We attribute the *consistency* to the oxides present on the sample, reducing variability in the Al/Si interface, and we attribute the long coherence times to a refined fabrication procedure (see section §4). In parallel, the coherence properties of the so-called *tunable flux qubits* (see section 2.3.2) were also improved by 1-2 orders of magnitude compared to state-of-the-art. These results are presented in detail in section §6.

2.3 Establishing resonant coupling

Working at the flux qubit optimal point is required to obtain the best coherence properties. It is therefore important to engineer the flux qubit gap to be as close as possible as that of the donor spin ($\sim 7.4\,\mathrm{GHz}$). However, even with identical design parameters, the measured flux qubit inherently possess a large[8] spread in the gap, due to its sensitivity to disorder. Techniques to achieve resonant coupling regardless of detuning between the flux qubit and the donor frequency is thus of paramount importance. In this section, we present three possible methods to achieve this goal.

[6] the observed spread of the gap despite possessing identical design and even undergoing the same fabrication run
[7] without resorting to capacitively shunted flux qubits. See [69].
[8] compared to the coupling rate between the flux qubit and the donor spin

2.3.1 Tuning the bismuth transition frequency

One straight-forward way consists of making use of the Zeeman effect to tune the splitting of the donor spins as shown in Fig.2.1B. Indeed, transition frequencies involving highly positive and negative m_{tot} will shift in opposite directions and are well described by Eq.2.1. The simplest way to exploit this tunability is to apply an in-plane magnetic field through a vector magnet, in which case the flux qubit should remain mainly near the optimal point. The maximum applicable field is fundamentally limited by the (in-plane) critical field of the aluminum thin layer used in the resonator and qubit. We expect to be able to bias the in-plane magnetic field to $\sim 100\,\mathrm{G}$ before high magnetic fields start to hinder the quality factor of the resonator.

2.3.2 Tuning the flux qubit gap

The flux qubit gap Δ is given by the tunneling probability between two degenerate minima of the potential energy of the circuit. Using WKB approximation, it is possible to estimate the value of Δ [72]:

$$\Delta\left(\alpha, E_J/E_c\right) \propto \exp\left[-\left|\sin\varphi^* - \frac{\varphi^*}{2\alpha}\right|\sqrt{4\alpha\left(1+2\alpha\right)\frac{E_J}{E_C}}\right]$$

where φ^* is the phase of the degenerate minimum. We see clearly that the gap is exponentially dependent on the parameters of the junctions. A slight change of these parameters will affect drastically the gap energy of the qubit.

If one wishes to control precisely the gap energy, a good strategy may consist of replacing one of the junction by a SQUID, which will act as a tunable junction. Indeed the potential energy U_S of the SQUID writes

$$U_S = -E_J\cos\left(\varphi_1\right) - E_J\cos\left(\varphi_2\right) = -\overbrace{\left[E_J\cos\left(\frac{\Phi_S}{2\varphi_0}\right)\right]}^{\Phi_S\text{-tunable}}\cos\left(\bar{\varphi}\right)$$

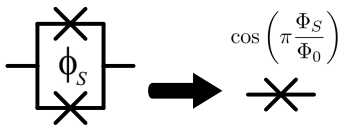

where $\varphi_1 = \bar{\varphi} + \frac{\Phi_S}{2\varphi_0}$ and $\varphi_2 = \bar{\varphi} - \frac{\Phi_S}{2\varphi_0}$ are the phases across the two identical junctions such that $\varphi_1 - \varphi_2 = \Phi_S/\varphi_0$ and $\varphi_0 = \hbar/2e$ is the reduced flux quantum.

The advantage of this approach is that another degree of freedom is added to the system; the flux Φ_S in the loop of the SQUID controls the critical current of the tunable junction formed by the SQUID and thus allows controlling the energy of the flux qubit while keeping it at its optimal point. In Ref.[73], this kind of strategy was implemented : a symmetric SQUID was introduced at the position of the α-junction of the flux qubit in order to control its gap energy. The results of the experiments were positive in terms of control of the qubit gap but the coherence times even at optimal point were

rather poor. The origin of these extremely short coherence times is flux noise [74, 75] in the SQUID loop, which leads to energy fluctuations even at the optimal point.

In this thesis, we show it is possible to get some control of the qubit gap by replacing one of the unitary junctions by a highly asymmetric SQUID, as shown in Fig.2.8. First, let us write the potential energy U_S of the asymmetric SQUID:

$$U_S = -\frac{1+d}{2} E_J \cos(\varphi_1) - \frac{1-d}{2} E_J \cos(\varphi_2)$$

where $d \in [0-1]$ is the asymmetry parameter. This expression can be rewritten as

$$U_S = -E_J \sqrt{\frac{(1+d^2) + (1-d^2)\cos(\Phi_S/\varphi_0)}{2}} \cos\left[\frac{\varphi_1+\varphi_2}{2} + \arctan[-d \cdot \tan(\Phi_S/2\varphi_0)\right]$$

The potential energy of the SQUID is therefore equivalent to the potential energy of a single Josephson junction with tunable Josephson energy E_J that varies between $d\,E_J$ to E_J. When the asymmetry is large ($d \to 1^-$), the Josephson energy of equivalent junction varies slightly and thus the qubit will be less sensitive to flux noise than for a symmetric SQUID ($d = 0$).

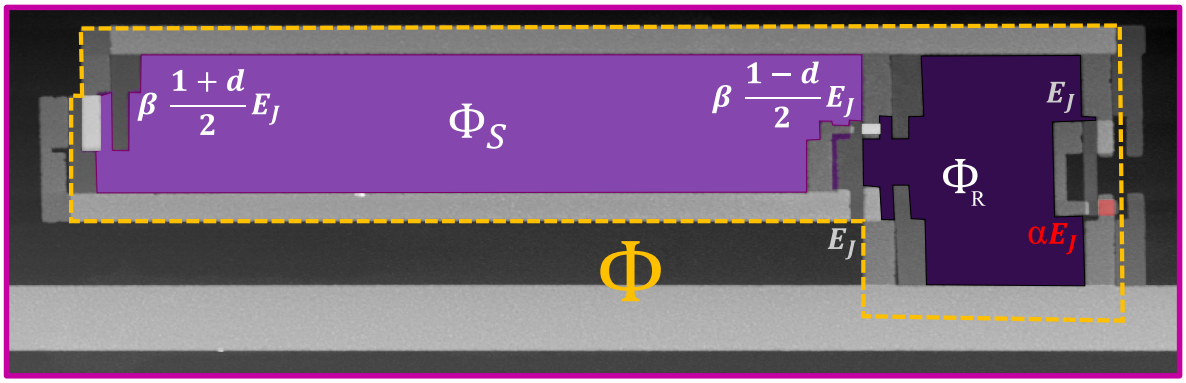

Figure 2.8: **Afm micrograph showing a tunable flux qubit with asymmetrical SQUID.**

In this work, the tunable flux qubits were fabricated on sapphire substrates, the tunability was measured to be $\pm 3.5\,\mathrm{GHz}$. Compared to previously reported tunable flux qubits [73], the coherence properties ($T_1 \sim 8\,\mu\mathrm{s}$ and $T_{2E}^{\varphi} \sim 4\,\mu\mathrm{s}$) were drastically improved. It is possible to enhance even more the coherence time T_2 by dialing down the tunability to $\pm 0.5\,\mathrm{GHz}$ around the center frequency (see 3.5.4).

2.3.3 Tuning the flux qubit gap in a rotating frame

Lastly, [60] gives a theoretical proposal in which a detuned flux qubit can be brought back into resonance with a single spin using strong Rabi drives. Here we give an intuitive picture of its working principle (see Fig.2.9), described more rigorously in section §3.6.

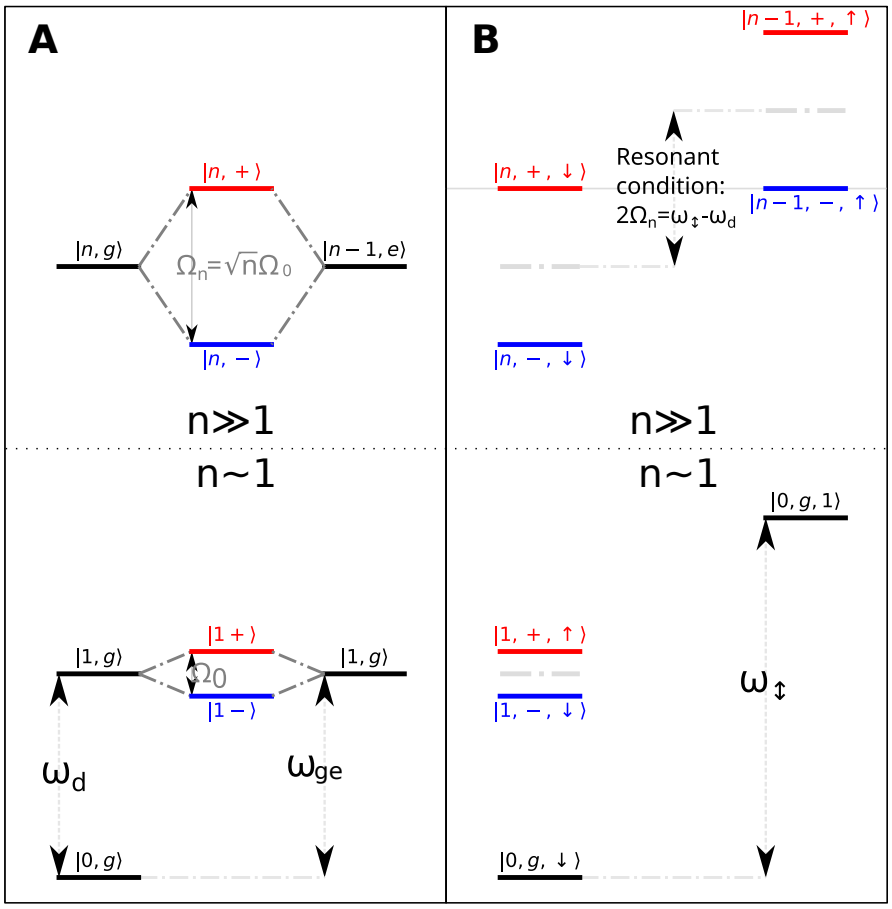

Figure 2.9: **Rabi Dressing of a flux qubit A.** Energy diagram in circuit QED showing Rabi-dressed states (red and blue) for high (above) and low (below) photon number n. **B.** Resonant coupling when the spin Hilbert space is considered.

Let us start by considering a photonic mode[9] $\hbar\omega_d$ in resonance with the flux qubit splitting $\delta = \omega_{ge} - \omega_d = 0$. Using the standard CQED framework (see section 3.3.4), we can define the following Rabi-dressed states

$$|n, \pm\rangle = (|g\rangle |n\rangle \pm |e\rangle |n-1\rangle) / \sqrt{2}$$

where $|g/e\rangle$ denotes the qubit state and n is the number of photons in the Rabi drive such that the Rabi frequency is $\Omega_n = 2\Omega_0\sqrt{n}$. Due to the coupling term $\sigma_+ a + \sigma_- a^\dagger$, the energies are shifted $E_{n,\pm} = n\omega_d \pm \frac{1}{2}\sqrt{\delta^2 + \Omega_n^2} = n\omega_d \pm \Omega_n/2$ (see Fig.2.9A), where the term $\pm\Omega_n/2$ gives rise to the standard Rabi oscillations at frequency $\Omega = \Omega_n$. When either of the energy difference $E_{n,\pm} - E_{n-1,\mp} = \omega_d \pm \Omega$

[9]Despite physically being in the resonator, this mode is *not* the resonator mode. It is a fictive mode determined principally by the drive bandwidth, and the subsequent zero-point fluctuation of current around that frequency filtered by the resonator (see section 3.3.2). Indeed, by putting one quanta of energy $\hbar\omega_d$ into the driving wavelet we can calculate the corresponding Rabi frequency Ω_0 from the zero-point fluctuations of current.

matches that of the spin $\omega_{\updownarrow}$,

$$\left|\omega_d - \omega_{\updownarrow}\right| = \Omega$$

resonant Rabi exchange may occur at half the coupling rate of the flux qubit - spin coupling $g_{qb\leftrightarrow\updownarrow}$ due to the factor $1/\sqrt{2}$ in the dressed state. For instance supposing the resonant condition $E_{n+1,+} - E_{n,-} = \omega_d + \Omega = \omega_{\updownarrow}$ (see Fig.2.9B), we can indeed verify resonance and calculate the coupling strength

$$\begin{aligned}\langle\swarrow| \langle n+1,+| H_{h\nu+qb+\updownarrow} |n+1,+\rangle |\swarrow\rangle &= \langle\nearrow| \langle n,-| H_{h\nu+qb+\updownarrow} |n,-\rangle |\nearrow\rangle \\ \langle\nearrow| \langle n,-| H_{qb\leftrightarrow\updownarrow} |n+1,+\rangle |\swarrow\rangle &= g_{qb\leftrightarrow\updownarrow}/2\end{aligned}$$

where $|\swarrow\ /\ \nearrow\rangle$ denotes the spin's state. To understand the dynamics, we may suppose an initial state of

$$|n\rangle |e\rangle |\swarrow\rangle = \left(\left(|n+1,+\rangle - |n+1,-\rangle\right)/\sqrt{2}\right) |\swarrow\rangle$$

The amplitude of $|n+1,+\rangle |\swarrow\rangle$ will Rabi-oscillate to and from $|n,-\rangle |\nearrow\rangle$, from which we could engineer a coherent swap gate. Indeed, under time evolution, this part of the initial state evolves as

$$e^{-i\omega_{\updownarrow}t/2}\left(\cos\left(g_{qb\leftrightarrow\updownarrow}/2\cdot t\right)|n+1,+\rangle|\swarrow\rangle - i\sin\left(g_{qb\leftrightarrow\updownarrow}/2\cdot t\right)|n,-\rangle|\nearrow\rangle\right) - e^{+i\omega_{\updownarrow}t/2}|n,-\rangle|\swarrow\rangle$$

Gathering the $|\swarrow\rangle$ states and $|\nearrow\rangle$ terms, we get

$$\left(e^{-i\omega_{\updownarrow}t/2}\cos\left(g_{qb\leftrightarrow\updownarrow}/2\cdot t\right)|n+1,+\rangle - e^{+i\omega_{\updownarrow}t/2}|n,-\rangle\right)|\swarrow\rangle - ie^{-i\omega_{\updownarrow}t/2}\sin\left(g_{qb\leftrightarrow\updownarrow}/2\cdot t\right)|n,-\rangle|\nearrow\rangle$$

We already see coherent oscillation of the probability amplitude of the excited spin state $|\nearrow\rangle$. The left terms may look orthogonal, but this is the result of the oversimplification of a classical Rabi drive to a Fock state. To correctly account for a classical drive, one should apply in the different steps a summation over $|n,\pm\rangle$ states, like in the decomposition of a bosonic coherent state

$$|\alpha\rangle = e^{-|\alpha|^2/2}\sum_{n=0}^{\infty}\alpha^n/\sqrt{n!}\,|n\rangle$$

Equivalently, we may also treat the drive classically, as is presented in section §3.6. Both of these correct treatments yield interference patterns on the left term resulting in a beating in the envelope of the Rabi oscillation as shown in Fig.2.10A. Compared to a direct resonant coupling, this approach should yield a signature less sensitive to the coherence properties of the flux qubit. This is because the rapid Rabi Oscillations constitute a powerful dynamical decoupling protocol, especially against low frequency noise such as the 1/f flux noise, which is considered the dominant source of dephasing for flux qubits. This can be understood easily by the Taylor expansion $\sqrt{\delta(t)^2+\Omega^2} \approx \Omega + \delta(t)\cdot(\delta(t)/2\Omega)$, which transform first order flux noise into second order, and second order into fourth order, and attenuating at least a factor $\delta/2\Omega < 1$ in the accumulated phase error. This robustness can be seen in Fig.2.10B, where we introduce a static (similar to low frequency) mismatch of the flux qubit transition

frequency of 1 MHz.

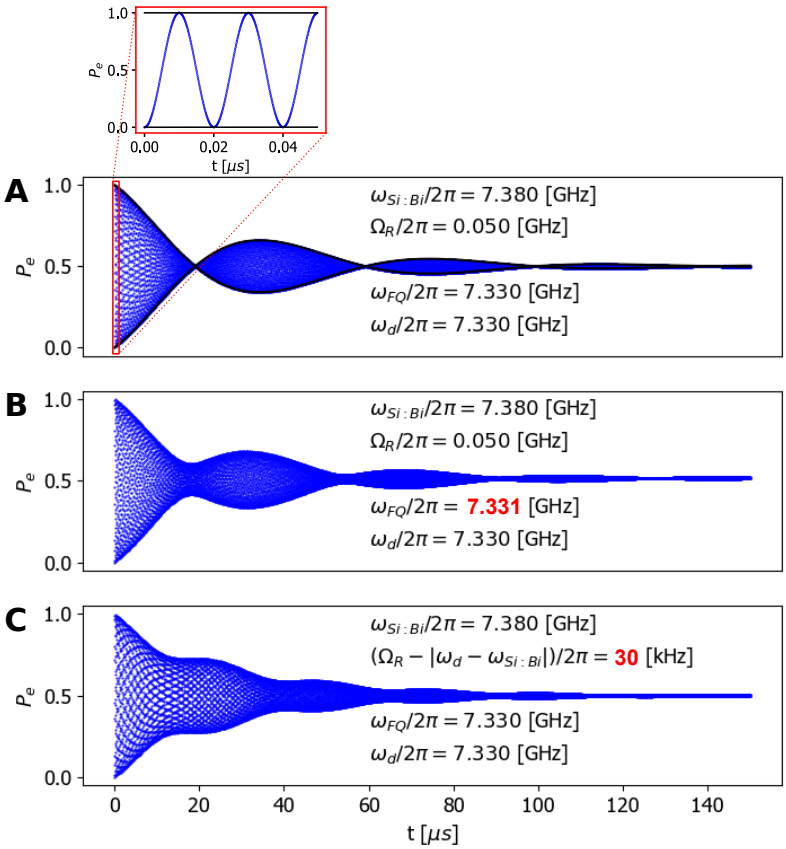

Figure 2.10: **Linblad simulations with only T1 jump operator ($T_1 = 20\,\mu$s) showing the Rabi Envelope A.** Protocol under resonant condition **B.** Mismatch between qubit frequency and drive frequency. **C.** Mismatch between dressed frequency $\omega_d \pm \Omega \neq \omega_{\text{Si:Bi}}$.

The phase-coherent exchange can be further adapted into other functionalities, such as spin state preparation and use of the spin as a quantum memory, as detailed in section §3.6. A real-time control of the Rabi drive power may even allow for different individual spins to be addressed through the same qubit. The limit of this method is fundamentally fixed by the maximal driving power we can apply into the system. In theory, for fixed power, we could increase the Rabi frequency through mode engineering (e.g. Purcell enhancement, placing on peaks, changing the characteristic impedance, reducing mode volume e.t.c). Nevertheless, a fundamental relation (proven in section 3.4.1) relates the Purcell rate Γ_P to the driving power P and Ω

$$\Gamma_P = \frac{\hbar\omega_{ge}\Omega^2}{4P}$$

A realistic trade-off must be found between tunability and degradation of the Rabi signal. In this thesis, from the results measured so far, we estimate the maximal tunability to be $\Omega^{\max}/2\pi = 80\,$MHz , driven by a power of $P^{\max} = -75\,$dBm and causing a Purcell rate $\Gamma_P = 10\,$kHz.

3 Theoretical Analysis

3.1 Flux qubit model

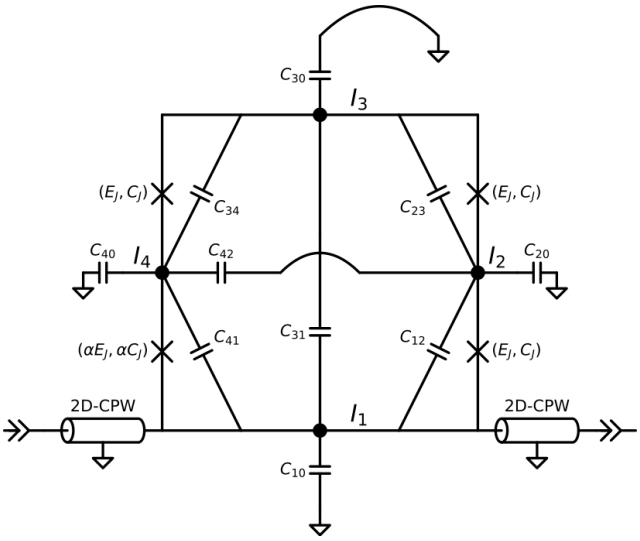

Figure 3.1: **Equivalent circuit diagram of a flux qubit.** The Josephson junctions are defined by their Josephson energy E_J and their bare capacitance C_J. The island I_1 is galvanically connected to the coplanar waveguide resonator. Each island is capacitively coupled to its surrounding by geometric capacitances denoted as C_{ij} where $(i, j) \in (0, 1, .., 4)$, the index 0 representing the ground.

The subsections that follow will introduce how one may model a flux qubit. Fig.3.1 shows a schematic drawing of a flux qubit. Each Josephson junction is characterized by its Josephson energy E_J and its bare capacitance C_J. The junctions divide the loop into four superconducting islands. The island I_1 is galvanically connected to the coplanar waveguide resonator. Each island is capacitively coupled to its surrounding by geometric capacitances denoted as C_{ij} where $(i, j) \in (0, 1, .., 4)$, the index 0 representing the ground.

3.1.1 Potential Energy

The potential energy of the circuit shown in Fig.3.1 corresponds to the inductive energy of the junctions and can be written as

$$U = -\sum_{j=1}^{3} E_J \cos \varphi_{j,j+1} - \alpha E_J \cos \varphi_{41} \tag{3.1}$$

where $\varphi_{j,k}$ denotes the phase difference $\varphi_k - \varphi_j$ between islands j and k. Faraday law implies that

$$\varphi_{41} = 2\pi \frac{\Phi}{\Phi_0} - \sum_{j=1}^{3} \varphi_{j,j+1} \tag{3.2}$$

where Φ is the flux threading the qubit loop and $\Phi_0 = h/2e$. When $\Phi = \Phi_0/2$, the potential energy has two degenerated minima. The positions of these minima are given by solving the partial differential equations $\partial_{\varphi_i} U = 0$. The two solutions verify the simple equation $\sin\varphi^* = \alpha \sin 3\varphi^*$ and correspond to two opposite persistent currents given by

$$I_p = \pm I_0 \sqrt{\frac{3}{4} - \frac{1}{4\alpha}} \tag{3.3}$$

where I_0 is the critical current of the Josephson junctions. As an example, it maybe helpful to draw intuition from the hypothetical case of a flux qubit with 2 unitary junctions and an α junction: the potential energy can be plotted in a 2D graph as shown in Fig.3.2. In the language of a particle in a potential, a weakly connected double well gives rise to the qubit gap after we consider the mass terms, which will be treated in the following subsection.

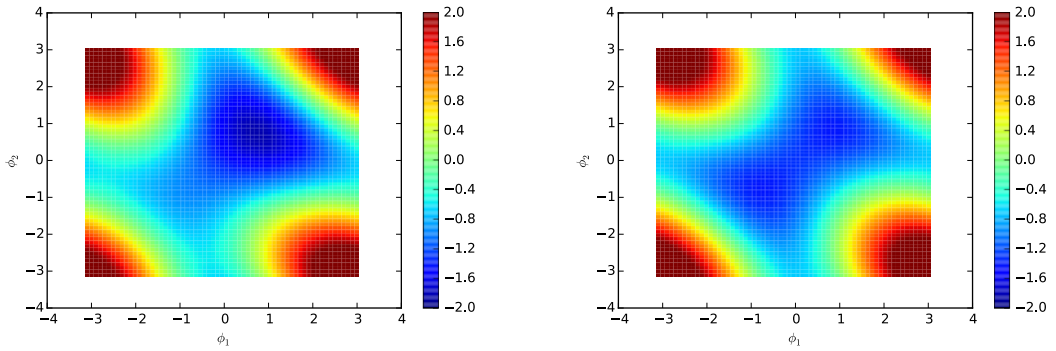

Figure 3.2: Potential energy landscape of a 3-island flux qubit with parameters $\alpha = 0.7$. Left: $\Phi/\varphi_0 = 0.8\pi$; Right: $\Phi/\varphi_0 = \pi$. We show only one period of $\varphi_{i,i+1}$ only.

3.1.2 Kinetic Energy

The kinetic energy K of the system is the sum of the capacitive energies of the circuit

$$\begin{aligned} K = &\frac{1}{2}\sum_{i\neq j} C_{ij}\left(V_j - V_i\right)^2 \\ &+ \frac{1}{2} C_J \left((V_1 - V_2)^2 + (V_2 - V_3)^2 + (V_3 - V_4)^2 + \alpha\left(V_4 - V_1\right)^2 \right) \end{aligned} \tag{3.4}$$

It is a quadratic form of the island voltages V_i and can thus be written as

$$K = \frac{1}{2}\mathbf{V}^T \mathbf{C} \mathbf{V} \tag{3.5}$$

where $\mathbf{V^T} = \begin{pmatrix} V_1 & , V_2 & , V_3, & V_4 \end{pmatrix}$ and $\mathbf{C}$ is a 4×4 matrix which we will refer in the following as the capacitance matrix. The matrix $\mathbf{C}$ can be written as the sum of the Josephson capacitance matrix

$\mathbf{C_J}$ and the geometric capacitance matrix $\mathbf{C_{geom}}$:

$$\mathbf{C} = \mathbf{C_J} + \mathbf{C_{geom}} \tag{3.6}$$

where

$$\mathbf{C_J} = C_J \begin{pmatrix} 1+\alpha & -1 & 0 & -\alpha \\ -1 & 2 & -1 & 0 \\ 0 & -1 & 2 & -1 \\ -\alpha & 0 & -1 & 1+\alpha \end{pmatrix} \tag{3.7}$$

and

$$\begin{aligned} \mathbf{C_{geom}} = & \begin{pmatrix} C_{10} & 0 & 0 & 0 \\ 0 & C_{20} & 0 & 0 \\ 0 & 0 & C_{30} & 0 \\ 0 & 0 & 0 & C_{40} \end{pmatrix} \\ & + \begin{pmatrix} \sum_{j\neq 1} C_{1j} & -C_{12} & -C_{13} & -C_{14} \\ -C_{21} & \sum_{j\neq 2} C_{2j} & -C_{23} & -C_{24} \\ -C_{31} & -C_{32} & \sum_{j\neq 3} C_{3j} & -C_{34} \\ -C_{41} & -C_{42} & -C_{43} & \sum_{j\neq 4} C_{4j} \end{pmatrix} \end{aligned} \tag{3.8}$$

The techniques for calculating $\mathbf{C_{geom}}$ is described in the following section 3.1.3.

3.1.3 Numerical Estimation of the Geometrical Capacitance

Numerical Estimation of the geometrical capacitance using finite element solvers is difficult due to the different length scales involved. The qubits have typically micron size dimensions while the oxide thickness is rather of the order of 1 nm. As a consequence, a fine meshing is difficult to establish. In this section, we will present an approach which provides satisfactory results.

Coarse estimation We first performed a coarse simulation using the electrostatic module of COMSOL. To perform this simulation, we assumed Neumann boundary conditions (zero charge) on a box of 30 µm surrounding the qubit (see Fig.3.3). The oxide of the Josephson junctions was replaced by a hollow box of thickness $l = 20\,\text{nm}$. We defined a minimum meshing size of 4 nm. For these mesh parameters, the far field components are accurately calculated. Isolated islands not participating in the flux qubit loop were set to charge conservation $Q = 0$ terminal settings.

We applied sequentially a voltage on each island in order to construct the capacitance matrix

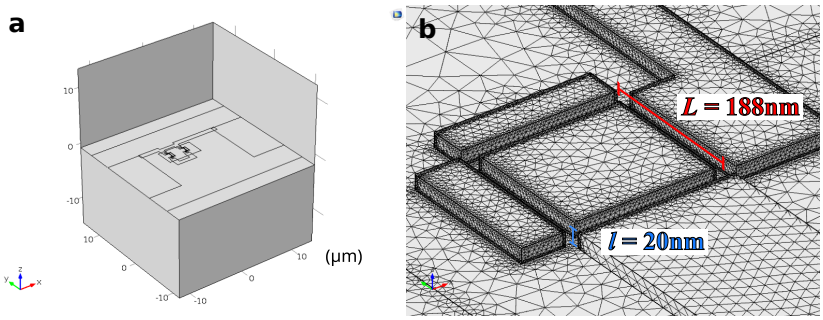

Figure 3.3: **Coarse Simulation using the electrostatic module of COMSOL. a**, The precise design of the qubit is imported to the simulator and put into a cubic box of 30 µm edge, where zero charge boundary condition is imposed. **b**, Close-up view of the meshing around one of the junction. The junction is modelized by conducting planes separated by 20 nm distance in order to keep a minimal meshing size of 4 nm.

$\mathbf{C_{coarse}}$. For instance, the coarse capacitance matrix of qubit B4 (see section §6.1) is

$$\mathbf{C_{coarse}} = \begin{pmatrix} 3.752 & -0.181 & -0.524 & -0.137 \\ -0.181 & 0.350 & -0.148 & -0.002 \\ -0.524 & -0.148 & 1.044 & -0.140 \\ -0.137 & -0.002 & -0.140 & 0.300 \end{pmatrix} \quad \text{fF}$$

Estimating the capacitance between edges In order to obtain more precise results, the capacitance between adjacent edges needs to be corrected. In Fig.3.4 , we represent a close-up view of a typical Josephson junction obtained by Dolan technique, where we show the four edge capacitances we need to consider. The two capacitances $C^{\text{Si}}_{\text{edge}}$ are dominant due to the high permittivity constant of Si and thus $C^{\text{air}}_{\text{edge}}$ can be neglected in a first approximation.

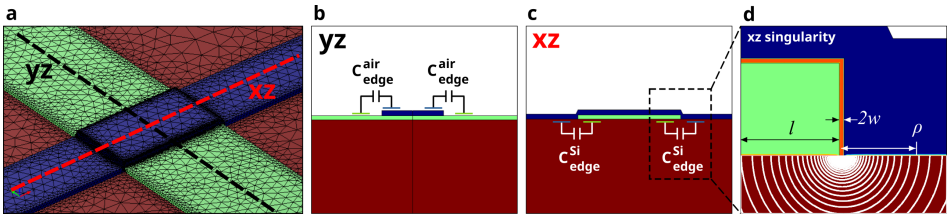

Figure 3.4: **Edge capacitances. a**, 3D representation of a Josephson junction obtained by double angle evaporation. **b**, View cut of the junction in the yz plane showing the C^{air}_{edge} edge capacitances. **c**, View cut of the junction in the xz plane showing the C^{Si}_{edge} edge capacitances. **d**, Close up view of the edge showing the electric field lines giving rise to the edge capacitances. We show the edge length l, the distance to the singularity ρ, and the oxide thickness $2w$.

The capacitance between adjacent edges of length $l = 20$ nm and width L separated by an oxide layer in the region $|\rho| < w$ (See Fig.3.4d) can be calculated analytically. By using Gauss theorem, we have

$$L\int_w^l \frac{V}{\pi\rho}d\rho = \frac{Q}{\epsilon_0\epsilon_r} \tag{3.9}$$

where V is the voltage potential in the silicon substrate at a distance ρ from the junction singularity, $\epsilon_0\epsilon_r$ is the dielectric permittivity of silicon and Q the charge accumulated on the surface of the metallic island. Thus, the capacitance is given by

$$C_{edge}^{Si} = L\frac{\epsilon_0\epsilon_r}{\pi}\ln\frac{l}{w} \tag{3.10}$$

For instance, the edge capacitance matrix of qubit B4 is

$$\mathbf{C_{edge}} = \begin{pmatrix} 0.069 & -0.042 & 0 & -0.027 \\ -0.042 & 0.084 & -0.042 & 0 \\ 0 & -0.042 & 0.084 & -0.042 \\ -0.027 & 0 & -0.042 & 0.069 \end{pmatrix} \quad \text{fF}$$

Numerical results Following the procedure described herein above, the capacitances matrix of qubit B4 is calculated and given here as an example:

$$\mathbf{C_J} = \begin{pmatrix} 7.898 & -5.265 & 0 & -2.633 \\ -5.265 & 10.531 & -5.265 & 0 \\ 0 & -5.265 & 10.531 & -5.265 \\ -2.633 & 0 & -5.265 & 7.898 \end{pmatrix} \quad \text{fF}$$

$$\mathbf{C_{geom}} = \mathbf{C_{coarse}} + \mathbf{C_{edge}} = \begin{pmatrix} 3.821 & -0.223 & -0.524 & -0.164 \\ -0.223 & 0.434 & -0.190 & -0.002 \\ -0.524 & -0.190 & 1.128 & -0.182 \\ -0.164 & -0.002 & -0.182 & 0.370 \end{pmatrix} \quad \text{fF}$$

This matrix is then inserted in the Lagrangian of the qubit as we will see herein below.

3.1.4 Legendre Transformation and Hamiltonian

The Lagrangian of the system is $\mathcal{L} = K - U$. The conjugate momenta of our system are given by

$$n_j \equiv \frac{1}{\hbar}\frac{\partial\mathcal{L}}{\partial\dot{\varphi}_{j,j+1}} \tag{3.11}$$

Since $\frac{\Phi_0}{2\pi}\dot{\varphi}_{j,j+1} = V_{j+1} - V_j$, it is neccessary to express the kinetic energy terms in a new basis. Since island I_1 is galvanically connected to the central conductor of the CPW, we can safely assume that $V_1 = 0\,\text{V}$, which simplifies considerably the transformation:

$$
\begin{aligned}
V_1 &= 0 \\
V_2 &= \cancelto{0}{V_1} + V_{12} \\
V_3 &= \cancelto{0}{V_1} + V_{12} + V_{23} \\
V_4 &= \cancelto{0}{V_1} + V_{12} + V_{23} + V_{34}
\end{aligned}
$$

where $V_{ij} = V_j - V_i$. The passage matrix P between these two bases can be thus written as

$$
\mathbf{P} = \begin{pmatrix} 0 & 0 & 0 \\ 1 & 0 & 0 \\ 1 & 1 & 0 \\ 1 & 1 & 1 \end{pmatrix} \tag{3.12}
$$

More generally, for non-galvanically connected islands, we remove a constant voltage on each of the configurations such that the total charge is conserved

$$
\mathbf{P}' = \mathbf{P} - \begin{pmatrix} 1 & 1 & 1 & 1 \end{pmatrix} \mathbf{C}
$$

The Hamiltonian H is then obtained by the Legendre transformation $\mathcal{H} = \hbar \sum_{j=1}^{3} \dot{\varphi}_{j,j+1} n_j - \mathcal{L}$ and thus writes

$$
H = \frac{(2e)^2}{2} \vec{n}^T \left(\mathbf{P}^T \mathbf{C} \mathbf{P} \right)^{-1} \vec{n} + U \tag{3.13}
$$

This Hamiltonian can be expressed in the so-called charge basis $|n_1, n_2, n_3\rangle$, $\forall n_1, n_2, n_3 \in \mathbb{Z}^3$, noting that

$$
\cos \varphi_{j,j+1} |n_1, n_2, n_3\rangle = \frac{1}{2} \left(|n_1 + \delta_{j1}, n_2 + \delta_{j2}, n_3 + \delta_{j3}\rangle + |n_1 - \delta_{j1}, n_2 - \delta_{j2}, n_3 - \delta_{j3}\rangle \right) \tag{3.14}
$$

In this basis the operator $\frac{(2e)^2}{2} \vec{n}^T \left(\mathbf{P}^T \mathbf{C} \mathbf{P} \right)^{-1} \vec{n}$ is diagonal while the operator U is sparse. The precision of the eigenvalues and eigenstates depends on the truncation of the n_j bases. With $n_k = -10...10$, we would need 21^3 coefficients just to describe the wavefunction and another $\left(21^3\right)^2$ to describe the Hamiltonian matrix. Thanks to the the sparsity of the Hamiltonian operator, the number of nonzero entries in this matrix is only $21^3 \times (1 + 4 \times 2)$. This resolution in charge space is computationally feasible both to store and diagonalize matrices efficiently. For reaching the necessary precision to resolve charge modulation, we used $n_k = -14...14$ and verified carefully the numerical convergence of the calculation.

3.1.5 Pseudo-Hamiltonian

Following the full diagonalization of the Hamiltonian, we obtain the spectrum of the flux qubit by subtracting the energy of the first excited state $|e\rangle$ from the energy of the ground state $|g\rangle$. It can be shown that close to $\Phi = \Phi_0/2$, the system behaves as a two level system and the spectrum can be fully described by two parameters:

- The value of the persistent current I_p, already discussed previously.
- The so-called flux qubit gap, denoted as Δ, which corresponds to the tunneling term between the two potential minima.

The value of the gap can be directly measured by the transition energy at half a flux quantum $\Phi = \Phi_0/2$. This point is known as the *optimal point* of the flux qubit due to its immunity at first order in flux noise, as will be explained in later sections. In the vicinity of the optimal point, the Hamiltonian of the system can be written using perturbation theory as

$$\begin{aligned} H &= H_0 - \alpha E_J \partial_\Phi \left(\cos\left(2\pi \frac{\Phi}{\Phi_0} - \sum_{j=1}^{3} \varphi_{j,j+1} \right) \right)_{\Phi=\Phi_0/2} \cdot \left(\Phi - \frac{\Phi_0}{2} \right) \\ &= H_0 + \frac{1}{\varphi_0} \left[\underbrace{\alpha E_J \sin\left(\varphi_{41}\right)}_{\hat{I}\cdot\varphi_0} \left(\Phi - \frac{\Phi_0}{2} \right) \right] = H_0 + \hat{I} \cdot \left(\Phi - \frac{\Phi_0}{2} \right) \end{aligned} \tag{3.15}$$

When the current operator is projected on the eigenstates $|g\rangle, |e\rangle$ of H_0 we get

$$\begin{aligned} \langle g| \hat{I} |g\rangle = 0 \quad &, \quad \langle g| \hat{I} |e\rangle = I_p \\ \langle e| \hat{I} |g\rangle = I_p \quad &, \quad \langle e| \hat{I} |e\rangle = 0 \end{aligned} \tag{3.16}$$

Therefore, the Hamiltonian of the system can be written in this basis as

$$H_{\text{eff}} = \frac{\hbar}{2} \left[\Delta \sigma_z + \varepsilon \sigma_x \right] \tag{3.17}$$

where $\varepsilon = \frac{2I_p}{\hbar} \left(\Phi - \frac{\Phi_0}{2} \right)$.
The frequency of the flux qubit is thus given by

$$\omega_{ge} = \sqrt{\Delta^2 + \varepsilon^2} \tag{3.18}$$

3.2 Tunable flux qubit model

As mentionned in section 2.3.2, the coherence times of tunable flux qubits are principally limited by flux noise in the SQUID loop [74, 75]. We mitigate this issue by replacing one unitary junction by an asymmetric SQUID formed by two different junctions having respectively a Josephson energy $(1+d)\, E_J/2$ and $(1-d)\, E_J/2$ with $d \in [0-1]$, as shown in Fig.3.5. The equivalent Josephson energy of such a SQUID $E_J(\Phi_S)$ varies according to the following expression [76]:

$$\boxed{E_J(\Phi_s) = E_J \sqrt{\frac{(1+d^2) + (1-d^2)\cos\left(\frac{\Phi_S}{\varphi_0}\right)}{2}}} \tag{3.19}$$

where $\varphi_0 = \hbar/2e$. For a given value of d, the function $E_J(\Phi_S)$ ranges between dE_J and E_J and consequently the dependence of the qubit energy on Φ_S is strongly reduced as d approches 1. This technique has been demonstrated recently for tuning transmon qubits while keeping good coherence properties [77, 78].

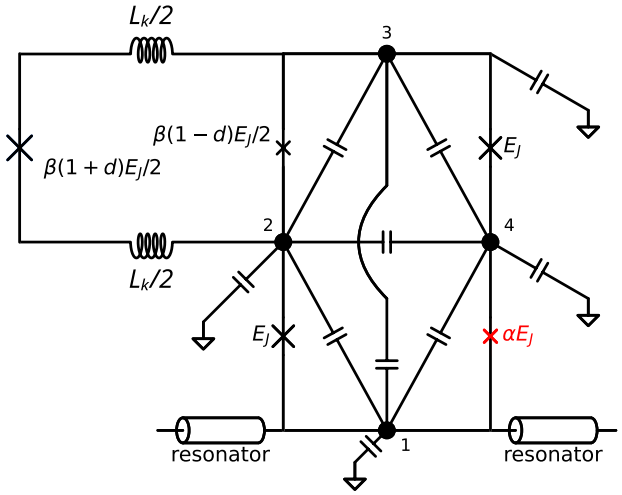

Figure 3.5: Tunable Flux qubit model including the kinetic inductance L_k and geometric capacitances. The island 1 is connected galvanically to the central conductor of the resonator.

3.2.1 Potential Energy

The potential energy of a tunable flux qubit corresponds to the total inductive energy of the junctions and can be written as

$$U = -E_J \cos\varphi_{12} - \beta\frac{1+d}{2\,(1+\eta)}E_J\cos\varphi_{23} - \beta\frac{1-d}{2}E_J\cos\varphi'_{23} - E_J\cos\varphi_{23} - \alpha E_J\cos\varphi_{41}$$

where $\varphi_{j,k}$ denotes the phase difference $\varphi_k - \varphi_j$ between islands j and k. The factor η comes from the renormalization (see section 3.2.2) of the junction due to the presence of L_k. Introducing

$$\bar{\beta} = \beta\left(\frac{1+d}{2\,(1+\eta)} + \frac{1-d}{2}\right) \tag{3.20}$$

$$\bar{d} = \frac{(2+\eta)\,d - \eta}{-\eta d + (2+\eta)} \tag{3.21}$$

enables us to write the potential energy *back* under the form

$$U = -E_J \cos\varphi_{12} - \bar{\beta}\frac{1+\bar{d}}{2}E_J \cos\varphi_{23} - \bar{\beta}\frac{1-\bar{d}}{2}E_J \cos\varphi'_{23} - E_J \cos\varphi_{23} - \alpha E_J \cos\varphi_{41} \tag{3.22}$$

Faraday law implies that

$$\varphi_{41} = \frac{\Phi}{\varphi_0} - \sum_{j=1}^{3}\varphi_{j,j+1} \tag{3.23}$$

$$\varphi'_{23} = \varphi_{23} - \frac{\Phi_S}{\varphi_0} \tag{3.24}$$

where Φ is the flux threading the qubit loop, Φ_S is the flux threading the SQUID loop and $\varphi_0 = \hbar/2e$. One can thus write

$$\begin{aligned}&\bar{\beta}\frac{1+\bar{d}}{2}E_J \cos\varphi_{23} + \bar{\beta}\frac{1-\bar{d}}{2}E_J \cos\varphi'_{23} \\ &= \bar{\beta}E_J\sqrt{\frac{\left(1+\bar{d}^2\right)+\left(1-\bar{d}^2\right)\cos\left(\frac{\Phi_s}{\varphi_0}\right)}{2}}\cos\left(\varphi_{23} - \frac{\Phi_s}{2\varphi_0} + \arctan\left(\bar{d}\tan\left[\frac{\Phi_s}{2\varphi_0}\right]\right)\right)\end{aligned} \tag{3.25}$$

At optimal point, the sum of the phases across all junctions (including the squid effective junction) should be a odd multiple of π. We thus obtain the condition for optimal points $\Phi_\star$ given by

$$\frac{\Phi_\star}{\varphi_0} - \frac{\Phi_s}{2\varphi_0} + \overline{\delta\varphi} = k\pi \tag{3.26}$$

with $k = \pm 1, \pm 3, \pm 5...$ and $\tan\overline{\delta\varphi} = \bar{d}\tan\left[\frac{\Phi_s}{2\varphi_0}\right]$.

3.2.2 Kinetic inductance of the SQUID loop

The kinetic inductance of the SQUID loop is represented in the circuit of Fig.3.5 as a an inductor of inductance L_k in series with the large SQUID junction. To find the renormalized parameters for this junction, we treat it as a linear element with admittance

$$Y_J(\omega) = \frac{1}{i\omega L_J} + i\omega C_J = \frac{1-(\omega/\omega_p)^2}{i\omega L_J} \tag{3.27}$$

with $\omega_p = 1/\sqrt{L_J C_J}$ the plasma frequency of the junction. Adding the kinetic inductance in series, we find for the total admittance:

$$Y_t(\omega) = \left(i\omega L_k + \frac{i\omega L_J}{1-(\omega/\omega_p)^2}\right)^{-1} = \frac{1-(\omega/\omega_p)^2}{i\omega L_J + i\omega L_k(1-(\omega/\omega_p)^2)} \tag{3.28}$$

For frequencies small compared to the plasma frequency, the expansion of this formula at first order in $(\omega/\omega_p)^2$ gives

$$Y_t(\omega) \simeq \frac{1-(\omega/\omega_p)^2\frac{L_J}{L_J+L_k}}{i\omega(L_J+L_k)} \tag{3.29}$$

Comparing the right-hand sides of Eq.3.27 and Eq.3.29, we see that the latter can be obtained from former upon the replacements

$$L_J \to L_J + L_k = L_J(1+\eta)$$
$$C_J \to C_J \left(\frac{L_J}{L_J + L_k}\right)^2 = \frac{C_J}{(1+\eta)^2}$$

where we introduced the dimensionless parameter $\eta = L_k/L_J$. In our model we use these replacement to take into account the kinetic inductance of the SQUID loop.

3.2.3 Kinetic Energy

The kinetic energy K of the system is the sum of the capacitive energies of the circuit

$$K = \frac{1}{2}\sum_{i\neq j} C_{ij}\left(V_j - V_i\right)^2 + \frac{1}{2}C_J\left(\left(V_1 - V_2\right)^2 + \beta'\left(V_2 - V_3\right)^2 + \left(V_3 - V_4\right)^2 + \alpha\left(V_4 - V_1\right)^2\right) \tag{3.30}$$

where C_{ij} is the capacitance between islands i and j and $\beta' = \beta\left(\frac{1+d}{2(1+\eta)^2} + \frac{1-d}{2}\right)$ according to Eq.3.20. It is a quadratic form of the island voltages V_i and can thus be written as

$$K = \frac{1}{2}\mathbf{V}^T\mathbf{C}\mathbf{V} \tag{3.31}$$

where $\mathbf{V}^T = \begin{pmatrix} V_1 & ,V_2 & ,V_3, & V_4 \end{pmatrix}$ and $\mathbf{C}$ is a 4×4 matrix which we will refer in the following as the capacitance matrix. The matrix $\mathbf{C}$ can be written as the sum of the Josephson capacitance matrix $\mathbf{C_J}$ and the geometric capacitance matrix $\mathbf{C_{geom}}$:

$$\mathbf{C} = \mathbf{C_J} + \mathbf{C_{geom}} \tag{3.32}$$

where

$$\mathbf{C_J} = C_J \begin{pmatrix} 1+\alpha & -1 & 0 & -\alpha \\ -1 & 1+\beta' & -\beta' & 0 \\ 0 & -\beta' & 1+\beta' & -1 \\ -\alpha & 0 & -1 & 1+\alpha \end{pmatrix} \tag{3.33}$$

and

$$\mathbf{C_{geom}} = \begin{pmatrix} C_{10} + \sum_{j\neq 1} C_{1j} & -C_{12} & -C_{13} & -C_{14} \\ -C_{21} & C_{20} + \sum_{j\neq 2} C_{2j} & -C_{23} & -C_{24} \\ -C_{31} & -C_{32} & C_{30} + \sum_{j\neq 3} C_{3j} & -C_{34} \\ -C_{41} & -C_{42} & -C_{43} & C_{40} + \sum_{j\neq 4} C_{4j} \end{pmatrix} \tag{3.34}$$

From this point onward, the tunable flux qubit can be treated in the same manner as already

explained in section 3.1.4 and section 3.1.5.

3.3 Resonator model and circuit QED

The flux qubit is coupled inductively to a coplanar waveguide resonator (CPW), necessary for flux qubit readout and control. In this section we will first describe the Hamiltonian of the CPW and calculate its coupling constant to the qubit. This coupling is essential to understand the flux qubit readout principle, and decoherence mechanisms such as Purcell effect and photon noise.

3.3.1 Hamiltonian of a CPW resonator with infinite quality factor

Let us first consider a coplanar waveguide of length L with open circuit termination on both sides. Contrary to a lumped-element resonator, such a distributed resonator possesses an infinite number of modes. We denote $\mathscr{C}$ the capacitance per unit length, $\mathscr{L}$ the inductance per unit length, $Z_0 = \sqrt{\mathscr{L}/\mathscr{C}}$ the characteristic impedance, and the generalized flux $\Phi = \Phi(\mathbf{x})$ such that $V = \partial_t \Phi$ at position $\mathbf{x} \in [0, L]$. The Lagrangian writes as follows:

$$\mathcal{L} = \int_0^L \frac{1}{2}\left(\mathscr{C}V^2 - \mathscr{L}I^2\right) d\mathbf{x} = \frac{1}{2}\int_0^L \left(\mathscr{C}\dot{\Phi}^2 - \frac{1}{\mathscr{L}}\left(\partial_x \Phi\right)^2\right) d\mathbf{x}$$

We thus decompose Φ into infinite stationary modes of mode number j, each verifying the open circuit boundary condition $I = 0$ at $\mathbf{x} = 0$ and $\mathbf{x} = L$, we thus write

$$\Phi = \sum_{j=1}^{\infty} \Phi_j \cos\left(\pi j \mathbf{x}/L\right)$$

which we inject into the Lagrangian expression and get

$$\mathcal{L} = \frac{L}{2}\sum_{j=1}^{\infty}\left(\frac{\mathscr{C}}{2}\dot{\Phi_j}^2 - \frac{1}{2\mathscr{L}}\left(\frac{\pi j}{L}\Phi_j\right)^2\right)$$

We obtain the Hamiltonian after performing the Legendre transformation

$$H = \sum_{j=1}^{\infty} H_j = \frac{1}{L}\sum_{j=1}^{\infty}\left(\frac{Q_j^2}{\mathscr{C}} + \frac{\pi^2 j^2}{4\mathscr{L}}\Phi_j^2\right)$$

where $Q_j = \partial\mathcal{L}/\partial\dot{\Phi_j} = \mathscr{C}L\dot{\Phi_j}/2$ is the conjugated variable of Φ_j. $[\Phi_n, Q_m] = i\hbar\delta_{nm}$. We can simplify in the language of harmonic oscillators to

$$H_j = \hbar\omega_j\left(a_j^\dagger a_j + 1/2\right)$$

where $a_j = \sqrt{\frac{j\pi}{4Z_0\hbar}}\Phi_j + i\sqrt{\frac{Z_0}{j\hbar\pi}}Q_j$, $\omega_j = j\omega_1 = j\left(\frac{\pi}{L}c\right)$ and $c = \sqrt{\frac{1}{\mathscr{C}\mathscr{L}}}$ the wave velocity in the CPW. Remembering that $I(\mathbf{x}) = -\partial_x\Phi(\mathbf{x})/\mathscr{L}$, we get

$$
\begin{aligned}
I(\mathbf{x}) &= \sum_{j=1}^{\infty} \sin(\pi j \mathbf{x}/L) \frac{\pi j}{L Z_0/c} \left(\sqrt{\frac{2Z_0\hbar}{j\pi}} \left(\frac{a_j + a_j^\dagger}{\sqrt{2}} \right) \right) \\
&= \sum_{j=1}^{\infty} \overbrace{\delta I_0 \sqrt{j} \sin(\pi j x/L)}^{\delta I_1(x)} \left(a_j + a_j^\dagger \right)
\end{aligned} \tag{3.35}
$$

where $\delta I_0 = \omega_1 \sqrt{\frac{\hbar}{\pi Z_0}}$ are the (spatially) maximal quantum vacuum fluctuations of the current in the first mode.

The coupling Hamiltonian between the qubit and the resonator is given by

$$
H_{\text{coupling}} = M I_p I(\mathbf{x}) \sigma_x \tag{3.36}
$$

which considering only the first mode, yields

$$
H_{\text{coupling}} = M I_p \delta I_1(\mathbf{x}) \left(a_1 + a_1^\dagger \right) \sigma_x
$$

Most effects (e.g. photon noise) in circuit Quantum Electro Dynamics are principally dominated by contributions of the first mode, due to the higher modes being highly out of resonance with the qubit. From this point onward, the mode index will be taken to be 1 unless stated otherwise, and the dependency on $\mathbf{x}$ may be omitted to lighten the notations.

3.3.2 Resonator modeled under the Filter Formalism

In practice the CPW resonator is delimited on both ends by *finite* coupling terminations that connects to the external input/output lines. In the following, we will show a formalism that generalizes the results of section 3.3.1 while taking into account the exact lumped-element composition of the resonator. Let us first recall some results from lumped-element electrical circuit engineering.

Propagation in a transmission line A CPW transmission line can be modeled as in Fig.3.6. The inductance per unit cell u is L_u and the capacitance to the ground per unit cell is C_u.

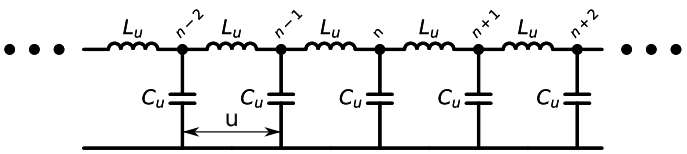

Figure 3.6: **Circuit model of a transmission line**. The unit cell length is u and the inductance (resp. capacitance) per unit cell is L_u (resp. C_u)

We write the equations for the voltage and currents in the transmission line using Kirchhoff equa-

tions

$$V_{n+1} - V_n = -L_u \partial_t I_{n\to n+1}$$
$$-C_u \partial_t V_n = I_{n\to n+1} - I_{n-1\to n}$$

Going to the continuum limit where $L_u/u \to \mathscr{L}$ and $C_u/u \to \mathscr{C}$, we get

$$\partial_x V = -\mathscr{L}\partial_t I$$
$$-\mathscr{C}\partial_t V = \partial_x I$$

We introduce the propagation wave amplitudes to decouple these equations. Namely,

$$A^{\rightarrow} = V/\sqrt{Z_0} + I\sqrt{Z_0}$$
$$A^{\leftarrow} = V/\sqrt{Z_0} - I\sqrt{Z_0}$$

where $Z_0 = \sqrt{\mathscr{L}/\mathscr{C}}$ and obtain two decoupled first order differential equations

$$\partial_t A^{\rightarrow} + c\partial_x A^{\rightarrow} = 0$$
$$\partial_t A^{\leftarrow} - c\partial_x A^{\leftarrow} = 0$$

where $c = 1/\sqrt{\mathscr{L}\mathscr{C}}$ is the propagation velocity in the transmission line. The solutions are of the form $A^{\rightarrow}(x,t) = \mathscr{A}(x - ct)$ and $A^{\leftarrow}(x,t) = \mathscr{A}(x + ct)$.

It is possible to look at individual Fourier components[10] of $A^{\rightarrow/\leftarrow}(x,t)$ at any given point in space x.

$$A^{\rightarrow/\leftarrow}(x,t) = \sum_n A_n^{\rightarrow/\leftarrow}(x)\, e^{-\boldsymbol{i}\omega_n t} + \text{c.c.}$$

Since the equations are linear, we will in the following sections, focus on monochromatic waves[11] only, thus dropping the sum and index n systematically. We write

$$A^{\rightarrow/\leftarrow}(x,t) = A^{\rightarrow/\leftarrow}(x)\, e^{-\boldsymbol{i}\omega t} + \text{c.c.}$$

For two different positions x_1, x_2, we can write that $\mathscr{A}(x_2 \mp ct) = \mathscr{A}\left(x_1 \mp c\left(t \pm \frac{x_1 - x_2}{c}\right)\right)$ and establish equality between

$$A^{\rightarrow/\leftarrow}(x_2,t) = A^{\rightarrow/\leftarrow}(x_2)\, e^{-\boldsymbol{i}\omega t} + \text{c.c.}$$
$$A^{\rightarrow/\leftarrow}\left(x_1, t \pm \frac{x_1 - x_2}{c}\right) = A^{\rightarrow/\leftarrow}(x_1)\, e^{\pm \boldsymbol{i}\omega \frac{x_2 - x_1}{c}} e^{-\boldsymbol{i}\omega t} + \text{c.c.}$$

[10] We adopt the quantum convention for wave propagation (i.e. $e^{\boldsymbol{i}(kx-\omega t)}$), which differs by a sign from the one found typically in the microwave textbooks (i.e. $e^{\boldsymbol{i}(\omega t - kx)}$).

[11] Notice that when we deal with coefficients of a specific frequency ω, we do not add c.c., since that corresponds to $-\omega$. This will valid be the case for subsequent sections: we restore c.c. to come back to the a time-dependent expression.

By unicity of the Fourier decomposition, we identify

$$\begin{aligned} A^{\rightarrow/\leftarrow}(x_2) &= A^{\rightarrow/\leftarrow}(x_1)\, e^{\pm i\omega \frac{x_2-x_1}{c}} \\ &= A^{\rightarrow/\leftarrow}(x_1)\, e^{\pm ik(x_2-x_1)} \end{aligned} \tag{3.37}$$

where $k = \omega/c$. Moreover, the modulus of $|A^{\rightarrow}|^2$ is proportional to the root-mean-square power (assuming $A^{\leftarrow} = 0$)

$$\begin{aligned} P(x,t) &= V(x,t)\, I(x,t) \\ &= \left(A^{\rightarrow}(x)\, e^{-i\omega t} + \text{c.c.}\right)^2 \\ &= 2\,|A^{\rightarrow}(x)|^2 + \left((A^{\rightarrow}(x))^2\, e^{-2i\omega t} + \text{c.c.}\right) \\ P_{\text{RMS}} &= 2\,|A^{\rightarrow}(x)|^2 \end{aligned} \tag{3.38}$$

Calculating transmission and reflection coefficients for simple elements Let us consider the circuit described in Fig.3.7A.

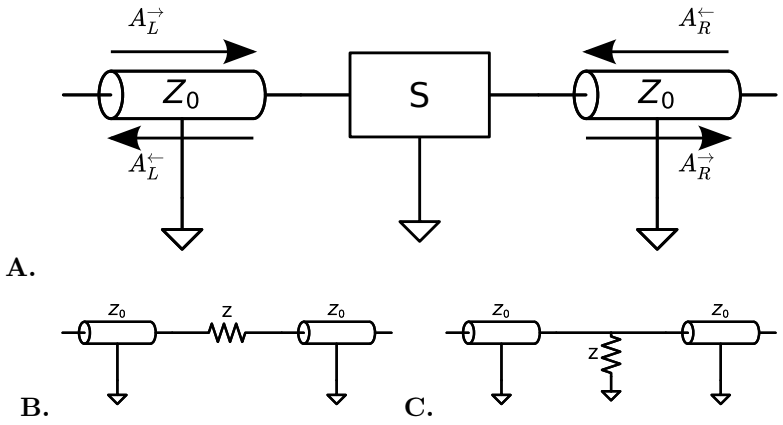

Figure 3.7: **A.** Generic lumped element. **B.** Circuit element in series. **C.** Shorting circuit element.

A scatterer separates the transmission line into two separate regions, namely the left side and the right side. When an incoming EM wave impinges on the scatterer, the propagation wave amplitude can be transmitted and/or reflected partially. We thus write the scattering matrix S

$$\begin{pmatrix} A_L^{\leftarrow} \\ A_R^{\rightarrow} \end{pmatrix} = \overbrace{\begin{pmatrix} r_{\hookleftarrow} & t_{\leftarrow} \\ t_{\rightarrow} & r_{\hookrightarrow} \end{pmatrix}}^{S} \begin{pmatrix} A_L^{\rightarrow} \\ A_R^{\leftarrow} \end{pmatrix}$$

S is unitary because of the conservation of energy.

For instance, we consider in Fig.3.7B a CPW waveguide intersected by an impedance Z in series. We calculate the scattering coefficients by writing the Kirchhoff equations of voltage and current

assuming $A_R^{\leftarrow} = 0$. We get

$$\begin{aligned} ZI &= V_L - V_R \\ &= \sqrt{Z_0}\left[(A_L^{\rightarrow} + A_L^{\leftarrow}) - (A_R^{\rightarrow} + A_R^{\leftarrow})\right] \\ I = I_L &= \frac{1}{\sqrt{Z_0}}\left(A_L^{\rightarrow} - A_L^{\leftarrow}\right) \\ &= I_R = \frac{1}{\sqrt{Z_0}}\left(A_R^{\rightarrow} + A_R^{\leftarrow}\right) \end{aligned}$$

using the scattering matrix, we have $A_R^{\rightarrow} = tA_L^{\rightarrow}$ and $A_L^{\leftarrow} = rA_L^{\rightarrow}$ and thus we get

$$\boxed{\begin{array}{c} r = z/\left(2+z\right) \\ t = 2/\left(2+z\right) \end{array}} \tag{3.39}$$

with $z = Z/Z_0$. If the scatterer is a capacitor[12] $Z = 1/\left(-\boldsymbol{i}\omega\right)C$, we get

$$\begin{aligned} t\left(\omega\right) &= \frac{2}{2 + 1/\left(-\boldsymbol{i}\omega\right)CZ_0} \\ r\left(\omega\right) &= \frac{1/\left(-\boldsymbol{i}\omega\right)CZ_0}{2 + 1/\left(-\boldsymbol{i}\omega\right)CZ_0} \end{aligned} \tag{3.40}$$

Another interesting case to consider is a shorting circuit element as shown in Fig.3.7C. In that case, the Kirchhoff equations gives

$$\begin{aligned} V = V_L &= \sqrt{Z_0}\left(A_L^{\rightarrow} + A_L^{\leftarrow}\right) \\ &= V_R = \sqrt{Z_0}\left(A_R^{\rightarrow} + A_R^{\leftarrow}\right) \\ 0 &= I_L - I_R - V/Z \\ &= \frac{1}{\sqrt{Z_0}}\left(A_L^{\rightarrow} - A_L^{\leftarrow}\right) - \frac{1}{\sqrt{Z_0}}\left(A_R^{\rightarrow} + A_R^{\leftarrow}\right) - V/Z \end{aligned}$$

Thus we get

$$\boxed{\begin{array}{c} r = -1/\left(2z+1\right) \\ t = 2z/\left(2z+1\right) \end{array}}$$

Next we consider finite CPW segments. On one hand, a finite CPW segment of length l with matching impedance acts simply as a phase plate according to Eq.3.37.

$$S = \begin{pmatrix} 0 & e^{ikl} \\ e^{ikl} & 0 \end{pmatrix}$$

[12]We adopt the quantum convention for wave propagation (i.e. $e^{\boldsymbol{i}(kx-\omega t)}$), which differs by a sign from the one found typically in the microwave textbooks (i.e. $e^{\boldsymbol{i}(\omega t-kx)}$).

Segments with different characteristic impedances should be treated as three entities in series: two scattering interfaces sandwiching a simple phase-plate. Each interface gives rise to scattering, and the intermediate region acts as a Fabry-Perot resonator. Let us therefore consider the interface $Z_1|Z_2$. The Kirchhoff equations writes

$$\begin{aligned} V_L = V_R &= \sqrt{Z_1}\,(A_L^{\rightarrow} + A_L^{\leftarrow}) \\ (A_L^{\rightarrow} - A_L^{\leftarrow})/\sqrt{Z_1} = I_L &= I_R = (A_R^{\rightarrow} - A_R^{\leftarrow})/\sqrt{Z_2} \\ V_L/I_L &= Z_1 \\ V_R/I_R &= Z_2 \end{aligned}$$

which we solve to get

$$\begin{aligned} t_{\rightarrow} &= \frac{2\sqrt{Z_1 Z_2}}{Z_1 + Z_2} \\ r_{\hookleftarrow} &= \frac{Z_2 - Z_1}{Z_1 + Z_2} \end{aligned}$$

Similarly, two other coefficients can be established by a swap operation $Z_1 \leftrightarrow Z_2$. Finally, we write

$$S = \begin{pmatrix} \frac{Z_2 - Z_1}{Z_1 + Z_2} & \frac{2\sqrt{Z_1 Z_2}}{Z_1 + Z_2} \\ \frac{2\sqrt{Z_1 Z_2}}{Z_1 + Z_2} & \frac{Z_1 - Z_2}{Z_1 + Z_2} \end{pmatrix} \tag{3.41}$$

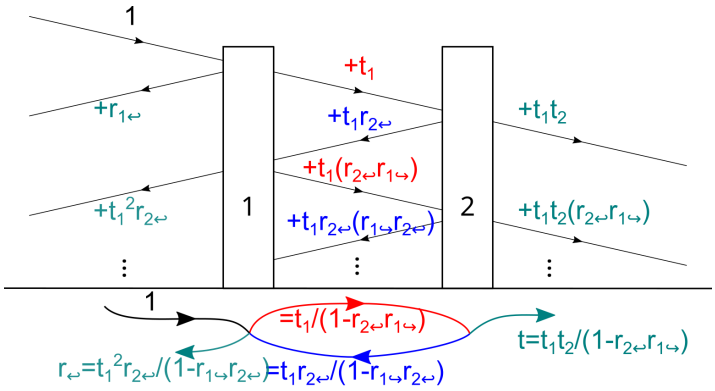

Figure 3.8: Scattering coefficients calculation for a composite scatterer 1 & 2

Recursive chaining Lumped Circuit Elements From the building blocks seen above, it is possible to build a composite element and evaluate the scattering coefficients. Considering two scatterers in series indexed 1 and 2 as shown in Fig.3.8, we may sum over all possible trajectories to get the

expression

$$
\begin{aligned}
t &= \frac{t_1 t_2}{1 - r_{1\hookrightarrow} r_{2\hookleftarrow}} \\
r_{\hookleftarrow} &= r_{1\hookleftarrow} + \frac{t_1 r_{2\hookleftarrow} t_1}{1 - r_{1\hookrightarrow} r_{2\hookleftarrow}} \\
r_{\hookrightarrow} &= r_{2\hookrightarrow} + \frac{t_2 r_{1\hookrightarrow} t_2}{1 - r_{1\hookrightarrow} r_{2\hookleftarrow}}
\end{aligned}
\tag{3.42}
$$

which form the bedrock of all numerical simulations of scattering coefficients in this thesis. Any composite scatterers built from the basic building blocks described above verifies time-reversal symmetry because of the independence on the magnetic field of each component. For the transmission coefficient considered in this thesis, we may thus *always* drop the direction index $t = t_{\rightarrow} = t_{\leftarrow}$.

$\lambda/2$ CPW Resonators with symmetrical terminations The use of symmetrical terminations on both ends of a CPW segment of length $L = \lambda/2$ ensures that exactly at the resonant frequency $\omega_r = 2\pi c/\lambda$, a continuous wave signal is fully transmitted, and no reflection is observed. This results from coherent interference of transmission amplitudes (see Fig.3.9), which converges to a unitary transmission coefficient after performing the substitution

$$
\tau(\omega) = \sum_{j=0}^{\infty} t(\omega)\, e^{\boldsymbol{i}kL} \left(r^2(\omega)\, e^{2\boldsymbol{i}kL}\right)^j t(\omega) = \sum_{j=0}^{\infty} t(\omega)\, e^{\pi \boldsymbol{i}\omega/\omega_r} \left(r^2(\omega)\, e^{2\pi \boldsymbol{i}\omega/\omega_r}\right)^j t(\omega)
$$

$$
\boxed{\tau(\omega) = \frac{t^2(\omega)\, e^{\pi \boldsymbol{i}\omega/\omega_r}}{1 - r^2(\omega)\, e^{2\pi \boldsymbol{i}\omega/\omega_r}}} \tag{3.43}
$$

where $kL = \frac{\omega}{c} \times L = \pi \frac{\omega}{\omega_r}$. At $\omega = \omega_r$, $\left|1 - r^2(\omega)\right| \approx 1 - |r(\omega)|^2$ and by energy conservation,

$$
1 - \left|r^2(\omega)\right| = \left|t^2(\omega)\right|
$$

and thus the transmission

$$
|\tau(\omega_r)| \approx \frac{\left|t^2(\omega)\right|}{1 - (1 - |t^2(\omega)|)} = 1
$$

An identity can be established relating the round trip frequency $\omega_r/2\pi$, the transmission coefficient, and the energy leakage κ

$$
\omega_r/Q \equiv \kappa = 2 \cdot \omega_r/2\pi \cdot |t|^2
$$

The factor 2 stems from the fact that per round trip, both terminations are met once, resulting in two leaking events per round trip. We thus get

$$
\boxed{Q = \pi/|t|^2}
$$

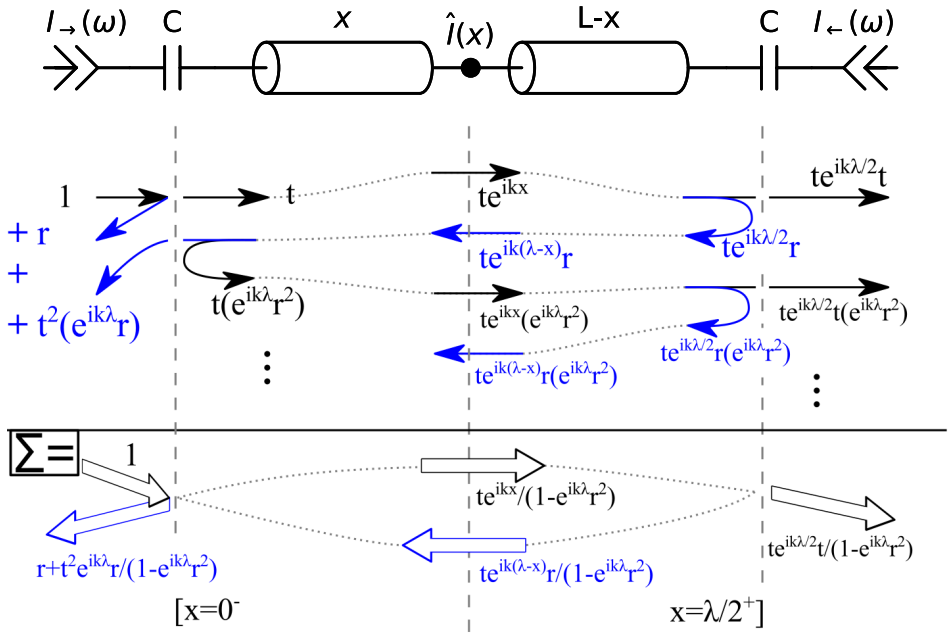

Figure 3.9: **A symmetrical readout resonator.** We show the calculation of the signal at position **x** given a injected unitary signal from the left, as well as the overall transmission coefficient.

Current/voltage seen at a given position in the resonator A qubit situated at the position **x** in the coplanar waveguide resonator of length L with a transition frequency at ω_{ge} will be coupled to the local current $I(\mathbf{x})$ and/or $V(\mathbf{x})$. In the case of a flux qubit, the coupling is mainly inductive as described by Eq.3.36. Working in frequency domain, we can solve the local current as a linear response of the propagation wave amplitudes $A_L^{\rightarrow}$ and $A_R^{\leftarrow}$.

The obtained linear map can be summarized as

$$\begin{aligned} I(x,\omega) &= \frac{1}{\sqrt{Z_0}}\left(f_{\rightarrow}(\omega,x)\,A_L^{\rightarrow} + f_{\leftarrow}(\omega,x)\,A_R^{\leftarrow}\right) \\ V(x,\omega) &= \sqrt{Z_0}\left(g_{\rightarrow}(\omega,x)\,A_L^{\rightarrow} + g_{\leftarrow}(\omega,x)\,A_R^{\leftarrow}\right) \end{aligned} \tag{3.44}$$

The exact numerical value of $f_{\rightarrow/\leftarrow}$ and $g_{\rightarrow/\leftarrow}$ can be calculated by considering the coherent interference from the scattering of all the elements (as done in Fig.3.9). We obtain

$$\boxed{f_{\rightarrow}(\omega,x) = t\frac{e^{i\mathbf{k}\mathbf{x}} - re^{ik(2L-\mathbf{x})}}{1-e^{ikL}r^2}} \tag{3.45}$$

$$\boxed{f_{\leftarrow}(\omega,x) = t\frac{e^{ik(L-\mathbf{x})} - re^{ik(L+\mathbf{x})}}{1-e^{ikL}r^2}}$$

similarly for the voltage, we get

$$g_{\rightarrow}(\omega, x) = t\frac{e^{i\mathbf{k}\mathbf{x}} + re^{i\mathbf{k}(2L-\mathbf{x})}}{1 - e^{i\mathbf{k}L}r^2}$$
$$g_{\leftarrow}(\omega, x) = t\frac{e^{i\mathbf{k}(L-\mathbf{x})} + re^{i\mathbf{k}(L+\mathbf{x})}}{1 - e^{i\mathbf{k}L}r^2}$$

where we see a denominator resulting from the coherent interference reflecting within the resonator.

Coupling between the flux qubit and the resonator In our formalism, the coupling of the qubit to the *resonator* is the result of the filtering of the external bath. The Hamiltonian of the external bath is given by

$$H_b/\hbar = \sum_n \omega_n \left(a^{\rightarrow}_{L,n}\right)^{\dagger} a^{\rightarrow}_{L,n} + \sum_n \omega_n \left(a^{\leftarrow}_{R,n}\right)^{\dagger} a^{\leftarrow}_{R,n}$$

where $\omega_n = n \cdot 2\pi c/\Lambda$, Λ being the length of external cables connected to each side of the system. For convenience, we introduce the density of states

$$\eta(\omega) \equiv \frac{1}{\Delta\omega} = \Lambda/2\pi c \tag{3.46}$$

The expressions of $A^{\rightarrow}_{L,n}$ and $A^{\leftarrow}_{R,n}$ are given by

$$A^{\rightarrow}_{L,n} = \sqrt{\frac{c}{2\Lambda}\hbar\omega_n}\, a^{\rightarrow}_{L,n} \tag{3.47}$$
$$A^{\leftarrow}_{R,n} = \sqrt{\frac{c}{2\Lambda}\hbar\omega_n}\, a^{\leftarrow}_{R,n}$$

Indeed, we verify using Eq.3.38

$$\begin{aligned} P(x,t) &= 2\left(A^{\rightarrow}_{L,n}e^{-i\omega_n t} + \text{H.c.}\right)^2 \\ &= \left(\frac{c}{2\Lambda}\hbar\omega_n\right)\left(2\left(a^{\rightarrow}_{L,n}\right)^{\dagger} a^{\rightarrow}_{L,n} + 1 + \left(e^{-i\omega_n t}a^{\rightarrow}_{L,n}\right)^2 + \left(e^{i\omega_n t}a^{\rightarrow\dagger}_{L,n}\right)^2\right) \\ P_{\text{RMS}}(x) &= \left(\frac{c}{\Lambda}\right)\cdot\hbar\omega_n\left[\left(a^{\rightarrow}_{L,n}\right)^{\dagger} a^{\rightarrow}_{L,n} + \frac{1}{2}\right] \end{aligned}$$

which indeed reflects the energy carried by the influx of photons.

We obtain

$$I(x,\omega_n) = \frac{1}{\sqrt{Z_0}}\left(f_{\rightarrow}(\omega_n, x)\, A^{\rightarrow}_{L,n} + f_{\leftarrow}(\omega_n, x)\, A^{\leftarrow}_{R,n}\right)$$

which gives us

$$\begin{aligned}\hat{I}(x) &= \sum_n \frac{1}{\sqrt{Z_0}} \left(f_{\rightarrow}(\omega_n, x)\, A^{\rightarrow}_{L,n} + f_{\leftarrow}(\omega_n, x)\, A^{\leftarrow}_{R,n} \right) \\ &= \sqrt{\frac{c}{2\Lambda}} \sum_n \sqrt{\frac{\hbar\omega_n}{Z_0}} \left(f_{\rightarrow}(\omega_n, x)\, a^{\rightarrow}_{L,n} + f_{\leftarrow}(\omega_n, x)\, a^{\leftarrow}_{R,n} \right) + \text{H.c.}\end{aligned} \tag{3.48}$$

Let us introduce a linear combination of $a^{\rightarrow}_{L,n}$ and $a^{\leftarrow}_{R,n}$

$$\mathbf{A} = \frac{\sum_n n \left(f_{\rightarrow}(\omega_n, x)\, a^{\rightarrow}_{L,n} + f_{\leftarrow}(\omega_n, x)\, a^{\leftarrow}_{R,n} \right)}{\sqrt{\sum_n n^2 \left(|f_{\rightarrow}(\omega_n, x)|^2 + |f_{\leftarrow}(\omega_n, x)|^2 \right)}} \tag{3.49}$$

which verifies $\left[\mathbf{A}, \mathbf{A}^{\dagger}\right] = 1$ and thus can rewrite the current operator under the form $\hat{I}(x) = \delta I(x) \left(\mathbf{A} + \mathbf{A}^{\dagger} \right)$, where

$$\begin{aligned}\delta I(x) &= \sqrt{\sum_n \frac{c}{2\Lambda Z_0} \hbar\omega_n \left(|f_{\rightarrow}(\omega_n, x)|^2 + |f_{\leftarrow}(\omega_n, x)|^2 \right)} \\ &= \sqrt{\int_{d\omega} \eta(\omega) \frac{c}{2\Lambda Z_0} \hbar\omega \left(|f_{\rightarrow}(\omega, x)|^2 + |f_{\leftarrow}(\omega, x)|^2 \right)}\end{aligned}$$

Injecting the expression of η , we recover an expression independent of Λ

$$\begin{aligned}\delta I(x) &= \sqrt{\int_{d\omega} \frac{\hbar\omega}{4\pi Z_0} \left(|f_{\rightarrow}|^2(\omega, x) + |f_{\leftarrow}|^2(\omega, x) \right)} \\ \delta V(x) &= \sqrt{\int_{d\omega} \frac{\hbar\omega Z_0}{4\pi} \left(|g_{\rightarrow}|^2(\omega, x) + |g_{\leftarrow}|^2(\omega, x) \right)}\end{aligned}$$

from which an expression for the coupling constant between the resonator and the qubit may be established

$$\boxed{\hbar g = M I_p \sqrt{\int_{d\omega} \frac{\hbar\omega}{4\pi Z_0} \left(|f_{\rightarrow}|^2(\omega, x) + |f_{\leftarrow}|^2(\omega, x) \right)}} \tag{3.50}$$

Let us try to reproduce the results from section 3.3.1. Considering the $\lambda/2$ length of the CPW

resonator, we may develop an approximation for $f_{\rightarrow}(x,\omega)$ around the first mode $\omega \approx \omega_1$

$$\begin{aligned} f_{\rightarrow}(x,\omega\approx\omega_1) &= \frac{t\left(\exp\left(2\pi\boldsymbol{i}\frac{\omega}{\omega_1}\frac{x}{\lambda}\right) - r\exp\left(2\pi\boldsymbol{i}\frac{\omega}{\omega_1}\frac{(\lambda-x)}{\lambda}\right)\right)}{1-r^2\exp\left(2\pi\boldsymbol{i}\frac{\omega}{\omega_1}\right)} \\ &\approx \frac{\boldsymbol{i}2x_C\sin\left(-\pi\frac{\omega}{\omega_1}\frac{2x-\lambda}{\lambda}\right)\exp\left(-\pi\boldsymbol{i}\frac{\omega}{\omega_1}\right)}{x_C^2 - 2\pi\boldsymbol{i}\frac{\omega-\omega_1}{\omega_1}} \\ |f_{\rightarrow}(x,\omega)|^2 &\approx \frac{1}{1+\left(\left(\omega-\omega_1\right)/\left[\frac{x_C^2\omega_1}{2\pi}\right]\right)^2}\cdot\frac{4}{x_C^2}\sin^2\left(\pi\frac{\omega}{\omega_1}\frac{2x-\lambda}{\lambda}\right) \end{aligned} \tag{3.51}$$

where $x_C = \omega C Z_0/2$. The first part converges to a Dirac distribution at ω_1 when $x_C \to 0$

$$\frac{1}{1+\left(\frac{2\pi}{x_C^2}\frac{\omega-\omega_1}{\omega_1}\right)^2} \overset{x_C\to 0}{\longrightarrow} \left[\frac{x_C^2\omega_1}{2\pi}\right]\pi\delta(\omega-\omega_1)$$

from which we get

$$\int_{d\omega}\frac{\hbar\omega}{4\pi Z_0}|f_{\rightarrow}(x,\omega)|^2 = \frac{\hbar\omega_1}{4\pi Z_0}\frac{x_C^2\omega_1}{2\pi}\frac{4}{x_C^2}\sin^2\left(2\pi\frac{x}{\lambda}\right) = \frac{\hbar\omega_1^2}{2\pi Z_0}\sin^2\left(2\pi\frac{x}{\lambda}\right)$$

By symmetry, we get $|f_{\leftarrow}(x,\omega)|^2 = |f_{\rightarrow}(\lambda-x,\omega)|^2$. Finally, we obtain

$$\delta I(x) = \left|\sin\left(2\pi\frac{x}{\lambda}\right)\right|\sqrt{\frac{\hbar\omega_1^2}{\pi Z_0}}$$

which is in agreement with the expression $\delta I_1(x) = \omega_1\sqrt{\frac{\hbar}{\pi Z_0}}\sin(\pi x/L)$ of Eq.3.35.

3.3.3 Band-cut Bragg Filters

In this section, we replace one of the coupling capacitors of the resonator with a the Bragg Filter, comprised of segments of CPW of length $L_{\mathrm{BF}} = \lambda_c/4$[13] with alternating impedance as shown in Fig.3.10. Let us focus on the Bragg filter in isolation. Recall Eq.3.41 from 3.3.2 that the scattering matrix for propagation amplitudes of an interface $Z_l|Z_h$ writes

$$S_{Z_l|Z_h} \equiv \begin{pmatrix} r_{\hookleftarrow} & t_{\leftarrow} \\ t_{\rightarrow} & r_{\hookrightarrow} \end{pmatrix} = \begin{pmatrix} \frac{Z_h-Z_l}{Z_l+Z_h} & \frac{2\sqrt{Z_lZ_h}}{Z_l+Z_h} \\ \frac{2\sqrt{Z_lZ_h}}{Z_l+Z_h} & \frac{Z_l-Z_h}{Z_l+Z_h} \end{pmatrix}$$

We see that the coefficients only depend on relative ratios between the source and destination impedance. The characteristic impedances $Z_{l/h}$ can be easily adjusted by modifying the width of the central conductor and the gap to the ground [79]. Practically speaking, the higher and lower impedance are $Z_h \approx 80\,\Omega$ and $Z_l = 35\,\Omega$. The reflection coefficients is thus $\left|r_{Z_l|Z_h}\right| \approx 40\%$ between the two interfaces, with the reflected power being $\left|r_{Z_l|Z_h}\right|^2 \approx 15\%$.

[13] Defined in the next paragraph (3.3.3)

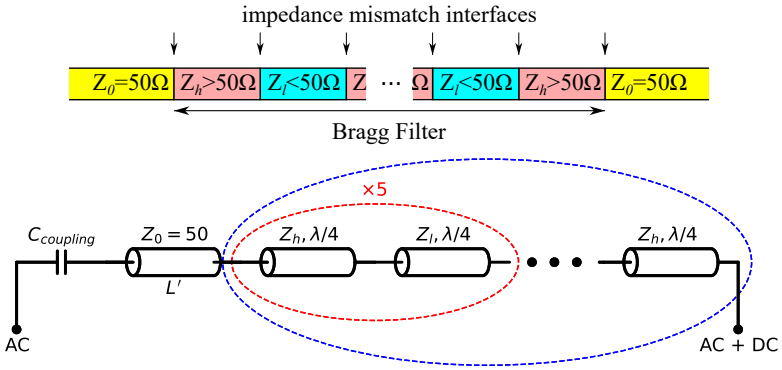

Figure 3.10: **Schematic diagram of the Bragg Filters** replacing a coupling capacitor.

Constructive interference of reflected signals Let us define the *central* frequency $\omega_c/2\pi$, such that the corresponding wavelength is $\lambda_c = 4L_{\mathrm{BF}}$. We will see as the name suggests, this corresponds to the center of the band-cut. Due to the alternating nature of the impedance, two adjacent interface scatterers will have opposite signs for the reflection coefficient. At the central frequency, we can thus write a recursive relationship for r_n, the reflection coefficient for n consecutive interfaces (i.e. $n+1$ alternating impedance segments in series):

$$r_0 = 0$$

$$r_{n+1} = (-1)^{n+1} r_1 + \frac{t_1^2 e^{i\pi} [r_n]}{1 - [(-1)^n r_1] e^{i\pi} [r_n]} \tag{3.52}$$

$$= \frac{(-1)^{n+1} r_1 - r_1^2 r_n - \left(1 - r_1^2\right) [r_n]}{1 + (-1)^n r_1 r_n}$$

$$= \frac{(-1)^{n+1} r_1 - r_n}{1 + (-1)^n r_1 r_n} \tag{3.53}$$

By posing $R_n = (-1)^n r_n$, we get a recursive relationship for R_n

$$R_{n+1} = \frac{r_1 + R_n}{1 + r_1 R_n}$$

By parametrizing $R_n = \tanh \theta_n$ and $r_1 = \tanh \theta_1$ we get the composition

$$R_{n+1} = \frac{\tanh \theta_n + \tanh \theta_1}{1 + \tanh \theta_n \tanh \theta_1} = \tanh (\theta_n + \theta_1)$$

This proves that $\theta_n = n\theta_1$[14], and that the efficiency of the reflection converges to 1 as the number of scatterers $n \to \infty$

$$|r_n| = |R_n| = \tanh (n\theta_1) = \frac{e^{n\theta_1} - e^{-n\theta_1}}{e^{n\theta_1} + e^{-n\theta_1}}$$

[14]Note that in practice, since all lines are eventually connected by 50 Ω, θ corresponding to the first and last interface should be treated separately (35/50 Ω or 80/50 Ω), and should be smaller than all other intermediate interfaces (35/80 Ω).

and the power leak rate decreases exponentially

$$|t_n|^2 = 1 - |r_n|^2 = \frac{2}{\left(e^{n\theta_1} + e^{-n\theta_1}\right)^2} \approx \frac{2}{e^{2n\theta_1}} \tag{3.54}$$

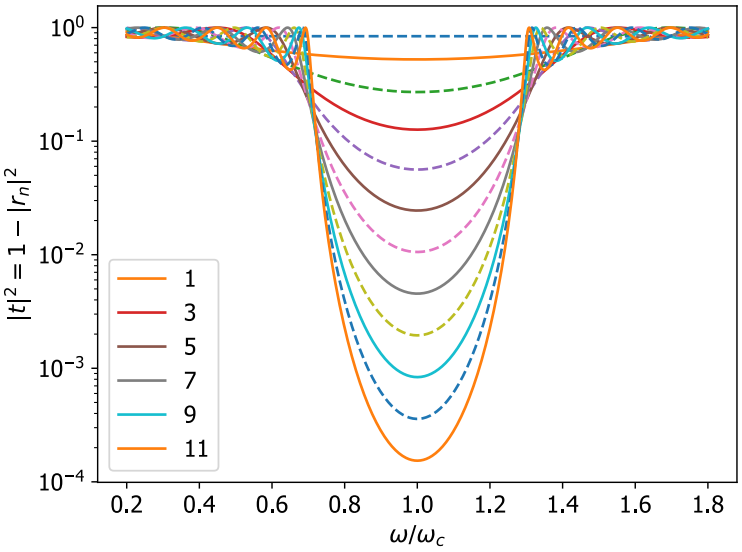

Figure 3.11: **Power transmission up to 12 bragg interfaces.**

Regarding the width of cut-band, it suffice to change the factor $e^{i\pi}$ in Eq.3.52 to a detuned version $e^{i\pi(1+\delta/\omega_c)}$, which amounts to replacing[15] $r_n \to r_n e^{i\pi\delta/\omega_c}$ in Eq.3.53 and leads to

$$R_{n+1} = \frac{r_1 + R_n e^{i\pi\delta/\omega_c}}{1 + r_1 R_n e^{i\pi\delta/\omega_c}}$$

The power transmission after the first 12 iterations of this recursive relationship is shown in Fig.3.11.

3.3.4 Flux qubit readout through the CPW using Cavity Quantum Electro Dynamics

In this section, we give an introduction to the framework of Cavity Quantum Electro Dynamics, and to how it allows for readout of the flux qubit. In the following, we suppose that the flux qubit is biased at its optimal point, where $\Phi = \Phi_0/2$ and thus $\omega_{ge} = \Delta$. By going to the rotating frame associated with $\hbar\omega_r \left(\mathbf{A}^\dagger\mathbf{A} + \frac{\sigma_z}{2}\right)$, we are left with the Hamiltonian

$$H/\hbar = (\Delta - \omega_r)\frac{\sigma_z}{2} + g\left(\sigma_+ e^{i\omega_r t} + \sigma_- e^{-i\omega_r t}\right)\left(\mathbf{A}e^{-i\omega_r t} + \mathbf{A}^\dagger e^{i\omega_r t}\right)$$

[15] A round trip is $2L_{\mathrm{BF}} = \lambda/2$

The rotating wave approximation throws out the rapidly rotating coupling terms, such that we are left with

$$H/\hbar \approx \delta \frac{\sigma_z}{2} + g\left(\sigma_+ \mathbf{A} + \sigma_- \mathbf{A}^\dagger\right)$$

where $\delta = \Delta - \omega_r$ is called the *detuning* of the qubit with respect to the resonator.

Under the effect of this Hamiltonian, the total number of excitation n, namely the operator $\sigma_z + \mathbf{A}^\dagger \mathbf{A}$, is conserved. It is thus interesting to work in the basis of individual stable subspaces, where we denote g/e for flux qubit ground and excited state, and an integer number for photon Fock states. The tensor product $\otimes$ is implicit.

$$\begin{aligned}
\mathfrak{B}_0 &= \{|g\rangle |0\rangle\} \\
\mathfrak{B}_1 &= \{|g\rangle |1\rangle, |e\rangle |0\rangle\} \\
\mathfrak{B}_2 &= \{|g\rangle |2\rangle, |e\rangle |1\rangle\} \\
&\vdots
\end{aligned}$$

For all $n \geq 1$, we have the reduced Hamiltonian matrix expressed in the subspace generated by basis $\mathfrak{B}_n$

$$H_n/\hbar = \frac{\delta}{2}\sigma_z + \sqrt{n} g \sigma_x = \sqrt{\left(\frac{\delta}{2}\right)^2 + ng^2}\left(\cos\theta \sigma_z + \sin\theta \sigma_x\right)$$

where $\cos\theta = \frac{\delta}{2}/\sqrt{\left(\frac{\delta}{2}\right)^2 + ng^2}$, and $\sin\theta = \sqrt{n}g/\sqrt{\left(\frac{\delta}{2}\right)^2 + ng^2}$. Diagonalization of this yields eigenvectors

$$\left(H_i/\hbar + \operatorname{sign}(\delta)\sqrt{\left(\frac{\delta}{2}\right)^2 + ng^2}\right)\left(\cos\frac{\theta}{2}|g\rangle|n\rangle + \sin\frac{\theta}{2}|e\rangle|n-1\rangle\right) = 0$$

$$\left(H_i/\hbar - \operatorname{sign}(\delta)\sqrt{\left(\frac{\delta}{2}\right)^2 + ng^2}\right)\left(-\sin\frac{\theta}{2}|g\rangle|n\rangle + \cos\frac{\theta}{2}|e\rangle|n-1\rangle\right) = 0$$

Let us define the *ground-like* states[16] $|G,n\rangle \equiv \cos\frac{\theta}{2}|g\rangle|n\rangle + \sin\frac{\theta}{2}|e\rangle|n-1\rangle$ and *excited-like* states $|E,n-1\rangle \equiv -\sin\frac{\theta}{2}|g\rangle|n\rangle + \cos\frac{\theta}{2}|e\rangle|n-1\rangle$. For completeness, we also extend the definition to $|G,0\rangle \equiv$

[16] most of the probability amplitude is in the ground state for the qubit

$|g\rangle|0\rangle$. For the situation in which $\left(\frac{\delta}{2}\right)^2 \gg ng^2$, the following properties hold true

$$\begin{aligned}
\sin\frac{\theta}{2} &\ll 1 \\
|G,n\rangle &\approx |g\rangle|n\rangle \\
|E,n-1\rangle &\approx |e\rangle|n-1\rangle \\
\sqrt{\left(\frac{\delta}{2}\right)^2 + ng^2} &\approx \frac{\delta}{2}\left(1 + \frac{ng^2}{2\left(\frac{\delta}{2}\right)^2}\right) \\
&= \frac{\delta}{2} + \frac{ng^2}{\delta}
\end{aligned}$$

We coin $\chi \equiv g^2/\delta$ as the *dispersive shift* for reasons which shall soon become apparent. To move back to the un-rotated frame, it suffices to add back the energy term $\hbar\omega_r\left(\mathbf{A}^\dagger\mathbf{A} + \frac{\sigma_z}{2}\right)$. Finally, the ladder of the ground-like states $|G,n\rangle$ form an energy ladder $E_{G,n}/\hbar = n\omega_r - \delta/2 - n\chi$. Similarly for $|E,n\rangle$ we have $E_{E,n} = n\omega_r + \delta/2 - n\chi$. These two energy ladders can be summarized under a new succinct form, thanks to the approximation $|G,n\rangle \approx |g\rangle|n\rangle$ and $|E,n-1\rangle \approx |e\rangle|n-1\rangle$

$$H/\hbar = \Delta\frac{\sigma_z}{2} + \omega_r\mathbf{A}^\dagger\mathbf{A} + \chi\sigma_z\mathbf{A}^\dagger\mathbf{A} \tag{3.55}$$

The physical interpretation of the above expression, which holds true only for $\left(\frac{\delta}{2}\right)^2 \gg ng^2$, is that the state of the qubit will induce a shift in the resonator resonance of $\pm\chi$. This constitutes the core principle of dispersive readout. Inversely, the transition of the flux qubit will fluctuate with the number of photon in the resonator, which gives rise to the so-called *photon-noise* decoherence, which we will treat in 3.5.5. Note that another way to arrive at the same result is to use the so-called Schrieffer-Wolf transformation [80]

$$\begin{aligned}
H_0 + H_c \rightarrow H_0 + \frac{1}{2}[S, H_c] + O\left(H_c^3\right) \\
H_0 \equiv \hbar\left(\omega_r\mathbf{A}^\dagger\mathbf{A}\otimes\mathbf{1} + (\omega_r+\delta)\,\mathbf{1}\otimes\frac{\sigma_z}{2}\right) \\
H_c \equiv \hbar g\left(\mathbf{A} + \mathbf{A}^\dagger\right)\otimes\sigma_x
\end{aligned}$$

where the generator S must obey $[H_0, S] = H_c$. In our case, it suffices to take $S = g/\delta\left(\sigma_-\mathbf{A}^\dagger - \sigma_+\mathbf{A}\right)$.

As a design principle, χ should be comparable to the loss rate of the resonator κ in order for the dispersive shift to be efficiently detected.

3.4 Flux Qubit Relaxation

3.4.1 Purcell loss

The Hamiltonian of the flux qubit can be written as

$$H = \hbar\omega_{ge}\frac{\sigma_z}{2} + MI_p\hat{I}(x)\,\sigma_x \tag{3.56}$$

Thus, according to the Fermi Golden Rule, the relaxation rates associated to fluctuations of the current in the resonator $\hat{I}(x)$ can be written as

$$\begin{aligned}\Gamma_{e\to g} &= \frac{2\pi}{\hbar^2}M^2I_p^2S_I(\omega_{ge})\\ \Gamma_{g\to e} &= \frac{2\pi}{\hbar^2}M^2I_p^2S_I(-\omega_{ge})\\ \Gamma_P &= \frac{2\pi}{\hbar^2}M^2I_p^2\left[S_I(\omega_{ge}) + S_I(-\omega_{ge})\right]\end{aligned}$$

where $\Gamma_{e\to g}$ (resp. $\Gamma_{g\to e}$) is the transition rate from $|e\rangle$ to $|g\rangle$ (resp. $|g\rangle$ to $|e\rangle$), Γ_P is the Purcell decay rate and S_I is the current power spectrum defined as

$$S_I(\omega) \equiv \frac{1}{2\pi}\int_{t\in\mathbb{R}}\langle I(t)\,I(0)\rangle\, e^{i\omega t}$$

We recall that $I(x,\omega)$ can be expressed as a function of the propagation wave amplitudes $A_L^{\rightarrow}(\omega)$ and $A_R^{\leftarrow}(\omega)$ in the incoming lines as

$$I(x,\omega) = \frac{1}{\sqrt{Z_0}}\left(f_{\rightarrow}(x,\omega)\,A_L^{\rightarrow}(\omega) + f_{\leftarrow}(x,\omega)\,A_R^{\leftarrow}(\omega)\right)$$

Due to the independence of signals $A_L^{\rightarrow}(\omega)$ and $A_R^{\leftarrow}(\omega)$, we have

$$S_I(\omega) = \frac{1}{Z_0}\left(\left|f_{\rightarrow}(\omega,x)\right|^2 S_{A_L^{\rightarrow}}(\omega) + \left|f_{\leftarrow}(\omega,x)\right|^2 S_{A_R^{\leftarrow}}(\omega)\right)$$

According to Eq.3.47

$$\begin{aligned}A_L^{\rightarrow}(t) &= \sum_n \sqrt{\frac{c}{2\Lambda}\hbar\omega_n}\,a_{L,n}^{\rightarrow}e^{-i\omega_n t} + \text{H.c.}\\ A_R^{\leftarrow}(t) &= \sum_n \sqrt{\frac{c}{2\Lambda}\hbar\omega_n}\,a_{R,n}^{\leftarrow}e^{-i\omega_n t} + \text{H.c.}\end{aligned}$$

We may thus calculate

$$\begin{aligned}
S_{A_L^{\rightarrow}}(\omega) &\equiv \frac{1}{2\pi}\int_{t\in\mathbb{R}} \langle A_L^{\rightarrow}(t)\, A_L^{\rightarrow}(0)\rangle\, e^{\boldsymbol{i}\omega t} \\
&= \frac{1}{2\pi}\sum_{n\geq 0}\left(\frac{c}{2\Lambda}\hbar\omega_n\right)\int_{t\in\mathbb{R}}\left(\left\langle \left(a_{L,n}^{\rightarrow}\right)^{\dagger} a_{L,n}^{\rightarrow}\right\rangle e^{+\boldsymbol{i}\omega_n t} + \left\langle a_{L,n}^{\rightarrow}\left(a_{L,n}^{\rightarrow}\right)^{\dagger}\right\rangle e^{-\boldsymbol{i}\omega_n t}\right) e^{\boldsymbol{i}\omega t} \\
&= \sum_{n\geq 0}\left(\frac{c}{2\Lambda}\hbar\omega_n\right)\left(\left\langle \left(a_{L,n}^{\rightarrow}\right)^{\dagger} a_{L,n}^{\rightarrow}\right\rangle \delta(\omega_n+\omega) + \left\langle a_{L,n}^{\rightarrow}\left(a_{L,n}^{\rightarrow}\right)^{\dagger}\right\rangle \delta(\omega_n-\omega)\right)
\end{aligned}$$

By replacing the discrete sum $\sum_{n\geq 0}$ by its equivalent integral $\int_{d\omega\in\mathbb{R}_+}\eta(\omega)$, we get

$$\begin{aligned}
S_{A_L^{\rightarrow}}(\omega) &= \int_{d\omega'\in\mathbb{R}_+}\eta(\omega')\left(\frac{c}{2\Lambda}\hbar\omega'\right)\left(\left\langle a^{\dagger}a\right\rangle\delta(\omega'+\omega) + \left\langle aa^{\dagger}\right\rangle\delta(-\omega'+\omega)\right) \\
&= \int_{d\omega'\in\mathbb{R}_+}\frac{\hbar\omega'}{4\pi}\left(\left\langle a^{\dagger}a\right\rangle\delta(\omega'+\omega) + \left\langle aa^{\dagger}\right\rangle\delta(-\omega'+\omega)\right) \\
&= \begin{cases} \frac{\hbar\omega}{4\pi}\left\langle aa^{\dagger}\right\rangle & \omega>0 \\ \frac{\hbar\omega}{4\pi}\left\langle a^{\dagger}a\right\rangle & \omega<0 \end{cases}
\end{aligned} \tag{3.57}$$

By considering that the photon bath is thermalized at a given temperature T,

$$\boxed{S_{A_L^{\rightarrow}}(\omega) = \begin{cases} \frac{\hbar\omega}{4\pi}\frac{1}{1-e^{-\beta\hbar\omega}} & \omega>0 \\ \frac{\hbar\omega}{4\pi}\frac{e^{-\beta\hbar\omega_{ge}}}{1-e^{-\beta\hbar\omega}} & \omega<0 \end{cases}} \tag{3.58}$$

where $\beta = \frac{1}{k_B T}$. Finally, the Purcell decay rate writes

$$\boxed{\Gamma_P = \left(\frac{MI_p}{\hbar}\right)^2 \frac{\hbar\omega_{ge}\coth\left(\frac{\hbar\omega_{ge}}{2k_BT}\right)\left(\left|f_{\rightarrow}(\omega,x)\right|^2 + \left|f_{\leftarrow}(\omega,x)\right|^2\right)}{2Z_0}} \tag{3.59}$$

which we separate into two parts

$$\Gamma_P = \Gamma^{\rightarrow} + \Gamma^{\leftarrow}$$

where

$$\Gamma^{\rightarrow/\leftarrow} = \left(\frac{MI_p}{\hbar}\right)^2 \frac{\hbar\omega_{ge}}{2Z_0}\left|f_{\rightarrow/\leftarrow}(\omega_{ge},x)\right|^2 \coth\left(\frac{\beta\hbar\omega_{ge}}{2}\right) \tag{3.60}$$

Comparison to Input output theory Compared to the widely-used formula predicted by input-output theory [81] $\Gamma = \kappa\frac{g^2}{\delta^2+\kappa^2/4}$, Eq.3.60 predicts exactly the same Lorentzian behavior *around* resonance. Indeed, it is possible to establish that the filter function writes approximately

$$f(\omega) \approx \frac{\text{cte.}}{\kappa/2 - i\delta} \tag{3.61}$$

However, the approximation breaks down, when δ becomes comparable to ω_{ge}. Indeed, the denominator $\kappa/2 - i\delta$ grows a lot quicker than the one described in this formalism $1 - e^{2ikL} r_C^2$, which curls up in the complex plane in a bounded fashion. Secondly, the dependence of t_C and r_C on ω is not negligible (see Eq.3.40). This property is specifically exploited in the Bragg Filter terminated resonator, where the Bragg Filter behavior around ω_{ge} (central region of the cut band) can be very different from around ω_r (edges of the cut band).

All in all, even for a standard capacitor terminated resonator, for a typical detunings of 2 GHz in front of $\frac{\omega_r}{2\pi} = 10\,\text{GHz}$, the experimental difference can be 2-10 fold compared to the predictions by Input-Output theory.

Rabi driving frequency as a function of driving power According to Eq.3.48

$$\hat{I}(x) = \frac{1}{\sqrt{Z_0}} \sum_n \left(f_{\rightarrow}(\omega_n, x)\, A^{\rightarrow}_{L,n} + f_{\leftarrow}(\omega_n, x)\, A^{\leftarrow}_{R,n} \right) + \text{H.c.}$$

Let us assume that we drive a monochromatic wave ($\omega_n = \omega_{ge}$) from the left such that $A^{\leftarrow}_{R,n} = 0, \forall n$. The resulting Rabi frequency (see Eq.3.56) is

$$\Omega^{\rightarrow} = \frac{2MI_p}{\hbar} \sqrt{\frac{1}{Z_0}} \left| f_{\rightarrow}(\omega_{ge}, x)\, A^{\rightarrow}_L(\omega_{ge}) \right|$$

Since $\left|A^{\rightarrow}_L(\omega_{ge})\right|^2 = P_{\text{RMS}}/2$ (see Eq.3.38), we get

$$\boxed{\left(\hbar\Omega^{\rightarrow}\right)^2 / P_{\text{RMS}} = \frac{\left(2MI_p\right)^2}{2Z_0} \left| f_{\rightarrow}(\omega_{ge}, x) \right|^2} \tag{3.62}$$

The same can be done for a monochromatic drive from the right, assuming $A^{\rightarrow}_{L,n} = 0, \forall n$. Thus we get

$$\boxed{\left(\hbar\Omega^{\leftarrow}\right)^2 / P_{\text{RMS}} = \frac{\left(2MI_p\right)^2}{2Z_0} \left| f_{\leftarrow}(\omega_{ge}, x) \right|^2} \tag{3.63}$$

Calculating the Purcell rate from Rabi frequency Considering Eq.3.60, Eq.3.62 and Eq.3.63, we establish a relationship valid at zero temperature

$$\boxed{\Gamma^{\rightarrow/\leftarrow}(0\,\text{K}) = \frac{\hbar\omega_{ge} \left(\Omega^{\rightarrow/\leftarrow}\right)^2}{4P_{\text{RMS}}}} \tag{3.64}$$

We thus get

$$\Gamma_P(0\,\text{K}) = \frac{\hbar\omega_{ge} \left[\left(\Omega^{\rightarrow}\right)^2 + \left(\Omega^{\leftarrow}\right)^2 \right]}{4P_{\text{RMS}}}$$

In the following this relationship will be used to establish the Purcell rates (see Fig.6.3B in section 6.1.4). The advantage of this formula is that it gives directly the Purcell rate via the measurement

of the Rabi frequency for a given power P_{RMS} with a precision limited by the uncertainty on P_{RMS}, which is typically $\pm 1\,\text{dB}$.

3.4.2 Dielectric Loss

Dielectric losses take place in the capacitors of the flux qubit and can be modeled by a small resistor of resistance R_{ij} in series with each capacitor. The value of R_{ij} is determined by the loss tangent of the dielectric material (see section §4) separating island i and j of capacitor C_{ij}[17] and is given by

$$R_{ij} C_{ij} \omega_{qb} = \tan\delta \tag{3.65}$$

Since this angle δ is very small, the impedance of the flux qubit circuit is much higher than R_{ij} and can thus be considered as an open circuit. As a result, the filter function is $g(\omega) = 1 + r \approx 2$, and the voltage at a point verifies the following power spectrum

$$S_{\delta V_{ij}}(\omega_{ge}) + S_{\delta V_{ij}}(-\omega_{ge}) = |g(\omega)|^2 \frac{R\hbar\omega_{ge}}{4\pi} \coth\left(\frac{\beta\hbar\omega_{ge}}{2}\right) \approx \frac{\hbar\omega_{ge} R}{\pi}$$

To calculate the relaxation rate, one must determine the transverse term $\sigma_{x/y}$ in the Hamiltonian introduced by a small perturbation δV_{ij}.

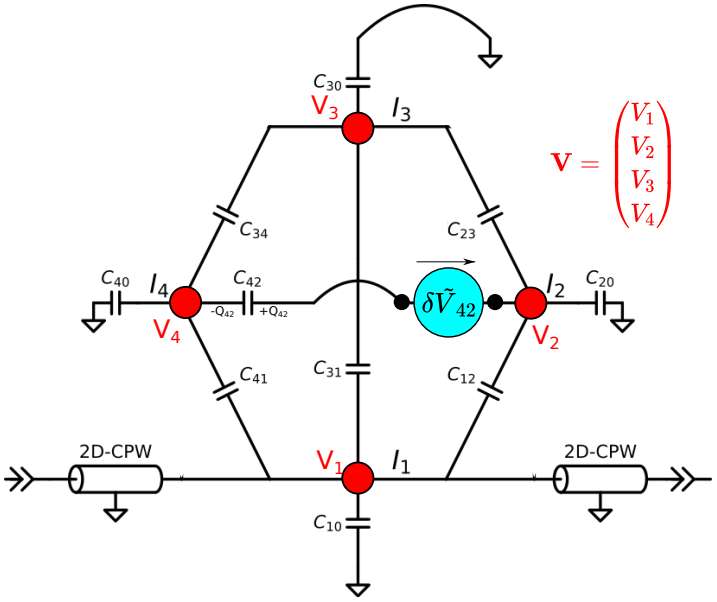

Figure 3.12: An external bias δV_{ij}(cyan) is applied. Here we show the example of $(i,j) = (4,2)$, where we write $Q_{42} = C_{42}\left(V_4 - \left(V_2 + \tilde{V}_{42}\right)\right)$

Let us suppose fixed a given voltage configuration[18] $\mathbf{V}$. As we can see in Fig.3.12, the variation of

[17] Contrary to Fig.3.1, C_{ij} is the i,j-th element of the total capacitance matrix $\mathbf{C}$, which *includes* the junction capacitances, although they present a much smaller contribution because of smaller $\tan\delta$ as we will soon see.

[18] Bold variables are either for matrices or the vectors that are of dimension 4, corresponding to physical islands. On

charge across the capacitor C_{42} due to δV_{42} is given by

$$\delta Q_{42} = -C_{42}\delta V_{42}$$

At first order in δV_{42}, this modifies the kinetic term by

$$\begin{aligned} dK_{42} &= \delta Q_{42}\left(V_2 - V_4\right) \\ &= -C_{42}\delta V_{42}\mathbf{V}^T \begin{pmatrix} 0 \\ 1 \\ 0 \\ -1 \end{pmatrix} \end{aligned}$$

Let us recall that $\mathbf{P}$ from Eq.3.12 is the 4×3 transfer matrix from the junction coordinates to the island phases such that $\mathbf{V} = \mathbf{P}\vec{\Phi} = \mathbf{P}\left(\mathbf{P}^T\mathbf{C}\mathbf{P}\right)^{-1}\vec{Q}$ (up to a constant). Injecting and generalizing to all other indices ij, we can write the total perturbation of the Hamiltonian to all perturbations δV_{ij}.

$$\begin{aligned} dH &= \sum_{i \neq j}\left(-dK_{ij}\right) \\ &= \sum_{i \neq j} C_{ij}\delta V_{ij}\vec{Q}^T\left(\mathbf{P}^T\mathbf{C}\mathbf{P}\right)^{-1}\mathbf{P}^T\left(\mathbf{e}_j - \mathbf{e}_i\right) \end{aligned}$$

where $\mathbf{e}_i$ is the sparse column vector with 1 only at position i.

Let us justify that $\vec{Q} = (2e)\,\vec{n}$ are transverse, i.e. Pauli X or Y and not Z. The gauge that we adopt in this thesis is that $|g\rangle$ and $|e\rangle$ are real symmetrical and anti-symmetrical wave functions of φ (such that the current operators $\langle e|\sin\left(\varphi_i\right)|g\rangle \in \mathbb{R}$, cf. Eq.3.16). Here, $n_i = -i\partial_\varphi$ which after application on $|g\rangle$ will produce anti-symmetrical and symmetrical pure imaginary wave functions.

$$\begin{aligned} \langle e|\, n_i\, |g\rangle &\in \boldsymbol{i}\mathbb{R} \\ \langle g|\, n_i\, |g\rangle &= 0 \\ \langle e|\, n_i\, |e\rangle &= 0 \end{aligned}$$

The two latter equations come from the flipping of inversion symmetry $I\,|x\rangle = \lambda\,|x\rangle \implies In\,|x\rangle = -\lambda n\,|x\rangle$. This proves that the operators $\vec{n}$ and $\vec{Q}$ are σ_y operators in our gauge.

Let us define the 3×3 real symmetrical matrix comprised of the quantum overlaps of the charge operators

$$\mathbf{Q^2} = \left(\langle e|\, Q_i\, |g\rangle \langle g|\, Q_j\, |e\rangle, \forall i,j \in \{1,2,3\}\right)$$

the other hand, a vectorial notation $\vec{\cdot}$ contains 3 elements, corresponding to the number of free phase variables in the Hamiltonian. Unless specified otherwise, normal scripts with indices denote the components of a matrix or vector.

Seeing that dH is linear in the $\vec{Q}$ operators we can write dH under the form

$$\begin{aligned} dH &= \delta V_{ij} \cdot \left(\vec{Q}^T \vec{L_{ij}}\right) \\ \vec{L_{ij}} &= C_{ij} \left(\mathbf{P}^T \mathbf{C} \mathbf{P}\right)^{-1} \mathbf{P}^T \left(\mathbf{e}_i - \mathbf{e}_j\right) \end{aligned}$$

Subsequently, the loss rate due to δV_{ij} writes

$$\begin{aligned} \Gamma_{ij} &= 2\pi \frac{\left[S_{\delta V_{ij}}\left(\omega_{ge}\right) + S_{\delta V_{ij}}\left(-\omega_{ge}\right)\right] \vec{L_{ij}}^T \mathbf{Q^2} \vec{L_{ij}}}{\hbar^2} \\ &= \left(2\omega_{ge} R/\hbar\right) \mathrm{Tr}\left(\vec{L_{ij}} \vec{L_{ij}}^T \mathbf{Q^2}\right) \\ &= \left(2 \tan\delta_{ij}/\hbar C_{ij}\right) \mathrm{Tr}\left(\vec{L_{ij}} \vec{L_{ij}}^T \mathbf{Q^2}\right) \end{aligned}$$

where we replace the expression of R in the last equality according to Eq.3.65. We get

$$\Gamma_{ij} = \frac{2}{\hbar} \mathrm{Tr}\left(\left(\mathbf{P}^T \mathbf{C} \mathbf{P}\right)^{-1} \left[\mathbf{P}^T \left(\mathbf{e}_i - \mathbf{e}_j\right) C_{ij} \tan\delta_{ij} \left(\mathbf{e}_i - \mathbf{e}_j\right)^T \mathbf{P}\right] \left(\mathbf{P}^T \mathbf{C} \mathbf{P}\right)^{-1} \mathbf{Q^2}\right)$$

After summation over all island pairs i, j in $[\cdot]$, we get

$$\boxed{\Gamma_{\text{dielectric}} = \frac{2}{\hbar} \mathrm{Tr}\left(\left(\mathbf{P}^T \mathbf{C} \mathbf{P}\right)^{-1} \left(\mathbf{P}^T \mathbf{C}' \mathbf{P}\right) \left(\mathbf{P}^T \mathbf{C} \mathbf{P}\right)^{-1} \mathbf{Q^2}\right)} \tag{3.66}$$

where $\mathbf{C}' = \sum_{ij} \left(\mathbf{e}_i - \mathbf{e}_j\right) C_{ij} \tan\delta_{ij} \left(\mathbf{e}_i - \mathbf{e}_j\right)^T$ is the capacitance matrix *weighted* by the $\tan\delta$ of individual capacitive elements (we recover, for the *unweighted* expression, the usual capacitance matrix $\mathbf{C} = \sum_{ij} \left(\mathbf{e}_i - \mathbf{e}_j\right) C_{ij} \left(\mathbf{e}_i - \mathbf{e}_j\right)^T$). For instance, in the case where $\tan\delta$ is homogeneous, we recover $\Gamma = \frac{2}{\hbar} \tan\delta \mathrm{Tr}\left(\left(\mathbf{P}^T \mathbf{C} \mathbf{P}\right)^{-1} \mathbf{Q^2}\right)$. Realistically, we have two different kind of $\tan\delta$, one for the Josephson junctions and another for the geometric capacitance, yielding

$$\mathbf{C}' = \tan\delta_{\mathrm{J}} \mathbf{C_J} + \tan\delta_{\mathrm{geom}} \mathbf{C_{geom}}$$

we may therefore separate into two parts in Eq.3.66

$$\Gamma_{\text{dielectric}} = \Gamma_{\mathrm{J}} + \Gamma_{\mathrm{geom}}$$

For the qubits on sample A, B, C, the value of the wavefunction overlap $\mathbf{Q^2}/\left(2e\right)^2$ is comprised between the range $0.05 - 0.09$. Numerical estimations supposing $\tan\delta_{\mathrm{J}} = 1 \times 10^{-7}$ and $\tan\delta_{\mathrm{geom}} = 1 \times 10^{-5}$ is shown in Tab.3.1.

	Δ	I_P	Γ_{J}	Γ_{geom}
Sample A	7.1 GHz	198 nA	2.9 kHz	50 kHz
Sample B	5.1 GHz	297 nA	1.7 kHz	28 kHz
Sample C	6.6 GHz	295 nA	2.5 kHz	40 kHz

Table 3.1: Numerical for a representative average qubit from each of the samples.

3.5 Flux Qubit Dephasing

3.5.1 General framework for calculating the pure dephasing noise

In an ideal system, the decoherence rate Γ_2 is limited by the energy relaxation rate of the qubit and is given by $\Gamma_2 = \Gamma_1/2$. In practice, the decoherence rate of a qubit may be much larger than this theoretical limit. There are several known sources of dephasing which are responsible for this. Among them, flux noise, charge noise and photon noise in the resonator. The pure dephasing rate of the flux qubit can be estimated by the so-called Ramsey sequence, where two identical $\pi/2$ pulses are played consecutively with a time delay t. It is possible to dynamically decouple the noise responsible for this dephasing by playing a more complex set of pulses. The most popular technique to achieve this is called Hahn Echo technique and consists of playing a π-pulse in between the two $\pi/2$ pulses. This π pulse inverses the time evolution and therefore cancels the contribution to dephasing of low frequency noise.

In the Ramsey sequence, the first $\pi/2$-pulse raises the qubit initially in its ground state into a coherent superposition of $|\Psi(0)\rangle = (|g\rangle + |e\rangle)/\sqrt{2}$. During time t, the qubit performs a free evolution and accumulates phase $\varphi(t)$ and becomes $|\Psi(t)\rangle = \left(|g\rangle + e^{i\varphi(t)}|e\rangle\right)/\sqrt{2}$. The phase $\varphi(t)$ consists of two parts $\varphi(t) = \omega_{ge}t + \delta(t)$, where $\delta(t)$ is the phase due to the small fluctuations $\delta\lambda(t)$ which slightly modify the qubit Hamiltonian. At first order, $\delta(t)$ is given by $\delta(t) = \frac{\partial\omega_{ge}}{\partial\lambda}\int_0^t \delta\lambda(t')dt'$. The decoherence rate of the system corresponds to the decay of the expectation value $\langle\sigma_x(t)\rangle$ and is given by

$$\langle\sigma_x(t)\rangle = \left\langle e^{i\varphi(t)} + e^{-i\varphi(t)} \right\rangle /2$$

When repeating the measurements, the value of $\langle\sigma_x(t)\rangle$ is changed due to the varying environmental noise $\delta(t)$. Therefore, one should average the value of $e^{\pm i\delta(t)}$ in order to determine the influence of this noise. If the fluctuations $\delta\lambda(t')$ are small enough, they can be considered as a random variable with Gaussian distribution [82]. Thus,

$$f_R(t) = \left\langle e^{\pm i\delta(t)} \right\rangle = e^{-1/2\left\langle\delta^2(t)\right\rangle}$$

The expectation value of $\langle\sigma_x(t)\rangle$ will therefore decay according to

$$f_R(t) = e^{-1/2\left(\frac{\partial\omega_{ge}}{\partial\lambda}\right)^2\left\langle\left(\int_0^t \delta\lambda(t')dt\right)^2\right\rangle} \tag{3.67}$$

$$= \exp\left(-\frac{t^2}{2}\left(\frac{\partial\omega_{ge}}{\partial\lambda}\right)^2 \int_{-\infty}^{\infty} d\omega\, S_\lambda(\omega)\,\mathrm{sinc}^2(\frac{\omega t}{2})\right) \tag{3.68}$$

In a Hahn echo sequence, the first $\pi/2$-pulse puts the state of the qubit in a coherent superposition state $|\Psi(0)\rangle = (|0\rangle + |1\rangle)/\sqrt{2}$. During the time t_1, the qubit performs a free evolution and accumulates phase $\varphi_1(t_1) = \omega_{ge}t_1 + \delta_1(t_1)$. The π - pulse flips the time evolution of the qubit such that during the time t_2 it acquires an opposite phase $\varphi_2(t_2) = -\omega_{ge}t_2 - \delta_2(t_2)$. The phase accumulated by $\omega_{ge}t_1$ and $\omega_{ge}t_2$ is canceled when $t_1 = t_2 = t/2$ and the decoherence rate of the qubit - corresponding to the decay $f_E(t) = \langle\sigma_x(t)\rangle$ - is given by

$$f_E(t) = \left\langle e^{\pm i(\delta_1-\delta_2)}\right\rangle \approx \exp\left(-1/2\left\langle\delta_1^2 + \delta_2^2 - \delta_1\delta_2 - \delta_2\delta_1\right\rangle\right)$$

The expectation value of $\langle\sigma_x(t)\rangle$ will therefore decay according to

$$f_E(t) = \exp\left(-\frac{t^2}{2}\left(\frac{\partial\omega_{ge}}{\partial\lambda}\right)^2 \int_{-\infty}^{\infty} d\omega\, S_\lambda(\omega)\sin^2(\frac{\omega t}{4})\,\mathrm{sinc}^2(\frac{\omega t}{4})\right) \tag{3.69}$$

3.5.2 Dephasing away from the optimal point

Away from the optimal point , the high magnetic moment of the circuit ($\sim 500\,\mathrm{GHz/G}$) make its frequency very sensitive to flux

$$\partial_\Phi\omega_{ge} = \frac{\partial\varepsilon}{\partial\Phi}.\frac{\partial\omega_{ge}}{\partial\varepsilon} = \left(\frac{2I_p}{\hbar}\right)^2 \frac{(\Phi - \Phi_0/2)}{\omega_{ge}}$$

The power spectrum of flux noise has a 1/f shape $S_\Phi[\omega] = A_\Phi^2/\omega$. For the Echo sequence, one can calculate exactly the integral given in Eq.3.69 without any additionnal assumption or approximation and one obtains [82]

$$\boxed{\Gamma_{2E}^{\varphi}(\Phi) = \left(\frac{2I_p}{\hbar}\right)^2 \frac{\Phi - \Phi_0/2}{\omega_{ge}(\Phi)} A_\Phi\sqrt{\ln 2}} \tag{3.70}$$

3.5.3 Dephasing at the optimal point: Monte Carlo simulation for second order flux noise

At the optimal point however, $\partial_\Phi\omega_{ge} = 0$ and therefore the qubit is immune to flux fluctuations to first order. Yet, $\partial_\Phi^2\omega_{ge} = \left(\frac{2I_p}{\hbar}\right)^2/(2\pi\Delta) \neq 0$ and thus second order flux noise should be taken into account. Unlike first order, deriving an analytical expression for 2nd order flux noise is not straight-forward. In

this work, we performed numerical Monte Carlo simulations in Python [83]. The source code of this simulation can be found on Github [84].

Microscopically, the flux noise is the sum of many independent uncorrelated sources, most likely spins on the surface of the loops [75]. Thus, it should be well described as a Gaussian variable. To simulate a flux noise trajectory in time, we first generate a series of $2\,n_{\mathrm{FFT}}$ normally distributed real and imaginary random numbers $a_i + \boldsymbol{i} b_i$ that will be used as Fourier components of the signal. These Fourier components are multiplied by an amplitude $A_\Phi \sqrt{\frac{n_{\mathrm{FFT}} dt}{i}}$ where dt is the time step unit of the simulation. Then, we apply an inverse fast Fourier transform in order to obtain a flux noise trajectory with power spectrum of A_Φ^2/f. In the code, the class NoiseGen1OverF is a generator of pink noise. Attributes includes the time step unit dt, and the total number n_{FFT} of samples to generate. The method generate is called to generate a single trajectory $\overrightarrow{\delta\Phi} = (\delta\Phi(t_1), \ldots, \delta\Phi(t_{n_{\mathrm{FFT}}}))$ around zero flux.

Ensemble averaging over noise trajectories The next step of our simulation consists of ensemble averaging of a complex function over different trajectories. For Ramsey sequence, this complex function is

$$f_R(t) = \exp\left(i \int_0^t \omega_{ge}(\Phi + \delta\Phi(u)) - \langle\omega_{ge}\rangle\, du\right)$$

where Φ is the flux threading the loop of the qubit. For Hahn-Echo sequence, the complex function is

$$f_E(t) = \exp\left(i \int_0^{t/2} \omega_{ge}(\Phi + \delta\Phi(u))\, du - i \int_{t/2}^t \omega_{ge}(\Phi + \delta\Phi(u))\, du\right)$$

In order to reduce the function call overheads, the function qb_plot_t2s_at performs the ensemble averaging by sampling the n_{FFT}-sized signal at fixed intervals, much like in a real experiment where ensemble repetitions occur in sequential order at a quasi-fixed period. To further increase the smoothness of the signal, we resample the same signal using the same period but with different time offsets.

```
for i in tqdm.tqdm(range(0, tobs_tstep, laziness)):#line 166
        ...# for different periodic offsets
```

In order to optimize the running complexity, the integral $\int_{t_i}^{t_j} \omega_{ge}(\Phi + \delta\Phi(u))\, du$ is calculated as a difference of pre-cached cumulative sums $\int_0^t \omega_{ge}(\Phi + \delta\Phi(u))\, du$:

$$\int_t^{t_j} \omega_{ge}(\Phi + \delta\Phi(u))\, du = \int_0^{t_j} \omega_{ge}(\Phi + \delta\Phi(u))\, du - \int_0^{t_i} \omega_{ge}(\Phi + \delta\Phi(u))\, du$$

The pre-caching step is performed in only $O(n_{\mathrm{FFT}})$ complexity. To further speed up the whole algorithm, we perform the computation described above by using np.reshape commands instead of writing python for-loops, to exploit the faster speed of C-implemented numpy libraries.

Here is a list of important arguments of the function qb_plot_t2s_at :

1. t_step_ns corresponds to the time step unit dt

2. t_observation_ns, time interval on which the interpulse time delay will be varied. This is the X axis of the final plot.

3. t_total_ns, this is the total length of the pink signal, equal to $n_{\mathrm{FFT}}dt$. The inverse is the resolution df in frequency space.

4. t_cut_off_ns. Its inverse is the low frequency cutoff of the power spectrum. We assume white noise below this threshold.

The default sample program provided under the __main__ statement performs the following steps. First a typical flux qubit transition with parameters Δ, I_p, under influence of pink noise of amplitude A_{Φ_0} is defined. Sanity checks on the calculations of the qubit's first and second derivatives are performed (cf. equality c1 == c1_sp and c2 == c2_sp). Finally, after the averaging is complete, a plot of the ensemble averaged signal should pop up. The titles prints the decoherence times $\tau_{2E/R}$, defined by $\left|c\left(\tau_{2E/R}\right)\right| = 1/e$. A standard example is shown in Fig.3.13, where a single trajectory as well as the overall flux dependency is shown.

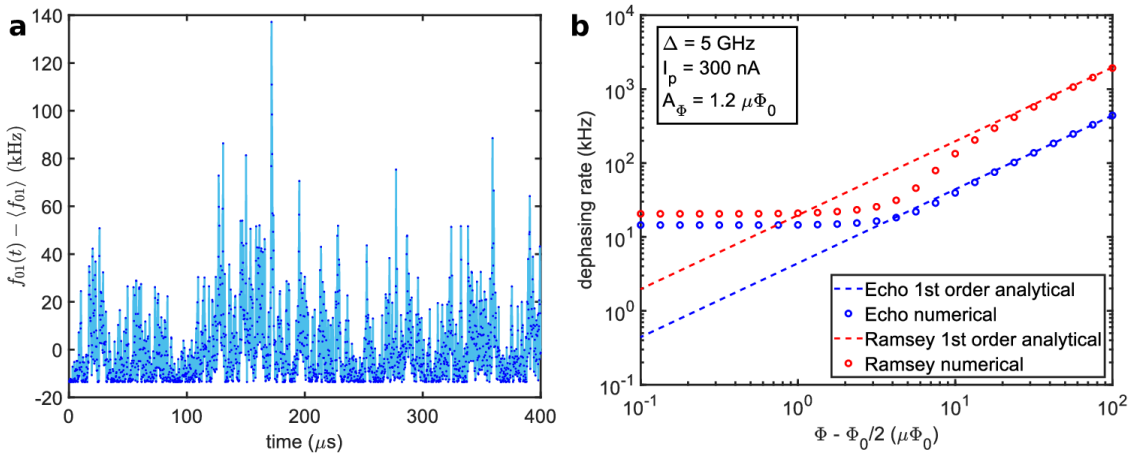

Figure 3.13: Calculated dephasing rates of a flux qubit. a, The frequency of a flux qubit at optimal point under influence of 1/f noise over a sub-sample of 400 µs. The flux qubit parameters were chosen to be $\Delta = 5\,\mathrm{GHz}$, $I_p = 300\,\mathrm{nA}$, $A_\Phi = 1.2\mu\Phi_0$. The parameters of the numerical simulation are $t_{\mathrm{step}} = 200\,\mathrm{ns}$, $t_{\mathrm{total}} = 1\,\mathrm{s}$, $t_{\text{cut-off}} = 0.2\,\mathrm{s}$. b, We numerically calculated the Ramsey and Echo dephasing rates and compared the results with analytical formula for first order flux noise. Away from the optimal point, analytical formula predict $\Gamma_{\varphi R} \sim 4.5\Gamma_{\varphi E}$ in agreement with the numerical simulations.

Empirical results for the second-order flux noise decoherence rates Using the tool described above, and sweeping many different flux qubit parameters, we were able to establish the following empirical law for any second-order transition

$$\Gamma_{\varphi E}^{(2)} = 14.4\frac{\partial^2 f_{01}}{\partial \Phi^2}A_{\Phi_0}^2 \tag{3.71}$$

where f_{01} is the transition frequency. For the particular case of the flux qubit at its optimal point, we obtain the easy-to-apply formula

$$\boxed{\Gamma_{\varphi E}^{(2)} = 56\frac{\left(I_p A_{\Phi_0}/h\right)^2}{\Delta}} \tag{3.72}$$

3.5.4 Bi-variate pure dephasing rates for tunable flux qubits

In the following we consider flux noise in tunable flux qubits, originating from the squid loop and the remaining loop as two independent noise sources. In order to estimate their influence on the coherence of the qubits, we will treat the Hamiltonian perturbatively versus the fluxes in the SQUID Φ_S and the remaining flux $\Phi_R = \Phi - \Phi_S$ around an optimal point.

$$\begin{aligned}
H &= H_0 - E_J\partial_{\Phi_S}\left(\alpha\cos\left(\frac{\Phi_R+\Phi_S}{\varphi_0} - \sum_{j=1}^{3}\varphi_{j,j+1}\right) + \bar{\beta}\frac{1-\bar{d}}{2}\cos\left(\varphi_{23} - \frac{\Phi_S}{\varphi_0}\right)\right)_{\Phi=\Phi_{opti}}\delta\Phi_S \\
&\quad - E_J\partial_{\Phi_R}\left(\alpha\cos\left(\frac{\Phi_R+\Phi_S}{\varphi_0} - \sum_{j=1}^{3}\varphi_{j,j+1}\right)\right)_{\Phi=\Phi_{opti}}\delta\Phi_R \\
&= H_0 + I_0\left(\alpha\sin\left(\varphi_{41}\right) - \bar{\beta}\frac{1-\bar{d}}{2}\sin\left(\varphi'_{23}\right)\right)\delta\Phi_S + I_0\alpha\sin\left(\varphi_{41}\right)\delta\Phi_R \\
&\equiv H_0 + \hat{I}_S\delta\Phi_S + \hat{I}_R\delta\Phi_R
\end{aligned} \tag{3.73}$$

One can express the operators $\hat{I}_{S/R}$ in the basis of the two lowest eigenstates of H_0 as $\hat{I}_{S/R} = I_{x,S/R}\sigma_x + I_{z,S/R}\sigma_z + I_{0,S/R}\mathbf{1}$ and thus write the Hamiltonian as

$$H = \hbar\frac{\Delta}{2}\sigma_z + \left(I_{z,S}\delta\Phi_S + I_{z,R}\delta\Phi_R\right)\sigma_z + \left(I_{x,S}\delta\Phi_S + I_{x,R}\delta\Phi_R\right)\sigma_x \tag{3.74}$$

The transition frequency of the qubit can be written as

$$\hbar\omega_{ge} \simeq \hbar\Delta + 2I_{z,S}\delta\Phi_S + 2I_{z,R}\delta\Phi_R + \frac{1}{2\hbar\Delta}\left(2I_{x,S}\delta\Phi_S + 2I_{x,R}\delta\Phi_R\right)^2 \tag{3.75}$$

Since the flux noise has a 1/f spectrum, one can show that the first and second order contributions to dephasing are given by [82]

$$\begin{aligned}
\Gamma_{S/R} &= \sqrt{\ln 2}A_{S/R}\left|\partial_{\Phi_{S/R}}\omega_{ge}\right| \\
\Gamma_{2\mathrm{nd},S/R} &\approx 2.3A_{S/R}^2\partial_{\Phi_{S/R}}^2\omega_{ge}
\end{aligned} \tag{3.76}$$

where A_S and A_R are the flux noise amplitudes in the squid and in the remaining loop respectively.

$$\partial_{\Phi_{S/R}}\omega_{ge} = \frac{2I_{z,S/R}}{\hbar} + \frac{1}{\hbar^2\Delta}\left(2I_{x,S}\delta\Phi_S + 2I_{x,R}\delta\Phi_R\right)\left(2I_{x,S/R}\right)$$
$$\partial^2_{\Phi_{S/R}}\omega_{ge} = \frac{1}{\hbar^2\Delta}\left(2I_{x,S/R}\right)^2$$

An interesting property of 1/f noise is that the decay is gaussian for first order contributions. And thus one can write

$$\Gamma_{1st} = \sqrt{\left(\Gamma_S\right)^2 + \left(\Gamma_R\right)^2} = \sqrt{\ln 2\left(A_S^2\left(\partial_{\Phi_S}\omega_{ge}\right)^2 + A_R^2\left(\partial_{\Phi_R}\omega_{ge}\right)^2\right)} \equiv A_\Phi\sqrt{\ln 2}\left|\partial_\Phi\omega_{ge}\right| \tag{3.77}$$

where A_Φ is the *apparent* measure of flux noise when the tunable qubit is biased by an external uniform magnetic field (see Fig.6.9a). Due to the geometrical configuration, $\Phi_S = \zeta\Phi$ and $\Phi_R = (1-\zeta)\,\Phi$ and thus

$$\partial_{\Phi_{S/R}}\omega_{ge} = \frac{2I_{z,S/R}}{\hbar} + \frac{1}{\hbar^2\Delta}\left(2I_{x,S}\zeta + 2I_{x,R}\left(1-\zeta\right)\right)\left(2I_{x,S/R}\right)\delta\Phi$$

Since $\hat{I} = \zeta\hat{I}_S + (1-\zeta)\,\hat{I}_R$ (see Eq.3.73), we have $I_P = \zeta I_{x,S} + (1-\zeta)\,I_{x,R}$ and thus using Eq.3.77, we get

$$A_\Phi I_P = \sqrt{A_S^2 I_{x,S}^2 + A_R^2 I_{x,R}^2} \tag{3.78}$$

Following Ref.[75], we assume that the flux noise amplitude is proportional to the square root of the perimeters $\sqrt{P_{S/R}}$ of the respective sections and define $\gamma \equiv \sqrt{P_S/P_R} = A_S/A_R$ such that

$$\boxed{A_S A_R = \frac{A_\Phi^2 I_P^2}{I_{x,S}^2\gamma + I_{x,R}^2/\gamma}} \tag{3.79}$$

Finally we get

$$\Gamma_{1st} = 2\sqrt{\ln 2}\frac{\sqrt{A_S A_R}}{\hbar}\sqrt{\left(I_{z,S} + I_{x,S}\frac{2I_P}{\hbar\Delta}\delta\Phi\right)^2\gamma + \left(I_{z,R} + I_{x,R}\frac{2I_P}{\hbar\Delta}\delta\Phi\right)^2/\gamma} \tag{3.80}$$

$$\Gamma_{2nd} \approx 9.2\frac{A_S A_R}{\hbar^2\Delta}\left(I_{x,S}^2\gamma + I_{x,R}^2/\gamma\right) \tag{3.81}$$

3.5.5 Calculating the photon noise dephasing rate

Let us recall the Hamiltonian of the system under dispersive shift in Eq.3.55

$$H/\hbar = \left(\Delta + 2\hat{N}\chi\right)\frac{\sigma_z}{2} + \omega_r\hat{N} \tag{3.82}$$

where $\hat{N} = \mathbf{A}^\dagger \mathbf{A}$, is the number of photons in the mode constructed in Eq.3.49. With respect to the temporal mean $\Delta + 2\left\langle \hat{N} \right\rangle \chi$, the additional accumulated phase thus writes

$$c(\tau) = \exp\left(-i2\chi \int_0^\tau \hat{N}(t) - \left\langle \hat{N} \right\rangle \right)$$

After taking the ensemble averaging, only even powered terms remain, and the expectancy of c writes

$$\langle c(\tau) \rangle = \exp\left(-\frac{(2\chi)^2}{2} \left\langle \left(\int_0^\tau \hat{N}(t_1) - \left\langle \hat{N} \right\rangle \right) \left(\int_0^\tau \hat{N}(t_2) - \left\langle \hat{N} \right\rangle \right) \right\rangle \right)$$

Our goal is thus to calculate the quantity

$$\left\langle \left(\int_0^\tau \hat{N}(t_1) - \left\langle \hat{N} \right\rangle \right) \left(\int_0^\tau \hat{N}(t_2) - \left\langle \hat{N} \right\rangle \right) \right\rangle = \int_0^\tau \int_0^\tau \left\langle \hat{N}(t_1) \hat{N}(t_2) \right\rangle - \left\langle \hat{N} \right\rangle^2$$

We have $\left\langle \hat{N}(t_1) \hat{N}(t_2) \right\rangle = \left\langle \hat{N}(\Delta t \equiv t_1 - t_2) \hat{N}(0) \right\rangle$ from the invariance of translation in time. We then inject $\mathbf{A} = \sum_i \alpha_i a_i$, with α_i being scalars verifying $\sum_i |\alpha_i|^2 = 1$, according to Eq.3.49. The term $\hat{N}(\Delta t) \hat{N}(0)$ contains terms in $a_k^\dagger(\Delta t) a_l(\Delta t) a_m^\dagger a_n$ each with corresponding coefficients. Recall also that $a_m(\Delta t) = a_m e^{-i\omega_m t}$. To take the ensemble average, only photon-numbers-conserving terms remain

$$\begin{aligned} \hat{N}(\Delta t) \hat{N}(0) = & \sum_{m,n} |\alpha_m|^2 |\alpha_n|^2 a_m^\dagger a_m a_n^\dagger a_n \\ & + \sum_{m \neq n} |\alpha_m|^2 |\alpha_n|^2 a_m^\dagger a_n e^{i(\omega_m - \omega_n)t} a_n^\dagger a_m \end{aligned}$$

We get

$$\begin{aligned} \left\langle \hat{N}(\Delta t) \hat{N}(0) \right\rangle &= \left\langle \hat{N} \right\rangle^2 + \sum_{m \neq n} |\alpha_m|^2 |\alpha_n|^2 a_m^\dagger a_n e^{i(\omega_m - \omega_n)t} a_n^\dagger a_m \\ &= \left\langle \hat{N} \right\rangle^2 + \sum_{m \neq n} |\alpha_m|^2 |\alpha_n|^2 \left\langle a_m^\dagger a_m \right\rangle \left\langle a_n^\dagger a_n + 1 \right\rangle e^{i(\omega_m - \omega_n)t} \end{aligned}$$

The latter sum can be written as

$$\sum_{m \neq n} = \sum_{m,n} - \sum_{m=n}$$

in which the latter converges to 0 as we head toward the continuum limit

$$\begin{aligned} & \sum_{m=n} |\alpha_m|^2 |\alpha_n|^2 \left\langle a_m^\dagger a_m \right\rangle \left\langle a_n^\dagger a_n + 1 \right\rangle e^{i(\omega_m - \omega_n)t} \\ & = \sum_m |\alpha_m|^4 \left\langle a_m^\dagger a_m \right\rangle \left\langle a_m^\dagger a_m + 1 \right\rangle \to 0 \end{aligned}$$

Finally, we establish

$$\left\langle \hat{N}\left(\Delta t\right)\hat{N}\left(0\right)\right\rangle -\left\langle \hat{N}\right\rangle ^{2}=\left(\sum_{m}\left|\alpha_{m}\right|^{2}\left\langle a_{m}^{\dagger}a_{m}\right\rangle e^{i\omega_{m}\Delta t}\right)\left(\sum_{n}\left|\alpha_{n}\right|^{2}\left\langle a_{n}^{\dagger}a_{n}+1\right\rangle e^{-i\omega_{n}\Delta t}\right)$$

For well formed resonance peaks (i.e. $Q\gg1$), $\left\langle a^{\dagger}a\right\rangle$ no longer depends on the index and can be taken out of the sum. Since the coefficients α are result of normalization of the resonance factor, approximately the complex root of a Lorentzian[19], we can write the vector of all coefficients

$$\left|\alpha_{m}\right|^{2}=\mathcal{N}\left(\left|\frac{1}{\kappa/2-i\delta_{m}}\right|\right)=\mathcal{N}\left(\frac{1}{\left(\kappa/2\right)^{2}+\delta_{m}^{2}}\right)$$

the dependency of $\sum_{m}\left|\alpha_{m}\right|^{2}e^{i\omega_{m}t}$ should therefore be exponentially decaying as $\exp\left(-\kappa\left|\Delta t\right|/2\right)$. We finally establish

$$\left\langle \hat{N}\left(\Delta t\right)\hat{N}\left(0\right)\right\rangle -\left\langle \hat{N}\right\rangle ^{2}=\left\langle a^{\dagger}a\right\rangle \left(\left\langle a^{\dagger}a\right\rangle +1\right)\exp\left(-\kappa\left|\Delta t\right|\right)$$

where $b^{(\dagger)}$ is used to emphasize that from this point onward, it suffices to use standard bosonic statistics at mode frequency $\omega_{r}/2\pi$. Under the condition that $\kappa\tau\gg1$, the double integration of the expression yields approximately:

$$\begin{aligned}\int_{t_{2}=0}^{\tau}\int_{t_{1}=0}^{\tau}\left\langle \hat{N}\left(t_{1}\right)\hat{N}\left(t_{2}\right)\right\rangle -\left\langle \hat{N}\right\rangle ^{2} & \approx\int_{t_{2}=0}^{\tau}\int_{\Delta t=-\infty}^{+\infty}\left\langle \hat{N}\left(\Delta t\right)\hat{N}\left(0\right)\right\rangle -\left\langle \hat{N}\right\rangle ^{2}\\ & =\tau\left\langle a^{\dagger}a\right\rangle \left(\left\langle a^{\dagger}a\right\rangle +1\right)\int_{\Delta t=-\infty}^{+\infty}\exp\left(-\kappa\left|\Delta t\right|\right)\\ & =\frac{2\tau}{\kappa}\left\langle a^{\dagger}a\right\rangle \left(\left\langle a^{\dagger}a\right\rangle +1\right)\end{aligned}$$

Finally, we establish

$$\begin{aligned}\left\langle c\left(\tau\right)\right\rangle & =\exp\left(-\frac{\left(2\chi\right)^{2}}{2}\frac{2\tau}{\kappa}\left\langle a^{\dagger}a\right\rangle \left(\left\langle a^{\dagger}a\right\rangle +1\right)\right)\\ & =\exp\left(-\frac{4\chi^{2}}{\kappa}\left\langle a^{\dagger}a\right\rangle \left(\left\langle a^{\dagger}a\right\rangle +1\right)\tau\right)\end{aligned}$$

and define

$$\boxed{\Gamma_{\text{phot}}=\frac{4\chi^{2}}{\kappa}\left\langle a^{\dagger}a\right\rangle \left(\left\langle a^{\dagger}a\right\rangle +1\right)} \tag{3.83}$$

In practice, since the cryogenic fridge has various levels of filtering at different temperatures, a should be treated as a composite mode from modes of different temperatures with various degree of participation

[19] See Eq.3.61

λ_i from each stage.

$$a = \sum_i \lambda_{T_i} a_{T_i}$$
$$\sum_i |\lambda_{T_i}|^2 = 1$$
$$\left|\lambda_{T_{i+1}}\right|^2 / |\lambda_{T_i}|^2 = \text{pow. att. from stage } i+1 \text{ down to } i$$

3.6 Rabi Dressing

A theoretical basis in which a detuned flux qubit can be brought back into resonance with a single spin using strong Rabi drives is described in [60]. This section will try to succinctly summarize the paper. In what follows, $|\swarrow / \nearrow\rangle$ will be used to denote the donor's ground/excited state, whereas $|g/e\rangle$ will be for the flux qubit. We apply a time-dependent Rabi drive that is resonant with the flux qubit ($\delta_{\text{fq}} = 0$). The driven Hamiltonian writes

$$H/\hbar = \overbrace{\Omega(t)\frac{e^{i\Delta t} + e^{-i\Delta t}}{2}\sigma_x^{qb}}^{H_d/\hbar} + (\Delta + \delta_{\text{fq}})\frac{\sigma_z^{qb}}{2} + g\sigma_x^{qb} \otimes \hat{\sigma}_x^s + \left(\Delta + \delta_{\updownarrow}\right)\frac{\hat{\sigma}_z^s}{2}$$

We can then move into the rotating frame using the evolution operator

$$U = e^{-i\Delta\left(\sigma_z^{qb} + \hat{\sigma}_z^s\right)t/2} \tag{3.84}$$

Keeping only the resonant terms ($e^{-i\Delta t}\sigma_+^{qb} + e^{i\Delta t}\sigma_-^{qb}$) under the rotating wave approximation. We get the following Hamiltonian in the rotating frame

$$\begin{aligned} H'/\hbar &= U^\dagger \left(H/\hbar - \Delta\left(\sigma_z^{qb} + \hat{\sigma}_z^s\right)/2\right) U \\ &\approx \cancelto{0}{\delta_{\text{fq}}}\frac{\sigma_z^{qb}}{2} + \Omega(t)\frac{\sigma_x^{qb}}{2} + g\left(\sigma_+^{qb}e^{i\Delta t} + \sigma_-^{qb}e^{-i\Delta t}\right)\left(\hat{\sigma}_+^s e^{i\Delta t} + \hat{\sigma}_-^s e^{-i\Delta t}\right) + \delta_{\updownarrow}\frac{\hat{\sigma}_z^s}{2} \end{aligned}$$

where $\delta_{\updownarrow} = \omega_s - \Delta$. The eigenstates associated to eigen-values $\pm\Omega/2$ of $\Omega(t)\,\sigma_x^{qb}/2$ are

$$|+\rangle = \frac{|g\rangle + |e\rangle}{\sqrt{2}}$$
$$|-\rangle = \frac{|g\rangle - |e\rangle}{\sqrt{2}}$$

The splitting of these two levels is at the origin of Rabi oscillations. The operators can be rewritten in the basis of $|\mp\rangle$ as

$$\begin{aligned}
\sigma_+^{qb} &= |e\rangle\langle g| = (|+\rangle - |-\rangle)(\langle +| + \langle -|)/2 \\
\sigma_-^{qb} &= |g\rangle\langle e| = (|+\rangle + |-\rangle)(\langle +| - \langle -|)/2 \\
\sigma_x^{qb} &= \sigma_+^{qb} + \sigma_-^{qb} = |+\rangle\langle +| - |-\rangle\langle -|
\end{aligned}$$

Under this basis change, the above operators can be replaced by

$$\begin{aligned}
\sigma_\pm^{qb} &\to \left(\sigma_z^{qb} \mp i\sigma_y^{qb}\right)/2 \\
\sigma_x^{qb} &\to \sigma_z^{qb}
\end{aligned}$$

With this replacement, we write

$$\begin{aligned}
H' &= H_0 + H_{int} \\
H_0/\hbar &= \Omega\frac{\sigma_z^{qb}}{2} + \delta_\updownarrow\frac{\hat{\sigma}_z^s}{2} \\
H_{int}/\hbar &= g\left(\frac{\sigma_z^{qb} - i\sigma_y^{qb}}{2}e^{i\Delta t} + \frac{\sigma_z^{qb} + i\sigma_y^{qb}}{2}e^{-i\Delta t}\right)\hat{\sigma}_+^s e^{i\Delta t} + \text{H.c.}
\end{aligned} \tag{3.85}$$

Recall that our goal is to dress $|\Omega| \approx \left|\delta_\updownarrow\right|$. Out of all terms all terms $\sigma_z^{qb}\hat{\sigma}_+^s e^{i(\Delta\pm\Delta)t}$, we first discard those without chance of becoming resonant under the RWA. In the same way, we also discard terms with $e^{2i\Delta t}$, which is is impossible to match phases with any of the four possibilities $e^{i\left(\pm\Omega\pm\delta_\updownarrow\right)t}$. We are left with

$$H_{int}/\hbar \approx \frac{g}{2}\left(\sigma_-^{qb} - \sigma_+^{qb}\right)\hat{\sigma}_+^s + \text{H.c.}$$

Placing once again in the rotating frame associated with H_0

$$U' = e^{-iH_0 t/\hbar} \tag{3.86}$$

we get

$$H_{int}/\hbar \approx \frac{g}{2}\left(\sigma_-^{qb}\hat{\sigma}_+^s e^{i\left(-\Omega+\delta_\updownarrow\right)t} - \sigma_+^{qb}\hat{\sigma}_+^s e^{i\left(+\Omega+\delta_\updownarrow\right)t}\right) + \text{H.c.}$$

Out of the four terms, we can freely switch between the two following modes of operation for $\Omega = \pm\delta_\updownarrow$, experimentally achieved by introducing a π phase-shift in the Rabi drive

$$\begin{aligned}
H_{\Omega=\delta}/\hbar &= \frac{g}{2}\left(\sigma_-^{qb}\hat{\sigma}_+^s + \sigma_+^{qb}\hat{\sigma}_-^s\right) \\
H_{\Omega=-\delta}/\hbar &= -\frac{g}{2}\left(\sigma_+^{qb}\hat{\sigma}_+^s + \sigma_-^{qb}\hat{\sigma}_-^s\right)
\end{aligned}$$

3.6.1 Flux qubit and single spin state preparation

Without loss of generality, any arbitrary state may be written as

$$|\psi\rangle = \left(\cos\alpha\,|+\rangle + e^{i\phi}\sin\alpha\,|-\rangle\right)\left(\cos\theta\,|\swarrow\rangle + e^{i\varphi}\sin\theta\,|\nearrow\rangle\right)$$

where $|\swarrow\,/\,\nearrow\rangle$ denotes the spin's energy state. The parameters α and ϕ will be used to describe the qubit state, whereas θ, φ will be used to describe the spin state. Full control of the flux qubit can be achieved by controlling with the phase of the Rabi pump with respect to a reference tone. The driven Hamiltonian writes

$$H_d/\hbar = \Omega\frac{e^{i\Delta t}e^{i\vartheta} + e^{-i\Delta t}e^{-i\vartheta}}{2}\left(\sigma_+^{qb} + \sigma_-^{qb}\right)$$

and will give a component after the rotating wave approximation in Eq.3.84 equal to

$$H_d/\hbar = \Omega\cdot\left(\cos(\vartheta)\,\sigma_x^{qb} + \sin(\vartheta)\,\sigma_y^{qb}\right)$$

Notice that the mode of operation $\Omega = -\delta$ is a special case where $|\Omega| = |\delta|$ but with an overall phase shifted of the drive by π. From the flux qubit ground state, we can easily reach thus any point in the equatorial plane of the Bloch sphere by a geodesic movement, notably $|-\rangle$ by setting $\vartheta = \pi/2$.

By driving $\Omega = \delta$ in sync with the reference $\vartheta = 0$ for a time $gt = \pi$. We may convert any arbitrary quantum amplitude associated to an excited spin into a flux qubit excited amplitude.

$$|-\rangle\left(\cos\theta\,|\swarrow\rangle + e^{i\varphi}\sin\theta\,|\nearrow\rangle\right) \rightarrow \left(-i\cos\theta\,|+\rangle + e^{i\varphi}\sin\theta\,|-\rangle\right)|\swarrow\rangle$$

After a typical timescale of the T_1 of the flux qubit, we would have initialized the spin state to $|\swarrow\rangle$. The same process can be used in the opposite direction: any arbitrary flux qubit state can be converted into a spin state superposition, then read back out. This allows for use of the spin as a quantum memory with long coherence times.

3.6.2 Detection of the coupling of the spin-qubit interaction

At millikelvin cryogenic temperatures, the thermal equilibrium of both the spin and flux qubit should be readily in the ground state. More precisely, the overall qubit state is

$$|g\rangle\,|\swarrow\rangle = \frac{|+\rangle + |-\rangle}{\sqrt{2}}\,|\swarrow\rangle$$

According to the previous section, the overall state will oscillate between the initial state and $|-\rangle\left(|\swarrow\rangle - i\,|1\rangle\right)/\sqrt{2}$ up to a global phase. For any time t, the exact solution is

$$|\psi(t)\rangle = \left[|-\rangle\,|\swarrow\rangle + \cos\left(\frac{g}{2}t\right)|+\rangle\,|\swarrow\rangle - i\sin\left(\frac{g}{2}t\right)|-\rangle\,|\nearrow\rangle\right]/\sqrt{2}$$

Reverting the RWA associated with Eq.3.86, we get

$$|\psi(t)\rangle = \left[e^{i\Omega t}|-\rangle|\swarrow\rangle + \cos\left(\frac{g}{2}t\right)e^{-i\Omega t}|+\rangle|\swarrow\rangle - i\sin\left(\frac{g}{2}t\right)e^{i\Omega t}|-\rangle|\nearrow\rangle\right]/\sqrt{2}$$

Collecting coefficients for flux qubit ground and excited states

$$\begin{aligned}|\psi(t)\rangle = |g\rangle&\left(\left(e^{i\Omega t} + \cos\left(\frac{g}{2}t\right)e^{-i\Omega t}\right)|\swarrow\rangle - i\sin\left(\frac{g}{2}t\right)e^{i\Omega t}|\nearrow\rangle\right)/2\\ &+ |e\rangle\left(\left(-e^{i\Omega t} + \cos\left(\frac{g}{2}t\right)e^{-i\Omega t}\right)|\swarrow\rangle + i\sin\left(\frac{g}{2}t\right)e^{i\Omega t}|\nearrow\rangle\right)/2\end{aligned}$$

We can then calculate the population

$$\begin{aligned}P_{g/e} &= \frac{1}{4}\left(\left|\sin\left(\frac{g}{2}t\right)e^{i\Omega t}\right|^2 + 1 + \cos^2\left(\frac{g}{2}t\right) \pm 2\cos(\Omega t)\cos\left(\frac{g}{2}t\right)\right)\\ &= \frac{1}{2}\left(1 \pm \cos(\Omega t)\cos\left(\frac{g}{2}t\right)\right)\end{aligned}$$

where we see that the envelope of the Rabi oscillation beats like $\cos\left(\frac{g}{2}t\right)$, with nodes appearing for values $gt = \pi, 3\pi, 5\pi\ldots$, corresponding to total transfer of the superposition into the spin. Fitting of the envelope would give a quantitative measure of the coupling constant.

One major advantage of Rabi oscillating the qubit at relatively fast rates is that the flux qubit undergoes a sort of dynamical decoupling and filters out low-frequency noises of decoherence such as flux noise. Under evolution of Linblad equations, the decay of a Rabi envelope of an *isolated* qubit can reach $\frac{4}{3}T_1$. Indeed, for a jump operator of $\sqrt{1/T_1 = \kappa_1}\sigma_-$,we write a differential function involving the Linbladian map $L(\rho)$

$$\partial_t\rho = L(\rho) \equiv \frac{[H,\rho]}{i\hbar} + \frac{1}{T_1}\left(\sigma_-\rho\sigma_+ - \frac{\sigma_+\sigma_-\rho + \rho\sigma_+\sigma_-}{2}\right)$$

which we replace the density matrice ρ with the coordinates in the Bloch sphere $\rho = x\frac{\sigma_x}{2} + y\frac{\sigma_y}{2} + z\frac{\sigma_z}{2} + \mathbf{1}/2$ with $\sqrt{x^2+y^2+z^2} \leq 1$. We thus get the following equations

$$\begin{pmatrix}\dot{x}\\ y\\ z\end{pmatrix} = \begin{pmatrix}-\frac{\kappa_1}{2} & & \\ & -\frac{\kappa_1}{2} & -\omega_r\\ & \omega_r & -\kappa_1\end{pmatrix}\begin{pmatrix}x\\ y\\ z\end{pmatrix} + \begin{pmatrix}0\\ 0\\ -\kappa_1\end{pmatrix}$$

The linear matrix has for eigen-values $-\frac{\kappa_1}{2}$, and the two roots of $\left(-\frac{\kappa_1}{2} - X\right)(-\kappa_1 - X) + \Omega^2 = X^2 + \frac{3}{2}\kappa_1 X + \Omega^2 + \frac{1}{2}\kappa_1^2$. The two roots of the polynomial are responsible for decaying Rabi oscillations

$$r_\pm = \frac{-\frac{3}{2}\kappa_1 \pm \sqrt{\left(\frac{3}{2}\kappa_1\right)^2 - 4\left(\Omega^2 + \frac{1}{2}\kappa_1^2\right)}}{2}$$

In the limit where $\Omega \gg \kappa_1$, the expression approximates to $r_\pm \approx -\frac{3}{4}\kappa_1 \pm \boldsymbol{i}\Omega$, prooving that a Rabi

decay of $\frac{4}{3}T_1$ may be experimentally observed.

In Fig.2.10, the simulations were performed for exactly the same Linblad model as above. Technically, we write the non-Hermitian matrix of the Linbladian, viewed as a linear map over density matrix *vectors* and diagonalize spectrally $L = PDP^{-1}$. From this point onward, it is possible to move to any point in time without needing to explicitly integrate in time using

$$\rho(t) = P \exp(Dt) P^{-1} \rho$$

4 Fabrication

Prior to fabrication, the wafers are diced into a format of 23×23 mm squares, denoted in the following as *coupons*. In this thesis, each coupon contains 14 samples of dimensions 3×10 mm. On each of them is fabricated a $\lambda/2$ coplanar waveguide resonator which can be galvanically-coupled to a series of flux qubits.

Provider	Wafer material	oxide	Density of Impurities	Reference in study
Virginia	Intrinsic Si	native	^{nat}Si, P ($< 10^{12}$cm^{-3})	sample A
Topsil	Intrinsic Si	thermally grown (5 nm)	^{nat}Si, P ($< 10^{12}$cm^{-3})	sample B, C
Crystec	sapphire c-axis	irrelevant	irrelevant	sample D
Isonics	10 µm isotopically pure epilayer	thermally grown (5 nm)	^{29}Si(730 ppm), P (10^{16}cm^{-3})	sample E, F

Table 4.1: Overview of samples

4.1 Substrate Surface treatment

Dielectric losses impact strongly the relaxation rate of superconducting circuits [85]. In theory, the internal quality factor of a coplanar waveguide resonator (CPW) is related to the loss tangent of the substrate by the relation

$$1/Q_i = p \tan\delta \tag{4.1}$$

where p is the participation ratio of the electric field energy stored in the substrate [86, 87]. Due to the high permittivity of the substrate ($\epsilon_{r,\mathrm{Si}} = 11.5$, $\epsilon_{r,\mathrm{sapphire}} = 10$), the participation ratio $p = \epsilon_r / (\epsilon_r + 1)$ is close to 90%. Thus, choosing a good substrate is critical. Since silicon and sapphire have both good $\tan\delta$, they are the materials of choice for such resonators. Indeed, the loss tangent of bulk silicon is of the order of 10^{-5} [88, 89] while in bulk sapphire the losses are even lower with $\tan\delta < 1 \times 10^{-6}$ [90].

In practice, the loss rate of superconducting circuits, especially for coplanar designs, never reaches the fundamental bulk limit, suggesting that the interface has an important role to play. The losses at the surface are generally attributed to two-level systems (TLS) near the interface [85].

In the last two decades, several studies have been carried out to improve CPW quality factors through surface treatments. Ref.[91] showed that fabricating a resonator on sapphire with liftoff techniques leads to low quality factors ($Q \sim$200k) and that fabrication involving etching of the aluminum gives rise to substantially higher $Q \sim 1M$. Ellipsometric measurements have shown the presence of a thin residual resist layer which can bring losses, even after ultrasonic acetone cleaning and/or hot N-Methyl-2-pyrrolidone (NMP) cleaning. Meanwhile, oxygen ashing leaves significantly less residues (see Fig.4.1). Moreover, ion milling prior to evaporation degrades the internal quality factor of resonators down to 400k [91]. In [92], $Q \sim$ 2M was achieved for silicon-based CPW resonator by combining

Unexposed resist residue (±0.3 nm)	Post-strip (nm)	Post-descum (nm)
E-beam resist on sapphire	4.2[a]	0.0[b]
E-beam resist on sapphire	2.5[c]	0.0[b]
E-beam resist on aluminum	2.8[c]	0.1[b]
E-beam resist on silicon	3.9[a]	1.6/0.0[d]
E-beam resist on silicon	0.4[c]	0.0[b]
Photoresist on sapphire	0.2[a]	0.1[b]
Photoresist on silicon	0.1[a]	0.1[b]
Photoresist on aluminum	0.6[a]	0.1[b]

[a]5 min ultrasonic agitation in acetone then isopropyl alcohol (IPA); spin dry.
[b]1 min downstream oxygen ash at 150 °C.
[c]1 h soak in heated N-Methyl-2-pyrrolidone (NMP) (∼70 °C), followed by 5 min ultrasonic agitation in heated NMP then IPA; spin dry.
[d]UV-ozone clean for 10/20 min, respectively.

Figure 4.1: **Residual resist after chemical or O2 ashing cleaning techniques**. Adapted from Ref.[91].

pre-evaporation chemical surface treatment and minimization of surface under high-E field by deep reactive ion etching (DRIE). More recently, Ref.[93] demonstrated reproducible improvement of coherence properties ($T_1 \sim 0.3$ ms) for a batch of 2D tantalum transmons fabricated on sapphire. This was achieved by extensive surface cleaning (Piranha solution and oxygen plasma cleaning) performed systematically between key steps of the fabrication, as well as a sputtering of the tantalum while heating to high temperatures ($T = 500$ °C) to ensure growth in a given crystallographic phase (BCC α).

Along these lines, Ref.[86] characterized quantitatively the contributions to the internal loss from TLS coming from the close vicinity (2 nm) of the different interfaces of the CPW (see Fig.4.2). The contribution of the metal-substrate interface is important because of its high participation ratio (see Eq.4.1). On silicon substrate, the oxygen ashing recommended by Ref.[91] may lead to growth of

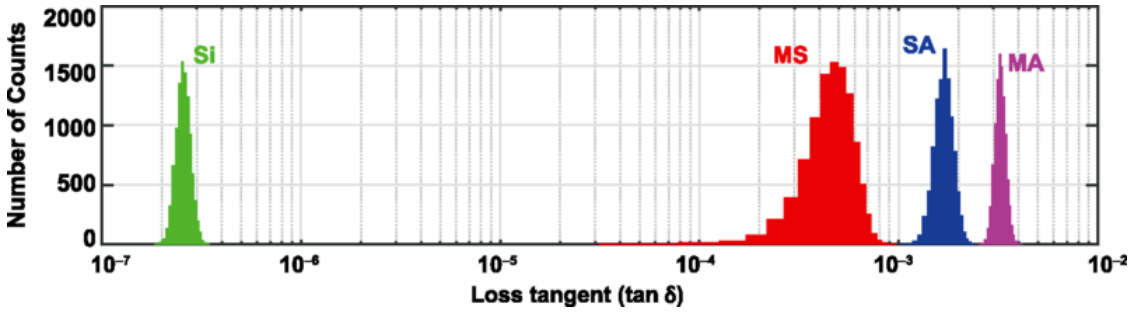

Figure 4.2: **The extracted TLS loss tangents for the different interfaces**. We show the metal-to-substrate (MS), substrate-vacuum or substrate-air interface (SA), metal-vacuum or metal-air interface (MA), and silicon substrate (Si) dielectric regions. Figure adapted from Ref.[86].

oxides of uncontrolled thickness and stochiometry. It is thus interesting to grow a thermal layer of SiO_2 under controlled conditions (pressure, temperature, and time). This layer is immune to oxygen ashing and enables a homogeneous good surface with less interface traps and fixed oxide charges.

From another point of view, thermal SiO_2 has been shown [88] to have a $\tan\delta \sim 3 \times 10^{-4}$ which is significantly higher than bulk silicon ($\sim 10^{-5}$). It is therefore required to limit the participation ratio of this SiO_2 layer. A good compromise is thus to grow a 5 nm layer of SiO_2. This step was done by our collaborators from the group of Prof. David Jamieson at Melbourne University and is detailed in Fig.4.3.

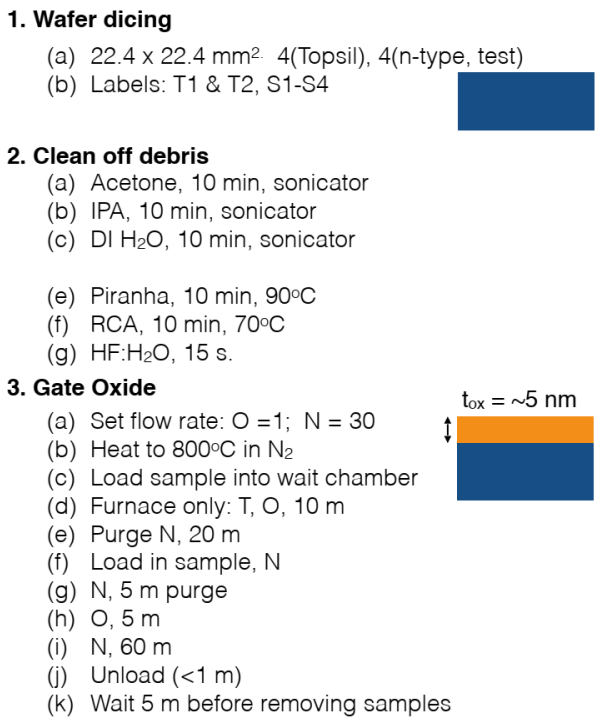

Figure 4.3: **Parameters for growth of the thermal oxide**

Before growing the thermal oxide on silicon, standard wafer cleaning techniques are employed. First, acetone/IPA/DI water cleaning are performed on the intrinsic silicon coupon, with sonication to remove large dust particles. Then, Piranha cleaning and RCA cleaning removes organic compounds. Finally, HF solution strips the silicon of its native oxide. The sample is heated to $\sim 800\,^{\circ}\mathrm{C}$ for 20 minutes inside a Si furnace with an ultra high purity oxygen ambient ($\geq$ 99:999% O2) which grows the thermal oxide [94].

4.2 Bismuth donor implantation

We implanted the bismuth donors on Isonics coupons with different implantation energy and density. The Stopping and Range of Ions in Matter software package (SRIM) [52] results show that a standard 200 nm layer of PMMA ebeam resist is enough to block the implanted bismuth ions (see Fig.4.4C).

This enables us to pattern an ebeam mask to delimit the implantation ion to a small region.

4.2.1 Bismuth Implantation profile

The area density of implantation for the first coupon (sample E) is $1 \sim 2 \cdot 10^{11}\mathrm{cm}^{-2}$. This is done through a PMMA mask of size $500 \times 100\,\mathrm{nm}$. The difference in the two dimensions allows for easier alignment of the constriction with a tolerance in the range of $\pm 250\,\mathrm{nm}$ in both directions. The energy of implantation is chosen to be 40 keV, yielding an average depth of 25 nm below the sample surface according to SRIM simulations. This corresponds to a volume density in the range of $1 \cdot 10^{17}\mathrm{cm}^{-3}$.

For the second coupon (sample F), the spin profile is spread out in order to reduce the volume density while keeping a high number of total spins. This is achieved by overlapping two profiles of different ion implantation voltages (100keV and 180keV) as shown in Fig.4.4. The average summed profile is around $1 \cdot 10^{18}\mathrm{cm}^{-3}$ over a range of 100 nm, with a peak density of $2 \cdot 10^{18}\mathrm{cm}^{-3}$. This implantation is done through a PMMA mask of size $1 \times 3\,\mu\mathrm{m}$. This rectangular shape was chosen to reduce strain-induced homogeneous broadening.

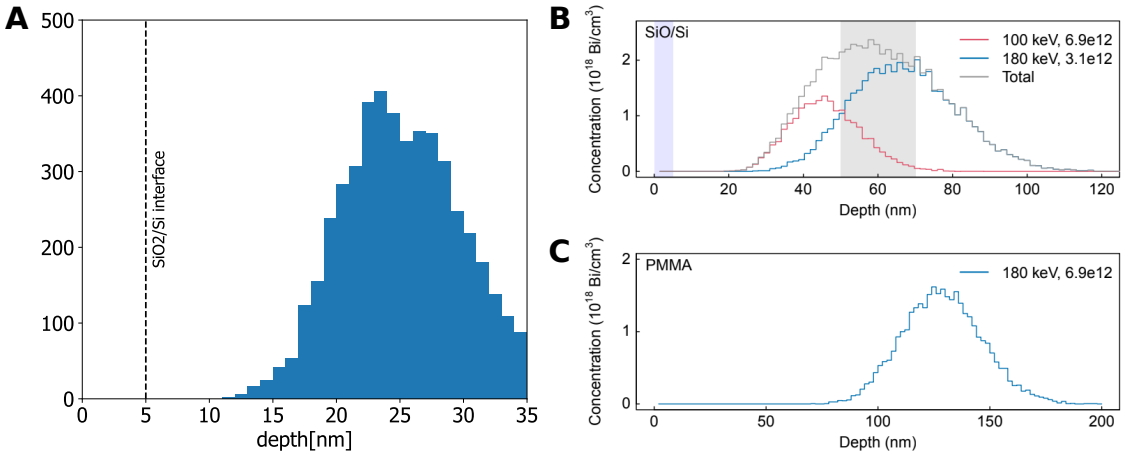

Figure 4.4: spin-ensemble profile

4.2.2 Bismuth Implantation process

In silicon lattice, a single implanted bismuth atom may occupy the meta-stable *substitutional* site and replace a single silicon atom. It is also possible for the bismuth to be pushed off into a more energetically favorable interstitial sites. One major figure of merit is thus the *activation rate*, which measures the ratio of the working substitutional sites to the total number of implanted spins.

Compared to other group V donors, the relatively heavy nature of Bi reduces straggling ($\sim 5\,\mathrm{nm}$) when implanted [52]. However, this also induces significantly more lattice damage [95]. The mentioned effects can be repaired by the so-called *Rapid Thermal Annealing* (RTA) step, which repairs the lattice damage and activates donors. This is done in forming gas (Ar/H) to passivate dangling bonds at the Si-SiO_2 interface. Time and temperature are critical parameters to reduce adverse diffusion of the

donors, which may increase the depth spread, as well as cause the entry of bismuth atoms into the *inactivated* interstitial structure [94, 96, 97]. The implantation process, the RTA ($T \sim 400\,^{\circ}\mathrm{C}$ for a duration t ~30 min), and its characterization were carried out by the group of Prof. David Jamieson at Melbourne University. We estimate that activation rate after all these steps to be around $\sim 60\%$.

4.3 Fabrication of superconducting devices

In the following we will present our fabrication process of the resonator and flux qubit in chronological order in the fabrication process.

4.3.1 Nb Alignment marks

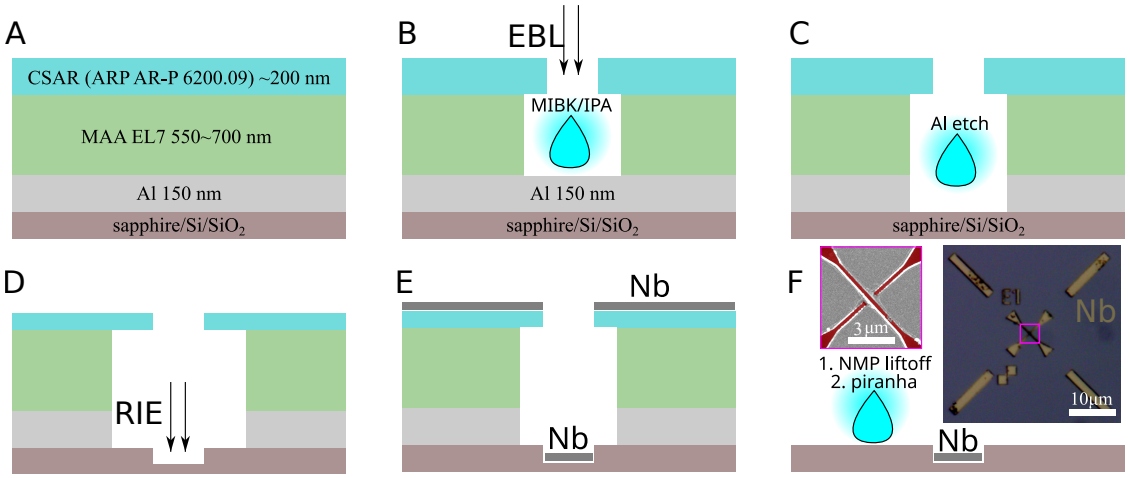

Figure 4.5: **Formation of Nb markers**

For E-beam lithography, precise alignment marks are needed as a universal spatial reference for both the implantation mask and the superconducting circuits (see Fig.4.5). Niobium marks with a thickness of around 100 nm present good contrast under electron beam lithography (EBL), even under multiple layers of resist, and/or germanium, and/or aluminum films. Conveniently, markers made of niobium are resistant to Piranha cleaning[20], and need only to be fabricated once per coupon, following the instructions in the table below. In practice, some Nb markers may disappear after the *first* Piranha cleaning, most likely due to residual substance underneath the Nb dissolving in Piranha and causing liftoff. Therefore, to ensure that there are always a pair of markers present for alignment, redundant backup markers must be designed. . We thus prepare between 4-9 markers for each 10×3 mm sample in the coupon.

Furthermore, it is imperative to choose a metal resisting the high heat of the RTA. Although Nb has an extremely high melting point (2470 °C), we still want to be protected against eventual diffusion

[20]When fabrication error occurs, we may start over anew with a Piranha solution cleaning, which will dissolve all organic material as well as aluminum structures.

onto the substrate during the process. We therefore pre-etch deep holes $\sim 90\,\mathrm{nm}$ using an SF6 Reactive Ion Etching (RIE) process prior to the Nb evaporation. Most of the Nb markers do indeed survive the RTA, although a color change of the evaporated Nb markers can be observed under the optical microscope, from silver to green/purple. For the markers that remain, the contrast under ebeam lithography nevertheless remains high.

Under EBL, the two strips forming the X shape (see Fig.4.5F) are approximately $\sim 250\,\mathrm{nm}$ wide. During marker alignment, we may designate the center of the cross with a precision of $\pm 30\,\mathrm{nm}$. The dominant limiting factor of alignment should be hardware systematic errors that are hard to pinpoint and solve (e.g. stage movement precision, change of configuration by the machine administrators etc). We estimate the overall alignment precision between different EBL exposures using the exact same pair of markers to be less than $\pm 100\,\mathrm{nm}$.

Fig.4.5	Process Name	About the process
	Cleaning	Piranha acid 10 min; water; IPA; N_2 blow-dry
A	Al spacer	Plassys MEB 550S: Al deposition of $> 150\,\mathrm{nm}$ at $0.5\mathrm{nm\,s^{-1}}$; $P < 2 \times 10^{-7}\,\mathrm{mBar}$
	Copolymer spacer	MMA(8.5)MAA-EL7[21] spun at 2000 rpm for 60 s
		Hotplate: 180 °C for 1 min
		MMA(8.5)MAA-EL7 [21]spun at 2000 rpm for 60 s
		Hotplate: 180 °C for 15 min
	EBL resist	CSAR AR-P 6200.09 [21]spun at 4500 rpm for 60 s
		Hotplate: 100 °C for 5 min
B	E-Beam lithography	Crestec 9000: 30 pA at 50keV, dose = $670\,\mu\mathrm{C\,cm^{-2}}$
	EBL Development	MIBK for 240 s; IPA rinse for 60s; N_2 blow-dry
C	Etching of Al-spacer	$\geq$ 15 minutes of Al etchant, Water
		1 min AZ726, Water
D	RIE etching of Si	SF_6 50 sccm, rf bias = 100 W, $\sim 80\,\mathrm{nm}$ etched in 20 s
	O2-N2 plasma	Recipe 13, 30s at 50% power
E	Evaporation	Plassys MEB 550S: Nb deposition of 100 nm at $0.5\mathrm{nm\,s^{-1}}$; $P = 3 - 8 \times 10^{-8}\,\mathrm{mBar}$
F	Lift off	NMP soak at 85 °C until the Niobium layer is removed
	Cleaning	Piranha acid 10 min; water; IPA; N_2 blow-dry

Table 4.2: **Formation of Nb markers**

[21] 5 s ramping to 500 rpm and hold for 5 s; then ramp to target speed in 6 s and hold for target time

4.3.2 Resonator fabrication

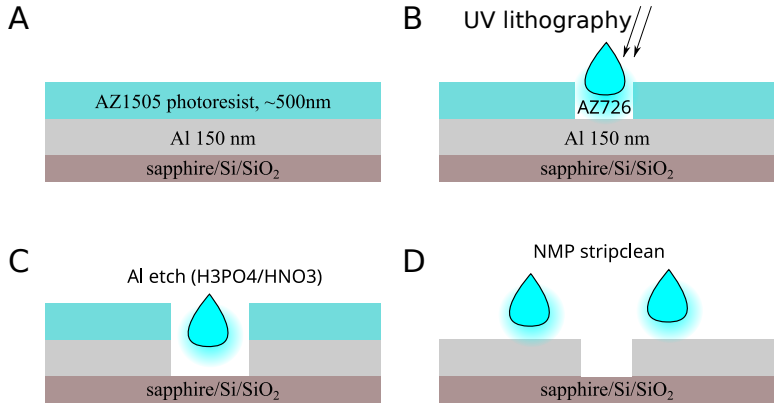

Figure 4.6: **Wet etch of aluminum resonators.**

In our fabrication, we took into account the considerations in section §4.1, and thus fabricated our coplanar resonators by wet aluminum etching (see Fig.4.6): We evaporate 150 nm of aluminum immediately after Piranha cleaning of the coupon. The CPW resonators are then formed by aluminum etchant (HNO3/H3PO4), through a resist spun directly on the aluminum film and patterned using maskless optical lithography.

The internal quality factor of several *plain* coplanar waveguide resonators was measured on the different samples. This measurement was done by designing a $\lambda/2$ CPW ($f \sim 8$ GHz) terminated by small capacitances such that the coupling loss rate Q_c ∼750k is negligible in front of the internal losses. We did not notice any significant difference between the quality factor of resonators fabricated on Virginia Semiconductor samples with native oxide (33k at single photon, 40k∼50k at high power) and those fabricated on Topsil samples with thermally grown 5 nm oxide layer (45k at single photon).

The precision of the positioning of the resonator with respect to the alignment mark is < 1.5 µm. The central conductor of the CPW resonators is interrupted by N open spaces in order to connect galvanically the qubits that will be fabricated in the next steps (see section 4.3.3).Typically, these spaces are 20 µm long. Electrical contact between the central strip of the CPW and the flux qubits is established after ion milling and evaporation of a final aluminum layer. It is important to avoid leaving any bare substrate exposed to ion-milling, which would lead to damage to the thermally grown oxide.

The designs of samples A, B/C/F, D, E can be found in Fig.4.7, along with design parameters.

Fig.4.6	Process Name	About the process
	Cleaning	Piranha acid 10 min; water; IPA; N_2 blow-dry
A	Evaporation	Plassys MEB 550S: Al deposition of 150 nm at 0.5nm s^{-1} $P = 3 - 8 \times 10^{-8}$ mBar
	O2-N2 plasma	Recipe 13, 60s at 50% power to remove moisture and increase the adhesion of the hydrophobic resist
	Photo-resist	AZ1505 [21]spun at 5000 rpm for 60 s
		Hotplate: 80 °C for 5 min
B	UV lithography	MLA150: dose = 23 mJ cm^{-2} at $\lambda = 405$ nm, CD=0
	Development	AZ726 45s (Dynamic rinsing), Water 45s, N_2 blow-dry
C	Post Bake	Hotplate: 120 °C for 5 min
	Etching	Al etch until no further visual change ($\approx 7 - 10$ min). Add +50% extra time; Water rinse; N_2 blow-dry
		1 min AZ726, Water
D	Cleaning	Acetone/IPA quick resist removal without drying. Then soak in NMP $80 - 90$ °C for > 3 h. Water, IPA, N_2 blow-dry

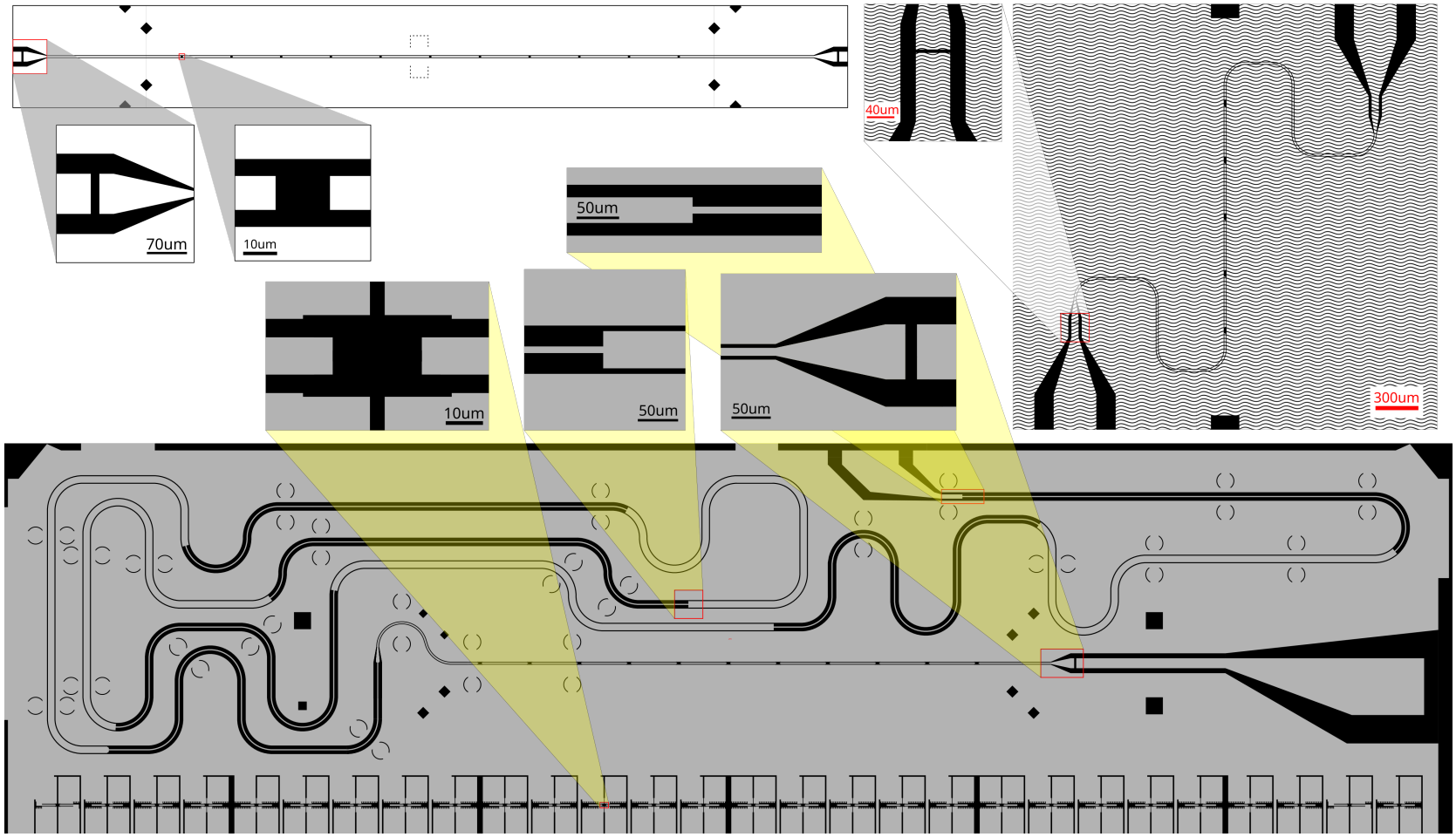

Figure 4.7: UV lithography resonator design. (Top left corner, white) The resonator design for samples A/B/C on silicon; (Top right corner, dashed) the resonator design of sample D for tunable flux qubits on sapphire; (Bottom, grey) the resonator design including Bragg filter for sample E on isotopically purified silicon.

4.3.3 Flux qubit fabrication

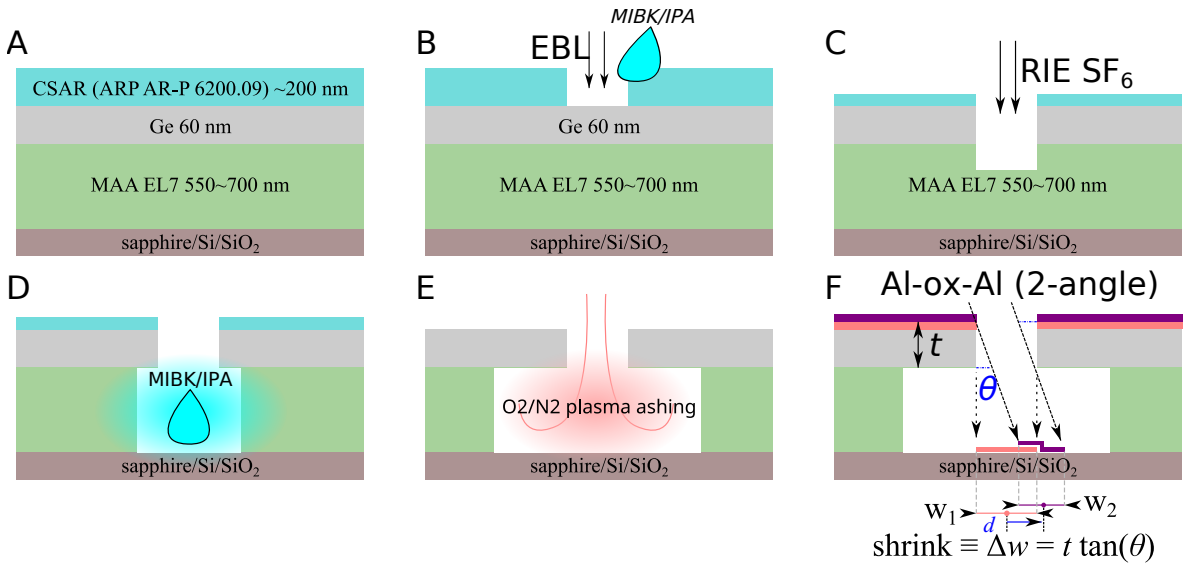

Figure 4.8: **Trilayer method, EBL mask patterning, evaporation and junction formation**

The trilayer technique The flux qubits are fabricated by ebeam lithography using the so-called Dolan technique [98]. The idea is to evaporate two thin layers of superconducting aluminum at different angles, separated by an intermediate oxidation step aimed to form the Josephson junction. In this project, we employ a trilayer process [70], in which a germanium mask, suspended on top of a $\sim 650\,\mathrm{nm}$ thick copolymer resist is employed. The rigidity and conductance of the Ge mask during EBL helps to achieve sharper resolution and more stable dimensions. Moreover, this mask is immune to oxygen ashing which allows for cleaning the region below the mask.

Formation of the suspended Ge mask The CSAR mask opening is patterned by Ebeam lithography using two kinds of beam current (30 pA and 120 pA) at 50 keV, and developped by MIBK/IPA=3:1. The Ge mask is patterned using an RIE process. We use a laser interferometer on a Ge calibration sample to fix precisely the etching time. We found that a 2.7-2.85 factor is required in order to etch small details such as constrictions, when compared to the calibration sample etching time. The use of the commercially available CSAR (AR-P 6200.09) resist instead of the standard PMMA resist adds extra resistance against RIE to the non-exposed regions as shown in the table herein-below.

Etched material	Rate of SF_6 RIE etch
Ge	$2.7-3.1\,\mathrm{nm\,s^{-1}}$
CSAR	$0.9-1.15\,\mathrm{nm\,s^{-1}}$
EL7	$\sim 1.5\,\mathrm{nm\,s^{-1}}$

After the RIE process, the copolymer resist (MMA(8.5)MAA-EL7) that has been exposed under EBL previously is developed using MIBK/IPA=3:1 (see Fig.4.8D). Areas under the qubit are thus

automatically cleaned all the way down to the substrate surface. The nominal dose to fully expose the copolymer resist is 30% that of CSAR resist ($d_{\mathrm{EL7}} = 220\,\mu\mathrm{C\,cm^{-2}}$). It is thus possible to remove the copolymer resist on expected regions of aluminum deposition that are not necessarily directly under Ge mask openings. This is done by adding underdosed (d_{EL7}) patterns in the EBL lithography design. During this MIBK/IPA=3:1 development step, the Ge mask doesn't collapse the solution, and the aluminum deposition regions become mostly clean of resist.

A final step of O2 ashing further cleans this undercut region. The boundary of the undercut extends isotropically by $\sim 400\,\mathrm{nm}$. The CSAR resist on top of the Ge mask is also removed. We measure the height of the Ge layer H by atomic force microscope (AFM), which is required for calibrating the evaporation angles.

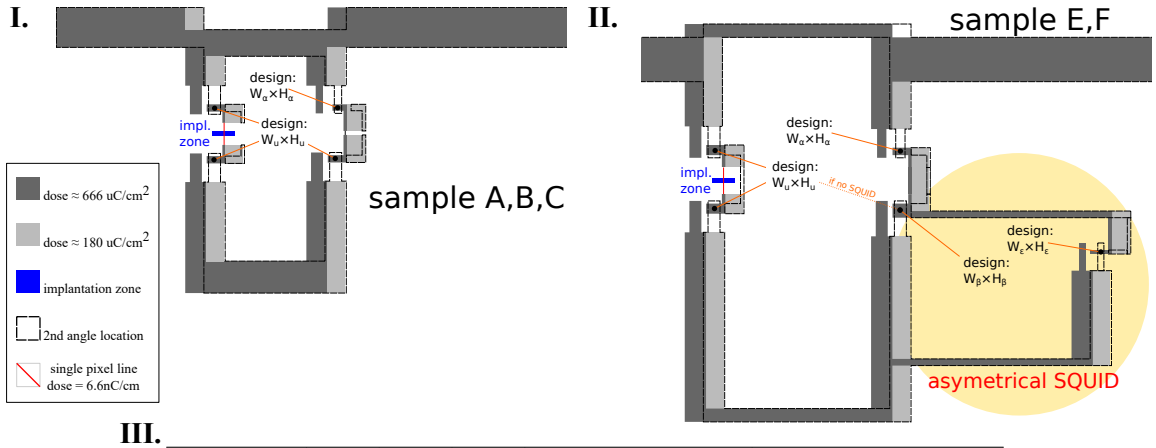

III.

sample	A	B	C	E,F (no SQUID)	E,F (with SQUID)
W_u (nm)	270	270	270	270	270
H_u (nm)	165	192	204	198±18	168±18
W_α (nm)	165	180	180	171	171
H_α (nm)	144	141	141	126	129
W_β (nm)	x	x	x	x	270
H_β (nm)					570
W_ε (nm)					117
H_ε (nm)					90

Figure 4.9: **Flux qubit EBL design paramters. I.** Format for Sample A, B & C. **II.** format for Sample E & F. **III.** table of dimensions.

Double angle evaporation and junction oxidation For achieving the best resolution, we evaporate a first Al layer of 20 nm perpendicularly into the sample ($\theta_1 = 0°$). This is done at low temperature ($\sim -45\,°\mathrm{C}$) to enable finer grain size, necessary for details such as constrictions. A dynamical oxidation of the first Al layer is performed, by introducing a dynamic flow of O2/N2 in the sample chamber (typ. $P \sim 19\,\mu\mathrm{bar}$).

For the second angle, we target a displacement $d = 420\,\mathrm{nm}$ with respect to the first image (see

Fig.4.8F). The angle can be calculated using trigonometry

$$d = \left(H - \frac{t_{\mathrm{Ge}}}{2} + \frac{t_{\mathrm{Al}}}{2} \right) \tan\theta$$

where H is the height from the substrate to the top of the Ge mask characterized using AFM. It is worth noting that H may fluctuate in vicinity of other thick structures, such as the CPW resonators which are 150 nm thick. It is therefore preferable to average over multiple measures of H to get an average displacement of 420 nm. Looking ahead, it is advised for the test junctions to replicate a similar environment (Fig.4.10A) to the real junctions, simulating the presence of a local CPW resonator, to avoid obtaining a different horizontal displacement.

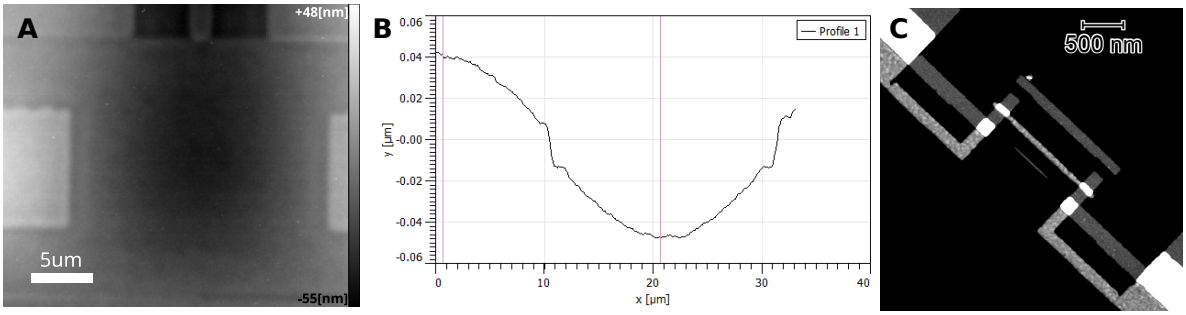

Figure 4.10: **A.** AFM micrograph showing height map H of the trilayer. **B.** Horizontal cut. A difference of 80 nm can be observed because of the thick 150 nm resonator layer. **C.** Test junction simulating the shrinking effect, achieving a width < 80 nm.

Since the first angle is evaporated at zero angle, it is observed (see Fig.4.8F) that the width of the second image shrinks by

$$w_{\mathrm{lim}} = (t_{\mathrm{Ge}} + t_{\mathrm{Al}}) \tan\theta \tag{4.2}$$

Consequently the evaporated second angle of small openings $w < w_{\mathrm{lim}}$ will not appear. In this thesis, we have $\theta \approx 35°$ which corresponds to $w_{\mathrm{lim}} \approx 56$ nm. This shrinking effect can be exploited to make extremely small junctions where the width $w_2 < 100$ nm while still using a bigger, robust mask opening $w \approx w_2 + w_{\mathrm{lim}}$, as shown in Fig.4.10C (and W_ε in Fig.4.9II).

After the two layers are deposited, we finish by static oxidation at $P = 10$ mbar for 10 minutes. This last step encapsulates the junctions with aluminum oxide and allows for a more controlled aging. The coupon is then soaked in NMP overnight to liftoff the trilayer mask.

Subfig.	Process Name	About the process
A	Copolymer spacer	MMA(8.5)MAA-EL7 [21]spun at 2000 rpm for 60 s
		Hotplate: 180 °C for 1 min
		MMA(8.5)MAA-EL7 [21]spun at 2000 rpm for 60 s
		Hotplate: 180 °C for 15 min
	Evaporation	Plassys MEB 550S: Ge deposition of 60 nm at $0.3\text{nm}\,\text{s}^{-1}$
	EBL resist	CSAR AR-P 6200.09[21]spun at 4500 rpm for 60 s
		Hotplate: 100 °C for 5 min
B	EBL	Crestec 9000: 30 pA at 50keV, dose = $670\,\mu\text{C}\,\text{cm}^{-2}$
	Development	MIBK for 240 s; IPA rinse for 60s; N_2 blow-dry
C	RIE etching of Ge	SF_6 20 sccm, rf bias = 20 W, laser calibration +180% extra time
D	Development	MIBK for 90 s; IPA rinse for 60s; N_2 blow-dry
E	O2-N2 plasma	Recipe 13, **4min30s** at 50% power
	Afm depth probing	AFM: check depth required to calculate the side angle.
F	Cold Evaporation	Plassys MEB 550S: Al deposition of 20 nm at $0.5\text{nm}\,\text{s}^{-1}$, $T = -44\,°\text{C}$
		dynamic oxidation $T = -10\,°\text{C} \mapsto +4\,°\text{C}$ at 0.019mbar
		Side angle: Plassys MEB 550S: Al deposition of 30 nm at $0.5\text{nm}\,\text{s}^{-1}$, $T \sim 9\,°\text{C}$
		Static oxidation for 10 min at 10mbar
	Cleaning	Liftoff: soak in NMP $80 - 90\,°\text{C}$ for > 6 h. Water, IPA, N_2 blow-dry

4.3.4 Ion-milling Recontact of flux qubit to resonator

Direct contact between the CPW resonator and the flux qubit will not form conductive contact due to the native oxide formed between the fabrication steps. We therefore connect both layers to a common $\sim$ 150 nm-thick aluminum strip from above (see blue strip in Fig.4.11). To achieve good electric contact, an ion milling step prior to evaporation removes the native oxide. The process follows similar steps as in section 4.3.3 except using a CSAR mask suspended on copolymer resist. The opening can thus be formed by a single step of MIBK/IPA=3:1 development, and an undercut which is beneficial for liftoff is automatically created. A small dose (30s) of O2-ashing is recommended to clean the exposed metal surface before the ionmilling and evaporation while keeping the CSAR mask robust.

The results on silicon substrates presented in this thesis used an ion-milling duration of 15s (Ar, 500V, 17.5mA). The rather low internal quality factors observed (2k, 6k, 18k) suggest that this may be insufficient and should be increased for future samples.

Process Name	About the process
Copolymer spacer	MMA(8.5)MAA-EL7 [21]spun at 2000 rpm for 60 s
	Hotplate: 180 °C for 1 min
	MMA(8.5)MAA-EL7 [21]spun at 2000 rpm for 60 s
	Hotplate: 180 °C for 15 min
EBL resist	CSAR AR-P 6200.09[21]spun at 4500 rpm for 60 s
	Hotplate: 100 °C for 5 min
E-Beam lithography	Crestec 9000: 120 pA at 50keV, dose = 670 µC cm^{-2}
EBL Development	MIBK for 240 s; IPA rinse for 60s; N_2 blow-dry
O2-N2 plasma	Recipe 13, 40s at 50% power
Ion-milling (in evaporator)	$P < 10^{-6}$ mBar; Argon at 20 sccm; 500V, 17.5 mA over an area 25 cm^2
Evaporation	Plassys MEB 550S: Al deposition of 200 nm at 0.5nm s^{-1}
Cleaning	Liftoff: soak in NMP 80 – 90 °C for > 6 h. Water, IPA, N_2 blow-dry

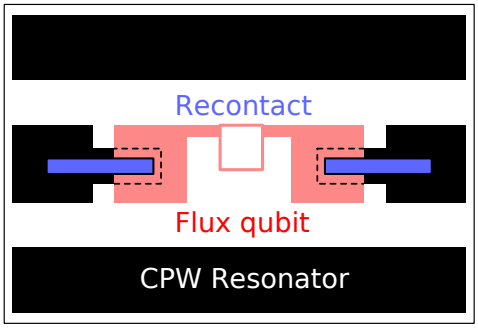

Figure 4.11: **Schema of Ion-milling recontact** viewed from top. The equivalent circuit diagram is shown in the inset: the recontact layer serves as an intermediary for the electrical contact. [[dimensions of IM

Material	@1 mA cm^{-2}	@17.5 mA/25 cm^2
Si	38 nm min^{-1}	0.44 nm s^{-1}
SiO_2	39 nm min^{-1}	0.45 nm s^{-1}
Al_2O_3	10 nm min^{-1}	0.11 nm s^{-1}
Al	73 nm min^{-1}	0.85 nm s^{-1}
S1822	< 100 nm min^{-1}	< 1.16 nm s^{-1}
Ge	8.5 nm min^{-1}	0.1 nm s^{-1}

Table 4.3: Ion milling etch rates using Ar ions at 500V at an angle normal to the wafer. Extracted from [99]

4.4 Characterization of constrictions

In the following, we characterize of the widths of the evaporated thin constrictions. As shown in Fig.4.12A, constrictions may manifest a penumbra effect when the Ge mask slit is sufficiently thin. This occurs when the viewing angle of the extended source is larger than the angle of the slit opening seen from the substrate surface. By conservation of matter, the quantity of evaporated aluminum passing through the slit is always given by $s \times t_{\mathrm{Al}}$, but it is evaporated over a broadened zone on the substrate, resulting in partially evaporated regions (*penumbra*). The resulting profile can be computed as a convolution of the slit to the point spread function of finite width, which corresponds to a minimal width attainable for the constrictions.

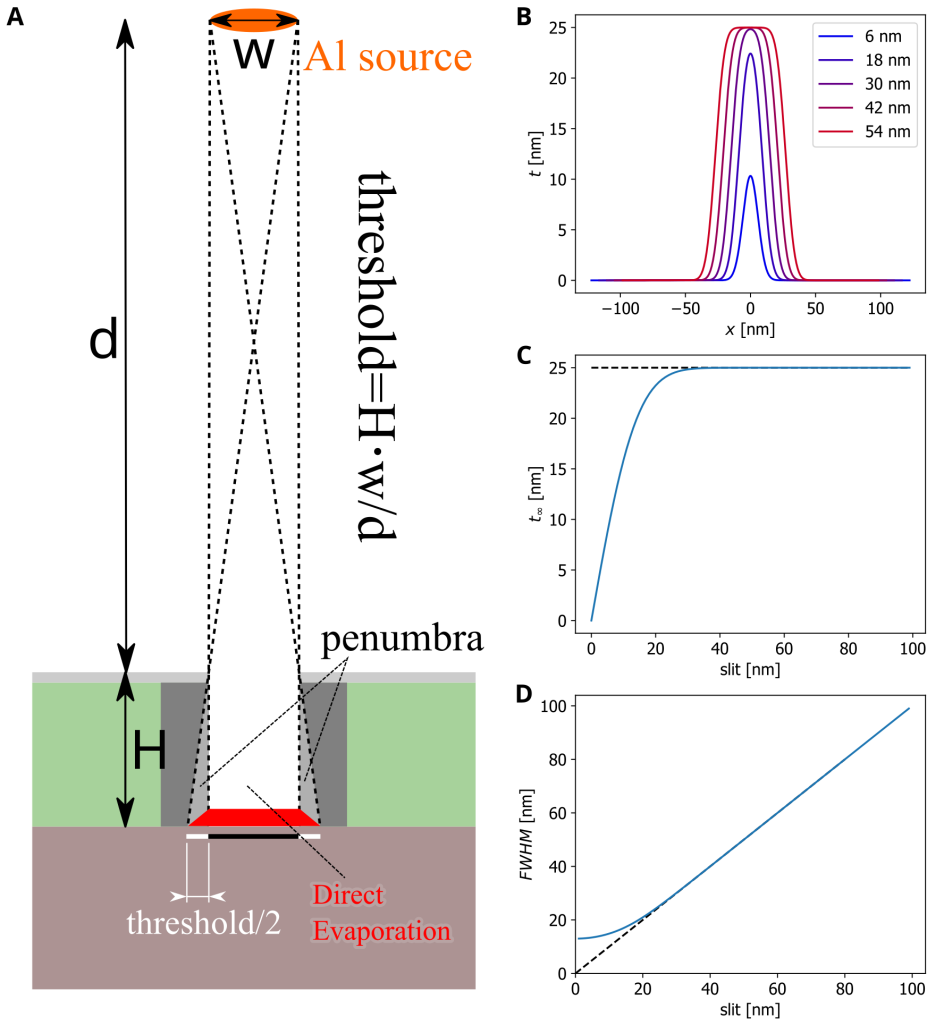

Figure 4.12: **Penumbra of the evaporator source cast by the suspended Ge mask A.** Schema of the penumbra formation. **B.** evaporated profile as a function of the slit size s. **C.** Peak thickness t_∞ as a function of the slit size s **D.** FWHM of the constriction profile as a function of s.

In Fig.4.12B, we show the broadened profile evaporated on the substrate as a function of the slit

width, supposing $t_{Al} = 25\,\text{nm}$, coming from a source with a gaussian distribution of diameter $w = 1\,\text{cm}$ at a distance $d = 500\,\text{mm}$ and a mask suspended at height $H = 650\,\text{nm}$. The peak thickness of the profile grows with the slit width and saturates only above a certain slit size $s \approx 25\,\text{nm}$ (see Fig.4.12C). In Fig.4.12D, we show the FWHM of the evaporated constriction profile versus the slit size s. The minimal width is $\approx 13\,\text{nm}$.

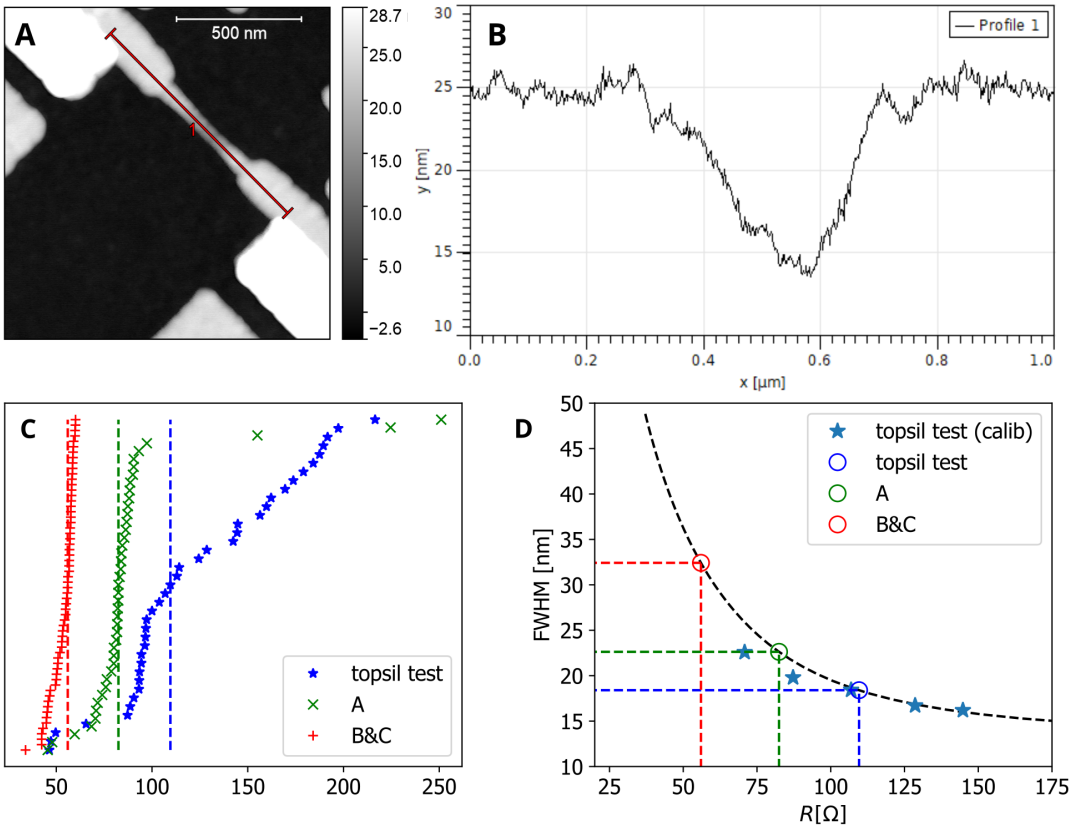

Figure 4.13: **A.** Afm micrograph of a test constriction on Topsil test sample. **B.** Profile along the cut 1 in E. **C.** The constriction resistance tested on different coupons and the median (dashed) **D.** The predicted FWHM of the evaporated profile supposing a bulk conductivity model.

In Fig.4.13A, we show an AFM micrograph of a typical constriction. The height profile of the constriction along the cut indicated in Fig.4.13A is shown in Fig.4.13B and illustrates the penumbra effect. We realize similar measurements for 5 different constrictions (blue stars in Fig.4.13D) and infer the FWHM of the constriction using the average height according to our model. These constrictions were also measured electrically which allows us to establish a calibration curve between constriction resistance and FWHM. In practice, measuring electrical resistance is much more rapid and convenient than measuring the height using AFM. This technique allows for establishing statistics on a large number of constrictions (see Fig.4.13C). As a rule of thumb, a width target of 30 nm corresponds to $R \approx 60\,\Omega$. This corresponds to $500/30 = 16.7\square$ which gives us a resistance per square of $3.6\,\Omega/\square$,

which is in good agreement with values found in the literature [100].

4.5 Room temperature characterization of the Josephson Junctions

Checking the resistance of junctions As mentioned earlier, each coupon can be diced into 14 samples of dimension (10×3mm each), each of which can be packaged for cryogenic measurement. The dicing step is a point of no return, since it is very difficult to restart the fabrication on small samples individually. It is therefore crucial to check the junction parameters before dicing. We principally check the resistance of test Josephson junctions and test constrictions, typically using four probe measurement with a lock-in amplifier.

Test junctions are fabricated on the same sample with the same design as the real ones intersecting the loop of the flux qubit. The critical current of a Josephson junction can be characterized using the Ambegaokar-Baratoff relation

$$I_0 R(T = 4\mathrm{K}) = \frac{\pi \Delta_g}{2e}$$

where Δ_g is the superconducting gap of our thin aluminum film. In practice, the resistance measurement is made at room temperature and this formula needs to be renormalized by the Residual-resistance ratio (RRR). For junctions fabricated by dynamical oxidation, we found the proportionality constant to be approximately

$$\boxed{I_0 R(T = \mathrm{R.T.}) \approx 287\,\mu\mathrm{V}} \tag{4.3}$$

In Fig.4.14, we show the histogram of the junction resistances for samples A,B and C obtained through four probe measurement. The spread of the unitary junctions is 6% for sample A, and 1.7% for sample B and C. The spread in α is $0.518 \pm 0.035\,(6.7\%)$ for sample A, $0.486 \pm 0.011\,(2.2\%)$ for sample B and $0.464 \pm 0.010\,(2.2\%)$ for sample C. We show in Fig.4.15b the spread of the resistance measurements for sample D obtained through two-probe measurement. The standard deviation of the unitary junctions for sample D is 2.3%, which corresponds to a spread of $\alpha = 0.423 \pm 0.012\,(2.7\%)$.

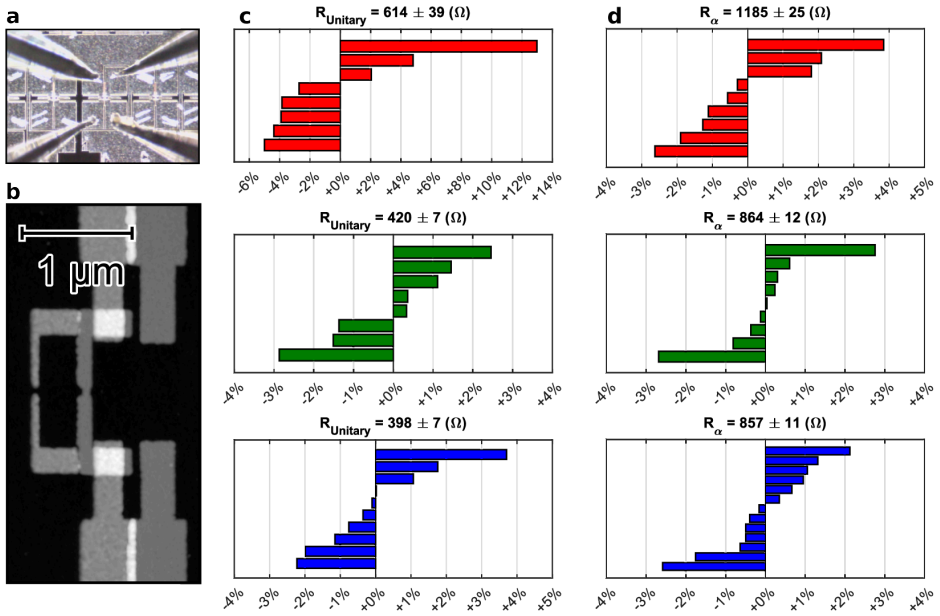

Figure 4.14: **Room temperature resistance measurements of samples A,B,C. a**, Microscope image showing 4 probe measurement of a test sample. **b**, AFM micrograph showing a close-up view on the test sample which consists of the two Josephson junctions in series. **c**, Resistance measurements of several unitary junctions for sample A (in red), B (in green) and C (in blue). The resistance of the unitary junctions is $614 \pm 39\,\Omega$, $420 \pm 7\,\Omega$, $398 \pm 7\,\Omega$ for sample A,B and C respectively. **d**, Resistance measurements of several α junctions for sample A (in red), B (in green) and C (in blue). The resistance of the α junctions is $1185 \pm 25\,\Omega$, $864 \pm 12\,\Omega$, $857 \pm 11\,\Omega$ for sample A,B and C respectively.

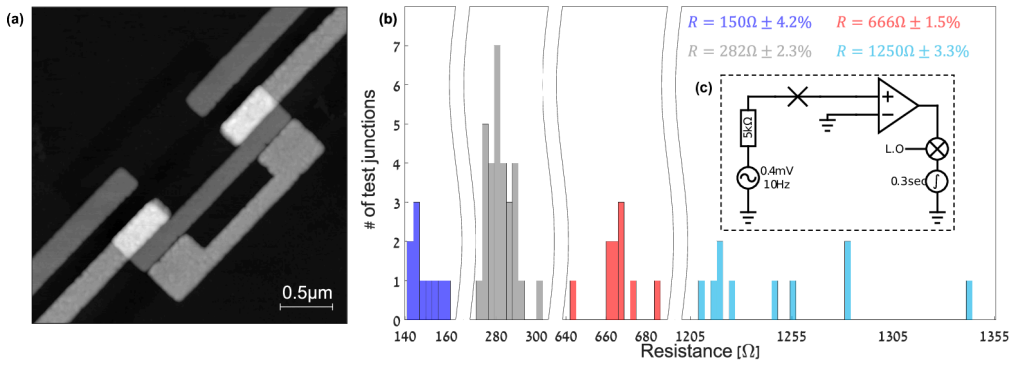

Figure 4.15: **Room temperature resistance measurements of sample D.** (a) Atomic force micrograph of two unitary test junctions in series. (b) Histogram representing the resistance distribution of an ensemble of 60 test junctions: 30 unitary junctions (gray), ten α junctions (red), ten $\beta(1+d)/2$ junctions (dark blue), and ten $\beta(1-d)/2$ junctions (light blue). The standard deviations of the resistances are in the range of $1.5\% \sim 4.2\%$. the extracted parameters of the qubit are $\alpha = 0.42 \pm 0.01$, $d = 0.79 \pm 0.01$ and $\beta = 2.11 \pm 0.09$. The critical current of the unitary junction can be estimated by Ambegaokar-Baratoff relation to be 1.08 μA. (c) Scheme of the room temperature lock-in measurement setup.

Validating the oxidation Eq.4.3 can be used to calculate the critical current of the junction, which is a product of area times the critical current per unit of area. The oxidation condition (time, pressure, humidity, gas decomposition) determines the latter. It is therefore required to have a measure of area to gauge the oxidation conditions. AFM measurements gives unreliable horizontal dimensions since each image depends on the type of tip used, the surface charging condition, as well as the tip's wear and tear. In this work, we adopt another strategy. We implement test junctions with different size design and check the relationship to the corresponding resistance. We make the hypothesis that the final junction area A_{JJ} is flat, and oxidation is homogeneous, and that the dimensions relate to the design in an affine manner. The affine offset takes into account empirically all complexities such as RIE underetch/overetch, EBL underdose/overdose as well as extra area resulting from the 3D overlapping around the edges.

$$\begin{aligned} A_{JJ} &= W_{JJ} \times H_{JJ} \\ W_{JJ} &= W_{\text{design}} + W_{\text{offset}} \\ H_{JJ} &= H_{\text{design}} + H_{\text{offset}} \end{aligned}$$

For a fixed design width W_{design}, the slope of the conductance to the height increments $\partial\sigma/\partial H_{\text{design}}$ may be calculated. By employing two or more W_{design}, we can easily calculate $\partial^2\sigma/\partial H_{\text{design}}\partial W_{\text{design}}$, for which the inverse can be put in units of $\Omega\,\mu\text{m}^2$, as more commonly used in literature. We get for our oxidation in the range of $22-25\,\Omega\,\mu\text{m}^2$, translated into $11.5-13\,\mu\text{A}\,\mu\text{m}^{-2}$ of critical current density. This spread may appear to be problematic, but it is worth noting that the two major parameters of the flux qubit Δ, I_P depends much less on this parameter than on the relative area ratios between the junctions. In other words, as long as the oxidation conditions change uniformly on the whole coupon, the parameters of the resulting qubit will only change globally (e.g. increased Δ and decreased I_P) and only slightly ($< 0.5\,\text{GHz}$, $< 50\,\text{nA}$). As a counter-measure, we may decide to change the ratio from sample to sample within the same coupon, such that no matter the oxidation, one of the samples will fall around the target parameters.

The mask opening design are also updated according to the last W_{offset} and H_{offset} measured on that particular kind of sample: We distinguish on one hand, those with native oxide (Silicon Virginia), and on the other hand those with thermally grown oxide (Topsil, Isonics). A major reason for this, besides the apparent different surface treatment used, is the difference in thickness in these two kinds of samples. We suspect strongly that the thickness will change the thermal conductivity during the RIE process and lead to a different offset resulting from underetch/overetch. Interestingly, we systematically measure an increase in the resistance by $5 \sim 12\%$ after dicing, suggesting a change in the oxide properties. We suspect this has to do with the heating, in presence of the copolymer resist during the dicing process. Indeed, we dice the coupon from the top side to properly delimit the samples. It is thus required to put 2-4 layers of copolymer resist to protect the surface from dicing debris. We bake these layers only up to 120° for 5 minutes per layer to prevent overheating of the junctions.

5 Experimental Setup

Experiments are performed at a temperature of 14 mK in a Cryoconcept dilution refrigerator, model Hexadry 200 with low mechanical vibrations. Fig.5.1 shows a detailed schematic of the experimental setup. The samples are glued on a microwave printed circuit board made out of TMM10 ceramics, then enclosed in a copper box with low mode volume which is itself embedded into a superconducting coil that is used to provide magnetic flux biases to the qubits. To reduce low frequency magnetic noise, the coil is surrounded by a superconducting enclosure (Copper plated by SnPb 60/40 15 µm) and magnetically shielded with a high permeability metal box (CryoPhy from Meca Magnetic). The apertures of the box are tightly closed using Eccosorb AN-72, in order to protect the sample from electromagnetic radiation that could generate quasiparticles.

The coil is powered by a BILT BE-2102 voltage source filtered by a custom designed ultra-stable voltage to current converter. The microwaves are generated by Keysight PSG E8257D analog microwave synthesizers. The pulses are modulated at an intermediate frequency of 10-200 MHz by a Quantum Machines OPX system connected to MITEQ IRM0618/IRM0408 mixers. Voltage controlled attenuators (Pulsar AAR-29-479) are used to adjust the pulse amplitude over a wide range (0.5-64 dB). The input line is attenuated at 4K stage (XMA -20 dB) and at the mixing chamber stage (XMA -40 dB) to minimize thermal noise and filtered with an homemade impedance-matched copper powder filter (-10 dB @ 10 GHz). In addition, the pulses are shaped with smooth rise and fall ($\sim$ 20 ns) in order to reduce the population of microwave photons in the resonator during coherent state evolution of the qubit.

Qubit state measurement is done using dispersive readout, by measuring the transmission of microwave pulses through the resonator, using a custom built setup. The readout output line is filtered by two shielded double circulators (LNF-CICIC8_12A) and a $8-12$ GHz band pass filter from Micro-Tronics, model BPC50406. The readout output signal is amplified using a low-noise cryogenic HEMT amplifier (LNF-LNC1_12A) and a room temperature amplifier (LNF-LNR1_15A). After demodulation, the quadratures of the readout output pulse are sampled and averaged using the IQ inputs of the OPX system. At this point, we perform a principal axis transformation on the data points by diagonalizing their covariance matrix. Using this transformation, we extract the largest principal component of the measured (I, Q) points and obtain the state of the qubit.

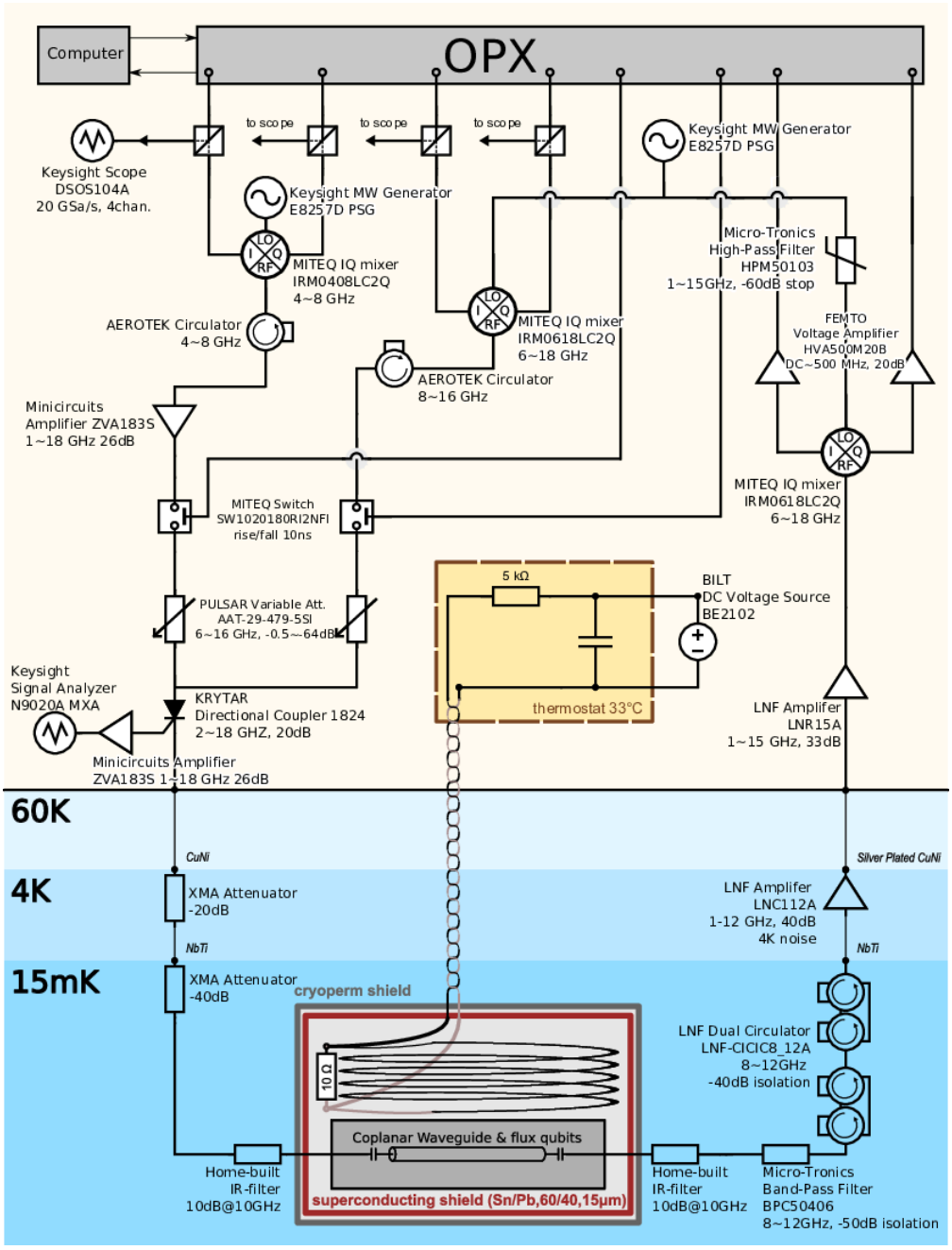

Figure 5.1: Experimental Setup.

6 Results and analysis

6.1 Reproducibility and gap control of superconducting flux qubits

6.1.1 Circuit implementation

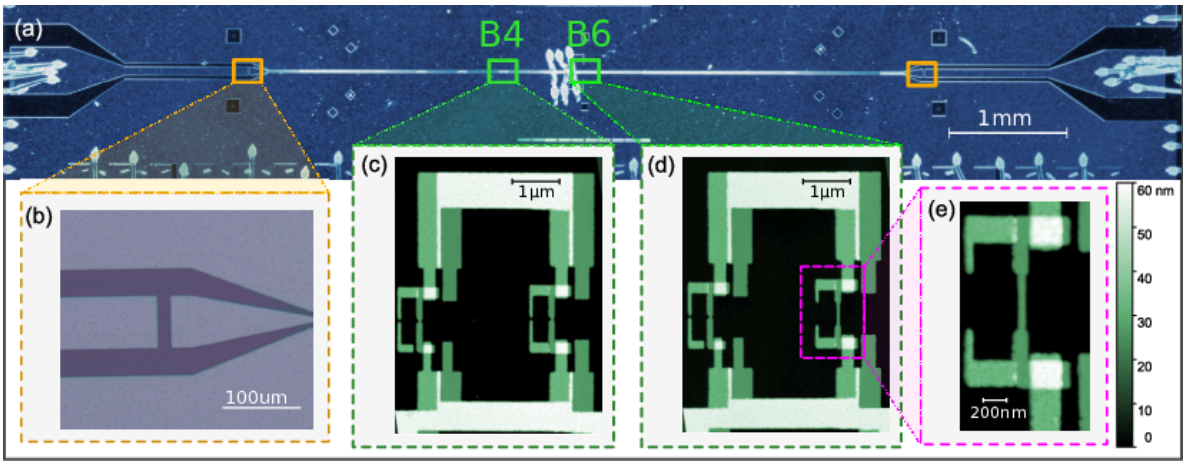

Figure 6.1: **Circuit implementation.** (a) Optical microscope image of a $\lambda/2$ CPW resonator (resonator B) intersected and galvanically coupled to a series of eleven flux qubits labelled $B1$ to $B11$. The CPW resonator length is chosen to be 5.73 mm, such that the first resonant mode is at $f_{rB} \simeq 9.8$ GHz. (b) Close up view of the coupling capacitor terminating at both ends the CPW resonator. The value of the capacitance is calculated by an electromagnetic simulator (Sonnet) to be $C_C \sim 5.0\,\mathrm{fF}$. (c) Colored AFM micrograph of qubit $B4$. The surface area of the unitary junction is $A_{uni} = 0.0526 \pm 0.0008\,\mu\mathrm{m}^2$ and the small junction was chosen to have $\alpha = 0.5$. (d) Colored AFM micrograph of qubit $B6$. The surface area of the unitary junction and the ratio α are identical to $B4$. The loop of this qubit includes a thin constriction. (e) Close up view of the 30-nm width constriction of qubit $B6$.

The three samples presented in this work are fabricated on silicon chips and contain a 150-nm thick aluminum coplanar waveguide (CPW) resonator, with two symmetric ports used for microwave transmission measurements (see Fig.6.1(a)). As mentioned in Tab.4.1, the CPW resonator A is directly fabricated on a high resistivity ($> 10\,\mathrm{k\Omega\,cm}$) silicon wafer with native oxide while resonators B and C are fabricated on a 5 nm thermally grown silicon oxide layer. A series of eleven flux qubits is galvanically coupled to each CPW resonator. In the following, the qubits are labelled according to their spatial position on the relevant resonator (e.g. $A1...A11, B1...B11, C1...C11$).

Fig.6.1(c) and (d) present Atomic Force Microscope (AFM) images of qubits $B4$ and $B6$. The loop area of qubit $B4$ (resp. $B6$) is $S_{B4} \simeq 13.3\,\mu\mathrm{m}^2$ (resp. $S_{B6} \simeq 12.4\,\mu\mathrm{m}^2$). The three identical junctions have a Josephson energy $E_J/h = 360\,\mathrm{GHz}$ and a single electron charging energy $E_C/h = 3.68\,\mathrm{GHz}$ while the fourth junction is smaller than others by α=0.5. In addition, qubit $B6$ contains a 30 nm width constriction over a length of 500 nm (see Fig.6.1(e)).

We first characterize the qubit-resonator system by spectroscopic measurements (see section §5). Fig.6.2(a-b) shows a continuous wave transmission scan of resonator B taken as a function of the

applied magnetic field. This measurement is performed with a vanishing power corresponding to an average of less than one photon in the resonator. We observe an anticrossing each time a qubit and the resonator are resonant. Far from the anticrossings, the resonance corresponding to the first mode of the resonator is $f_{rB} = 9.804$ GHz and its quality factor is $Q_B = 2800$ (see Tab.6.1).

Resonator	Length (µm)	C_C (fF)	f_r (GHz)	Q_{tot}	κ (rad.s^{-1})	Q_C	Q_{int}	$\bar{n}_{thermal}$
A	7250	5	7.756	1400	3.5×10^7	5500	1878	8.88×10^{-4}
B	5730		9.805	2800	2.2×10^7	3500	14000	6.82×10^{-4}
C	5730		9.850	2200	2.8×10^7	3500	5923	6.78×10^{-4}

Table 6.1: **Resonator parameters.** Length of the resonator, coupling capacitance C_C, bare frequency of the resonator $\omega_r/2\pi$, quality factor Q of the resonator, photon loss rate κ, coupling Q_C and internal Q_{int} quality factor of the resonator given by $\frac{1}{Q} = \frac{1}{Q_C} + \frac{1}{Q_{int}}$, estimated number of thermal photons in the resonator $\bar{n}_{thermal}$.

6.1.2 Spectroscopic measurements

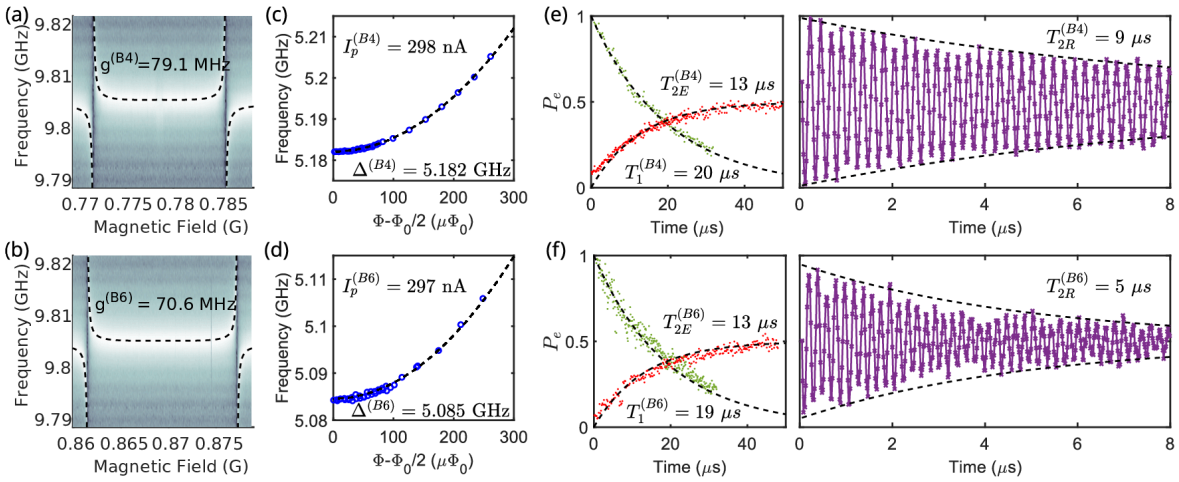

Figure 6.2: **Characterisation of qubit $B4$ (top panels) and $B6$ (bottom panels).** (a-b) Transmission spectrum of CPW resonator B versus applied magnetic field showing anticrossing of qubit B4/B6. For each qubit we fit the anticrossing to our qubit-resonator coupling model and extract the value of the coupling constant g of the qubit with the resonator. (c-d) Measured qubit frequency (blue dots) and fit (black dashed curve) yielding the qubit parameters Δ and I_p. (e-f) (left panel) Qubit energy relaxation and spin echo measurements. The excited state probability P_e is plotted as a function of the delay between the π pulse and the readout pulse (green dots) or between the two $\pi/2$ pulses of the echo sequence (red dots). The black dashed line is an exponential fit to the energy relaxation (spin-echo) data. (Right panels) Measured Ramsey fringes (purple solid line) with fit to its exponentially decaying envelope.

The frequency dependence of qubit $B4$ and $B6$ on Φ is shown in Fig.6.2(c-d), respectively. The transition frequency of each qubit follows $f_{01} = \sqrt{\Delta^2 + \varepsilon^2}$ with $\varepsilon = 2I_P\left(\Phi - \Phi_0/2\right)/h$, yielding $\Delta^{(B4)} = 5.182\,\text{GHz}$ and $I_P^{(B4)} = 298\,\text{nA}$ (resp. $\Delta^{(B6)} = 5.085\,\text{GHz}$, $I_P^{(B6)} = 297\,\text{nA}$). Since both qubits were designed to have the same parameters, this demonstrates excellent reproducibility of our

e-beam lithography and oxidation parameters. Taking into account the contribution of geometric capacitance between neighboring islands allows us to fit the parameters of the flux-qubits in good agreement with the measured values of α and E_J extracted from Ambegaokar-Baratoff formula (see Eq.4.3). We now turn to the coherence times at the so-called optimal point where the qubit frequency $f_{01} = \Delta$ is insensitive to first order to flux-noise [64, 65]. Energy relaxation decay is shown in Fig.6.2(e) and f to be exponential for both qubits, with $T_1 = 20\,\mu s$ for $B4$ and $19\,\mu s$ for $B6$. Ramsey fringes show an exponential decay for $B4$ with $T_{2R} = 9\,\mu s$, for $B6$ with $T_{2R} = 5\,\mu s$. Spin-echo decays exponentially with identical dephasing times $T_{2E} = 13\,\mu s$. Apparently, the presence of the constriction in qubit $B6$ does not seem to influence the coherence time of the qubit. This property is particularly exciting if one wishes to coherently couple a single spin to this circuit [101].

6.1.3 Reproducibility and Control of gap

We repeat this procedure for the qubits of our three samples. Each qubit is thus characterized by its spectroscopic parameters Δ and I_P, extracted from the dependence of its transition frequency on the applied flux. In Fig.6.3(a), we represent a graph showing the gaps Δ of the different qubits versus their persistent currents I_P. In order to optimize our qubit design, we varied the size of the unitary junctions of samples A, B and C while keeping an approximately constant critical current density of $\sim 13.5\,\mu A\,\mu m^{-2}$. Within each sample, the qubit parameters (E_J, E_C, α) were designed to be identical and thus the qubits should be clustered within a well defined region. The extent of this region indicates the level of reproducibility of our fabrication process. A slight improvement in the data spread is observed for Sample B and C in comparison to sample A. Quantitatively speaking, the gap average values are 6.9 ± 1GHz, 5.1 ± 0.7 GHz and 6.6 ± 0.6 GHz for samples A, B and C respectively. A principal component analysis (PCA) is performed on the covariance matrix of the (Δ, I_P) data-points in order to define regions with high probability to find a qubit. For each sample, a dashed line is represented and corresponds to the result of qubit numerical diagonalizations (see section §2.2) while varying the parameter α by $\pm 5\%$ around their respective average value $\left(\langle E_J \rangle_{A/B/C}, \langle E_c \rangle_{A/B/C}, \langle \alpha \rangle_{A/B/C}\right)$. For the three samples, the principal axis and the numerical diagonalizations are well aligned indicating that the main origin of disorder is indeed uncontrolled variations of the value of the parameter α. The variation of the critical current density of the junctions due to different oxidation of samples A, B and C ($\pm 5\%$) leads to an additional uncertainty of $\pm 150\,MHz$ in the control of the desired qubit gap.

6.1.4 Relaxation and dephasing

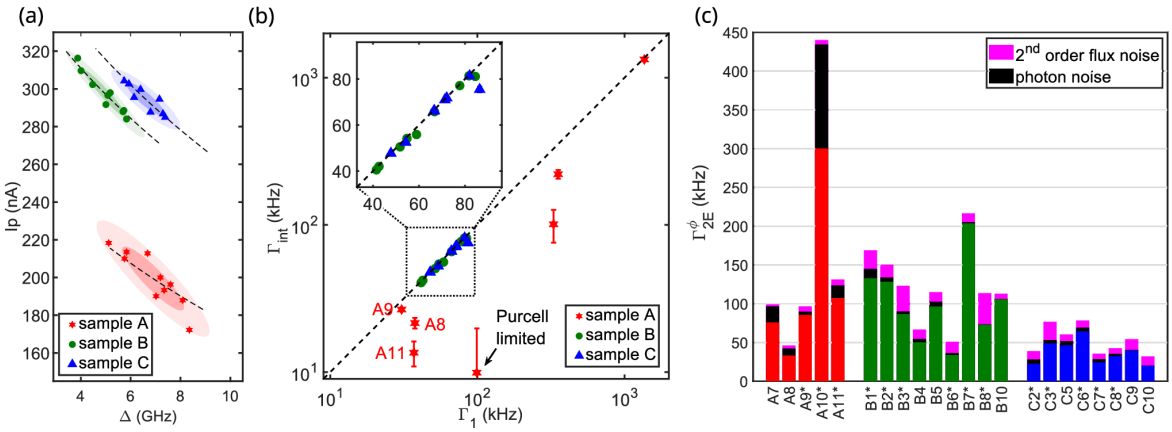

Figure 6.3: **Reproducibility and control.** (a) Persistent current I_P versus gap Δ of the qubits of sample A (native oxide, red stars), sample B (5 nm grown silicon oxide layer, green dots) and sample C (5 nm grown silicon oxide layer, blue triangles). The colored regions are obtained by assuming a normal distribution along axes defined by principal component analysis (PCA). The probability to find a qubit within the dark (resp. light) colored area is 50% (resp. 90%). The dashed black lines are obtained by numerical simulations of the flux qubits (see section §2.2 at their average value $\left(\langle E_J\rangle_{A/B/C}, \langle E_c\rangle_{A/B/C}, \langle\alpha\rangle_{A/B/C}\right)$ while varying the parameter α by $\pm 5\%$. (b) The estimated intrinsic relaxation rates $\Gamma_{int} = \Gamma_1 - \Gamma_P$ versus measured relaxation rates Γ_1 for qubits of sample A (red stars), B (green dots) and C (blue triangles). The error bars stem from calibration uncertainties of ± 1 dB of the incoming power at the resonator input. (c) Stacked bar chart showing the pure dephasing rates Γ^{ϕ}_{2E} at optimal points of the measured qubits of sample A (red), B (green) and C (blue). The black color corresponds to the calculated decoherence rate due to photon noise in the resonator. The pink color corresponds to calculated decoherence rate due to second order flux noise. The black stars indicate the presence of a 30-nm width constriction in the loop of the qubit. The presence of a constriction does not seem to affect significantly the relaxation or the dephasing of the qubits.

In Fig.6.3(b), we represent the spread of the relaxation rates Γ_1 of the different qubits. Qubit $A9$ exhibits the longest relaxation time with $T_1 = 32\,\mu$s. Several mechanisms contribute to relaxation of qubits; among them, spontaneous emission by the qubit to the resonator (the so-called Purcell effect [102]). As shown in section 3.4.1, the Purcell rate Γ_P can be quantitatively determined by measuring the qubit Rabi frequency ω_r for a given microwave power P_{in} at the resonator input. For a qubit coupled symmetrically to the input and output lines, a simple expression for Γ_P was obtained in Ref.[70]. We thus calculated Γ_P for each qubit and represented the intrinsic relaxation rates of the qubits defined as $\Gamma_{int} = \Gamma_1 - \Gamma_P$. The average values of the intrinsic relaxation rates are 260 ± 440 kHz, 61 ± 15 kHz and 68 ± 11 kHz for samples A, B and C, respectively. These average numbers are comparable to those obtained in Ref.[69] for C-shunted flux qubits. Relaxation due to $1/f^{\gamma}$-flux noise can be safely neglected for qubits in our frequency range [69]. The spread of the relaxation rates in sample B and C is remarkable compared to sample A and more generally to the state of the art [70, 66]. We thus come to the conclusion that better qubit reproducibility in terms of relaxation rates

is obtained on samples with a thermally grown 5 nm width silicon oxide layer. It is yet important to stress that the best relaxation rates ($\sim 25\,\mathrm{kHz}$) were obtained on intrinsic silicon (e.g. A11, A8). These findings are consistent with previous studies comparing loss tangents for silicon oxide and silicon at low temperatures [103, 104, 105]. Yet, the high variability of the devices on native oxide points towards an extreme sensitivity of the dielectric losses to the nanoscale variations in the stoichiometry and thickness of the oxide.

In the rest of this section, we will focus on the origin of the dephasing rates of the qubits. Indeed, the noticeable reproducibility of the qubits enables us to analyze the different noise sources that influence the coherence times and systematically eliminate possible noise factors. We begin this analysis away from the optimal point, where the flux qubit decoherence is dominated by flux noise. The power spectrum of flux noise has a 1/f shape $S_\Phi[f] = A_\Phi^2/f$ [64, 67, 68, 66]. Thus, measuring the flux qubit decoherence versus ε gives us directly access to the flux noise amplitude A_Φ [82, 75]. Interestingly, we obtain almost the same flux noise amplitude $A_\Phi = 1.2 \pm 0.2\,\mu\Phi_0$ for all the qubits whether on sample A, B or C including those with constrictions or not (see section 6.1.5).

In Fig.6.3(c), we show the pure echo dephasing rate $\Gamma_{2E}^{\phi} = \Gamma_{2E} - \Gamma_1/2$ at the optimal point for the different qubits. At this point, the qubits are protected against flux noise at first order. Yet, second order effects may still impact the dephasing rates. To account for these effects, we performed a numerical Monte Carlo simulation detailed in 3.5.3. At the optimal point, a simple formula is obtained:

$$\Gamma_{2E}^{opti} \simeq 56 \frac{(I_p A_\Phi/h)^2}{\Delta}$$

The results of our analysis show that second order flux noise can only explain partially the observed dephasing at the optimal point. Other well-known mechanisms of dephasing are related to photon noise in the resonator [64, 69] and charge noise [70]. As shown in Fig.6.3(c), photon noise has some impact on several qubits whose resonance happens to be close to the one of the resonator. The sensitivity of flux qubits to charge-noise is highly dependent on the ratio between the Josephson energy E_J and the charging energy E_C. We thus calculated the maximum amplitude of the charge modulation for each qubit. In average, the charge modulation is equal to 100 kHz, 5 kHz and 1 kHz for samples A, B and C respectively. Clearly, this is more than one order of magnitude smaller than the measured pure dephasing rate for sample B and C and cannot explain the data. Thus, another mechanism is necessary to explain at least qualitatively the remaining dephasing rate of these qubits. Critical current fluctuations are for instance a possible channel of dephasing in our system. These fluctuations are due to charges localised in the barrier of the Josephson junctions. They also produce a 1/f shape spectral density [106, 107]. Assuming that the remaining dephasing rate of sample C is fully due to this microscopic source of noise, we get $S_{I_0}[1\,\mathrm{Hz}] \simeq (0.5\,\mathrm{pA})^2\,\mu\mathrm{m}^{-2}$, which seems compatible with previously reported values in the literature.

6.1.5 Extracting the flux noise amplitudes

We use the formula established in 3.5.2 to to extract the amplitude of the flux noise as shown in Fig.6.4.

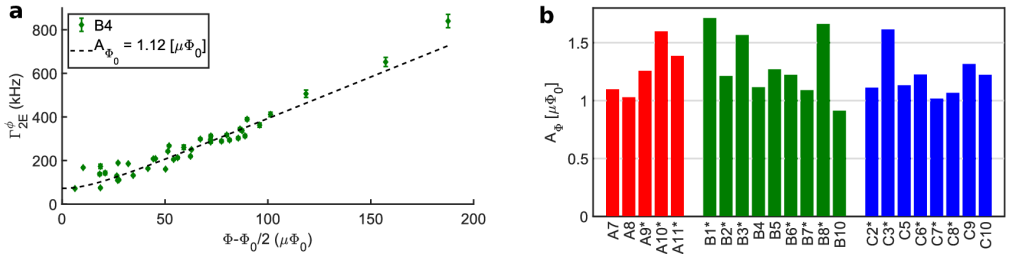

Figure 6.4: **Flux noise amplitude.** **a**, Echo pure dephasing rates of qubit B4 as a function of $\Phi - \Phi_0/2$. Fitting the measured data with Eq.3.70 yields $A_\Phi = 1.12\,\mu\Phi_0$. **b**, Extracted amplitude of flux noise for different qubits in red for sample A, green for sample B and blue for sample C. We obtain almost the same flux noise amplitude $A_\Phi = 1.2 \pm 0.2\,\mu\Phi_0$ for all the qubits whether on sample A , B or C and including those with constrictions.

6.1.6 Doublet behavior at optimal point

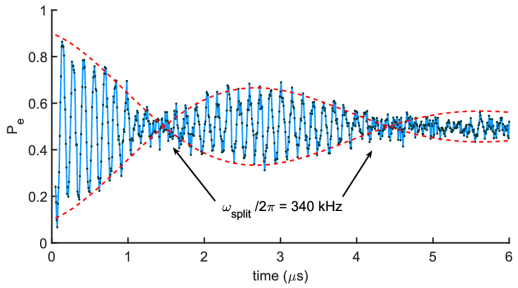

Figure 6.5: **Ramsey measurement of qubit B5 showing beating.**

Some of the measured qubits exhibit a doublet line shape at optimal point. This lineshape is manifested as a beating of the Ramsey oscillations as shown in Fig.6.5. For qubit $B5$, the frequency of this beating is 340 kHz, almost two orders of magnitude larger than the charge modulation $\delta\Delta^{n_g} = 4.3$ kHz and thus cannot be attributed to slow fluctuations of the electron number parity on one of the qubit's islands [70, 108]. An alternative explanation for the origin of this doublet is related to trapping and un-trapping of a single quasiparticle in the α junction.

By simple arguments, we can give a rough estimate for this effect. The area of the α junction of qubit $B5$ is $A_\alpha = 0.0257\,\mu\text{m}^2$ while the Fermi wavelength of electrons in aluminum is $\lambda_F = 0.36$ nm. Thus, the number of channels in such a junction is large and can be estimated as $A_\alpha/\lambda_F^2 \sim 2 \times 10^5$. Assuming that all channels have the same transmission τ, we can estimate the change of the Josephson energy of the α junction to be around 1 MHz. We then calculate numerically the variation $\delta\Delta^{\text{trapping}}$ of the qubit gap and obtain 300 kHz , which is close to the observed value of the doublet. We thus

come to the conclusion that these doublets are most likely due to the trapping and un-trapping of a quasiparticle in the α junction.

6.1.7 Conclusion and summary tables

In conclusion, we have shown that flux qubits can be fabricated in a reproducible way both in terms of gap transition energy and in terms of decoherence rates. Reproducible relaxation times have been measured with $T_1 \sim 15 - 20\,\mu s$ for samples fabricated on a thermally grown 5-nm SiO_2 layer. These numbers are comparable to those observed in Ref.[69] for C-shunted flux qubits. The major advantages of our design are its large anharmonicity ($f_{12} \sim 30\,GHz$) and high persistent current ($I_p \sim 300\,nA$). This makes flux qubits ideal candidates for magnetic coupling to spins such as NV centers [109, 101] or other impurities in silicon [110]. In all the samples, the amplitude of flux noise was low and reproducible $A_\phi = 1.2 \pm 0.2\,\mu\Phi_0/\sqrt{Hz}$. At the optimal point, long and reproducible pure dephasing times were measured with $T_{2E}^{\phi} = 15 - 30\,\mu s$. At this level, the pure dephasing times are most likely limited by critical current fluctuations of the small junction of the qubits. Our results prove that flux qubits can reliably reach long coherence times and open interesting new perspectives for both hybrid quantum circuits and scalable quantum processing.

Qubit ref.	Δ	I_p	g	χ	E_J	E_J/E_C	α	$\delta\Delta^{\text{geom}}$	$\delta\Delta^{n_g}$	Γ_1	Γ_P	Γ_{2E}^{ϕ}	Γ_{2E}^{2nd}	$\Gamma_{2E}^{\text{phot}}$
units	GHz	nA	MHz	MHz	GHz	1	1	GHz	kHz	kHz	kHz	kHz	kHz	kHz
A2	7.19	188	28	1.29	265	69	0.492	-1.09	78.4	1363	36	x	x	10
A6	8.33	244	50	4.48	256	67	0.487	-0.51	95.1	354	143	x	x	131
A7	8.69	187	40	1.8	240	63	0.476	-1.34	136.3	99	96	99	3	21
A8	6.35	202	43	1.19	264	69	0.504	-0.83	94.5	38	17	46	4	9
A9	5.24	201	50	0.82	251	66	0.514	-1.25	154.6	31	4	97	7	4
A10	8.35	182	52	4.66	255	67	0.477	-1.54	88.1	330	245	440	6	134
A11	5.81	201	61	1.64	258	67	0.503	-1.49	110.1	37	25	131	8	16
B1	5.73	289	94	1.59	362	98	0.489	-1.61	3.7	84	4	169	24	12
B2	4.48	302	95	1.05	360	98	0.504	-1.36	5.0	78	1	151	17	5
B3	4.01	310	92	0.86	361	98	0.511	-1.24	5.4	82	0	123	33	4
B4	5.18	298	79	0.94	364	99	0.497	-1.30	4.0	52	1	67	12	4
B5	5.84	284	77	1.11	357	97	0.490	-1.46	4.3	67	1	115	13	6
B6	5.08	297	71	0.72	361	98	0.499	-1.27	4.5	43	1	51	15	2
B7	5.01	292	64	0.57	354	96	0.500	-1.31	5.4	55	1	217	11	1
B8	3.88	316	63	0.37	366	100	0.512	-1.17	4.8	41	1	113	40	1
B10	5.69	288	40	0.29	360	98	0.490	-1.53	4.0	59	3	113	7	0
C2	5.93	303	90	1.56	387	111	0.481	-1.54	1.0	72	0	39	11	6
C3	5.74	304	85	1.29	386	110	0.484	-1.47	1.1	54	2	77	24	4
C5	6.80	288	75	1.5	380	109	0.474	-1.52	1.1	66	0	60	9	5
C6	7.39	285	64	1.43	383	110	0.470	-1.50	0.9	82	1	78	9	5
C7	7.16	295	67	1.4	394	113	0.470	-1.54	0.7	71	0	35	7	4
C8	7.30	287	58	1.11	386	110	0.469	-1.61	0.8	86	12	42	7	3
C9	6.14	295	55	0.63	380	109	0.480	-1.48	1.2	48	0	54	14	1
C10	6.40	300	42	0.41	391	112	0.477	-1.57	0.8	67	0	32	12	0

Table 6.2: **Qubit parameters, and Decoherence rates (kHz).** The values of Δ,I_p, g and χ were extracted from fit of the data as described in the main text. We simulated the design of each qubit with the electrostatic simulator of COMSOL in order to obtain the geometric capacitance matrix of the system. This matrix was corrected according to the prescriptions described herein above. Then, we fitted the parameters E_J and α for each qubit assuming that the junctions have a capacitance per unit area $Cc = 100\,\text{fF}/\mu\text{m}^2$. The capacitance energy of the junctions is defined as $E_c = \frac{e^2}{2C_J}$. $\delta\Delta^{\text{geom}}$ is the difference between the value of the gap calculated with and without taking into account the geometric capacitance. As a rule of thumb, the geometric capacitance reduces the gap of the qubit by approximately 1-1.5 GHz. $\delta\Delta^{n_g}$is the charge modulation calculated for the fitted parameters E_J and α of each qubit. Measured relaxation rate Γ_1,calculated Purcell decay rate Γ_P, measured pure echo dephasing rate at optimal point Γ_{2E}^{ϕ}, calculated second order flux noise dephasing rate Γ_{2E}^{2nd}, calculated photon dephasing rate $\Gamma_{2E}^{\text{phot}} \approx 4\,\frac{(2\pi\chi)^2}{\kappa}\bar{n}_{thermal}\,(\bar{n}_{thermal}+1)$.

6.2 Tunable superconducting flux qubits with long coherence times

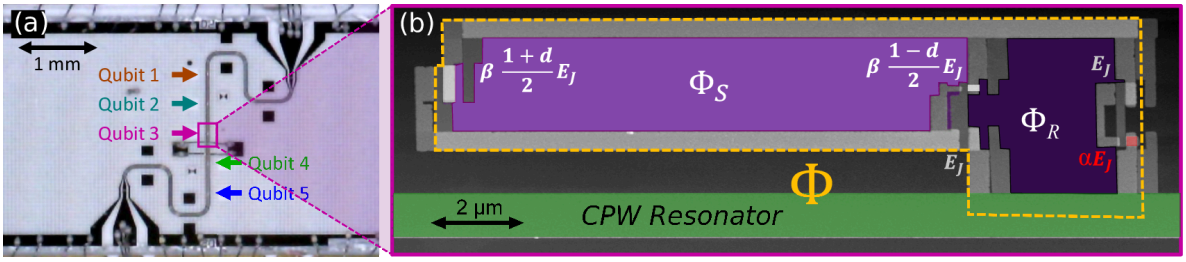

Figure 6.6: (a) Microscope picture of the sample, showing the coplanar waveguide resonator inductively coupled to five tunable flux qubits labelled according to their position on the resonator. The resonator is fabricated on a sapphire wafer by evaporation of a 150 nm- thick aluminum layer and UV lithography. (b) Colored atomic force micrograph of flux qubit 3. The qubit is galvanically coupled to the central conductor of the resonator (colored in green). It consists of two loops: The surface of the main loop is $S^{(3)}_{main} = 43.71\,\mu m^2$ while the surface of the SQUID loop is $S_{squid} = 30.82\,\mu m^2$ giving a ratio $\zeta^{(3)} = 0.705$. In our experimental setup, the magnetic field is applied uniformly such that the flux threading the SQUID loop is $\Phi_S = \zeta\Phi$ and $\Phi_R = (1-\zeta)\Phi$.

Here we study a series of tunable flux qubits inductively coupled to a coplanar waveguide resonator fabricated on a sapphire substrate. Each qubit includes an asymmetric superconducting quantum interference device which is controlled by the application of an external magnetic field and acts as a tunable Josephson junction. We replace one of the unitary junctions of the flux qubit by an assymmetric SQUID and study the controllability of the qubits and their coherence properties. The tunability of the qubits is $\pm 3.5\,GHz$ around their central frequency. The intrinsic relaxation rates are limited by dielectric losses in the substrate and can be as low as $\Gamma_{int} \sim 130\,kHz$ ($T_1 \sim 8\,\mu s$) while the pure echo dephasing rates at optimal points are limited by flux noise even at optimal points and are typically $\Gamma_{\varphi E} \sim 260 \pm 90\,kHz$ ($T^{\varphi}_{2E} \sim 4\,\mu s$). These decoherence rates are much smaller than the state of the art for tunable flux qubits [73, 111, 112]. We show that these decoherence rates are mostly limited by flux noise, even at optimal points. The sample studied in this work is presented in Fig.6.6. It is fabricated on a sapphire chip and contains a $\lambda/2$ aluminum coplanar waveguide (CPW) resonator with two symmetric ports for microwave transmission measurements. The resonator has a first resonant mode at $\omega_r/2\pi \sim 10.23\,GHz$ with quality factor $Q \sim 3500$. Five tunable flux qubits labelled according to their position on the resonator $i = \{1, ..., 5\}$ are galvanically coupled to the CPW resonator with coupling constant $\sim 120\,MHz$.

Fig.6.6b presents a colored atomic force micrograph (AFM) of one of these qubits. The circuit consists of two loops. The main loop indicated by a yellow dashed line is intersected by two identical Josephson junctions of Josephson energy E_J and one smaller junction colored in red of Josephson energy αE_J. The SQUID loop is intersected by two additionnal Josephson junctions of Josephson energy $\beta(1+d)E_J/2$ and $\beta(1-d)E_J/2$. Its surface is smaller than the main loop by a factor $\zeta \sim 0.7$.

6.2.1 Spectroscopic Measurements and fit to the model

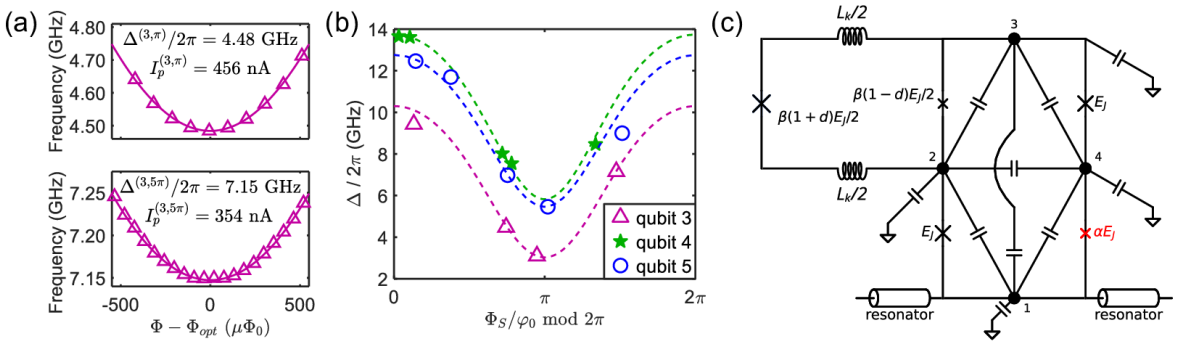

Figure 6.7: (a) Measured qubit frequency of qubit 3 versus Φ (magenta triangles) and fit (magenta curve) yielding the qubit parameters Δ and I_p at optimal points π and 5π. (b) Measured gaps of qubit 3 (magenta triangles), 4 (green stars) and 5 (blue circles) versus Φ_s/φ_0. The dashed curves are calculated for arbitrary values of Φ_S according to the model illustrated in (c) with fitting parameters E_J, α and d. (c) Flux qubit model including the kinetic inductance L_k and geometric capacitances. The island 1 is connected galvanically to the central conductor of the resonator.

The inductive energy of the circuit exhibits two local minima which correspond to a persistent current I_P flowing clockwise or anticlockwise in the main loop. These two minima become degenerate when the flux threading the main loop $\Phi = \Phi_\star$ is such that

$$\boxed{\frac{\Phi_\star}{\varphi_0} - \frac{\Phi_S}{2\varphi_0} + \delta\varphi = k\pi} \tag{6.1}$$

with $k = \pm 1, \pm 3, \pm 5...$ and $\tan\delta\varphi = d\tan\left[\frac{\Phi_s}{2\varphi_0}\right]$. At these *optimal* points, the two quantum states hybridise into symmetric and antisymmetric superpositions and give rise to an energy splitting $\hbar\Delta$ called the flux-qubit gap. In our experimental setup, the magnetic field is applied uniformly such that the flux threading the SQUID loop is $\Phi_S = \zeta\Phi$. One can therefore solve Eq.6.1 and get the values of the fluxes $\Phi_\star$ and Φ_S at each optimal point. For different values of k, the value of the effective Josephson energy of the SQUID changes according to Eq.3.19 and consequently, the value of the gap of each qubit depends on k. In the following, the gap of qubit i at each optimal point will be denoted as $\Delta^{(i,k\pi)}$ and its associated persistent current as $I_P^{(i,k\pi)}$.

Fig.6.7a shows the frequency dependence of qubit 3 on Φ around the π and 5π optimal points. The transition frequency of the qubit around each optimal point follows $\omega_{ge} = \sqrt{\Delta^2 + \varepsilon^2}$ with $\varepsilon = 2I_P(\Phi - \Phi_\star)/\hbar$, yielding $\Delta^{(3,\pi)}/2\pi = 4.48\,\text{GHz}$, $I_P^{(3,\pi)} = 456\,\text{nA}$ and $\Delta^{(3,5\pi)}/2\pi = 7.15\,\text{GHz}$, $I_P^{(3,5\pi)} = 354\,\text{nA}$. We repeat this procedure for the five qubits at their respective optimal points $\pm\pi, \pm 3\pi, \pm 5\pi, \pm 7\pi, \pm 9\pi$ (See Tab.6.3).

		π	$3\,\pi$	$5\,\pi$	$7\,\pi$	$9\,\pi$	Units
qubit 1	$\Delta/2\pi$	7.30	12.16	8.15	6.05	11.96	GHz
	I_P	376	230	342	401	230	nA
	$\chi/2\pi$	5.05	-5.93	6.37	3.16	-6.26	MHz
qubit 2	$\Delta/2\pi$	6.84	12.82	9.82	5.60	11.91	GHz
	I_P	388	238	282	440	263	nA
	$\chi/2\pi$	3.61	-4.31	33.1	3.41	-4.31	MHz
qubit 3	$\Delta/2\pi$	4.48	9.43	7.15	3.10	NaN	GHz
	I_P	457	289	354	NaN	NaN	nA
	$\chi/2\pi$	2.85	16.3	5.65	3.06	NaN	MHz
qubit 4	$\Delta/2\pi$	8.02	13.65	8.46	7.54	13.61	GHz
	I_P	365	224	353	341	246	nA
	$\chi/2\pi$	8.86	-4.66	11.3	8.21	-4.05	MHz
qubit 5	$\Delta/2\pi$	6.98	12.46	9.00	5.46	11.69	GHz
	I_P	392	254	332	444	NaN	nA
	$\chi/2\pi$	2.83	-4.08	6.48	NaN	-4.23	MHz

Table 6.3: Qubit Parameters: Δ, I_P and the dispersive shift of the resonator χ.

Fig.6.7b presents the gaps of qubits 3, 4 and 5 versus Φ_s/φ_0. This data together with the persistent currents obtained for each optimal point enables us to fit parameters of the model shown in Fig.6.7c. In this model, the qubit consists of two superconducting loops intersected by five Josephson junctions. Each Josephson junction is characterized by its Josephson energy E_J and its bare capacitance energy $E_C = e^2/2C_J$. The junctions divide the loops into four superconducting islands. Each island is capacitively coupled to its surrounding by geometric capacitances. These geometric capacitances are calculated using the electrostatic module of COMSOL (see section 3.1.3). They reduce the gaps of the qubits by approximately $\sim 1\,\mathrm{GHz}$ but barely modify their persistent currents.

Qubit #	E_J (GHz)	E_J/E_C	α	d	ζ	$\sqrt{A_R A_S}$ ($\mu\Phi_0$)
1	550	318	0.429	0.759	0.696	2.2
2	558	323	0.426	0.715	0.687	2.6
3	559	323	0.442	0.711	0.705	2.3
4	518	300	0.421	0.707	0.677	2.3
5	563	326	0.426	0.740	0.714	3.0

Table 6.4: Parameters of the qubits. The charging energy is fixed at $E_C = 1.73\,\mathrm{GHz}$ assuming a specific capacitance of the junction $C/A = 100\,\mathrm{fF\,\mu m^{-2}}$. The ratio ζ is measured by AFM. The value $\beta = 2.11$ is taken according to room temperature measurements. The inductance $L_k = 72.5\,\mathrm{pH}$ is determined according to the resistance measurement of wires at low temperatures. The value of E_J, d and α are obtained by fit with the model shown in Fig.6.7c. The amplitude of the flux noise $\sqrt{A_R A_S}$ is extracted for each qubit from the dependence of $\Gamma_{\varphi E}$ versus ε.

It is also neccessary to take into account the kinetic inductance of the SQUID loop in order to match the parameters of the model with the experimental results. The kinetic inductance is estimated

by measuring the resistance of evaporated aluminum wires at low temperature and is added in our model as a renormalization of the large Josephson junction of the SQUID described in section 3.2.2. We summarize the results of the fits in Tab.6.4. These values are in good agreement with the measured values of α, d and E_J extracted from room temperature resistance measurements (see 4.15 on page 93).

6.2.2 Decay times

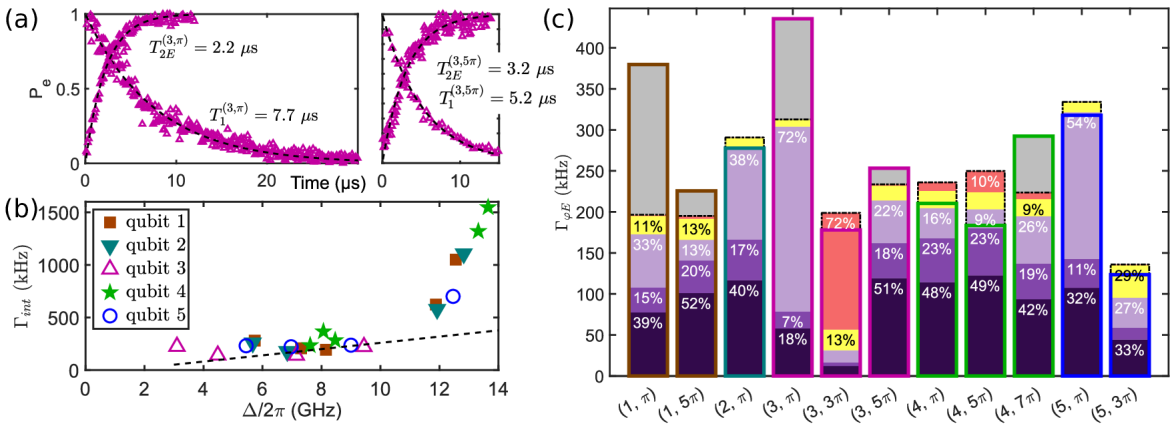

Figure 6.8: (a) Energy relaxation and spin-echo measurements of qubit 3 at optimal points π and 5π. (b) Intrinsic relaxation rates Γ_{int} versus Δ. The dashed line corresponds to calculated dielectric losses in the substrate assuming $\tan\delta = 5 \times 10^{-5}$. (c) Stacked bar chart showing the measured pure echo dephasing rates $\Gamma_{\varphi E}^{(i,k\pi)}$. The calculated contributions to dephasing are represented in different colors: flux noise (purple), critical current noise Γ_α (yellow) and photon noise Γ_{phot} (red). The flux noise dephasing can be separated into first order flux noise in the qubit loop Γ_R (dark purple), first order flux noise in the SQUID loop Γ_S (purple) and second order effects Γ_{2nd} (light purple). The total $\Gamma_{tot} = \sqrt{\Gamma_R^2 + \Gamma_S^2 + \Gamma_{2nd}^2 + \Gamma_\alpha^2 + \Gamma_{\text{phot}}^2}$ is represented as a dot-dashed black segment. For each contribution $X \in \{R, S, 2nd, \alpha, \text{phot}\}$, the percentage indicated in the relevant colored stack represents $\Gamma_X^2/\Gamma_{tot}^2$.

The change of the gap modifies the relaxation rate. For illustration, we represent in Fig.6.8a the energy relaxation decay of qubit 3 at two different optimal points. The decay is exponential in both cases but the relaxation times are different, namely $T_1^{(3,\pi)} = 7.7\,\mu s$ and $T_1^{(3,5\pi)} = 5.2\,\mu s$. Several mechanisms may give rise to such a phenomenon; among them, Purcell effect. The Purcell rate Γ_P is quantitatively determined by measuring the qubit Rabi frequency ω_r for a given microwave power P_{in} at the resonator input [70]. This enables us to analyze and compare the intrinsic relaxation rates defined as $\Gamma_{int} = \Gamma_1 - \Gamma_P$ of all the qubits at various optimal points. Such an analysis shows that qubit 3 has approximately the same intrinsic relaxation rate at optimal points π and 5π.

Fig.6.8b unveils a general behavior of intrinsic relaxation rates versus frequency. Previous measurements of flux qubits [70] identified dielectric losses in the substrate as a major contributor to relaxation at low temperature [105]; using the approach of Ref.[70] and a loss tangent of 5×10^{-5}, we obtain the dashed line in Fig.6.8b. Clearly dielectric losses account for most of the relaxation at

intermediate frequencies but cannot explain the increased relaxation rates at high frequencies when the flux in the SQUID Φ_S/φ_0 is close to 2π. A second source of losses could be quasiparticle tunneling [113, 114, 115]. A single quasiparticle trapped in one of the large qubit islands would lead to a relaxation rate larger than what is observed, at least at low frequencies, as well as to non-exponential decay due to fluctuations in the number of trapped quasiparticles [116, 117]. Alternatively, quasiparticles can reach the qubits from the CPW resonator. However, a relatively high normalized quasiparticle density, corresponding to an effective quasiparticle temperature of order 150mK, would be needed to explain a decay rate of the order of tens of kHz. Therefore we conclude that quasiparticles do not significantly account for relaxation and cannot explain explain the residual decay rate observed at high frequencies.

		π	$3\,\pi$	$5\,\pi$	$7\,\pi$	$9\,\pi$	Units
qubit 1	Γ_1	236	1073	271	296	647	kHz
	Γ_P	28	23	77	14	23	kHz
	Γ_{int}	208	1050	194	282	624	kHz
qubit 2	Γ_1	194	1141	NaN	268	625	kHz
	Γ_P	16	34	NaN	9	47	kHz
	Γ_{int}	178	1107	NaN	259	578	kHz
qubit 3	Γ_1	142	373	185	225	NaN	kHz
	Γ_P	1	151	45	0	NaN	kHz
	Γ_{int}	141	222	140	225	NaN	kHz
qubit 4	Γ_1	446	1858	341	298	1568	kHz
	Γ_P	79	310	58	62	248	kHz
	Γ_{int}	367	1548	283	236	1320	kHz
qubit 5	Γ_1	236	709	298	236	NaN	kHz
	Γ_P	14	8	60	5	NaN	kHz
	Γ_{int}	222	701	238	231	NaN	kHz

Table 6.5: Relaxation Rates: measured relaxation rate Γ_1, estimated Purcell rate Γ_P, and the estimated intrinsic rate $\Gamma_{int} = \Gamma_1 - \Gamma_P$.

6.2.3 Dephasing due to Flux noise

At their respective optimal points, the amplitude of the spin-echo signal shown in Fig.6.8a decays with pure dephasing times $T_{\varphi E}^{(3,\pi)} = 2.6\,\mu s$ and $T_{\varphi E}^{(3,5\pi)} = 4.6\,\mu s$. In Fig.6.8c, we present a stacked bar chart showing the measured pure echo dephasing rates at various optimal points and the different contributions of flux noise, critical current noise, charge noise, and photon noise[22]. The dephasing due to photon noise (represented in red) has been estimated by measuring the dispersive shifts at optimal points and by estimating the number of thermal photons in the resonator [64]. It is the dominant dephasing mechanism for $(3, 3\pi)$ since at that point the qubit gap happens to be very close to the resonator transition. The contribution of charge noise is strongly reduced by the ratio $E_J/E_C \sim 300$

[22]For simplicity, we use the 2-norm. This allows us to be able to compare easily the relative ratios of contributions

and was found to be always completely negligible ($< 1\,\mathrm{kHz}$). We also considered critical current fluctuations in the α junction assuming $S_{I_\alpha}(\omega) = A_{I_\alpha}^2 / |\omega|$, with $A_{I_0} \sim 0.1\,\mathrm{pA}$ [106, 107], and found an approximately constant contribution of $\sim 70\,\mathrm{kHz}$ (represented in yellow in Fig.6.8c). The flux noise shown in purple represents the main source of dephasing of the qubits even at optimal points.

Away from their optimal points, the decoherence of flux qubits is known to be governed by flux noise [65, 67, 68]. The flux noise power spectrum $S_\Phi(\omega) = A_\Phi^2 / |\omega|$ implies that the pure echo dephasing rate is given by $\Gamma_{\varphi E}^{\Phi} = A_\Phi \sqrt{\ln 2}\, |\partial\omega_{ge}/\partial\Phi|$ with $|\partial\omega_{ge}/\partial\Phi| \simeq 2\, I_P\, |\varepsilon| / \hbar\Delta$ [82]. At the optimal points, $\varepsilon = 0$ and thus this decoherence mechanism should be cancelled. Yet, contrary to *standard* flux qubits, our design contains two independent degrees of freedom (Φ_S, Φ_R) [111]. These degrees of freedom add σ_z components in the Hamiltonian of the system, namely $H = \hbar\frac{\Delta}{2}\sigma_z + (I_{z,S}\delta\Phi_S + I_{z,R}\delta\Phi_R)\,\sigma_z$ (See 3.5.4). Thus, even at optimal point where $I_{z,S}\zeta + I_{z,R}(1-\zeta) = 0$, $\partial\omega_{ge}/\partial\Phi_{S/R} \neq 0$ will give first order contributions to dephasing:

$$\Gamma_{S/R} = 2\sqrt{\ln 2}\frac{I_{z,S/R} A_{S/R}}{\hbar} \tag{6.2}$$

For each qubit, we measure $\Gamma_{\varphi E}$ versus ε and extract the apparent flux noise amplitude A_Φ around each optimal point. The amplitudes $A_{S/R}$ of the flux noise in the different loops can be directly extracted from A_Φ and from the ratio $\gamma = \sqrt{P_S/P_R}$ where P_S and P_R are the perimeters of the two loops [75]. As expected, we find that A_S and A_R do not change significantly for the different optimal points of a given qubit and thus $\sqrt{A_S A_R}$ is a good indicator of flux noise in each qubit (See Tab.6.4). A more rigorous derivation of flux noise contributions including second order effects is given in 3.5.4. We find that such effects can be also significant as shown in Fig.6.8c.

In Fig.6.9b, we represent the calculated contributions of first and second order flux noise to the dephasing rates for qubits 3 and 4 at optimal point when the flux Φ_S/φ_0 is varied between 0 and 2π. The first order contributions are cancelled when the $\partial_{\Phi_S}\omega_{ge} = 0$ and reach a maximum of around 200 kHz approximately. The second order contributions are small for large gap and tend to become dominant when the flux qubit gap is small.

6.2.4 Conclusion

In conclusion, we have shown that it is possible to control the gap of flux qubits by using an asymmetric SQUID. This method mitigates the decoherence due to flux noise in the SQUID loop while keeping a tunability range of $\pm 3.5\,\mathrm{GHz}$. It should be possible to improve further the coherence properties of the qubits by reducing the persistent currents down to 200 nA and by exchanging the locations of the small and large junctions of the SQUID. This exchange will further reduce the tunability of the qubit to the level of $\pm 500\,\mathrm{MHz}$ and thus decrease the pure dephasing rates related to the presence of the SQUID. According to our simulations, the dephasing rate due to flux noise should then be comprised between 15 and 100 kHz.

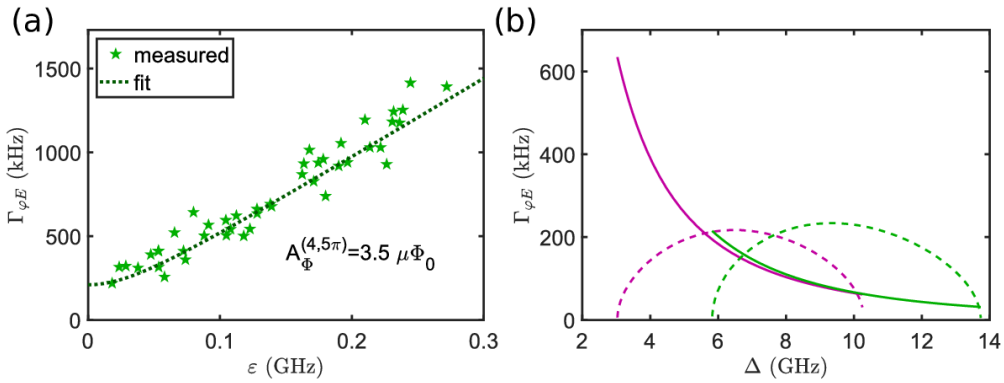

Figure 6.9: (a) Measured pure dephasing rate $\Gamma_{\varphi E}^{(4,5\pi)}$ versus ε. We extract the apparent flux noise amplitude from the slope of the graph using Eq.3.77. (b) Calculated contribution of first (dashed line) and second order (solid line) flux noise to the dephasing rates for qubits 3 (magenta) and 4 (green) at optimal point. The curves are calculated for arbitrary values of Φ_S while keeping the qubit at its optimal point.

6.3 Bragg Filter resonators

As explained in 2.1.3, we would like to apply a DC voltage on the central conductor of the coplanar waveguide in order to overcome the Schottky potential arising from the Si/Al interface. To this end, the most elegant solution is to replace one of the termination of the CPW resonator by a Bragg Filter (BF). In the following, we will briefly describe preliminary results concerning design and measurements of these resonators.

6.3.1 Considerations for designing a Bragg Filter termination

We follow the theoretical guidelines of section 3.3.3. The main considerations of the design are the following:

At resonance, the transmission is 100%. This condition allows for having a good signal to noise ratio for qubit measurements. This is achieved by matching the transmission modulus of the Bragg Filter and the coupling capacitor $|t_C(\omega_r)| = |t_{\text{Bragg}}(\omega_r)|$. To achieve this, we can either modify the period length L_{BF} of the filter (shifting ω_c), control the ratio between impedances Z_h/Z_l) and/or modify the number of segments n.

In Fig.6.10, we show $|t_{\text{Bragg}}(\omega)|$ assuming $n = 11$ segments, $L_{\text{BF}} = 3.44\,\text{mm}$ corresponding to $\omega_c/2\pi = \frac{c}{4L_{\text{BF}}} = 8.33\,\text{GHz}$ and $Z_h/Z_l = 2.3$. The first inner segment of the Bragg Filter is chosen to have high impedance $Z_h > Z_0$. The transmission $|t_C(\omega)|$ of the capacitor is calculated for $C_c = 6.6\,\text{fF}$.

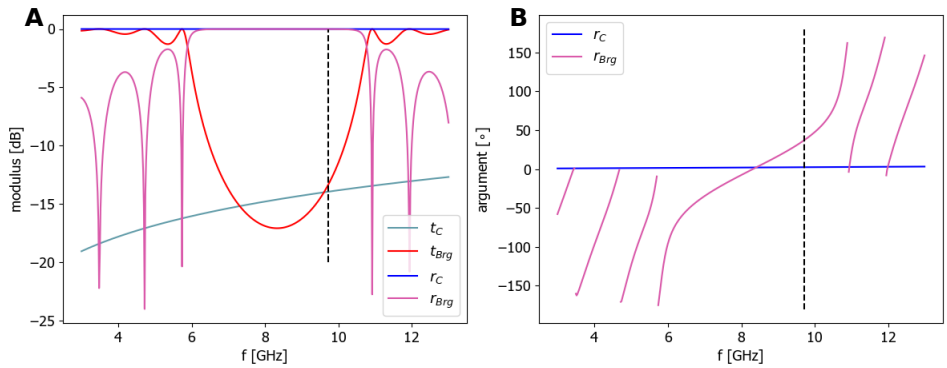

Figure 6.10: **The coefficients of reflection and transmission of Bragg and capacitor terminations versus the frequency. A.** Modulus in dB. **B.** Argument in degree of the reflection coefficients. The resonance frequency of the resonator (shown in dashed) is chosen to be 9.8 GHz such that $|t_C| = |t_{\text{Bragg}}|$, at that point the phase of the BF is non-zero $\arg(r_{\text{Bragg}}) = 37°$.

Fixing the resonance of the CPW resonator at ω_r. In a CPW resonator of length L with symmetrical terminations (see Eq.3.43), the resonance factor R is given by:

$$R(\omega) = \sum_j \left(r^2(\omega) e^{i2\omega L/c}\right)^j = \frac{1}{1 - r^2(\omega) e^{ie^{i2\omega L/c}}}$$

At resonance, the factor $r^2(\omega) e^{i2\omega L/c}$ should be a positive real number. When the termination is a capacitor, the imaginary part of $r(\omega)$ is negligible and thus the resonance frequency is given by

$$\omega_r = \frac{\pi}{L} c$$

Contrary to a standard capacitor terminated CPW resonator, the imaginary part of the reflection coefficient of a Bragg Filter is *not* zero (see Fig.6.10). The resonance factor becomes

$$R(\omega) = \frac{1}{1 - r_C(\omega) r_{\text{Bragg}}(\omega) e^{i2\omega L/c}} \tag{6.3}$$

The accumulated phase $\varphi_{acc}(\omega) = \arg\left(r_C(\omega) r_{\text{Bragg}}(\omega) e^{i2\omega L/c}\right)$ should be equal to 0 modulo 2π at the resonance. This is mainly adjusted by the length L of the central segment between the Bragg Filter and the coupling capacitor. We calculate numerically the $\arg(r_{\text{Bragg}}(\omega))$ by chaining interfaces and segments according to 3.3.2 and show it in Fig.6.10B.

In the case of a standard capacitor terminated CPW resonator, the accumulated phase is a linear function exactly

$$\varphi_{acc}(\omega) = 2\pi \frac{\omega}{\omega_r}$$

As for the resonator with Bragg-filter terminations, the function is no longer linear. In the vicinity of the resonance frequency, one can describe it as

$$\varphi_{acc}\left(\omega_r+\delta\omega\right)=2\pi\gamma\frac{\delta\omega}{\omega_r}\mod 2\pi \tag{6.4}$$

In our design, we get $\gamma=1.80>1$. In other words, the round trip travel time $\tau=2\pi\partial_\omega\varphi_{acc}\left(\omega_r\right)$ for a quanta of energy can be longer than both the period $2\pi/\omega_r$ and the round trip time between the two terminations $2L/c$. The Bragg filter has a non-zero dwell time for the quanta of energy. EM waves propagate into the Bragg Filter as an evanescent wave, before reflecting the energy back. Thus we will achieve a higher quality factor- by a factor γ- despite keeping the same capacitor as before and matching the transmission of both terminations at ω_r.

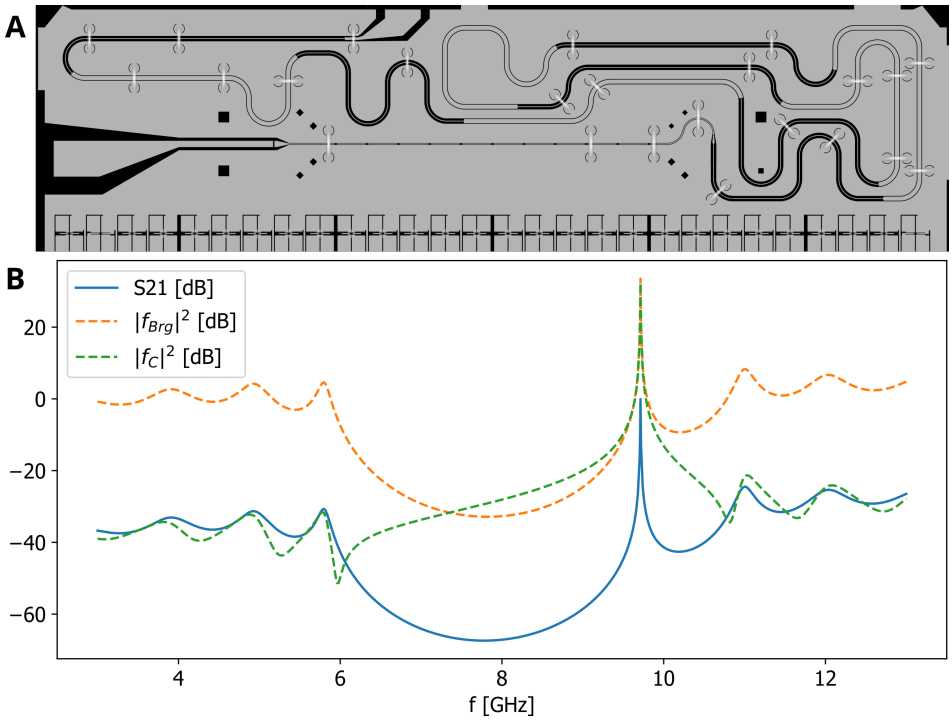

Figure 6.11: **A.** We show the design of the resonator, with wirebonding. **B.** Simulation using the filter formalism (see section 3.3.2), showing the transmission S21 in decibels (solid lines), and the filter function modulus $|f^{\rightarrow}\left(\omega\right)|^2=|f_C\left(\omega\right)|^2$ in decibels (orange dashed), and $|f^{\leftarrow}\left(\omega\right)|^2=|f_{\text{Bragg}}\left(\omega\right)|^2$ in decibels (green dashed).

Relaxation of qubits due to Purcell rate. The Purcell relaxation of a flux qubit situated at a frequency of 7.4 GHz should be controlled and limited. From Eq.3.60, we can establish that the Purcell rate of the left and right ports depends on the filter function modulus $\Gamma^{\rightarrow/\leftarrow}\propto\left|f_{\rightarrow/\leftarrow}\left(\omega_{ge},x\right)\right|^2$ where

$$\begin{aligned}
|f_{\rightarrow}\left(\omega_{ge},x\right)|=|f_C\left(\omega_{ge},x\right)|&=\left|\frac{t_C\left(\omega_{ge}\right)\left(e^{\boldsymbol{i}kx}-r_{\text{Bragg}}\left(\omega_{ge}\right)e^{\boldsymbol{i}k(2L-x)}\right)}{1-|r_C\left(\omega_{ge}\right)|\,|r_{\text{Bragg}}\left(\omega_{ge}\right)|\exp\left(\boldsymbol{i}\varphi_{acc}\left(\omega_{ge}\right)\right)}\right| \\
|f_{\leftarrow}\left(\omega_{ge},x\right)|=|f_{\text{Bragg}}\left(\omega_{ge},x\right)|&=\left|\frac{t_{\text{Bragg}}\left(\omega_{ge}\right)\left(e^{\boldsymbol{i}k(L-x)}-r_C\left(\omega_{ge}\right)e^{\boldsymbol{i}k(L+x)}\right)}{1-|r_C\left(\omega_{ge}\right)|\,|r_{\text{Bragg}}\left(\omega_{ge}\right)|\exp\left(\boldsymbol{i}\varphi_{acc}\left(\omega_{ge}\right)\right)}\right|
\end{aligned} \tag{6.5}$$

ω_{ge} being the frequency of the qubit, and $x \in [0, L]$ its position in the resonator assuming the capacitor termination is on the left side.

As shown in Fig.6.10, $|t_{\text{Bragg}}|$ depends strongly on ω, contrary to $|t_C|$which remains relatively stable. To make sure that the qubit is well protected, we design the bragg filter such that its band cut minimum is deep enough and its band cut center is close to the qubit frequency. This is principally adjusted by the ratio of impedances Z_h/Z_l and the number of segments n. On the other side, the factor $|f_C|$ remains comparable to a standard CPW resonator with capacitor terminations. Indeed, the modulus of the resonance factor $|R|$ is close to 1 when out of resonance ($|\varphi_{acc}(\omega)|$ of order 45°).

Taking into account the above considerations, and a design is reached as shown in Fig.6.11.

6.3.2 Characterizing experimentally BF resonators

We characterize the BF-terminated resonators using the experimental setup depicted in Fig.6.12. The main advantage of this setup is that both the transmission (Bragg-in-capacitance-out) and reflection (capacitance-in-capacitance-out) could be easily compared. Indeed, as mentioned already, away from resonance, R is of order of magnitude 1 and thus $t_C^2 R$ cannot interfere with the quasi-full reflection of the capacitance. We may interpolate the reflected power measured on a Vector Network Analyzer to resonant regions which serves as a 0 dB reference for the transmission. We therefore dis-embed all attenuation/amplification in the transmission lines.

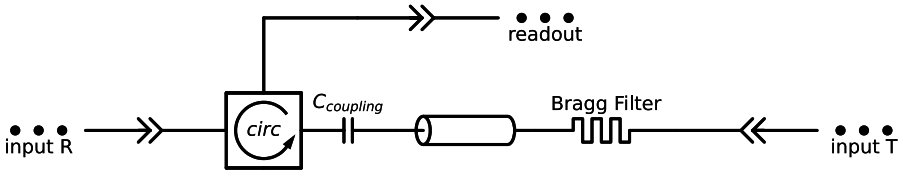

Figure 6.12: Experimental Setup for auto-calibrating the power

A first test sample is measured without the presence of flux qubits, and we fully bond the ground planes along the Bragg and the inter-region (position L,C,R in the L'-long inter regions in Fig.6.14). This reference measurement (see Fig.6.13) shows that the filtering effect is compatible with theory (see Fig.6.11). The *primary*[23] resonance occurs at 10.182 GHz exactly in accordance with the design specs $\approx$ 10 GHz. A mere -2 dB was observed with respect to the reflection signal. Stray resonances appear around 10.7 GHz, with peak transmission at -10 dB and at 11.7 GHz with a peak transmission of -5 dB. These resonances could match with the one calculated (11 GHz and 12 GHz) shown in Fig.6.11.

[23] as opposed to strays that are unintentional

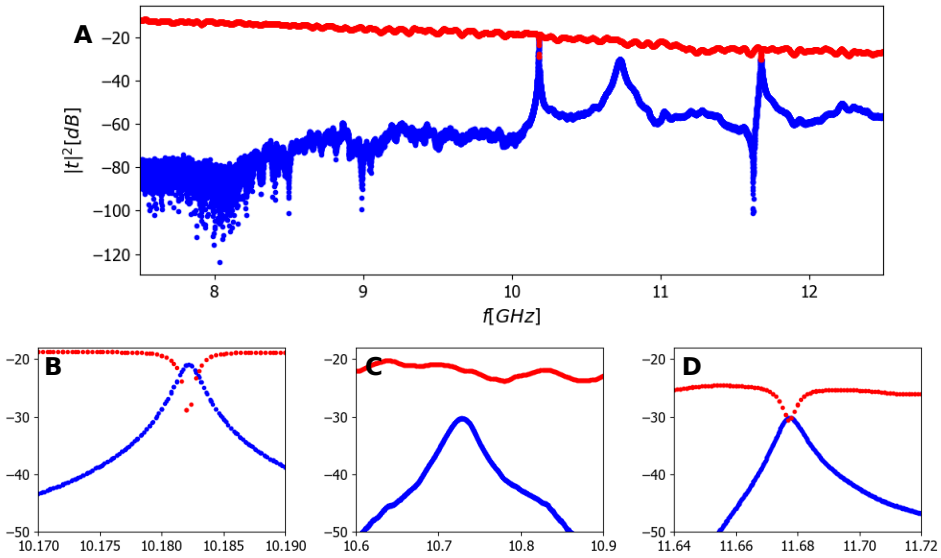

Figure 6.13: **Reference measurement A.** Transmission (blue) and reflection (red) **B-D.** Zooms around local resonances

6.3.3 Wire bonding strategy preventing Meissner Loops

It is good practice to bond-wire the two ground plane along the resonator to prevent any unintentional resonances. These bonds may complete loops where Meissner current can flow. In Fig.6.14, we give two examples of continuous conductive loops (purple dashed lines circling green regions) that form from these bondings. It is difficult to vary the total magnetic flux inside these regions because a counter current canceling out the external field may arise in this loop due to the Meissner effect giving rise to strong magnetic hysterisis. Thus, it is difficult to bias flux qubits to their optimal points in such regions. As a rule of thumb for our design, we ensure that hypothetical magnetic vortices may travel from the external boundaries to regions of the flux qubit along a continuous path in non-metallic regions, without ever crossing over wire-bonds.

Taking into account the above considerations, we leave unbonded the positions L and C, as shown in Fig.6.14. We observe an additional stray resonance at 9.7 GHz that was not anticipated by our model. This stray resonance may be due to other modes of the resonator released due to the absence of constraints.

6.3.4 Stray resonances and photon noise

Asymmetry factor Let us now try to understand the impact of such stray modes. We treat the stray mode exactly as we would treat the principal mode. Let us now consider a resonant mode at ω_s with linewidth ω_s/Q and with power transmission T (measured in dB), assumed to be without internal losses. We describe the mismatch between the power transmission at resonance of the two

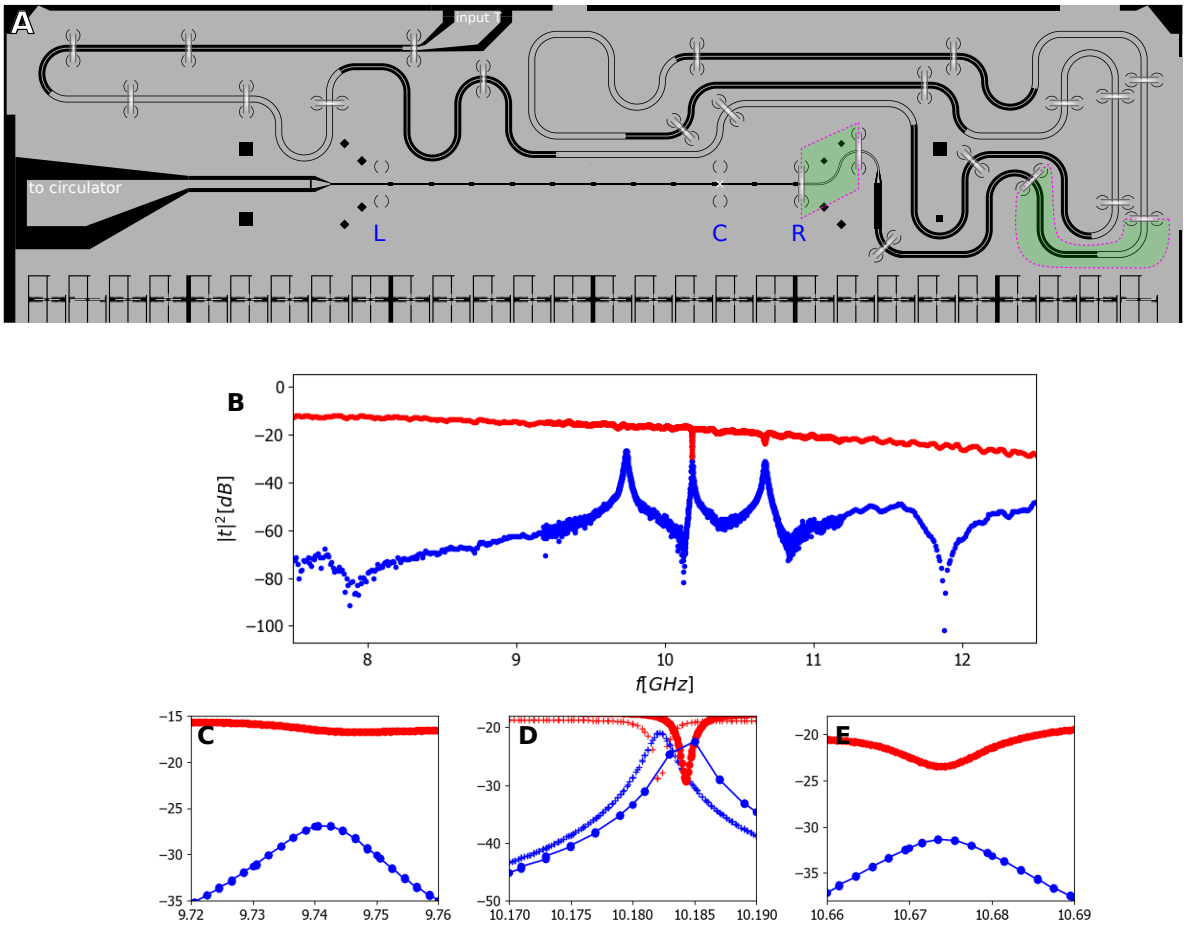

Figure 6.14: **Wire bonding induced Meissner Loops. A.** The case where position L and C are left unbonded is shown. The green dashed zones delimit two (non-exhaustive) examples of Meissner Loops closed by wire bonding (white shadows), where the magnetic field may not penetrate into. Bonding of site L and/or C would give rise to Meissner Loops covering the qubits, preventing them from reaching their optimal points. **B.** We show the corresponding transmission and reflection measurements and their zooms (**C.-E.**), in **D.** we also plot the values in the reference measurement (unconnected cross)

ports $|t_C(\omega_s)|^2$ and $|t_{\text{Bragg}}(\omega_s)|^2$ by an asymmetry factor $\alpha \in [-1,1]$, writing

$$\begin{aligned} |t_C(\omega_s)|^2 &\equiv |\bar{t}|^2 (1+\alpha) \\ |t_{\text{Bragg}}(\omega_s)|^2 &\equiv |\bar{t}|^2 (1-\alpha) = \frac{1-\alpha}{1+\alpha} |t_C(\omega_s)|^2 \end{aligned} \tag{6.6}$$

In this parametrization, the resonance factor depends solely on the average power transmission coefficient $|\bar{t}|^2$

$$\begin{aligned} R(\omega) &= \frac{1}{1 - |r_C(\omega)|\,|r_{\text{Bragg}}(\omega)| \exp(\boldsymbol{i}\varphi_{acc}(\omega))} \\ &\approx^{(\star)} \frac{1}{1 - \left(1 - \frac{1}{2}|\bar{t}|^2(1+\alpha)\right)\left(1 - \frac{1}{2}|\bar{t}|^2(1-\alpha)\right) \exp(\boldsymbol{i}\varphi_{acc}(\omega))} \\ &= \frac{1}{|\bar{t}|^2 - \boldsymbol{i}\varphi_{acc}(\omega)} \end{aligned}$$

where we apply in $(\star)$ the approximation $|r| = \sqrt{1-|t|^2} \approx 1 - \frac{|t|^2}{2} + \mathcal{O}\left(|t|^4\right)$, which gives us

$$\begin{aligned} T &= \left| \frac{t_C(\omega_s)\, t_{\text{Bragg}}(\omega_s)}{1 - |r_C(\omega_s)|\,|r_{\text{Bragg}}(\omega_s)|} \right|^2 \\ &\approx \left| \frac{|\bar{t}|^2 (1+\alpha)(1-\alpha)}{|\bar{t}|^2} \right|^2 = \left(1-\alpha^2\right)^2 \end{aligned} \tag{6.7}$$

An incomplete transmission thus gives us access to the modulus of the asymmetry factor $|\alpha|$. Recall that this may be measured with good precision by comparing against the (interpolated) reference reflection from the capacitor (see Fig.6.12).

We may also apply Eq.6.7 to the principal resonance. Assuming no internal loss, the corresponding asymmetry factor is estimated to be $|\alpha| \sim 0.45$. This asymmetry could be due to the BF transmission coefficient being highly sensitivity to design/fab inaccuracies as n becomes large (see Eq.3.54). It may also be an overestimation if internal losses are non negligible.

Photon noise To check the photon noise dephasing rate, let us recall the expression in 3.5.5

$$\Gamma_{\text{phot}} \approx \frac{4\chi^2}{\kappa} \langle a^\dagger a \rangle$$

where $\chi \approx g^2/\delta$ is the dispersive shift (cf section 3.3.4), and κ is the energy loss rate. We verify that the linewidth is equivalent to κ, even after taking into account the lengthening of the round trip. Indeed,

we establish from the dependency of the resonance factor R (Eq.6.3) an expression for the linewidth

$$\begin{aligned}\Delta\omega \equiv \omega_s/Q &\equiv \text{FWHM} \\ &= \overbrace{2}^{\text{FW}} \cdot \overbrace{\varphi_{acc}^{-1}\left(|\bar{t}|^2\right)}^{\text{HM}} = 2\frac{\omega_s |\bar{t}|^2}{2\pi\gamma}\end{aligned} \tag{6.8}$$

We show that an identical expression for the energy loss rate κ can be obtained. We write κ as a product of the round trip frequency and the energy ratio lost per round trip

$$\begin{aligned}\kappa &= \left[|\bar{t}|^2(1+\alpha) + |\bar{t}|^2(1-\alpha)\right]\frac{\omega_s}{2\pi\gamma} = \frac{\omega_s}{\pi}\frac{|\bar{t}|^2}{\gamma} \\ Q &= \frac{\pi\gamma}{|\bar{t}|^2}\end{aligned}$$

Let us now consider the coupling constant between the flux qubit and these stray modes, since it intervenes in $\chi \approx g^2/\delta$. We can verify inside the integral of Eq.3.50 that for $\omega \approx \omega_s$,

$$\begin{aligned}&|f_{\rightarrow}|^2(\omega,x) + |f_{\leftarrow}|^2(\omega,x) \\ \approx^{(\star 1)}\ &\frac{|\bar{t}|^2\left|e^{\boldsymbol{i}kx} - e^{-\boldsymbol{i}kx}\right|^2\left[(1+\alpha)^2 + (1-\alpha)^2\right]}{\left|1 - |r_C(\omega_s)|\,|r_{\text{Bragg}}(\omega_s)|\exp\left(\boldsymbol{i}\varphi_{acc}(\omega)\right)\right|^2} \\ \approx^{(\star 2)}\ &\frac{1}{1+\left(\frac{\omega-\omega_s}{\Delta\omega/2}\right)^2}\frac{2\left(2\sin\frac{kx}{2}\right)^2\left(1+\alpha^2\right)}{|\bar{t}|^2}\end{aligned}$$

where $(\star 1)$ expands the numerator using Eq.6.5, Eq.6.6, and the resonance condition rewritten as

$$\begin{aligned}\varphi_{acc}(\omega) \approx \varphi_{acc}(\omega_s) = \cancelto{\approx 0}{\arg(r_C)} + \arg(r_{\text{Bragg}}) + 2kL = 0 \mod 2\pi \\ \arg\left(r_C e^{\boldsymbol{i}k(2L-x)}\right) \approx -kx \\ k \equiv \omega_s/c\end{aligned}$$

and where $(\star 2)$ expands the denominator using $|r| \approx 1 - \frac{|t|^2}{2}$, $\exp\left(\boldsymbol{i}\varphi_{acc}(\omega)\right) \approx 1 + \boldsymbol{i}\gamma(\omega-\omega_s)/\omega_s$, and Eq.6.8. The integration yields

$$\begin{aligned}\int |f(\omega)|^2 + |f_{\text{Bragg}}(\omega)|^2 &= (\pi\cdot\Delta\omega/2)\cdot\frac{2\left(2\sin\frac{kx}{2}\right)^2\left(1+\alpha^2\right)}{|\bar{t}|^2} \\ &= \frac{\omega_s}{\gamma}\left(1+\alpha^2\right)\left(2\sin\frac{kx}{2}\right)^2\end{aligned}$$

which finally gives

$$\begin{aligned}\hbar g &= MI_p\sqrt{\frac{\hbar\omega_s}{4\pi Z_0\gamma}\int |f_C(\omega)|^2 + |f_{\text{Bragg}}(\omega)|^2} \\ &= MI_p\omega_s\sqrt{\frac{\hbar(1+\alpha^4)}{\pi Z_0\gamma}}\,|\sin(kx/2)| \end{aligned} \tag{6.9}$$

As a sanity check, Eq.6.9 is in agreement with Eq.3.35 for the limit $\alpha \to 0$ and $\gamma \to 1$. The physical significance behind this is that the Bragg Filter increases the overall mode volume and dilutes the quantum fluctuations inside the resonator, leading to less coupling strength.

$$g \propto \sqrt{\frac{1}{\gamma}} \tag{6.10}$$

Injecting into the the expression of Γ_{phot}, we establish that the dependencies of photon noise on unfixed factors are

$$\Gamma_{\text{phot}} \propto \chi^2/\kappa = \left(\frac{MI_p\omega_s}{\hbar}\sqrt{\frac{\hbar(1+\alpha^2)}{\pi Z_0\gamma}}\,|\sin(kx/2)|\right)^4 /\delta^2\Delta\omega \propto \frac{\left(1+\alpha^4\right)^2}{\gamma^2\Delta\omega}$$

where the dependency on $\alpha \in [-1,1]$ is limited $\left(1+\alpha^2\right)^2 \in [1,4]$. In Fig.6.14C/E, the two peaks are around $-12\,\text{dB}$ from the reflected reference, for which $\alpha \approx 0.71$, which yields $\left(1+\alpha^2\right)^2 = 2.26$ (compared to 1.44 for the principal resonance). By assuming that the dwell time in the BF is non-negative (for causality reasons), we may establish that γ obeys $\gamma \geq \gamma_{L'} \sim 1$. Typically, for stray resonances to occur, the winding number is added in a small frame of frequency, resulting in large γ, before returning back to the steady increase. Consequently, this has the tendency to lower Γ_{phot} for stray modes. The dominant dependency of Γ_{phot} due to the introduction of the BF is $\Delta\omega$. We verify that in our samples, the broad linewidth $\Delta\omega$ of the stray resonances are at least one magnitude broader than the principal resonance (25 MHz vs. 2 MHz). As a conclusion, we therefore estimate that the photon noise should be dominated by the principal resonance, which is approximately $1/\gamma$ times smaller than the capacitance-terminated design $\frac{1}{\gamma^2\Delta\omega} \propto \frac{1}{\gamma|t_C|^2}$.

6.3.5 Conclusion

We present preliminary measurements on resonators with partial Bragg-filter termination that is required for the application of a DC voltage on the substrate. We realistically consider a wirebonding strategy that will not hinder the ability to bias flux qubits magnetically. The results are compatible with the theory section 3.3.3, except for the appearance of stray resonances. We show theoretically that no additional photon noise dephasing is introduced by the stray modes. We show that at resonance, $\gamma = 1.80$ (obtained by simulation) plays a crucial role since it increases the mode volume. This leads to dilution of the quantum fluctuations in the resonator, sharpening the linewidth inversely $\Delta\omega \propto 1/\gamma$,

and decreasing the coupling constant $g \propto \sqrt{\frac{1}{\gamma}}$. Consequently, the measurement efficiency is roughly similar, since $\chi/\Delta\omega$ is unchanged, as well as the factor $Q_{int}/Q_{C/\mathrm{Bragg}}$ remaining almost the same.

7 Conclusion and Perspectives

The ultimate goal of this work is to develop a spin-based quantum processor. One of the required tools for building such a processor is a quantum bus that allows controlling the coupling between spins. To this end, we consider using a superconducting circuit as a mediator between spins and try to establish a strong coupling between these entities. Over the course of this PhD, many intermediate results necessary to prove the feasibility of this approach have been established. Here is a summary of the principle results:

1. **Control and reproducibility of the flux qubit** : We experimentally improved upon the control of the flux qubit transition energy and demonstrated reproducibility through a batch of more than 20 flux qubits fabricated on three different silicon samples. The best sample yielded long and reproducible coherence times ($T_1 \sim 15 - 20\,\mu s$, $T_{2E}^{\varphi} \sim 15 - 30\,\mu s$). We observed that the sample surface had some impact on the reproducibility of the coherence, while the presence of a local constriction had no apparent effect.

2. **Constrictions and precise positioning of the circuit with respect to the implanted spins** : We developed a fabrication technique involving cold evaporation permitting the fabrication of thin constrictions ($20 - 35\,nm$), which we are able to position in the vicinity of implanted spins.

3. **Tunable flux qubits exhibiting long coherence times** : A study on tunable flux qubits was conducted on a sapphire sample. By replacing one of the unitary junctions with an asymmetrical SQUID, we were able to demonstrate tunability on a range of $\pm 3.5\,GHz$ and measure coherence times (up to $T_1 \sim 8\,\mu s$ and $T_{2E}^{\varphi} \sim 4\,\mu s$) one or two orders of magnitude better than state-of-the-art.

4. **Bragg-Filtered resonators** : designing a readout resonator delimited on one side by Bragg Filters allows for direct application of a gate voltage to the flux qubit. Preliminary theoretical and experimental work has been conducted. The band-cut feature was observed as intended. The sharpening of the peak due to prolonged photon round-trip time was also compatible with theory.

All these results contribute to the goal of having a resonant flux qubit with good coherence properties in close proximity to a single bismuth donor. The implanted bismuth donor can be kept unionized through a gate voltage at the Bragg port, while ensuring the qubits do not suffer from additional Purcell loss. The close proximity of the constriction and the high persistent current of the qubit enhances the coupling to the spin. The flux qubit transition frequency may be designed with good control and even scanned to a certain extent. Finally, the good coherence properties of the qubits should allow us to reach the strong coupling regime.

7.1 Short term research directions

As of the writing of this thesis, the fabrication of a Bragg-filtered resonator galvanically coupled to flux qubits on a sample of isotopically pure silicon containing implanted bismuth donors (sample E in Tab.4.1) is almost achieved. The characterization of the coherence properties and transition energies of these flux qubits should be performed in the coming months. Our plan is to find a flux qubit with good coherence properties and a gap close to the Si:Bi transition frequency in order to detect the coupling of a spin and the qubit. Several questions remain open:

1. What are the coherence properties of a flux qubit fabricated on the slightly doped isotopically purified layer?
2. Is it possible to reinitialize the spin state by application of a gate voltage?
3. What is the impact of the gate voltage on the quality factor of the resonator and/or the coherence properties of the qubit?
4. Are the coherence properties of the donor spin affected by the close proximity to a flux qubit?
5. What kind of power stability can we realistically expect? How will this degrade the the protocol described in Ref.[60]?
6. Would it be possible to engineer superposition of hyperfine ground states using Ref.[60], and characterize their coherence properties?

7.2 Future perspectives

The architecture of resonantly coupling spins to flux qubits using the Rabi dressing protocol provides a robust way of coupling otherwise non-resonant quantum objects. In addition, the dynamical decoupling effect of the Rabi suppresses sensitivity to T_2 originating from low frequency noise. This provides a powerful method of multiplexing control sequences intended for different spins by power modulation. Using only spin-FQ swap gate, it is possible to realize a swap gate between two spins coupled to the same flux qubit bus. Furthermore, by coupling many such buses to a common resonator, spatially distant spins coupled by respective buses may be entangled. All in all, this architecture has the potential to increases many-fold the scalability of spin-based quantum processors : selecting the flux qubit bus by drive frequency and selecting the spin by drive power.

8 Table of acronyms and variables

variable	description
Math	
$\vec{e_x}$, $\vec{e_y}$, $\vec{e_z}$	The normalized basis vectors in 3D euclidean space. When applicable, the z+ direction is coming out of the sample substrate, or defined by the static magnetic field.
$\boldsymbol{i}$	Imaginary number
$\mathcal{N}$	Hermitian Normalization of coefficients $\mathcal{N}(c_i) = c_i / \sqrt{\sum_j \lvert c_j \rvert^2}$
Tr	Trace operator
$\mathfrak{B}$	Vector basis, comprised usually of kets
n_{FFT}	Number of Fourier frequencies in the (fast) Fourier Transform(ation). Equivalent to number of spatial or temporal data-points.
$\mathbf{1}$	Identity matrix or the identity operator
$\mathbf{0}$	Vectorial or matricial zero
Re	Real part function
Im	Imaginary part function
H	Symbol for an Hamiltonian operator
$\mathcal{L}$	Symbol for Lagrangian
c.c.	Complex conjugate
H.c.	Hermitien conjugate
Chemistry	
AFM	Atomic Force Microscope/Microscopy
Si	Silicon
SiO_2	Silicon oxide
^{28}Si	Silicon 28 isotope
^{29}Si	Silicon 29 isotope
$^{\mathrm{nat}}$Si	Silicon with natural isotopic abundance. Typically having 4.7% ^{29}Si and 3.1% ^{30}Si.
Spin related	
B_0	Static DC magnetic field. Could either be vector $\overrightarrow{B_0}$ or a scalar B_0
Si:Bi	Symbol for bismuth donors in silicon
Si:P	Symbol for phosphorous donors in silicon
$\updownarrow$	Symbol for the electronic spin qubit.
N_{ens}	Number of spins in the (homogeneous) ensemble.
A	Hyperfine interaction strength in GHz

$\|\uparrow\Uparrow\rangle$	Ket states where double arrows indicate nuclear while simple arrow indicate spin. Up direction defined by static field.
$\|\swarrow / \nearrow\rangle$	To differentiate from the above, a tilted arrow represents the donor spin ground (downward) and excited (upward) state, which are *a priori* not pure states of the electron spin operator, but rather entangled states of nuclear and electronic spin states. Under high fields, the definitions may align
$\hat{\sigma}^s$	Pauli operators in the spin logical space $\{\|\swarrow\rangle, \|\nearrow\rangle\}$. For $\hat{\sigma}_z^s$, the eigenvalue $+1$ is automatically associated to the excited state.

superconducting circuit	
cpw	Coplanar waveguide
fq	Flux Qubit
$\mathscr{L}$	Linear inductance of the 2D coplanar waveguide
$\mathscr{C}$	Linear capacitance of the 2D coplanar waveguide
Z_0	Characteristic impedance. $\sqrt{L/C}$ in the lumped element resonator or $\sqrt{\mathscr{L}/\mathscr{C}}$ in a distributed CPW.
L	Length of the coplanar waveguide
ω_1	Frequency of the first mode of the CPW
$\mathbf{x}$	Position (usually of a flux qubit) in the coplanar waveguide
I	Current at a particular position in the CPW, all modes included. The first mode dominates.
δI	Quantum fluctuations of current
$\mathbf{C}$	Capacitance matrix
	Pauli operators in the flux qubit logical space $\{\|g\rangle, \|e\rangle\}$. For σ_z, the eigenvalue $+1$ is automatically associated to the excited state.

circuit QED	
Ω	Frequency (rad·Hz) of Rabi oscillations
phot	Shorthand for photon. To resolve the ambiguity, hf or $\hbar\omega$ denotes the photon energy
$\hat{N}$	Photonic number operator. $\hat{N} = a^\dagger a$
η	Density of states per unit of angular frequency
I_0	Critical current of a Josephson junction
$\vec{n}$	Column vector of the charge number operators, which are unitless conjugate momenta of the three *free* junction phases.
Γ_P	Purcell rate of a flux qubit
Δ	Flux qubit gap, i.e. splitting at the optimal point. Units in frequency (rad GHz)
ω_{ge}	Flux qubit transition frequency

I_p	Flux qubit persistent current.
$\Phi_\star$	Flux threading the qubit main loop at an optimal point.

9 List of publications

1. **Protection of Quantum Information in a Chain of Josephson Junctions**
   Paul Brookes, Tikai Chang, Marzena Szymanska, Eytan Grosfeld, Eran Ginossar, and Michael Stern. Physical Review Applied, 17(2):024057, 2022.

2. **Reproducibility and gap control of superconducting flux qubits**
   T Chang, I Holzman, T Cohen, BC Johnson, DN Jamieson, and M Stern. Reproducibility and control of superconducting flux qubits. Physical Review Applied, *Accepted*. Preprint [118]

3. **Tunable superconducting flux qubits with long coherence times**
   T Chang, T Cohen, I Holzman, G Catelani, and M Stern. Tunable superconducting flux qubits with long coherence times. Physical Review Applied, *Under Review*. Preprint [119]

References

[1] Peter W. Shor. Polynomial-Time Algorithms for Prime Factorization and Discrete Logarithms on a Quantum Computer. *SIAM Journal on Computing*, 26(5):1484–1509, October 1997. 7

[2] Lov K. Grover. A fast quantum mechanical algorithm for database search. 7

[3] David P. Divincenzo. The physical implementation of quantum computation. *Fortschr. Phys*, 48:2000, 2000. 7

[4] M. Saffman, T. G. Walker, and K. Mølmer. Quantum information with rydberg atoms. *Rev. Mod. Phys.*, 82:2313–2363, Aug 2010. 7

[5] Colin D. Bruzewicz, John Chiaverini, Robert McConnell, and Jeremy M. Sage. Trapped-ion quantum computing: Progress and challenges. *Applied Physics Reviews*, 6(2):021314, 2019. 7

[6] Daniel Loss and David P. DiVincenzo. Quantum computation with quantum dots. *Phys. Rev. A*, 57:120–126, Jan 1998. 7

[7] Christoph Kloeffel and Daniel Loss. Prospects for spin-based quantum computing in quantum dots. *Annual Review of Condensed Matter Physics*, 4(1):51–81, 2013. 7

[8] Andrea Morello, Jarryd J. Pla, Patrice Bertet, and David N. Jamieson. Donor spins in silicon for quantum technologies. *Advanced Quantum Technologies*, 3(11):2000005, 2020. 7, 9

[9] M. H. Devoret and R. J. Schoelkopf. Superconducting circuits for quantum information: An outlook. *Science*, 339(6124):1169–1174, 2013. 7

[10] Morten Kjaergaard, Mollie E. Schwartz, Jochen Braumüller, Philip Krantz, Joel I.-J. Wang, Simon Gustavsson, and William D. Oliver. Superconducting qubits: Current state of play. *Annual Review of Condensed Matter Physics*, 11(1):369–395, 2020. 7

[11] Gopalakrishnan Balasubramanian, Philipp Neumann, Daniel Twitchen, Matthew Markham, Roman Kolesov, Norikazu Mizuochi, Junichi Isoya, Jocelyn Achard, Johannes Beck, Julia Tissler, Vincent Jacques, Philip R. Hemmer, Fedor Jelezko, and Jörg Wrachtrup. Ultralong spin coherence time in isotopically engineered diamond. *Nature Materials*, 8(5):383–387, April 2009. 7, 8

[12] Juha T. Muhonen, Juan P. Dehollain, Arne Laucht, Fay E. Hudson, Rachpon Kalra, Takeharu Sekiguchi, Kohei M. Itoh, David N. Jamieson, Jeffrey C. McCallum, Andrew S. Dzurak, and Andrea Morello. Storing quantum information for 30 seconds in a nanoelectronic device. *Nature Nanotechnology*, 9(12):986–991, October 2014. 7, 8, 17, 18, 20

[13] Y. Nakamura, Yu. A. Pashkin, and J. S. Tsai. Coherent control of macroscopic quantum states in a single-cooper-pair box. *Nature*, 398(6730):786–788, April 1999. 7

[14] D. Vion, A. Aassime, A. Cottet, P. Joyez, H. Pothier, C. Urbina, D. Esteve, and M. H. Devoret. Manipulating the quantum state of an electrical circuit. *Science*, 296(5569):886–889, 2002. 7

[15] I. Chiorescu, Y. Nakamura, C. J. P. M. Harmans, and J. E. Mooij. Coherent quantum dynamics of a superconducting flux qubit. *Science*, 299(5614):1869–1871, 2003. 7

[16] Leonid V. Abdurakhimov, Imran Mahboob, Hiraku Toida, Kousuke Kakuyanagi, and Shiro Saito. A long-lived capacitively shunted flux qubit embedded in a 3d cavity. *Applied Physics Letters*, 115(26):262601, December 2019. 7

[17] Alexander P. M. Place, Lila V. H. Rodgers, Pranav Mundada, Basil M. Smitham, Mattias Fitzpatrick, Zhaoqi Leng, Anjali Premkumar, Jacob Bryon, Andrei Vrajitoarea, Sara Sussman, Guangming Cheng, Trisha Madhavan, Harshvardhan K. Babla, Xuan Hoang Le, Youqi Gang, Berthold Jäck, András Gyenis, Nan Yao, Robert J. Cava, Nathalie P. de Leon, and Andrew A. Houck. New material platform for superconducting transmon qubits with coherence times exceeding 0.3 milliseconds. *Nature Communications*, 12(1), March 2021. 7

[18] Aaron Somoroff, Quentin Ficheux, Raymond A. Mencia, Haonan Xiong, Roman V. Kuzmin, and Vladimir E. Manucharyan. Millisecond coherence in a superconducting qubit, 2021. 7

[19] Frank Arute, Kunal Arya, Ryan Babbush, Dave Bacon, Joseph C. Bardin, Rami Barends, Rupak Biswas, Sergio Boixo, Fernando G. S. L. Brandao, David A. Buell, Brian Burkett, Yu Chen, Zijun Chen, Ben Chiaro, Roberto Collins, William Courtney, Andrew Dunsworth, Edward Farhi, Brooks Foxen, Austin Fowler, Craig Gidney, Marissa Giustina, Rob Graff, Keith Guerin, Steve Habegger, Matthew P. Harrigan, Michael J. Hartmann, Alan Ho, Markus Hoffmann, Trent Huang, Travis S. Humble, Sergei V. Isakov, Evan Jeffrey, Zhang Jiang, Dvir Kafri, Kostyantyn Kechedzhi, Julian Kelly, Paul V. Klimov, Sergey Knysh, Alexander Korotkov, Fedor Kostritsa, David Landhuis, Mike Lindmark, Erik Lucero, Dmitry Lyakh, Salvatore Mandrà, Jarrod R. McClean, Matthew McEwen, Anthony Megrant, Xiao Mi, Kristel Michielsen, Masoud Mohseni, Josh Mutus, Ofer Naaman, Matthew Neeley, Charles Neill, Murphy Yuezhen Niu, Eric Ostby, Andre Petukhov, John C. Platt, Chris Quintana, Eleanor G. Rieffel, Pedram Roushan, Nicholas C. Rubin, Daniel Sank, Kevin J. Satzinger, Vadim Smelyanskiy, Kevin J. Sung, Matthew D. Trevithick, Amit Vainsencher, Benjamin Villalonga, Theodore White, Z. Jamie Yao, Ping Yeh, Adam Zalcman, Hartmut Neven, and John M. Martinis. Quantum supremacy using a programmable superconducting processor. *Nature*, 574(7779):505–510, October 2019. 7

[20] Ze-Liang Xiang, Sahel Ashhab, J. Q. You, and Franco Nori. Hybrid quantum circuits: Superconducting circuits interacting with other quantum systems. *Rev. Mod. Phys.*, 85:623–653, Apr 2013. 7

[21] Gershon Kurizki, Patrice Bertet, Yuimaru Kubo, Klaus Mølmer, David Petrosyan, Peter Rabl, and Jörg Schmiedmayer. Quantum technologies with hybrid systems. *Proceedings of the National Academy of Sciences*, 112(13):3866–3873, March 2015. 7

[22] D. N. Jamieson, C. Yang, T. Hopf, S. M. Hearne, C. I. Pakes, S. Prawer, M. Mitic, E. Gauja, S. E. Andresen, F. E. Hudson, A. S. Dzurak, and R. G. Clark. Controlled shallow single-ion implantation in silicon using an active substrate for sub-20kev ions. *Applied Physics Letters*, 86(20):202101, 2005. 8

[23] Jessica van Donkelaar, C Yang, A D C Alves, J C McCallum, C Hougaard, B C Johnson, F E Hudson, A S Dzurak, A Morello, D Spemann, and D N Jamieson. Single atom devices by ion implantation. *Journal of Physics: Condensed Matter*, 27(15):154204, March 2015. 8

[24] Alexander M. Jakob, Simon G. Robson, Vivien Schmitt, Vincent Mourik, Matthias Posselt, Daniel Spemann, Brett C. Johnson, Hannes R. Firgau, Edwin Mayes, Jeffrey C. McCallum, Andrea Morello, and David N. Jamieson. Deterministic shallow dopant implantation in silicon with detection confidence upper-bound to 99.85% by ion–solid interactions. *Advanced Materials*, 34(3):2103235, 2022. 8

[25] L. Childress, M. V. Gurudev Dutt, J. M. Taylor, A. S. Zibrov, F. Jelezko, J. Wrachtrup, P. R. Hemmer, and M. D. Lukin. Coherent dynamics of coupled electron and nuclear spin qubits in diamond. *Science*, 314(5797):281–285, October 2006. 8

[26] Jarryd J. Pla, Kuan Y. Tan, Juan P. Dehollain, Wee H. Lim, John J. L. Morton, David N. Jamieson, Andrew S. Dzurak, and Andrea Morello. A single-atom electron spin qubit in silicon. *Nature*, 489(7417):541–545, September 2012. 8, 9, 17, 18

[27] Gary Wolfowicz, Alexei M. Tyryshkin, Richard E. George, Helge Riemann, Nikolai V. Abrosimov, Peter Becker, Hans-Joachim Pohl, Mike L. W. Thewalt, Stephen A. Lyon, and John J. L. Morton. Atomic clock transitions in silicon-based spin qubits. *Nat Nano*, 8(11):881–881, November 2013. 8, 18, 19

[28] Susan J. Angus, Andrew J. Ferguson, Andrew S. Dzurak, and Robert G. Clark. Gate-defined quantum dots in intrinsic silicon. *Nano Letters*, 7(7):2051–2055, June 2007. 8

[29] Lilian Isabel Childress. *Coherent manipulation of single quantum systems in the solid state*. PhD thesis, Harvard University, 2007. 8

[30] Emanuele Albertinale. *Measuring spin fluorescence with a microwave photon detector*. PhD thesis, L'UNIVERSITE PARIS-SACLAY, 2021. 10

[31] H. Bernien, B. Hensen, W. Pfaff, G. Koolstra, M. S. Blok, L. Robledo, T. H. Taminiau, M. Markham, D. J. Twitchen, L. Childress, and R. Hanson. Heralded entanglement between solid-state qubits separated by three metres. *Nature*, 497(7447):86–90, April 2013. 10

[32] B. E. Kane. A silicon-based nuclear spin quantum computer. *Nature*, 393(6681):133–137, May 1998. 10

[33] Juan P. Dehollain, Juha T. Muhonen, Kuan Y. Tan, Andre Saraiva, David N. Jamieson, Andrew S. Dzurak, and Andrea Morello. Single-shot readout and relaxation of singlet and triplet states in exchange-coupled ^{31}P electron spins in silicon. *Phys. Rev. Lett.*, 112:236801, Jun 2014. 10

[34] M. F. Gonzalez-Zalba, André Saraiva, María J. Calderón, Dominik Heiss, Belita Koiller, and Andrew J. Ferguson. An exchange-coupled donor molecule in silicon. *Nano Letters*, 14(10):5672–5676, September 2014. 10

[35] Y. He, S. K. Gorman, D. Keith, L. Kranz, J. G. Keizer, and M. Y. Simmons. A two-qubit gate between phosphorus donor electrons in silicon. *Nature*, 571(7765):371–375, July 2019. 10

[36] Guilherme Tosi, Fahd A. Mohiyaddin, Vivien Schmitt, Stefanie Tenberg, Rajib Rahman, Gerhard Klimeck, and Andrea Morello. Silicon quantum processor with robust long-distance qubit couplings. *Nature Communications*, 8(1), September 2017. 10, 11

[37] Rostyslav Savytskyy, Tim Botzem, Irene Fernandez de Fuentes, Benjamin Joecker, Fay E. Hudson, Kohei M. Itoh, Alexander M. Jakob, Brett C. Johnson, David N. Jamieson, Andrew S. Dzurak, and Andrea Morello. An electrically-driven single-atom 'flip-flop' qubit, 2022. 10, 11

[38] P. Haikka, Y. Kubo, A. Bienfait, P. Bertet, and K. Mølmer. Proposal for detecting a single electron spin in a microwave resonator. *Physical Review A*, 95(2), February 2017. 11

[39] Audrey Bienfait. *Magnetic resonance with quantum microwaves*. PhD thesis, L'UNIVERSITE PARIS-SACLAY, 2016. 12, 22

[40] Cécile Grèzes. *Towards a Spin-Ensemble Quantum Memory for Superconducting Qubits*. Springer International Publishing, 2016. 12

[41] Y. Kubo, F. R. Ong, P. Bertet, D. Vion, V. Jacques, D. Zheng, A. Dréau, J.-F. Roch, A. Auffeves, F. Jelezko, J. Wrachtrup, M. F. Barthe, P. Bergonzo, and D. Esteve. Strong coupling of a spin ensemble to a superconducting resonator. *Phys. Rev. Lett.*, 105:140502, Sep 2010. 12

[42] D. I. Schuster, A. P. Sears, E. Ginossar, L. DiCarlo, L. Frunzio, J. J. L. Morton, H. Wu, G. A. D. Briggs, B. B. Buckley, D. D. Awschalom, and R. J. Schoelkopf. High-cooperativity coupling of electron-spin ensembles to superconducting cavities. *Phys. Rev. Lett.*, 105:140501, Sep 2010. 12

[43] P. Bushev, A. K. Feofanov, H. Rotzinger, I. Protopopov, J. H. Cole, C. M. Wilson, G. Fischer, A. Lukashenko, and A. V. Ustinov. Ultralow-power spectroscopy of a rare-earth spin ensemble using a superconducting resonator. *Phys. Rev. B*, 84:060501, Aug 2011. 12

[44] Matthias U Staudt, Io-Chun Hoi, Philip Krantz, Martin Sandberg, Michaël Simoen, Pavel Bushev, Nicolas Sangouard, Mikael Afzelius, Vitaly S Shumeiko, Göran Johansson, Per Delsing, and C M Wilson. Coupling of an erbium spin ensemble to a superconducting resonator. *Journal of Physics B: Atomic, Molecular and Optical Physics*, 45(12):124019, jun 2012. 12

[45] Brian Julsgaard, Cécile Grezes, Patrice Bertet, and Klaus Mølmer. Quantum memory for microwave photons in an inhomogeneously broadened spin ensemble. *Phys. Rev. Lett.*, 110:250503, Jun 2013. 12

[46] C. Grezes, B. Julsgaard, Y. Kubo, M. Stern, T. Umeda, J. Isoya, H. Sumiya, H. Abe, S. Onoda, T. Ohshima, V. Jacques, J. Esteve, D. Vion, D. Esteve, K. Mølmer, and P. Bertet. Multimode storage and retrieval of microwave fields in a spin ensemble. *Phys. Rev. X*, 4:021049, Jun 2014. 12

[47] A. Bienfait, J. J. Pla, Y. Kubo, X. Zhou, M. Stern, C. C. Lo, C. D. Weis, T. Schenkel, D. Vion, D. Esteve, J. J. L. Morton, and P. Bertet. Controlling spin relaxation with a cavity. *Nature*, 531(7592):74–77, February 2016. 12, 17

[48] J. J. Viennot, M. C. Dartiailh, A. Cottet, and T. Kontos. Coherent coupling of a single spin to microwave cavity photons. *Science*, 349(6246):408–411, 2015. 12

[49] X. Mi, J. V. Cady, D. M. Zajac, P. W. Deelman, and J. R. Petta. Strong coupling of a single electron in silicon to a microwave photon. *Science*, 355(6321):156–158, 2017. 13

[50] X. Mi, M. Benito, S. Putz, D. M. Zajac, J. M. Taylor, Guido Burkard, and J. R. Petta. A coherent spin–photon interface in silicon. *Nature*, 555(7698):599–603, February 2018. 13

[51] Moonjoo Lee. Ultrahigh-quality-factor superconducting microwave resonator on diamond for quantum information processing. *Japanese Journal of Applied Physics*, 58(10):100914, oct 2019. 14

[52] James F. Ziegler, M.D. Ziegler, and J.P. Biersack. Srim – the stopping and range of ions in matter (2010). *Nuclear Instruments and Methods in Physics Research Section B: Beam Interactions with Materials and Atoms*, 268(11):1818–1823, 2010. 19th International Conference on Ion Beam Analysis. 14, 78, 79

[53] John J. L. Morton, Alexei M. Tyryshkin, Richard M. Brown, Shyam Shankar, Brendon W. Lovett, Arzhang Ardavan, Thomas Schenkel, Eugene E. Haller, Joel W. Ager, and S. A. Lyon. Solid-state quantum memory using the 31p nuclear spin. *Nature*, 455(7216):1085–1088, October 2008. 18

[54] A. M. Tyryshkin, S. A. Lyon, A. V. Astashkin, and A. M. Raitsimring. Electron spin relaxation times of phosphorus donors in silicon. *Physical Review B*, 68(19), November 2003. 18

[55] V Ranjan, B Albanese, E Albertinale, E Billaud, D Flanigan, JJ Pla, T Schenkel, D Vion, D Esteve, E Flurin, et al. Spatially resolved decoherence of donor spins in silicon strained by a metallic electrode. *Physical Review X*, 11(3):031036, 2021. 18, 22

[56] J. Mansir, P. Conti, Z. Zeng, J. J. Pla, P. Bertet, M. W. Swift, C. G. Van de Walle, M. L. W. Thewalt, B. Sklenard, Y. M. Niquet, and J. J. L. Morton. Linear hyperfine tuning of donor spins in silicon using hydrostatic strain. *Phys. Rev. Lett.*, 120:167701, Apr 2018. 21

[57] J. J. Pla, A. Bienfait, G. Pica, J. Mansir, F. A. Mohiyaddin, Z. Zeng, Y. M. Niquet, A. Morello, T. Schenkel, J. J. L. Morton, and P. Bertet. Strain-induced spin-resonance shifts in silicon devices. *Phys. Rev. Applied*, 9:044014, Apr 2018. 21

[58] J. Twamley and S. D. Barrett. Superconducting cavity bus for single nitrogen-vacancy defect centers in diamond. *Phys. Rev. B*, 81:241202, Jun 2010. 24

[59] D. Marcos, M. Wubs, J. M. Taylor, R. Aguado, M. D. Lukin, and A. S. Sørensen. Coupling Nitrogen-Vacancy Centers in Diamond to Superconducting Flux Qubits. *Physical Review Letters*, 105(21):210501, November 2010. 24

[60] Tom Douce, Michael Stern, Nicim Zagury, Patrice Bertet, and Pérola Milman. Coupling a single nitrogen-vacancy center to a superconducting flux qubit in the far-off-resonance regime. *Phys. Rev. A*, 92:052335, Nov 2015. 24, 28, 71, 122

[61] J. Twamley and S. D. Barrett. Superconducting cavity bus for single nitrogen-vacancy defect centers in diamond. *Physical Review B*, 81(24):241202, 2010. 24

[62] T. P. Orlando, J. E. Mooij, Lin Tian, Caspar H. van der Wal, L. S. Levitov, Seth Lloyd, and J. J. Mazo. Superconducting persistent-current qubit. *Phys. Rev. B*, 60:15398–15413, Dec 1999. 25

[63] J. E. Mooij, T. P. Orlando, L. Levitov, Lin Tian, Caspar H. van der Wal, and Seth Lloyd. Josephson persistent-current qubit. *Science*, 285(5430):1036–1039, August 1999. 25

[64] P. Bertet, I. Chiorescu, G. Burkard, K. Semba, C. J. P. M. Harmans, D. P. DiVincenzo, and J. E. Mooij. Dephasing of a superconducting qubit induced by photon noise. *Phys. Rev. Lett.*, 95:257002, Dec 2005. 25, 26, 99, 101, 109

[65] F. Yoshihara, K. Harrabi, A. O. Niskanen, Y. Nakamura, and J. S. Tsai. Decoherence of flux qubits due to $1/f$ flux noise. *Phys. Rev. Lett.*, 97:167001, Oct 2006. 25, 26, 99, 110

[66] J.-L. Orgiazzi, C. Deng, D. Layden, R. Marchildon, F. Kitapli, F. Shen, M. Bal, F. R. Ong, and A. Lupascu. Flux qubits in a planar circuit quantum electrodynamics architecture: Quantum control and decoherence. *Phys. Rev. B*, 93:104518, Mar 2016. 25, 26, 100, 101

[67] Jonas Bylander, Simon Gustavsson, Fei Yan, Fumiki Yoshihara, Khalil Harrabi, George Fitch, David G. Cory, Yasunobu Nakamura, Jaw-Shen Tsai, and William D. Oliver. Noise spectroscopy through dynamical decoupling with a superconducting flux qubit. *Nature Physics*, 7(7):565–570, May 2011. 25, 26, 101, 110

[68] M. Stern, G. Catelani, Y. Kubo, C. Grezes, A. Bienfait, D. Vion, D. Esteve, and P. Bertet. Flux qubits with long coherence times for hybrid quantum circuits. *Phys. Rev. Lett.*, 113:123601, Sep 2014. 25, 101, 110

[69] Fei Yan, Simon Gustavsson, Archana Kamal, Jeffrey Birenbaum, Adam P Sears, David Hover, Ted J. Gudmundsen, Danna Rosenberg, Gabriel Samach, S Weber, Jonilyn L. Yoder, Terry P. Orlando, John Clarke, Andrew J. Kerman, and William D. Oliver. The flux qubit revisited to enhance coherence and reproducibility. *Nature Communications*, 7(1), November 2016. 26, 100, 101, 103

[70] M. Stern, G. Catelani, Y. Kubo, C. Grezes, A. Bienfait, D. Vion, D. Esteve, and P. Bertet. Flux Qubits with Long Coherence Times for Hybrid Quantum Circuits. *Phys. Rev. Lett.*, 113(12):123601, September 2014. 26, 85, 100, 101, 102, 108

[71] P. Forn-Díaz, J. Lisenfeld, D. Marcos, J. J. García-Ripoll, E. Solano, C. J. P. M. Harmans, and J. E. Mooij. Observation of the bloch-siegert shift in a qubit-oscillator system in the ultrastrong coupling regime. *Phys. Rev. Lett.*, 105:237001, Nov 2010. 26

[72] T. P. Orlando, J. E. Mooij, Lin Tian, Caspar H. van der Wal, L. S. Levitov, Seth Lloyd, and J. J. Mazo. Superconducting persistent-current qubit. *Phys. Rev. B*, 60:15398–15413, Dec 1999. 27

[73] F. G. Paauw, A. Fedorov, C. J. P. M Harmans, and J. E. Mooij. Tuning the gap of a superconducting flux qubit. *Phys. Rev. Lett.*, 102:090501, Mar 2009. 27, 28, 105

[74] C. M. Quintana, Yu Chen, D. Sank, A. G. Petukhov, T. C. White, Dvir Kafri, B. Chiaro, A. Megrant, R. Barends, B. Campbell, Z. Chen, A. Dunsworth, A. G. Fowler, R. Graff, E. Jeffrey, J. Kelly, E. Lucero, J. Y. Mutus, M. Neeley, C. Neill, P. J. J. O'Malley, P. Roushan, A. Shabani, V. N. Smelyanskiy, A. Vainsencher, J. Wenner, H. Neven, and John M. Martinis. Observation of classical-quantum crossover of $1/f$ flux noise and its paramagnetic temperature dependence. *Phys. Rev. Lett.*, 118:057702, Jan 2017. 28, 38

[75] Jochen Braumüller, Leon Ding, Antti P. Vepsäläinen, Youngkyu Sung, Morten Kjaergaard, Tim Menke, Roni Winik, David Kim, Bethany M. Niedzielski, Alexander Melville, Jonilyn L. Yoder, Cyrus F. Hirjibehedin, Terry P. Orlando, Simon Gustavsson, and William D. Oliver. Characterizing and optimizing qubit coherence based on squid geometry. *Phys. Rev. Applied*, 13:054079, May 2020. 28, 38, 65, 68, 101, 110

[76] Jens Koch, Terri M. Yu, Jay Gambetta, A. A. Houck, D. I. Schuster, J. Majer, Alexandre Blais, M. H. Devoret, S. M. Girvin, and R. J. Schoelkopf. Charge-insensitive qubit design derived from the cooper pair box. *Phys. Rev. A*, 76:042319, Oct 2007. 38

[77] J. D. Strand, Matthew Ware, Félix Beaudoin, T. A. Ohki, B. R. Johnson, Alexandre Blais, and B. L. T. Plourde. First-order sideband transitions with flux-driven asymmetric transmon qubits. *Phys. Rev. B*, 87:220505, Jun 2013. 39

[78] M. D. Hutchings, J. B. Hertzberg, Y. Liu, N. T. Bronn, G. A. Keefe, Markus Brink, Jerry M. Chow, and B. L. T. Plourde. Tunable superconducting qubits with flux-independent coherence. *Phys. Rev. Applied*, 8:044003, Oct 2017. 39

[79] Brian C Wadell. *Transmission line design handbook*. Artech House Microwave Library, 1991. 52

[80] J. R. Schrieffer and P. A. Wolff. Relation between the anderson and kondo hamiltonians. *Phys. Rev.*, 149:491–492, Sep 1966. 56

[81] C. W. Gardiner and M. J. Collett. Input and output in damped quantum systems: Quantum stochastic differential equations and the master equation. *Phys. Rev. A*, 31:3761–3774, Jun 1985. 58

[82] G. Ithier, E. Collin, P. Joyez, P. J. Meeson, D. Vion, D. Esteve, F. Chiarello, A. Shnirman, Y. Makhlin, J. Schriefl, and G. Schön. Decoherence in a superconducting quantum bit circuit. *Phys. Rev. B*, 72:134519, Oct 2005. 63, 64, 67, 101, 110

[83] Paul Brookes, Tikai Chang, Marzena Szymanska, Eytan Grosfeld, Eran Ginossar, and Michael Stern. Protection of quantum information in a chain of josephson junctions. *Phys. Rev. Applied*, 17:024057, Feb 2022. 65

[84] `https://github.com/teacup123123/pink_flux_noise_analysis`. 65

[85] John M Martinis, Ken B Cooper, Robert McDermott, Matthias Steffen, Markus Ansmann, KD Osborn, Katarina Cicak, Seongshik Oh, David P Pappas, Raymond W Simmonds, et al. Decoherence in josephson qubits from dielectric loss. *Physical review letters*, 95(21):210503, 2005. 76

[86] Wayne Woods, Greg Calusine, Alexander Melville, Arjan Sevi, Evan Golden, David K Kim, Danna Rosenberg, Jonilyn L Yoder, and William D Oliver. Determining interface dielectric losses in superconducting coplanar-waveguide resonators. *Physical Review Applied*, 12(1):014012, 2019. 76, 77

[87] Zlatko K Minev, Zaki Leghtas, Shantanu O Mundhada, Lysander Christakis, Ioan M Pop, and Michel H Devoret. Energy-participation quantization of josephson circuits. *npj Quantum Information*, 7(1):1–11, 2021. 76

[88] Aaron D O'Connell, M Ansmann, Radoslaw C Bialczak, Max Hofheinz, Nadav Katz, Erik Lucero, C McKenney, Matthew Neeley, Haohua Wang, Eva Maria Weig, et al. Microwave dielectric loss at single photon energies and millikelvin temperatures. *Applied Physics Letters*, 92(11):112903, 2008. 76, 78

[89] Jerzy Krupka, Paweł Kamiński, Roman Kozłowski, Barbara Surma, Alexander Dierlamm, and Michał Kwestarz. Dielectric properties of semi-insulating silicon at microwave frequencies. *Applied Physics Letters*, 107(8):082105, 2015. 76

[90] Daniel L Creedon, Yarema Reshitnyk, Warrick Farr, John M Martinis, Timothy L Duty, and Michael E Tobar. High q-factor sapphire whispering gallery mode microwave resonator at single photon energies and millikelvin temperatures. *Applied Physics Letters*, 98(22):222903, 2011. 76

[91] CM Quintana, A Megrant, Z Chen, A Dunsworth, B Chiaro, R Barends, B Campbell, Yu Chen, I-C Hoi, E Jeffrey, et al. Characterization and reduction of microfabrication-induced decoherence in superconducting quantum circuits. *Applied Physics Letters*, 105(6):062601, 2014. 76, 77

[92] A Bruno, G De Lange, S Asaad, KL Van Der Enden, NK Langford, and L DiCarlo. Reducing intrinsic loss in superconducting resonators by surface treatment and deep etching of silicon substrates. *Applied Physics Letters*, 106(18):182601, 2015. 76

[93] Alexander PM Place, Lila VH Rodgers, Pranav Mundada, Basil M Smitham, Mattias Fitzpatrick, Zhaoqi Leng, Anjali Premkumar, Jacob Bryon, Andrei Vrajitoarea, Sara Sussman, et al. New material platform for superconducting transmon qubits with coherence times exceeding 0.3 milliseconds. *Nature communications*, 12(1):1–6, 2021. 77

[94] Danielle Holmes. *Donor activation and isotopic enrichment of silicon via ion implantation for quantum computing*. PhD thesis, U. Melbourne (main), 2020. 78, 80

[95] James F Gibbons. Ion implantation in semiconductors—part ii: Damage production and annealing. *Proceedings of the IEEE*, 60(9):1062–1096, 1972. 79

[96] D. Holmes, W. I. L. Lawrie, B. C. Johnson, A. Asadpoordarvish, J. C. McCallum, D. R. McCamey, and D. N. Jamieson. Activation and electron spin resonance of near-surface implanted bismuth donors in silicon. *Phys. Rev. Materials*, 3:083403, Aug 2019. 80

[97] D. Holmes, B. C. Johnson, C. Chua, B. Voisin, S. Kocsis, S. Rubanov, S. G. Robson, J. C. McCallum, D. R. McCamey, S. Rogge, and D. N. Jamieson. Isotopic enrichment of silicon by high fluence $^{28}\mathrm{si}^{-}$ ion implantation. *Phys. Rev. Materials*, 5:014601, Jan 2021. 80

[98] GJ Dolan. Offset masks for lift-off photoprocessing. *Applied Physics Letters*, 31(5):337–339, 1977. 85

[99] Kirt R Williams, Kishan Gupta, and Matthew Wasilik. Etch rates for micromachining processing-part ii. *Journal of microelectromechanical systems*, 12(6):761–778, 2003. 89

[100] J.W.C. De Vries. Temperature and thickness dependence of the resistivity of thin polycrystalline aluminium, cobalt, nickel, palladium, silver and gold films. *Thin Solid Films*, 167(1):25 – 32, 1988. 92

[101] Tom Douce, Michael Stern, Nicim Zagury, Patrice Bertet, and Pérola Milman. Coupling a single nitrogen-vacancy center to a superconducting flux qubit in the far-off-resonance regime. *Phys. Rev. A*, 92:052335, Nov 2015. 99, 103

[102] A. A. Houck, J. A. Schreier, B. R. Johnson, J. M. Chow, Jens Koch, J. M. Gambetta, D. I. Schuster, L. Frunzio, M. H. Devoret, S. M. Girvin, and R. J. Schoelkopf. Controlling the spontaneous emission of a superconducting transmon qubit. *Phys. Rev. Lett.*, 101:080502, Aug 2008. 100

[103] John M. Martinis, K. B. Cooper, R. McDermott, Matthias Steffen, Markus Ansmann, K. D. Osborn, K. Cicak, Seongshik Oh, D. P. Pappas, R. W. Simmonds, and Clare C. Yu. Decoherence in josephson qubits from dielectric loss. *Phys. Rev. Lett.*, 95:210503, Nov 2005. 101

[104] J. Krupka, J. Breeze, A. Centeno, N. Alford, T. Claussen, and L. Jensen. Measurements of permittivity, dielectric loss tangent, and resistivity of float-zone silicon at microwave frequencies. *IEEE Transactions on Microwave Theory and Techniques*, 54(11):3995–4001, November 2006. 101

[105] Aaron D. O'Connell, M. Ansmann, R. C. Bialczak, M. Hofheinz, N. Katz, Erik Lucero, C. McKenney, M. Neeley, H. Wang, E. M. Weig, A. N. Cleland, and J. M. Martinis. Microwave dielectric loss at single photon energies and millikelvin temperatures. *Applied Physics Letters*, 92(11):112903, March 2008. 101, 108

[106] R. W. Simmonds, K. M. Lang, D. A. Hite, S. Nam, D. P. Pappas, and John M. Martinis. Decoherence in josephson phase qubits from junction resonators. *Phys. Rev. Lett.*, 93:077003, Aug 2004. 101, 110

[107] J. Eroms, L. C. van Schaarenburg, E. F. C. Driessen, J. H. Plantenberg, C. M. Huizinga, R. N. Schouten, A. H. Verbruggen, C. J. P. M. Harmans, and J. E. Mooij. Low-frequency noise in josephson junctions for superconducting qubits. *Applied Physics Letters*, 89(12):122516, September 2006. 101, 110

[108] M. Bal, M. H. Ansari, J.-L. Orgiazzi, R. M. Lutchyn, and A. Lupascu. Dynamics of parametric fluctuations induced by quasiparticle tunneling in superconducting flux qubits. *Phys. Rev. B*, 91:195434, May 2015. 102

[109] D. Marcos, M. Wubs, J. M. Taylor, R. Aguado, M. D. Lukin, and A. S. Sørensen. Coupling nitrogen-vacancy centers in diamond to superconducting flux qubits. *Phys. Rev. Lett.*, 105:210501, Nov 2010. 103

[110] Emanuele Albertinale, Léo Balembois, Eric Billaud, Vishal Ranjan, Daniel Flanigan, Thomas Schenkel, Daniel Estève, Denis Vion, Patrice Bertet, and Emmanuel Flurin. Detecting spins by their fluorescence with a microwave photon counter. *Nature*, 600(7889):434–438, December 2021. 103

[111] Simon Gustavsson, Jonas Bylander, Fei Yan, William D. Oliver, Fumiki Yoshihara, and Yasunobu Nakamura. Noise correlations in a flux qubit with tunable tunnel coupling. *Phys. Rev. B*, 84:014525, Jul 2011. 105, 110

[112] M J Schwarz, J Goetz, Z Jiang, T Niemczyk, F Deppe, A Marx, and R Gross. Gradiometric flux qubits with a tunable gap. *New Journal of Physics*, 15(4):045001, apr 2013. 105

[113] G. Catelani, J. Koch, L. Frunzio, R. J. Schoelkopf, M. H. Devoret, and L. I. Glazman. Quasiparticle relaxation of superconducting qubits in the presence of flux. *Phys. Rev. Lett.*, 106:077002, Feb 2011. 109

[114] G. Catelani, R. J. Schoelkopf, M. H. Devoret, and L. I. Glazman. Relaxation and frequency shifts induced by quasiparticles in superconducting qubits. *Phys. Rev. B*, 84:064517, Aug 2011. 109

[115] Leonid I. Glazman and Gianluigi Catelani. Bogoliubov Quasiparticles in Superconducting Qubits. *SciPost Phys. Lect. Notes*, page 31, 2021. 109

[116] Ioan M. Pop, Kurtis Geerlings, Gianluigi Catelani, Robert J. Schoelkopf, Leonid I. Glazman, and Michel H. Devoret. Coherent suppression of electromagnetic dissipation due to superconducting quasiparticles. *Nature*, 508(7496):369–372, April 2014. 109

[117] Simon Gustavsson, Fei Yan, Gianluigi Catelani, Jonas Bylander, Archana Kamal, Jeffrey Birenbaum, David Hover, Danna Rosenberg, Gabriel Samach, Adam P. Sears, Steven J. Weber, Jonilyn L. Yoder, John Clarke, Andrew J. Kerman, Fumiki Yoshihara, Yasunobu Nakamura, Terry P. Orlando, and William D. Oliver. Suppressing relaxation in superconducting qubits by quasiparticle pumping. *Science*, 354(6319):1573–1577, December 2016. 109

[118] T Chang, I Holzman, T Cohen, BC Johnson, DN Jamieson, and M Stern. Reproducibility and control of superconducting flux qubits. *arXiv preprint arXiv:2207.01427*, 2022. 126

[119] T Chang, T Cohen, I Holzman, G Catelani, and M Stern. Tunable superconducting flux qubits with long coherence times. *arXiv preprint arXiv:2207.01460*, 2022. 126

תוכן

תקציר

מחשבים קוונטיים עוררו עניין רב מאז גילוי האלגוריתמים הקוונטיים הראשונים לפני שני עשורים. ואכן, הוכח באופן תיאורטי שמחשבים אלה יכולים לפתור בקלות בעיות מסוימות וקשות כמו הפקת מספרים גדולים למספרים ראשוניים או חיפוש יעיל במסדי נתונים. תכונות ייחודיות אלו הובילו מדענים לדמיין בניית מעבדים קוונטיים המבוססים על מערכות פיזיקליות שונות.

בנייתו של מחשב קוונטי מייצגת אתגר מדעי וטכנולוגי אדיר בשל השבריריות הקיצונית של המידע הקוונטי. הקיוביט חייב להיות מופעל על ידי שערים כדי לחשב מידע ומנותק היטב מהסביבה כדי לשמור על ההתנהגות הקוונטית שלו. מערכת פיזיקלית מעניינת למימוש קיוביטים הם זיהומים מגנטיים במוליכים למחצה, כמו ספינים של ביסמוט בסיליקון. ואכן, ספינים במוליכים למחצה יכולים להגיע לזמני קוהרנטיות ארוכים במיוחד - בסדר גודל של שניות. עם זאת, קשה מאוד לשלוט בצימוד ספין-ספין יעיל. המטרה של עבודה זו היא לפתור בעיה זו ולפתח דרך יעילה לצמד ספינים מרוחקים. כדי להשיג מטרה זו, אנו משתמשים במעגל מוליך-על הנקרא *קיוביט שטף* שמתנהג כמתווך בין ספינים שונים.

בעבודה זו, אנו מפתחים את הכלים הדרושים לפתרון מספר סוגיות מרכזיות למימוש תכנית זו. ראשית, על מנת להשתמש בקיוביט השטף עלינו להגיע למה שנקרא צימוד חזק, שבו הצימוד בין הקיוביט והספין גדול משיעור הדה-קוהרנטיות שלו. בעבודה ראשונה, אנו מדגימים קיוביטים שטף עם מאפייני קוהרנטיות חסרי תקדים. שנית, תדר של הקוביט שטף צריך להיות ניתן לשליטה על מנת להפעיל ולכבות את הצימוד שלו לספין. בעבודה שנייה, אנו מדגימים קיוביטים שטף שניתן לכוונון עם זמני קוהרנטיות ארוכים. לבסוף,הביסמוט צריך להיות בסביבה הקרובה של לולאת הקיוביט, על מנת למקסם את הצימוד. עם זאת, נוכחות של מעגל מתכתי קרוב לזיהום עשויה ליינן אותו. השפעה זו צריכה להיות נשלטת על ידי הפעלת מתח. כדי להשיג זאת, פיתחנו קיוביטים שטף עם גשרים צרים (20-30nm) ומהודים עם מסנני Bragg המאפשרים הפעלת מתח על המצע, תוך שמירה על הקוהרנטיות של הקיוביט.

עבודה זו נעשתה בהדרכתו של ד"ר מיכאל שטרן מן המחלקה לפיסיקה של אוניברסיטת בר-אילן

צימוד של מעגל מוליך-על עם ספיני ביסמוט

חיבור לשם קבלת התואר "דוקטור לפילוסופיה" מאת:

טיקאי שנג

המחלקה לפיזיקה

הוגש לסנט של אוניברסיטת בר אילן

כ"ו בחשון תשפ"ג